

INVESTIGATION OF HETEROGENEOUS PROTEINS AND PROTEIN
COMPLEXES WITH NATIVE ION MOBILITY-MASS SPECTROMETRY
AND THEORY

by

AMBER DAWN ROLLAND

A DISSERTATION

Presented to the Department of Chemistry and Biochemistry
and the Division of Graduate Studies of the University of Oregon
in partial fulfillment of the requirements
for the degree of
Doctor of Philosophy

June 2022

DISSERTATION APPROVAL PAGE

Student: Amber Dawn Rolland

Title: Investigation of Heterogeneous Proteins and Protein Complexes with Native Ion Mobility-Mass Spectrometry and Theory

This dissertation has been accepted and approved in partial fulfillment of the requirements for the Doctor of Philosophy degree in the Department of Chemistry and Biochemistry by:

Michael Harms	Chairperson
James Prell	Advisor
Victoria DeRose	Core Member
Cathy Wong	Core Member
Matthew Barber	Institutional Representative

and

Krista Chronister	Vice Provost for Graduate Studies
-------------------	-----------------------------------

Original approval signatures are on file with the University of Oregon Division of Graduate Studies.

Degree awarded June 2022

© 2022 Amber Dawn Rolland
This work is licensed under a Creative Commons
Attribution 4.0 International (CC BY 4.0)



DISSERTATION ABSTRACT

Amber Dawn Rolland

Doctor of Philosophy

Department of Chemistry and Biochemistry

June 2022

Title: Investigation of Heterogeneous Proteins and Protein Complexes with Native Ion Mobility-Mass Spectrometry and Theory

Native ion mobility-mass spectrometry (IM-MS) offers many advantages for the study of biomolecules and their complexes. High mass accuracy and sensitivity enable unambiguous determination of complex stoichiometries with respect to subunit composition as well as bound ligands. Ion mobility spectrometry adds an additional dimension of separation and can provide some structural information. Native IM-MS experiments are also fast with minimal sample requirements. Because of these reasons, native IM-MS has become an important tool in structural biology, able to investigate challenging samples that may not be amenable to study by other techniques.

However, there are still some major challenges for using native IM-MS in the study of biomolecules. Heterogeneity—arising from the presence of multiple conformations, subunit compositions, ligands and small molecules, for example—results in complicated native mass spectra that can be difficult or even impossible to deconvolute and interpret. Characterizing the heterogeneity of these samples is desirable, as reports of lipids, small drugs, and metals being important for physiological structure and function continue to accumulate. Additionally, interpretation of structural information from IM data has remained largely qualitative, and more fundamental questions about this

technique persist, including detailed understanding of the nature of gas-phase protein structure and behavior and how it might differ from solution-phase. Investigation into this aspect is required to make structural interpretation from native IM-MS data quantitative.

In the first half of this dissertation, strategies to overcome the challenges of heterogeneity are explored, and computational methods are developed to solve the quantitation problem. With these methods, key features of gas-phase protein ion compaction are revealed, allowing more informed interpretation of structural details from this technique. The second half of this dissertation illustrates the wealth of information that can be accessed for challenging, heterogeneous biomolecules in native IM-MS experiments upon application of these computational methods. With results from both experiment and computation, oligomeric states of the membrane pore-forming protein toxin Cytolysin A are identified, and the composition and topology of multimeric β -crystallin protein complexes, which are implicated in cataract formation, are characterized.

This dissertation includes previously published and unpublished co-authored material.

CURRICULUM VITAE

NAME OF AUTHOR: Amber Dawn Rolland

GRADUATE AND UNDERGRADUATE SCHOOLS ATTENDED:

University of Oregon, Eugene
University of Central Arkansas

DEGREES AWARDED:

Doctor of Philosophy, 2022, University of Oregon
Bachelor of Science, Chemistry, 2016, University of Central Arkansas

AREAS OF SPECIAL INTEREST:

Native Ion Mobility-Mass Spectrometry
Protein Biochemistry
Biomolecular Mass Spectrometry
Gas-Phase Protein Structure

PROFESSIONAL EXPERIENCE:

Graduate Teaching Fellow, University of Oregon Department of Chemistry and
Biochemistry, 2016-2017 and 2020-2021

Summer Student Researcher, National Center for Toxicological Research, 2016

GRANTS, AWARDS, AND HONORS:

Graduate Student Travel Award, American Society for Mass Spectrometry, 2022

Pete von Hippel Graduate Scholar Award, University of Oregon Institute of
Molecular Biology, 2021

Doctoral Dissertation Research Fellowship, University of Oregon, 2021

Doctoral Student Service Award, University of Oregon, 2021 and 2020

Centurion Award, University of Oregon, 2021

Peter O'Day Fellowship in Biological Sciences, University of Oregon, 2020

John R. Moore Scholarship, University of Oregon, 2020

National Institutes of Health Molecular Biology and Biophysics Training Grant,
University of Oregon, 2017-2020

Recipient of Diversity, Equity, and Inclusion Grant, University of Oregon
Department of Biology, 2019

ARCS Scholar, ARCS Foundation Oregon Chapter, 2016-2019

Dean's First-Year Merit Award, University of Oregon, 2016

Jerry Manion Chemistry Student Award for Distinction in Academics, Research,
and Service, University of Central Arkansas, 2016

Who's Who Among Students in American Universities and Colleges, University
of Central Arkansas, 2015

PUBLICATIONS:

Rolland, A.D.; Biberic, L.S.; Prell, J.S. Investigation of Charge-State-Dependent Compaction of Protein Ions with Native Ion Mobility-Mass Spectrometry and Theory. *J. Am. Soc. Mass Spectrom.* **2022**, *33*, 369-381.

Rolland, A.D.; Prell, J.S. Approaches to Heterogeneity in Native Mass Spectrometry. *Chem. Rev.* **2022**, *122*, 7909-7951.

Townsend, J.A.; Sanders, H.M.; Rolland, A.D.; Park, C.; Horton, N.; Prell, J.S.; Wang, J.; Marty, M.T. Influenza A M2 Channel Oligomerization is Sensitive to Its Chemical Environment. *Anal. Chem.* **2021**, *93*, 16273-16281.

Forsythe, H.M.; Rodriguez Galvan, J.; Yu, Z.; Pinckney, S.; Reardon, P.; Cooley, R.B.; Zhu, P.; Rolland, A.D.; Prell, J.S.; Barbar, E. Multivalent Binding of the Partially Disordered SARS-CoV-2 Nucleocapsid Phosphoprotein Dimer to RNA. *Biophys. J.* **2021**, *120*, 2890-2901.

Baker, K.; Kwok, E.; Reardon, P.; Rodriguez, D.J.; Rolland, A.D.; Wilson, J.W.; Prell, J.S.; Nyarko, A. Yorkie-Warts Complexes are an Ensemble of Interconverting Conformers Formed by Multivalent Interactions. *J. Mol. Bio.* **2021**, *433*, 166776.

Zhang, J.D.; Donor, M.T.; Rolland, A.D.; Leeming, M.G.; Wang, H.; Trevitt, A.J.; Kabir, K.M.M.; Prell, J.S.; Donald, W.A. Protonation Isomers of Highly Charged Protein Ions can be Separated in FAIMS-MS. *Int. J. Mass Spectrom.* **2020**, *457*, 116425.

Reardon, P.N.; Jara, K.A.; Rolland, A.D.; Smith, D.A.; Hoang, H.T.M.; Prell, J.S.; Barbar, E.J. The Dynein Light Chain 8 (LC8) Binds Predominantly “In-Register” to a Multivalent Intrinsically Disordered Partner. *J. Biol. Chem.* **2020**, *295*, 4912-4922.

Wilson, J.W.; Rolland, A.D.; Klausen, G.M.; Prell, J.S. Ion Mobility-Mass Spectrometry Reveals that α -Hemolysin from *Staphylococcus aureus* Simultaneously Forms Hexameric and Heptameric Complexes in Detergent Micelle Solutions. *Anal. Chem.* **2019**, *91*, 10204-10211.

Rolland, A.D.; Prell, J.S. Computational Insights into Compaction of Gas-Phase Protein and Protein Complex Ions in Native Ion Mobility-Mass Spectrometry. *TrAC Trends Anal. Chem.* **2019**, *116*, 282-291.

ACKNOWLEDGMENTS

I would first like to thank my advisor Professor Jim Prell for all of his guidance and mentorship throughout my graduate school career. Working with Jim has given me the chance to work on many exciting projects and has made me a better scientist. I made lifelong friends by being in the Prell lab, and I want to thank my lab colleagues for making our office an enjoyable place to work, for their input and help in the lab, and their friendship outside the lab. I also want to thank my committee members: Professors Mike Harms, Matt Barber, Cathy Wong, and Vickie DeRose. Their insight and curiosity has led to many helpful discussions that guided my research. Lastly, I want to thank my coauthors and collaborators for the opportunity to work on interdisciplinary research projects on a variety of interesting topics.

The research reported in this dissertation was supported by the National Institute of General Medical Sciences (Award 2T32GM00759 to A.D.R.), National Institute of Allergy and Infectious Diseases (Award R21AI125804 to J.S.P.), National Science Foundation (Award CHE-1752994 to J.S.P.), Oregon Health & Science University-University of Oregon Collaborative Seed Grant (to J.S.P. and K.J.L.), and the National Eye Institute (Award R01EY027012 to K.J.L.). A.D.R. was also supported by the ARCS Foundation as an Oregon Chapter Scholar, by the University of Oregon Doctoral Dissertation Fellowship, and by the Peter O'Day Fellowship in Biological Sciences and Office of the Vice President for Research and Innovation at the University of Oregon (co-awardee with L.S.B.).

TABLE OF CONTENTS

Chapter	Page
I. INTRODUCTION	1
1. Native Mass Spectrometry	2
2. Ion Mobility Spectrometry.....	5
II. APPROACHES TO HETEROGENEITY IN NATIVE MASS SPECTROMETRY	9
1. Introduction.....	9
1.1. How Does Heterogeneity Arise in Native Mass Spectrometry?.....	9
1.2. “Charge-State-Specific” and “Zero-Charge” Mass Spectra	14
2. State-of-the-Art Approaches to Heterogeneity in Native Mass Spectrometry.....	16
2.1. Deconvolution and Construction of a Zero-Charge Mass Spectrum	16
2.1.1. MaxEnt.....	16
2.1.2 Fenn Averaging and Deconvolution Algorithms.....	20
2.1.3. ZScore	22
2.1.4. SOMMS	24
2.1.5. Massign.....	26
2.1.6. PeakSeeker	28
2.1.7. Bayesian Deconvolution: UniDec and PMI Intact.....	29
2.1.8. Game-Theoretic Approach: AutoMass	33
2.1.9. Fourier Transform Approaches: iFAMS.....	35
2.1.10. MetaOdysseus	38
2.2. Data Reduction.....	39

Chapter	Page
2.2.1. Monomer Mass	39
2.2.1.1. FT Methods	39
2.2.1.2. “Double FT”	40
2.2.2. Base Mass or “De-Adducting” Measurements	41
2.2.2.1. SWARM	42
2.2.3. Mass Defect Analysis	44
2.2.3.1. Kendrick Mass Defect Analysis.....	44
2.2.3.2. Macromolecular Mass Defect Analysis.....	45
2.2.4. Modeling Complex Topologies	46
2.2.4.1. SOMMS	47
2.2.4.2. CHAMP	48
2.2.4.3. SUMMIT.....	48
2.3. Instrumental and Experimental Approaches	49
2.3.1. Charge Detection of Single Particles	49
2.3.1.1. Benner Trap	50
2.3.1.2. CDMS in Orbitrap Instruments.....	53
2.3.2. Cutting-Edge IM-MS Instrumentation.....	53
2.3.3. Ion Reactions for Improved Separation	59
2.3.3.1. Charge Manipulation	59
2.3.3.2. Ion/Ion Reactions	61
2.4. Global Approaches to Heterogeneity.....	63
2.4.1. Average Composition	63

Chapter	Page
2.4.1.1. Inference from Fragmentation Data.....	64
2.4.1.2. “Double FT” Approach.....	65
2.4.1.3. Distinguishing Compositional Heterogeneity Types Using FT-Based Methods.....	65
2.4.2. Assigning Biomolecular Ions to Chemical and Structural Class.....	68
2.4.2.1. Small Biomolecular Ions.....	68
2.4.2.2. Classification of Large Biomolecular Ion Conformation Using Native IM-MS Data.....	69
2.4.2.3. Gábor-Transform Isolation of Biomolecular Ion Signal from High-Salt Background Signal	71
3. Conclusions and Outlook.....	72
3.1. Current State of the Field.....	72
3.2. Remaining Challenges	75
3.2.1. Recalcitrant Features of Heterogeneity.....	75
3.2.2. Is There a “Complexity Limit” in Native Mass Spectrometry?.....	76
3.2.3. Education Barriers	77
3.3. Future Strategies and Best Practices	78
III. COMPUTATIONAL INSIGHTS INTO COMPACTION OF GAS-PHASE PROTEIN AND PROTEIN COMPLEX IONS IN NATIVE ION MOBILITY-MASS SPECTROMETRY	82
1. Introduction.....	82
2. What are “Native” nESI Conditions?	83
3. What Happens to Folded Protein Ions upon Transfer to the Gas Phase?	87
3.1. Ubiquitin	91

Chapter	Page
3.2. Cytochrome <i>c</i>	93
3.3. Retention and Loss of Condensed-Phase Structure in Peptides and Small Proteins	94
3.4. Protein Complexes	95
3.5. Explicit Modeling of nESI Droplet Evaporation and Ion Charging Process	97
4. Comparison of MD Results with Different Force Fields for Ion Compaction upon Transfer to Vacuum	98
4.1. MD Simulation Method	98
4.2. Maximal Degree of Compaction Predicted from MD Simulations	99
4.3. Changes in Secondary Structure and Number of Hydrogen Bonds and Salt Bridges	100
4.4. Collapse of Cavities and Grooves	101
4.5. Comparison of MD Results to Native IM-MS CCS Data	103
5. Summary and Outlook	104
IV. INVESTIGATION OF CHARGE-STATE-DEPENDENT COMPACTION OF PROTEIN IONS WITH NATIVE ION MOBILITY-MASS SPECTROMETRY AND THEORY	106
1. Introduction	106
2. Experimental Section	111
2.1. Molecular Dynamics Simulations, Charge Placement, and Collision Cross-Section Calculations	111
2.2. CCS Calculations for Identical Structures Varying Only in Charge	113
2.3. Projection Approximation CCS Calculations	113
2.4. Analysis of Structural Features	113

Chapter	Page
3. Results and Discussion	114
3.1. Experimental Trends in Collision Cross-Section with Charge for Globular Protein Ions	114
3.2. Global Trends in Protein Ion Structural Features with Charge State.....	116
3.3. Trends in Structural Features across Protein Native Charge State Distributions	121
3.4. Expected Collision Cross-Section Trends for Identical Structures Varying Only in Charge.....	125
3.5. Principal Component Analyses of Structural Features	129
4. Conclusions.....	132
 V. SYMMETRIC DISSOCIATION OF OLIGOMERIC COMPLEXES OF CYTOLYSIN A UPON COLLISIONAL ACTIVATION IN DIFFERENT MASS SPECTROMETER PLATFORMS	138
1. Introduction.....	138
1.1. Cytolysin A Oligomeric Pore Complexes.....	139
1.2. Gas-Phase Dissociation Techniques	140
2. Methods.....	143
2.1. Cytolysin A Expression and Purification.....	143
2.2. Screening Detergents for ClyA Oligomerization.....	145
2.3. Native Mass Spectrometry of ClyA.....	145
3. Results and Discussion	146
3.1. Detergent-Induced Oligomerization of ClyA	146
3.2. Symmetric Dissociation Observed upon Collisional Activation	147
3.3. Surface-Induced Dissociation Supports Quaternary Structure Involving Equal Subunit Interfaces	150

Chapter	Page
3.4. Correlating Dissociation Pathway with Collisional Activation in Different Instrument Regions for ClyA Octamers.....	151
3.5. Larger ClyA Oligomers Only Followed Symmetric Dissociation Pathways	155
4. Conclusions.....	158
VI. NATIVE ION MOBILITY-MASS SPECTROMETRY REVEALS COMPOSITION AND TOPOLOGY OF HETEROOLIGOMERIC COMPLEXES FORMED BY EYE LENS β-CRYSTALLIN PROTEIN ISOFORMS	161
1. Introduction.....	161
2. Methods.....	165
2.1. Protein Expression and Purification.....	165
2.2. Native Electrospray Ionization Ion Mobility-Mass Spectrometry Experiments	166
2.3. Homo-Oligomer Formation as a Function of Concentration.....	167
2.4. Kinetics of Heterodimer Formation.....	168
2.5. Analysis of Ion Species Abundance	168
2.6. Generation of Model Structures, Molecular Dynamics Simulations, and Collision Cross-Section Calculations.....	169
3. Results and Discussion	170
3.1. β -Crystallin Isoforms β B2 and β A3 Readily Homo-Oligomerize, While β B1 is Primarily Monomeric.....	170
3.2. β -Crystallin Isoform β A3 Forms Heterodimers with β B2 with a Greater Rate than with β B1	175
3.3. β -Crystallin Oligomeric Complexes Adopt Compact Topologies.....	179
4. Conclusions.....	182
VII. OUTLOOK.....	185

Chapter	Page
APPENDIX: SUPPLEMENTAL INFORMATION FOR CHAPTER IV	188
REFERENCES CITED.....	216

LIST OF FIGURES

Figure	Page
1. Example of MaxEnt mass spectral deconvolution for an intact antibody	17
2. Deconvolution of carbonic anhydrase II ESI spectrum using Fenn’s deconvolution algorithm	22
3. Deconvolution of both low and high resolution ESI mass spectra for a mixture of three proteins using ZSCORE	24
4. Assignment of peaks in native mass spectrum for rotary ATPase using Massign	27
5. Peak fitting and deconvolution of native mass spectrum for human TCP-1 ring complex using PeakSeeker	29
6. Native mass spectrum of native oligomeric state distribution for polydisperse α B-crystallin as revealed using UniDec.....	31
7. Native mass spectrum of aquaporin Z with bound lipids after application of UniDec’s SoftMax function.....	32
8. Comparison of deconvolution of ESI mass spectra for PEGylated granulocyte colony stimulating factor protein using different deconvolution algorithms.....	34
9. Schematic of iFAMS Fourier transform-based algorithm	36
10. Deconvolution of native mass spectrum of MSP1D1 Nanodiscs using iFAMS Fourier transform-based algorithm	37
11. UniDec-based “double FT” analysis of native mass spectrum of Nanodiscs containing mixtures of lipids	41
12. Native mass spectrum of human galectin-3 from application of SWARM.....	43
13. Native mass spectra of charge-reduced Nanodisc-embedded melittin MMD profiles reconstructed using MetaUniDec	47
14. Representative native mass spectra of intact yeast exosome and its subcomplexes interaction networks generated by SUMMIT.....	50
15. Two-dimensional histogram of single-ion signals measured using Orbitrap CDMS of immunoglobulin-M oligomers	54

Figure	Page
16. Arrival time distribution of reverse-sequence peptides as a function of number of passes around cyclic TWIM cell	56
17. Schematic of entrance and exit gate synchronous chirped pulsing for FT-drift tube ion mobility-MS experiments	58
18. Native mass spectrum of ammonia channel B trimers illustrating charge reduction by TMAO and observable lipid adducts	61
19. Native mass spectrum of bovine serum albumin and yeast enolase dimer CAPTR.....	62
20. Post-ion attachment mass spectrum of 70S ribosome-related subunits.....	63
21. Different classes of compositional heterogeneity for analyte mixtures.....	66
22. Composite nitrogen drift tube IM-MS data illustrating separation according to structure type.....	70
23. Representative native mass spectra of globular proteins and intrinsically disordered proteins.....	71
24. Native-like anthrax toxin Lethal Factor N-terminal domain Gábor spectrogram illustrating separation of protein signal and sodium chloride clusters.....	73
25. Depiction of charging and self-solvation for globular protein ions during evaporation of the nanoelectrospray droplet.....	85
26. Illustration of condensed-phase protein structure types and typical charge state and CCS distributions in IM-MS experiments.....	86
27. Compaction of protein ions produced by nESI measured by IM-MS as compared to CCSs for condensed-phase structures	88
28. Structures of protein ions before and after MD simulation of gas-phase compaction.....	100
29. Plot of experimental drift tube CCS values versus charge state and mass	109
30. Example of typical compaction before and after simulation	118
31. Structural feature trends as a function of charge state for set of simulations of 17 IM-MS calibrant proteins.....	119

Figure	Page
32. Average percent difference between experimental drift tube and simulated CCS for BLG, ConA, and GDH charge state conformations	123
33. Relatively strong correlations of surface residues and hydrogen bonds with charge state for BLG	125
34. Plots of computed CCSs for simulated charge conformers of BLG, ConA, and GDH, with values re-calculated assuming identical protein ion structure.....	126
35. Average percent differences in CCS for simulated charge conformers using the Trajectory Method and Projection Approximation.....	128
36. Principal component analysis of BLG, ConA, and GDH structural features	130
37. ClyA octameric complexes formed in DDM dissociate symmetrically into tetramers as well as into canonical CID products	148
38. Dissociation of ClyA octameric complexes formed in DDM upon activation in the trap region of a Waters time-of-flight mass spectrometer	150
39. Surface-induced dissociation of octameric ClyA complexes formed in C12E8....	151
40. Dissociation of octamers of ClyA formed in DDM with activation in both the source and collisional cell of a ThermoFisher Orbitrap UHMR instrument	154
41. Native mass spectra for a dilution series of individual β -crystallin isoforms and relative abundances of homo-oligomers	174
42. Homodimer abundance for each of the three β -crystallin isoforms.....	174
43. Native mass spectra illustrate differences in the formation of β B1/ β A3 and β B2/ β A3 heterodimers	177
44. Example illustrations of various topologies of model structures.....	180
45. Comparison between experimental collision cross-section for oligomeric species of β -crystallin proteins and those computed for model structures	182

LIST OF TABLES

Table	Page
1. Overview of types of theory used to simulate gas-phase protein ions.....	89
2. Overview of programs for computing collision cross sections of gas-phase ions	90
3. Summary of results from MD simulations of ion compaction on transfer to gas phase.....	102
4. Measured accurate monomer mass of each of the three β -crystallin isoforms.....	171

CHAPTER I

INTRODUCTION

Development of new pharmaceuticals and biotechnologies (such as vaccines and treatments against diseases and pathogens, therapeutics to selectively target malignant cells, and drug delivery systems) relies upon accurate understanding of the structure and function of biomolecules and their complexes. For proteins and protein complexes, important features to characterize include mass and oligomeric state (the number of individual protein subunits bound together in the complex), composition (identity and number of subunits), binding of small molecules (e.g., lipids, detergents, sugars, metals, and other co-factors), and structure at all levels of detail from primary to quaternary, as well as different conformations adopted.¹⁻⁶ A major category of proteins of interest for these applications is membrane proteins, which are targeted by more than half of all new pharmaceuticals.^{7,8}

A host of biophysical techniques (including X-ray crystallography, nuclear magnetic resonance, and, more recently, cryo-electron microscopy) have enabled determination of protein structure at atomic resolution.^{2,9-14} These highly-detailed structures can reveal many of the features listed above: oligomeric state, subunit composition, bound ligands, and, of course, secondary, tertiary, and quaternary structure.¹⁵ However, these methods can be time-intensive and costly and have restrictions on the size, concentration, and solution conditions of the samples amenable for study, which could lead to determination of structures that are not physiologically relevant, exhibit non-specific interactions, or form spurious oligomers.¹⁶⁻²³ In addition to

these possible drawbacks (which exist even for soluble proteins),²⁴⁻²⁷ membrane proteins present additional challenges of their own due to their dependence upon a membrane-like (i.e., lipid and detergent) environment for stability.^{28,29} Although many structures of membrane proteins have been solved with much effort using these techniques, it remains challenging to resolve bound lipids and detergents.³⁰ The requirement for solution conditions conducive to crystallization and/or immobilization, which can often exclude many lipids and detergents, prohibits complete understanding of the structure and function of these and other heterogeneous biomolecular complexes.³¹⁻³⁸ In the following chapters, I illustrate how advances in native mass spectrometry, ion mobility spectrometry, and adjuvant computational chemistry can address some of these major challenges.

1. Native Mass Spectrometry

Native mass spectrometry (MS), which aims to preserve non-covalent interactions and thus allow study of intact complexes, is a powerful technique that can in many cases overcome these limitations for heterogeneous and membrane protein complexes.³⁹⁻⁵² Highly sensitive and accurate mass measurements enable unambiguous determination of the oligomeric state, subunit composition, and bound ligands, even when multiple different proteins and ligands are present and the composition of their complexes is heterogeneous.⁵³⁻¹⁰⁰ Crucially, solution conditions can be easily varied with electrospray ionization, enabling exploration of a wide variety of sample environments and development of a more comprehensive understanding of biomolecular structure.¹⁰¹⁻¹⁰⁶ Once the native ions have been transferred into the vacuum environment of the mass spectrometer, a wide and flexible variety of tools are available to further interrogate their

composition, size, and structure during their journey toward the detector.^{82,107-141} These methods may or may not include dissociation of covalent and non-covalent interactions and can inform on structure from amino acid sequence and locations of post-translational modifications all the way up to the three-dimensional topology of large, hetero-oligomeric membrane protein complexes with attached lipids.^{61,73,84,86,97,142-151}

Because of these advantages and improvements to instrument design,¹⁵²⁻¹⁵⁶ native MS has been used to characterize biomolecules of ever-increasing complexity and in impressive detail.^{3,41,42,53,157} Methods developed by Robinson and by Sharon now enable the study of membrane proteins directly from membrane and vesicle environments, as well as endogenous proteins from crude media and lysates.^{54,83,158-161} Careful investigation of lipid dissociation from membrane protein complexes in the gas phase has been used to discriminate between structural and annular lipids.^{91,162-165} Collision-induced unfolding,¹¹⁴ a technique pioneered by Ruotolo and coworkers, has been used to distinguish between very subtle differences in antibody and antibody-drug complexes.^{98,146,166} The development of surface-induced dissociation¹¹⁷ by Wysocki and coworkers has made it possible to learn details of quaternary structure and subunit arrangement from native MS experiments.^{58,86,118,144} Development of membrane mimetic technology and deconvolution tools^{44,167-172} enables resolving lipid binding events, including their kinetics.¹⁷³⁻¹⁷⁵ MDa complexes such as viral particles are now commonly studied with native MS, an advance made possible by innovation in charge detection MS, with many useful applications in structural biology and biotechnology.^{124,156,176-178} The native MS literature is continually expanding with examples that push the boundaries of the size and complexity limits of what can be studied with this technique.

However, one major problem can still arise in native mass spectrometric analysis of these challenging biomolecules involving multiple subunits, ligands, and conformations. Any variation in the number or identity of bound ligands, presence of multiple conformations, or differences in complex stoichiometries, to give a few examples, complicates the mass spectrum, sometimes to such a great extent that the data cannot be interpreted by conventional approaches.^{157,179} For just one type of biomolecule analyzed with native ESI-MS, multiple peaks will be present in the mass spectrum, representing an approximately Gaussian-shaped distribution of charge states.^{104,180-182} As the complexity of the sample increases, so too does the mass spectrum, resulting from overlapping signal for ions differing not only in charge state but also the numbers and identities of bound ligands. Incomplete desolvation and adduction of small molecules and salts broaden peaks further. If more than one structure or subunit stoichiometry is present, the spectrum becomes even more congested. Often, this results in a broad peak that can span several thousand m/z values that are extremely difficult to interpret manually.^{71,183}

While there are many strategies to reduce the heterogeneity of samples before introduction into the mass spectrometer (e.g., additional purification schemes to separate out the different biomolecular species or use of enzymes to remove ligands and other small molecules),^{47,184} often it is desirable to preserve native heterogeneity in order to access interesting, biologically relevant information. There are many examples of protein structure and function being dependent upon the presence of ligands, where removing them would perturb the biomolecular system of interest and prohibit study of the most physiologically relevant states.^{55,69,90,94,164,178,184-188} Recently, breakthroughs in mass spectrometry have dramatically increased the sample heterogeneity that can be tolerated

in native MS—from the development of new deconvolution algorithms and computational tools to the use of solution additives to manipulate charge and facilitate interpretation, to the design of new powerful instrumentation, and many other efforts.^{41,42,157} Even with all of the unique advantages native MS offers for the study of challenging biomolecules—minimal sample requirements, experiment speed, flexible solution conditions, high mass accuracy and sensitivity—no useful information can be gleaned if the spectrum is uninterpretable, highlighting the importance of overcoming the problem of heterogeneity first and foremost before any biologically-relevant problems can be addressed.

2. Ion Mobility Spectrometry

With the integration of ion mobility spectrometry into commercial mass spectrometer instruments,^{127,152,189-199} native MS can also provide some structural information. This gas-phase electrophoretic technique provides an orthogonal dimension of information by separating ions based on size and shape due to differences in drag force created by flow of an inert gas in the opposite direction of the ions.^{135-138,140,200} Measurement of the drift time (how long it takes ions to traverse the ion mobility cell) enables determination of the collision cross-section,²⁰¹⁻²⁰⁴ akin to the rotationally-averaged shadow of the ion with units of nm². Importantly, in the ion mobility spectrogram, ions which overlap in m/z can be visually separated based on their drift time. Based on the range of drift times occupied by the same ion species, researchers can also often qualitatively gauge whether ions have adopted globular or unfolded conformations, as well as whether multiple conformations are present.^{201,205-211} Collision cross-section measurements alone are not very meaningful, as a single value could in

principle correspond to many different structures. Thus, it is common to compute an expected collision cross-section value for a condensed-phase structure coordinate file with which to compare.^{207,212-220} However, this is complicated by the well-documented observation that the experimental CCSs are often smaller than their computed counterparts due to compaction of ions upon transfer to the gas-phase.^{215,221-225} With differences of up to ~30% between experimental CCSs and those computed from condensed-phase structures and a lack of benchmarking, conclusions are largely limited to saying whether a proposed structure is or is not consistent with the experimental data.

From the qualitative nature of these results, it is clear that IM-MS technology has outpaced the ability to interpret the structural information contained in its data. This represents a fundamental drawback in native ion mobility-mass spectrometry. To fully take advantage of these experiments' speed, flexibility, and mass accuracy and sensitivity, the interpretation of IM-MS structural measurements must be made quantitative. Thus, the first goal of this dissertation research was to develop computational methods to resolve this issue by enabling quantitative comparison between experimental and computed collision cross-sections with a well-defined expected range of error and to investigate features of gas-phase protein ion structure and compaction. The second objective was to combine these computational approaches with native ion mobility-mass spectrometry investigation of heterogeneous protein complexes to uncover new features important for understanding their structure and function. The more complex, detailed information that improving the interpretation of ion mobility structural data enables researchers to access underscores the utility of this technique in advancing understanding and applications of structural biology.

In Chapter II, I discuss sources of heterogeneity that complicate native mass spectrometry analysis and comprehensively review state-of-the-art computational, instrumental, and experimental strategies aimed at facilitating deconvolution and interpretation of heterogeneous native mass spectra. This chapter includes co-authored material from James S. Prell. In Chapter III, I review computational and theoretical efforts to understand gas-phase protein ion compaction. I then validate a force field molecular dynamics simulation protocol that robustly produces structures for which the computed collision cross-sections match literature values within a narrow range of error for a large set of native protein ions. This chapter includes co-authored material from James S. Prell. In Chapter IV, I further discuss features of gas-phase protein ion compaction in the context of the relationship between structure and charge both generally and for ions from the same protein native charge state distribution. This chapter includes co-authored material from Lejla S. Biberic and James S. Prell.

In Chapters V and VI, I combine these computational methods with native ion mobility-mass spectrometry experimental work to investigate features of heterogeneous protein complexes. In Chapter V, I demonstrate the dependence of complex oligomeric state upon the detergent environment for a pore-forming toxin protein, highlighting the advantage of native IM-MS to enable the study of biomolecules in a variety of solution conditions not possible with other state-of-the-art techniques. Different dissociation pathways are also investigated in the context of different levels of activation available within different mass spectrometer platforms. This chapter includes co-authored material from Jesse W. Wilson, Sophie R. Harvey, Vicki H. Wysocki, and James S. Prell. In Chapter VI, I apply these computational and experimental methods to identify the

oligomeric states, stoichiometries, and possible topologies of the complexes formed by human eye lens β -crystallin protein isoforms. This chapter includes co-authored material from Takumi Takata, Micah T. Donor, James S. Prell, and Kirsten J. Lampi.

CHAPTER II

APPROACHES TO HETEROGENEITY IN NATIVE MASS SPECTROMETRY

Includes co-authored material reprinted with permission from:

Rolland, A.D.; Prell, J.S. Approaches to Heterogeneity in Native Mass Spectrometry. *Chem. Rev.* 2022, 122, 7909-7951. © 2022 American Chemical Society.

1. Introduction

1.1. How Does Heterogeneity Arise in Native Mass Spectrometry?

Native mass spectrometry (MS) enables preservation of noncovalent interactions and thus study of intact biomolecular complexes.^{47,67,226} With this technique analytes are gently ionized from aqueous solution into the gas phase, and the mass-to-charge ratio (m/z) is measured. Instrumental parameters are carefully controlled to produce ion populations with low charge states and minimally-perturbed structures, in line with the general goal of native MS to preserve native-like structure (i.e., as close to structures present in the condensed phase as possible). This is most commonly achieved using electrospray ionization (ESI) from approximately micron-diameter capillaries (“nanoelectrospray ionization”, nESI).²²⁷ Volatile buffer salts (e.g., ammonium acetate), which disproportionate into volatile neutral molecules that evaporate during nESI, are often used in native MS to produce adequate ionic strength (~100 mM or greater) to maintain biomolecular folds in solution rather than common non-volatile biochemical buffer salts (e.g., sodium chloride). This is due to the propensity of the latter to condense onto the biomolecular ions in essentially random stoichiometries, spread the signal of interest into many peaks, and reduce resolution, as well as to suppress ionization and signal of analytes of interest.^{104,180,181,228-231} Though it is possible to use other ionization

methods, such as Matrix-Assisted Laser Desorption Ionization (MALDI)^{232,233} or “Inlet Ionization”,²³⁴ to transfer native-like ions to the gas phase, this review focuses on approaches to heterogeneity in native nESI-MS.

Since the introduction of biomolecular ESI in 1989 by Fenn and coworkers²³⁵ and subsequent pioneering work in the study of intact biomolecular complexes,²³⁶⁻²⁵⁴ the capabilities of native MS have rapidly advanced. While a comprehensive treatment of the history of this field^{101,226,255-258} is beyond the scope of this review, we highlight major advancements in instrumentation in the 1990s and early 2000s, including the extension of quadrupole m/z ranges, improvements in transmission of large complexes and mass resolution, and development and commercialization of quadrupole-time-of-flight (Q-TOF), ion mobility-mass spectrometry (IM-MS), and Orbitrap instruments.^{72,153,154,191-193,259-267} These early improvements in turn enabled native MS investigation of samples of ever-increasing size and complexity, including intact viruses and MDa-size complexes.^{247,249,268,269} Landmark achievements in the mid-2000s and 2010s expanded the use of native MS to membrane proteins embedded in detergent micelles,^{270,271} lipid Nanodiscs,²⁷²⁻²⁷⁴ and other membrane mimetics,^{44,275,276} as well as proteins with numerous proteoforms and extensive glycosylation.^{148,277} These advancements together with the advantages offered over classic techniques, such as easily-changed solution conditions, minimal sample requirements, and experiment speed, have led to a rapid rise in the use of native MS as a valuable tool in structural biology.^{47,50,139,185,256,258,278-280}

However, the expansion of native MS to study more complex samples has introduced concomitant challenges in interpreting their often highly complicated mass spectra. Ions of large biomolecules and their complexes produced by nESI typically

exhibit a distribution of charge states, owing in part to the stochastic nature of the number of charges in the late nESI droplet at the time the biomolecule/complex is ionized.^{104,180,181} For relatively homogeneous ion populations, this charge state distribution is often approximately Gaussian,¹⁸² and the presence of a non-Gaussian charge state distribution may indicate heterogeneity. In either case, the signal of each biomolecule/complex is thus spread out across the m/z spectrum at several peaks, and a basic goal of native MS is to determine the mass and charge state of each ion from this peak distribution. How, then, does heterogeneity arise in native MS? For the purposes of this review, we define a “heterogeneous” ion population to be one composed of multiple ions that differ in ways beyond their isotopic composition, charge state, or the identity of the charge carrier. Heterogeneity can arise from the biology that produces the individual biomolecules in question (e.g., proteoforms of a protein), distributed association of these biomolecules into complexes (e.g., different stoichiometries of the protein or other biomolecule monomers in related complexes), the presence of multiple conformations or topologies of the same biomolecule/complex in solution, binding of small molecules and ligands (such as lipids, polysaccharides, or other cofactors), adduction of metals and salts present in the aqueous buffer solution, or even from artifacts of the nESI process, such as unwanted activation and dissociation of otherwise homogeneous complexes.^{48,181,281,282} In some extreme cases, the mass spectrum for a heterogeneous native ion population may even superficially resemble that of a polydisperse long-chain polymer ion population produced by ESI, with tens or even hundreds of overlapped peaks in the mass spectrum and a wide distribution of charge states.^{60,63,71,283}

It has therefore long been recognized that combatting heterogeneity is essential for the success of MS in accurately characterizing native biomolecular samples. Much discussion in the literature to date,^{47,184,257,284} especially early in the history of this field, has focused on approaches that aim to reduce complexity and heterogeneity at the sample preparation stage with additional or refined purification steps and chromatographic separations or through gas-phase fragmentation/dissociation (such as in tandem MS,^{113,128,133,239,252,285} native top-down MS,^{109,110,286,287} and other methods^{77,111,112,115,129,131,134,165,239,241,248,261,284,288-303}) of the heterogeneous subunits. However, advancement in structural biology relies fundamentally upon accurate understanding of biomolecular structure and function in physiologically relevant states, and examples illustrating the importance of heterogeneous features, such as different proteo- and glycoforms, stoichiometries and identities of bound ligands and other cofactors, and multiple coexisting stoichiometries or conformations, in both functional and disease-associated systems abound.^{55,69,90,164,178,184-188}

Thus, this review focuses on approaches which do not seek to rid biomolecular samples of their inherent heterogeneity and instead aim to facilitate interpretation and analysis of their complicated spectra. Strategies of this kind include use of software tools and deconvolution algorithms to directly analyze all mass spectral data as recorded by the instrument (data post-processing and analysis, which are the topics of §2.1 and §2.2), instrumental and experimental approaches aimed at separating ion signals online with mass and charge measurements (§2.3), and manipulation of ion populations to spread out otherwise overlapped signals with solution additives or ion/ion reactions (§2.3). Strategies for extracting composition and structural information without complete

analysis of mass spectral data are described in §2.4, including a classification of common heterogeneity types. The order in which algorithms and computational methods are presented should not be taken to imply strict chronology or judgment of value. We also note that the first three algorithms described (§2.1.1-2.1.3) were developed originally for interpretation of denatured ion mass spectra but have also been applied to intact native MS data. We begin discussion of algorithms with MaxEnt (§2.1.1), though this algorithm is not the earliest described here, because it is still widely available and used today through commercial implementations and because its underlying theory predates even the application of ESI to the study of biomolecular complexes.

Below, we highlight some of the most important and widely-used data analysis, experimental, and instrumentation-based approaches to tackling the problem of heterogeneity in native MS, dating from the 1990s to the present and focusing on developments in the last decade. We note that, while available deconvolution algorithms and data analysis tools have been discussed in other reviews,^{212,304-306} these have largely focused on their applications, rather than their theoretical basis, benefits, and potential drawbacks. In the interest of filling this gap in the literature, we devote a majority of our discussion to the sections describing data analysis approaches to heterogeneity, as a major objective of this review is to educate potential users on both theoretical and practical aspects of the available tools. While the focus of this review is not on the applications of these algorithms and other methods, we provide references of this kind for interested readers. We follow this with discussion of other (instrumental and experimental) approaches which, in parallel to data analysis algorithms, aim to facilitate interpretation of heterogeneous mass spectra through data simplification and reduction

while preserving heterogeneity instead of through sample preparations and/or dissociation methods that result in loss of information. In these sections we draw upon the numerous comprehensive reviews of these specific topics. Although many online solution-phase separation approaches (such as online chromatography methods³⁰⁷⁻³¹⁸ and capillary zone electrophoresis³¹⁹⁻³²⁵) have been introduced to help solve this problem, our discussion is confined to instrumentation and techniques commonly available within mass spectrometers themselves or with small modifications. As this review is written from an academic viewpoint, we refer readers not only to recent native MS work on biotherapeutics^{6,59,122,307,326-330} but also to many recent efforts and helpful perspectives on this topic from industry scientists representing a variety of biopharmaceutical companies, drawing upon these insights where possible.^{45,76,109,145,184,311,331-337} Importantly, though implementation of the methods we describe below faces unique challenges in industry (namely, rigorous standardization and commercialization),³³¹ we hold that educating potential users on the theoretical aspects of these approaches is important and beneficial to all who utilize native MS, regardless of background. We conclude by reflecting upon the progress of native MS with respect to the problem of heterogeneity, discussing remaining challenges and future strategies for the field, and providing our view of optimal approaches to facilitate analysis and interpretation of the complicated mass spectra of heterogeneous biomolecules, which is paramount for continued growth of this technique as a tool in structural biology.

1.2. “Charge-State-Specific” and “Zero-Charge” Mass Spectra

In principle, every mass spectrum can be decomposed into separate mass spectra for ions of each particular charge state in the observed ion population. For a completely

monodisperse ion population, in which all ions are identical but for their isotopic contents, charge state, and charge carriers, these “charge-state-specific” mass spectra will each contain essentially the same information, varying only in abundance according to the charge state distribution. However, for an ion population whose composition varies as a function of charge state, extracting charge-state-specific mass spectra from the observed mass spectrum may make these composition differences much clearer and inform further investigation of the possible physiological or other relevance of these differences. At other times, it can be useful to compile the mass and charge information from all identifiable charge states into a single plot of abundance versus mass (i.e., not m/z), possibly after subtracting the mass of any charge carriers. Such a plot is called a “zero-charge” mass spectrum and is akin to other mass distribution measurements, as in size exclusion chromatography, multi-angle light scattering, and analytical ultracentrifugation, albeit with the typically much greater sensitivity and mass resolution offered by mass spectrometry.²²⁶

Beyond producing either zero-charge and/or charge-state-specific mass spectra after deconvolution (§2.1), it can often be useful to accurately determine the mass of the repeated subunit within a polydisperse sample or the mass which is conserved across all members of the polydisperse ion populations (§2.2). Some software tools also enable deduction of the subunit topology of complexes (§2.2), which provides additional useful information in understanding biological structure and function. Instrumental and experimental methods, such as those which separate ions in dimensions other than m/z and those which manipulate ion charge states, add to the arsenal of information which can be gleaned from otherwise complicated mass spectra of heterogeneous samples

(§2.3). Even with these state-of-the-art methods, it is sometimes not possible to fully analyze the mass spectrum, but useful information can often be obtained from a more coarse-grained or global perspective (§2.4).

In the following section, we discuss how these different types of information can be obtained from native mass spectra of heterogeneous samples using state-of-the-art computational, instrumental, and experimental methods. These strategies enable uncovering a plethora of valuable information important for proper understanding of structure and function as well as for quality control of manufactured biotherapeutics for extremely challenging samples, such as membrane proteins, lipid Nanodiscs, polymers, antibodies, viruses, and other large biomolecular complexes.^{49,93,95,177,184,338} This includes, for example, identities and stoichiometries of lipids, detergents, and other small molecules bound, profiling of glyco- and proteoforms, determination of subunit composition and topology, and characterization of the conformation and polydispersity of large complexes.

2. State-of-the-Art Approaches to Heterogeneity in Native Mass Spectrometry

2.1. Deconvolution and Construction of a Zero-Charge Mass Spectrum

2.1.1. MaxEnt

One of the oldest and most widely-used approaches to deconvolution of biomolecular mass spectra, especially those exhibiting multiple charge states for each ion, is the maximum-entropy or “MaxEnt” method introduced by Skilling in 1984.³³⁹ Although application to deconvolution of mass spectra and commercialization was not achieved until the 1990s, this algorithm traces its roots back much earlier to work³⁴⁰⁻³⁴² by Shannon, Shore and Johnson, and Tikochinsky, Tishby, and Levine, who developed

the concept of information entropy relating to the probability of observing various noisy data sets based on a hypothetical underlying (i.e., noiseless) data set. After initially applying the algorithm to challenges in image processing,³³⁹⁻³⁴² Skilling, Ferrige and coworkers recognized the potential for applying it more generally to other signal processing problems, including deconvolution of electrospray mass spectra.³⁴³⁻³⁴⁵ MaxEnt is still employed today in deconvolution of mass spectra, including as recently as 2021 in which this method was used to characterize structural glycoform heterogeneity of the SARS-CoV-2 spike protein receptor-binding domain.⁹⁶ **Figure 1** illustrates use of MaxEnt for intact antibody samples and glycan-mediated heterogeneity.³⁴⁶ Additional examples of applications of MaxEnt deconvolution to investigation of various intact noncovalent complexes throughout the past several decades are provided in the references.^{96,346-365}

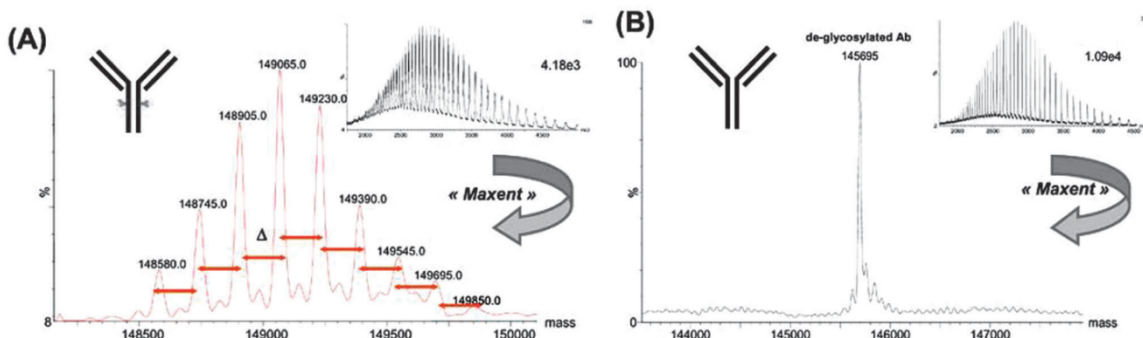


Figure 1. Example of MaxEnt mass spectral deconvolution for an intact antibody exhibiting multiple glycoforms (A) and after de-glycosylation (B). Insets show mass spectra used for deconvolution. Reprinted in part with permission from ref. 346. © 2008 Bentham Science Publishers Ltd.

Broadly, the MaxEnt algorithm attempts to explain observed data in the mass spectrum by 1) generating a hypothetical zero-charge spectrum, 2) dividing the hypothetical masses by each of the charge states assumed to be present in the ion distribution (with a correction for the charge carrier mass), and 3) adding the resulting

m/z distributions with a charge-state-specific abundance scaling together in the mass spectrum and comparing these to the observed data.³⁴³⁻³⁴⁵ Ideally, mismatches (i.e., “error”) between the hypothetical and observed mass spectra should be randomly distributed over all m/z values. Mathematically, this means that the plausibility for a particular hypothetical mass spectrum given an observed mass spectrum is greatest when the “evidence”, defined as $-\sum_{m/z} p(\varepsilon(m/z)) \log(p(\varepsilon(m/z)))$, with $\varepsilon(m/z)$ the error at a given m/z value and $p(\varepsilon(m/z))$ its probability, is maximized.^{339,343} In other words, a “good” fit to an experimental mass spectrum should not have error piled up into just a few m/z values, rather the error should be spread out over all m/z values. Marshall and coworkers introduced an implementation of MaxEnt in 1997 in which the distribution of charge states is assumed to be “smooth” for electrospray mass spectra, i.e., there is an “evidence” penalty for abrupt discontinuities in the charge state distribution assigned to each peak in the zero-charge spectrum.³⁶⁶

Practically, MaxEnt requires specification of the mass range for the reconstructed zero-charge spectrum (which automatically determines the range of possible charge states based on the m/z range of the experimental mass spectrum) as well as a target full-width-at-half-maximum of the peaks (assumed symmetrical) expected in the zero-charge spectrum.^{343,344} Because MaxEnt software assumes symmetrical Gaussian peak shapes in fitting, determination of the accurate mass of ions with asymmetric peak shapes (e.g., those with adducts) can be difficult or even prohibitive, as noted in early ESI-MS studies of large (~310-2.2 kDa) biological oligomeric complexes from bacteria and crabs.^{349,350} It is possible to run MaxEnt with an intentionally very broad zero-charge mass range and concomitant charge state range, but better results are obtained the more closely the user

can restrict the mass range (and thus also charge state range) to those actually present in the ion population. This belies a fundamental pitfall of the MaxEnt method in analyzing experimental data, namely that it does not inherently distinguish between noise and true signal and thus will attempt to explain *all* data used as input, including any baseline or noise left in the experimental mass spectrum, by forcing it into a mass bin in the zero-charge spectrum. This can result in numerous artifactual peaks in the deconvolved zero-charge mass spectrum, occasionally with intensities matching that of the true average mass distribution which may complicate interpretation and analysis, as exemplified through comparison of deconvolution of empty MSP1D1 Nanodisc sample spectra acquired using three different mass spectrometer platforms.³⁶⁵

Thus, MaxEnt often performs better with an initial background subtraction (such as a low-order polynomial that excludes ~30% of the raw experimental data), noise thresholding, and/or smoothing of the input data.^{343,345} Two major artifacts that can be caused by these mitigating steps include unwanted exclusion of low-abundance peaks and a reconstructed spectrum that can in some cases be highly dependent on the background subtraction and denoising/smoothing used. If an overly broad or narrow charge state or mass range is specified, additional artifact peak distributions can arise.³⁵⁰ Commercially available MaxEnt algorithms^{343,345,367-370} (such as those available from mass spectrometer manufacturing companies such as Waters Corporation, Bruker Corporation, Agilent Technologies, ThermoFisher Scientific, and SCIEX) for deconvolving mass spectra do not report mass distributions specific to each charge state, thus charge-state-specific information is largely lost. Finally, the assumed noise statistics used for calculating the “evidence” of a hypothetical zero-charge spectrum and for iterating the algorithm may be

different in different commercial implementations of the algorithm, e.g., Gaussian noise statistics in the Micromass/Waters implementation^{343,358,368} and Poisson noise statistics in that from SCIEX.³⁶⁹ Thus, even if convergence of the algorithm is achieved (which may not even happen if the “evidence space” does not have a single, large extremum), different final zero-charge mass spectra may be obtained using the same input parameters but different commercial implementations of MaxEnt.

2.1.2. Fenn Averaging and Deconvolution Algorithms

In 1989 Mann, Meng, and Fenn introduced two simple methods for determining the mass and charge state belonging to a sequence of well-resolved peaks in protein electrospray mass spectra.¹⁸² The first of these methods, which they call an “averaging algorithm”, begins by assigning charge states to all of the ostensibly related peaks in the mass spectrum by assuming that the mass of the charge carrier is known. (If the adduct mass is not known, its effect on charge state assignments is mitigated by fortuitous cancellation of some of the adduct mass terms.) Although the mass of the protein can then be calculated directly from the observed m/z values and assigned charge states (for example, by averaging the mass values calculated for each charge state), a simple way to “tune” the mass of the ion to improve the fit to experimental data is also described in detail.¹⁸² This method accounts to some extent for instrument calibration error as well as inaccuracies in determining a nominal mass for each peak in the observed sequence. Ion abundances play no role in this algorithm.

The second algorithm described in the same paper calculates the sum of abundances in the mass spectrum for all m/z values that can be associated with a trial protein mass, a charge carrier mass, and a set of assigned charge states. For a simple

sequence of well-resolved peaks with identical abundances, the algorithm produces a “deconvolved” spectrum with large peaks at the protein mass (and multiples thereof), as well as a sequence of smaller peaks that can be used to confirm the highest charge state present in the ion population (see **Figure 2**).^{182,371-378} The algorithm produces poorer results for experimental mass spectra with lower resolution and/or with different abundances for each charge state, and an early comparison of the commercial implementation of this algorithm and that of MaxEnt found the latter to be superior especially when the signal-to-noise ratio (S/N) is poor.³⁵⁸ Additionally, as seen in **Figure 2**, the deconvolved spectrum produced using Fenn’s algorithm is prone to a large, increasing baseline and high-intensity sidebands relative to the true protein mass.¹⁸² Charge state assignments can also have large uncertainties for large proteins and complexes due to their typically poor desolvation, as has been previously discussed.³⁷⁹ While these algorithms are not widely used today as they were in the decade following their introduction,³⁷²⁻³⁷⁸ they illustrate fundamental mathematical relationships between the spacings of peaks in biomolecular electrospray mass spectra that set the stage for powerful algorithms introduced later on that can be used to analyze much more complex mass spectra. An article by Hagen and Monnig³⁷¹ compares this method to Reinhold and Reinhold’s implementation of MaxEnt³⁸⁰ as well as their own “multiplicative correlation” algorithm (MCA), in which signals at expected m/z values for a given mass and charge assignment are multiplied rather than added. This method can be less prone to outputting a large baseline or artifact peaks.

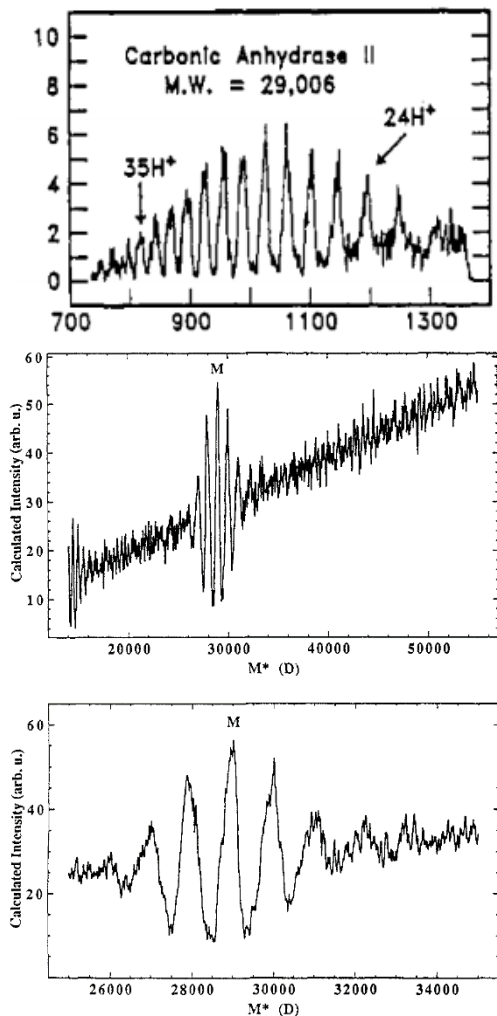


Figure 2. Deconvolution of carbonic anhydrase II ESI spectrum using Fenn’s deconvolution algorithm. Mass spectrum (top), zero-charge mass spectrum (middle), and “zoom” of zero-charge mass spectrum near the determined accurate mass showing sidebands (bottom). Adapted with permission from ref. 182. © 1989 American Chemical Society.

2.1.3. ZSCORE

Following their work improving results from application of MaxEnt to ESI mass spectra,³⁶⁶ in 1998 Zhang and Marshall introduced a deconvolution method,³⁸¹ ZSCORE, in the MagTran data analysis package that fits broadly into the category of “onion-peeling” algorithms (see also Massign,⁶¹ discussed in §2.1.5). In such

algorithms, one attempts to identify and computationally remove a signal that dominates the spectrum, leaving only less dominant signals. The removed signal is normalized for charge and added to a zero-charge spectrum to which more signals will be successively added. One repeats this process until only uninterpretable data and noise remain in the mass spectrum, and all assigned signals have been added to the zero-charge spectrum. Two essential characteristics of ZSCORE are that the onion-peeling starts with the highest-abundance peak in the mass spectrum and proceeds through successively lower-abundance peaks, and that, to be considered “interpretable”, a peak must have a set of “partner” peaks corresponding to adjacent charge states and/or isotopomer peaks. This

latter characteristic is determined from the “ZScore” value, which is related to either 1) the logarithmic sum of the S/N in the mass spectrum at m/z values where an interpretable peak and all its expected partners should be located (for mass spectra), or 2) the (resolution-weighted) sum of the reciprocals of the differences in the expected and measured m/z of an interpretable peak and its partners (for centroided or “stick” spectra).³⁸¹

Advantages of ZSCORE include the ability to work with either raw mass spectra or centroided data over a wide range of mass spectral resolution. The ZScore itself for a hypothetical peak assignment tends to increase as more partner peaks for it are found, thus the accuracy of the algorithm in assigning charge states increases the more partner peaks are present. Because each set of partner peaks need not be related to any other set of partner peaks in composition, ZSCORE can often straightforwardly deconvolve mixtures of ions of interest and/or contaminants (see **Figure 3**),³⁸¹ such as protein mixtures, peptide digests (including in hydrogen/deuterium exchange experiments), and protein fragments by gas-phase dissociation, as illustrated in the literature.³⁸²⁻³⁸⁷ ZSCORE has also been utilized in MS analysis of binding sites of the chemotherapeutic cisplatin to native proteins.^{388,389} The algorithm requires no user input parameters, tends to run very quickly on modern computers, and is fully automated. However, difficulties can arise for ions with overlapping sets of partner peaks, as can often be the case for biomolecular complexes with different oligomeric states.³⁸¹ Furthermore, the accuracy of the algorithm tends to decrease for lower-abundance partner peak sets, as artifacts leftover from “peeling away” previous peak sets begin to dominate the mass spectrum. Ojha and coworkers later introduced an algorithm³⁹⁰ similar to the component of ZSCORE for low-

resolution spectra³⁸¹ but which incorporates charge state assignments based on Reinhold and Reinhold's entropy-based algorithm,³⁸⁰ selected after comparison with Hagen and Monnig's MCA algorithm³⁷¹ (see §2.1.2). They found the entropy-based algorithm to be relatively insensitive to overestimation of charge state maxima and to be an improvement over ZSCORE through allowance of single m/z values to correspond to more than one charge state distribution. Kelleher and coworkers combined ZSCORE with filtering of high-frequency data, arguing that such data are very likely to be noise and that filtering them out before processing with ZSCORE can result in cleaner zero-charge mass spectra.³⁸⁵

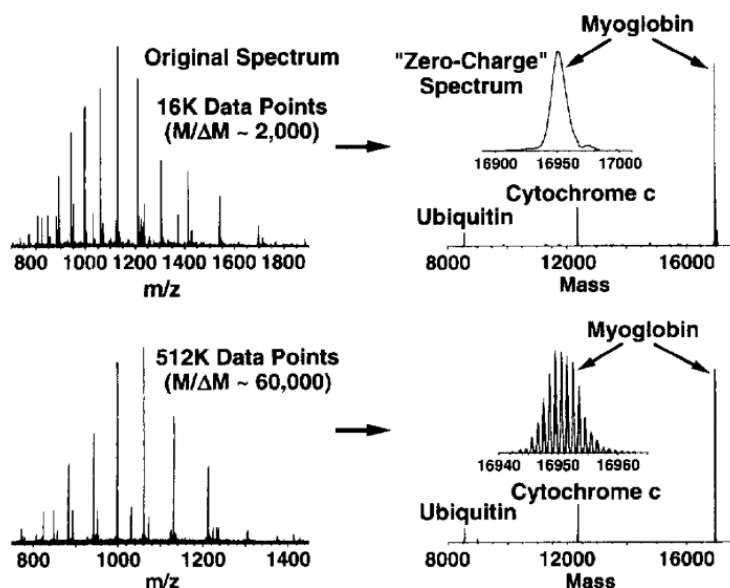


Figure 3. Deconvolution (right) of both low (top) and high (bottom) resolution ESI mass spectra (left) for a mixture of three proteins using ZSCORE. Reprinted with permission from ref. 381. © 1998 American Society for Mass Spectrometry.

2.1.4. SOMMS

As the ability of mass spectrometers to ionize and detect more complex distributions of analyte ions improved,^{63,72} many researchers began to realize that methods originally developed for interpretation of denatured mass spectra such as

MaxEnt and others described above could often be insufficient for native mass spectra with highly-overlapped peaks. In 2006, van Breukelen, van den Heuvel, and coworkers introduced SOMMS⁶⁶ (SOLving complex Macromolecular Mass Spectra) as an adjuvant method to assist interpretation with other algorithms like MaxEnt, especially in cases where a heterogeneous mixture of protein complexes and subcomplexes is present in the ion population, as exemplified in the literature.^{66,178,391-394} In contrast to MaxEnt, SOMMS has the user input as much information as the user knows ahead of time about the expected sample composition: subunit masses, charge state distribution, and likely complex stoichiometries. Using either a user-suggested charge state range or one calculated based on the Rayleigh charge limit, as well as a multinomial distribution (building off previous work using binomial distributions⁷²) of all possible subcomplexes, the algorithm first identifies all m/z at which overlaps of signals from more than one ion composition are expected. Data at these m/z are ignored, and the remaining “unique” signals are then assigned to a composition and charge state based on the table of calculated possible m/z values for the intact complex or subcomplexes. “Partner” peaks belonging to the same ion composition are then identified by scanning over charge states, and the charge state distribution thereby found is fit to a Gaussian intensity distribution. After this process is repeated for each set of partner peaks, a reconstructed mass spectrum is calculated using the identified (sub)complex masses and fitted charge-state distributions. The reconstructed mass spectrum can be compared visually to experimental data to confirm proper assignment of ions in the mass spectrum and locate unidentified peaks. The program CHAMP by Benesch and coworkers³⁹⁵ builds off the tools in SOMMS for many of the same goals, as discussed further in §2.2.4.2.

2.1.5. Massign

This program, introduced by Morgner and Robinson,⁶¹ is an “onion-peeling” algorithm (see also ZSCORE,³⁸¹ §2.1.3) in which readily-identified peak series are assigned and computationally “removed” from the experimental mass spectrum, leaving behind more challenging peaks. The algorithm is designed to handle overlapped peaks (for example, a dimer with twice the charge of a corresponding monomer) by assuming the charge state distribution for each ion is Gaussian. This process is iterated until essentially only noise and uninterpretable peaks remain, and the output is a “stack” of reconstructed mass spectra for each identified complex as well as the experimental and summed, reconstructed mass spectrum. As with programs like SOMMS⁶⁶ and CHAMP,³⁹⁵ the user can input information about component protein masses and possible complex stoichiometries to identify and eliminate as many peaks series as possible before unknowns are addressed. The composition of unknown series of peaks identified by this algorithm are assigned, if possible, by Massign based on user-input subunit masses and composition constraints.

Charge states for “partner” peaks belonging to the same ion composition can be assigned either automatically or with some user intervention, based on the fit between experimental peak maxima and predicted peak positions for the series based on an assumed charge state assignment. In addition to specifying trial peak widths, the user can also adjust a “broadening factor” to account for non-Gaussian peak shapes caused by, e.g., unresolved non-specific adducts. Similarly to CHAMP³⁹⁵ (see §2.2.4.2), Massign can also incorporate an empirical mass correction representing non-specific adduction of buffer and water molecules that is based on the expected surface area of globular proteins

as a function of sequence mass. Morgner and Robinson demonstrated, using a small number of topological constraints based on condensed-phase data, almost unique assignment of several subcomplexes produced by collisional activation of native rotary ATPase from *E. hirae*, which contains 9 different protein subunit types and 19-26 total subunits in its intact form (see **Figure 4**).⁶¹

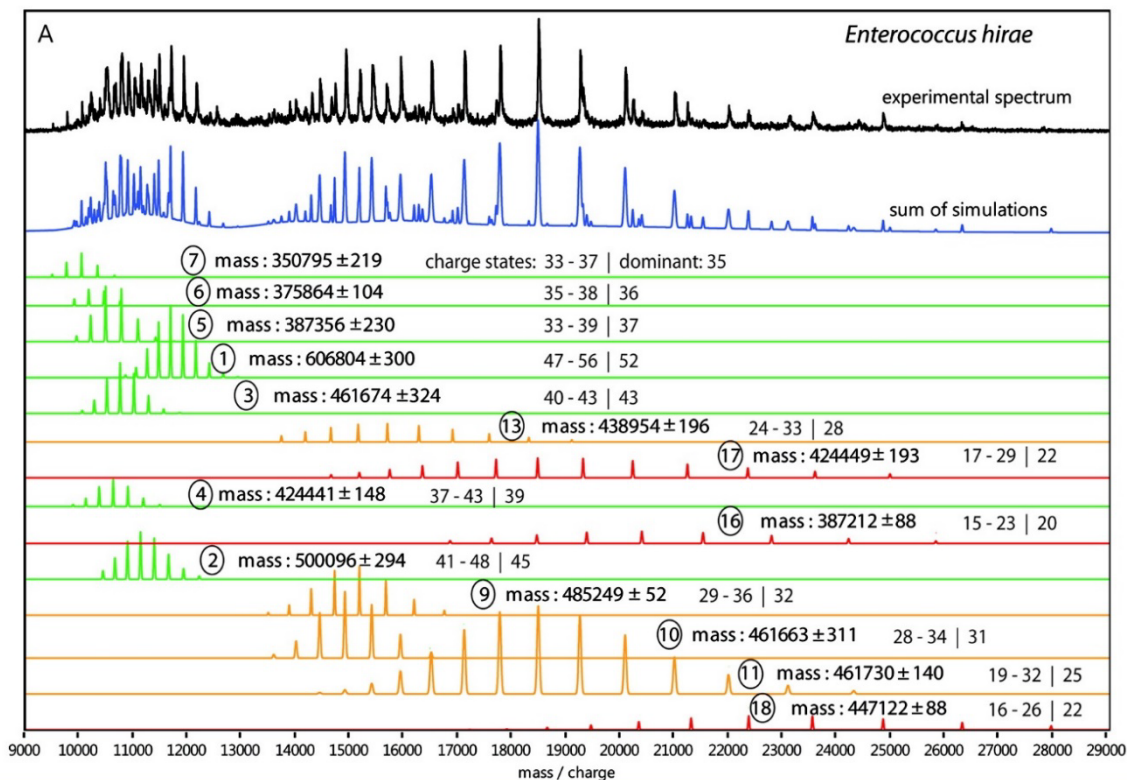


Figure 4. Assignment of peaks in native mass spectrum (black trace) for subcomplexes (colored traces) for rotary ATPase from *Enterococcus hirae* using Massign. Reprinted in part with permission from ref. 61. © 2012 American Chemical Society.

Massign can perform well for even large, multi-component complexes (such as membrane proteins) when subunit mass, stoichiometry, and topological constraints are supplied (**Figure 4**), as has been demonstrated for many different sample types in the literature.^{78,85,164,396-412} Fundamentally, the complexity of the problem in the absence of these constraints is superexponential (i.e., factorial) in the number of subunits, thus

Massign performs best when a large amount of user-supplied information from prior mass measurements or condensed-phase structural data is available.

2.1.6. PeakSeeker

Sometimes native mass spectra contain series of peaks with similar masses and charge states that are not well resolved. In such situations, the resulting mass spectral peaks may have multiple local maxima or shoulders representing different ion masses. PeakSeeker,³⁹⁶ introduced by Lu et al., uses two main strategies to identify all the overlapped peaks under a “complex” experimental peak by 1) identification of all readily apparent peak maxima, optionally with the use of Mexican-hat wavelet-based noise filtering and 2) a subsequent shoulder detection algorithm that uses the second derivative of the (smoothed) mass spectrum. The first level of peak identification can be based on either local maxima exceeding an absolute or intensity-adjusted signal-to-noise ratio, or on the presence of local maxima after convolution with a Mexican-hat wavelet (which ideally sharpens the component peaks). The second level of peak identification relies on the fact that the second derivative of a smooth shoulder peak has a characteristic number of zero-crossings that indicate its presence. Though PeakSeeker’s shoulder peak detection is adapted from Massign⁶¹ (§2.1.5), its deconvolution algorithm differs in that up to five simulated charge state series can be fit to the experimental mass spectrum at a time using least squares regression, rather than “onion-peeling”. **Figure 5** illustrates use of PeakSeeker to interpret a native mass spectrum of a ~1 MDa protein complex,³⁹⁶ and it has also been used to investigate chromatin.^{413,414}

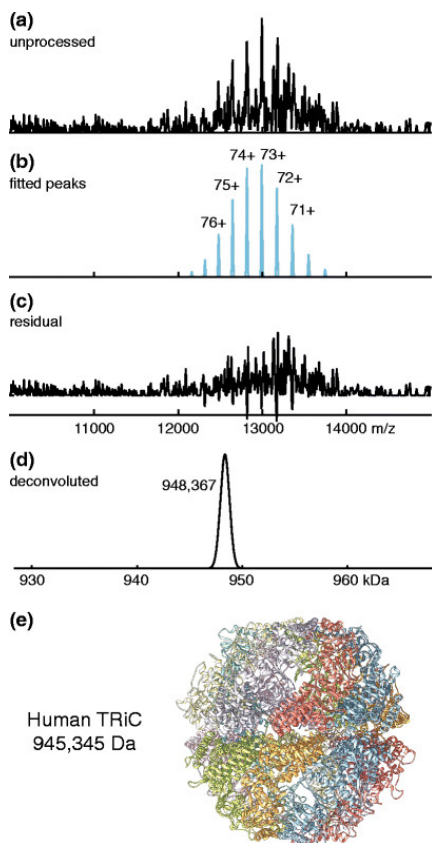


Figure 5. Peak fitting and deconvolution of native mass spectrum for human TCP-1 ring complex (pictured in (e)) using PeakSeeker. Reprinted with permission from ref. 396. © 2015 American Society for Mass Spectrometry.

2.1.7. Bayesian Deconvolution: UniDec and PMI Intact

As native MS sample preparation and instruments improved, the 2010s saw the advent of highly polydisperse native analytes,⁴¹⁵ such as lipoprotein Nanodiscs (with^{81,165,365,401,416-418} and without^{71,168,172,183,272,365,419} embedded membrane proteins) or membrane proteins embedded in detergent micelles.^{64,173,420} Mass spectra of these

complexes can be extremely challenging to analyze due to their relatively broad charge states distributions and overlapped adduct (detergent, lipid, glycan, or other small molecule) distributions, resulting in tens or possibly hundreds of peaks spanning a few thousand m/z (or even hundreds of thousands of peaks, as expected for glycoproteins with extremely varied glycoforms⁴²¹). Adduct distributions are often not identical for different charge states, in part because ESI tends to add more charges to native-like larger ions (i.e., with more bound ligands), and also because gas-phase collisional activation of the ions to remove solvent can often dislodge some of the adducts. MaxEnt³⁴³⁻³⁴⁵ (§2.1.1) and other relatively simple deconvolution algorithms may perform poorly for these types of samples, owing to the flatness of the probability surface, the challenge of accurately guessing input charge and mass parameters, and other factors. In this section we describe

UniDec and PMI Intact, both Bayesian deconvolution algorithms developed for interpreting heterogeneous native MS data.

Following on Marty, Gross, and Sligar's use of a maximum entropy-like algorithm¹⁷² for deconvolving "empty" lipoprotein Nanodisc native mass spectra, Marty and Robinson introduced the Bayesian analysis suite "UniDec" in 2015.^{167,171} The UniDec algorithm begins by conceiving of the information in an experimental mass spectrum as being decomposed into a rectangular matrix with m/z and charge state as its axes and a peak profile with a user-selected shape and width. The matrix is initialized as a uniform distribution. Three steps are iterated to achieve a final matrix: 1) smoothing of the charge state distribution to avoid "orphan" masses at a particular charge state that have no corresponding peaks at adjacent charge states, 2) summation of the matrix along the charge state axis and convolution with the chosen peak shape to produce a simulated m/z spectrum, and 3) adjustment of the matrix entries to reflect the mismatch between the simulated and experimental m/z spectrum. Once convergence of the algorithm is achieved, a final zero-charge spectrum is produced by multiplying each m/z trace in the matrix assigned a particular charge state by that charge state, correcting for charge carrier mass, summing the resulting data for all charge states, and convolving with a user-chosen peak shape function. UniDec requires an input charge state range (either a default range or user-specified) and allows the user to input a subunit mass filter for multiply-adducted species such as lipids or detergents. Outputs include charge-state-specific mass spectra (see **Figure 6**), zero-charge deconvolved spectra, and heat maps of m/z versus charge, all of which can be highly useful in interpreting native MS data for heterogeneous samples.^{57,80,93,158,168,174,187,283,422-435}

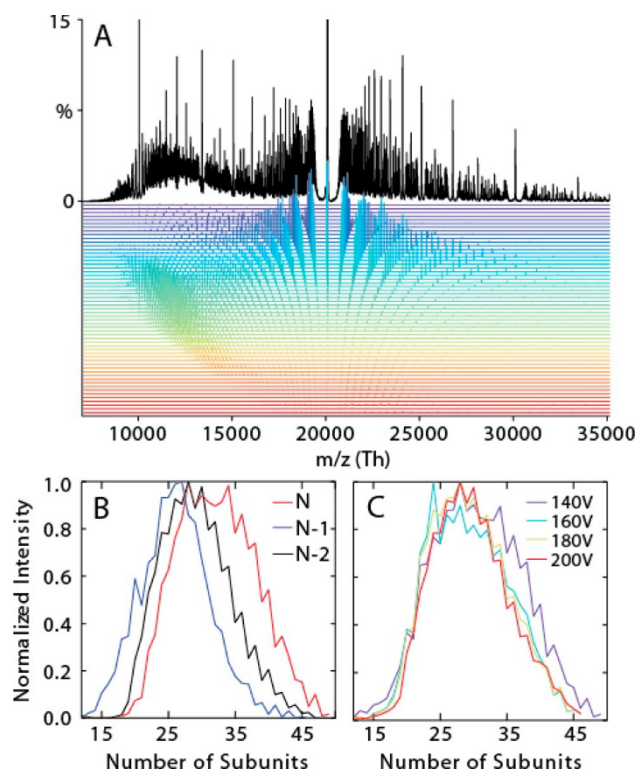


Figure 6. Native mass spectrum (black trace) of native oligomeric state distribution for polydisperse α B-crystallin, with deconvoluted charge-state-specific mass spectra (colored traces), (A). Dependence of subunit stoichiometry distribution on collisional activation (B, C) as revealed using UniDec. Reprinted with permission from ref. 171. © 2015 American Chemical Society.

Marty has added numerous tools for analyzing the output, including macromolecular mass defect analysis¹⁶⁵ (to identify, e.g., peptide stoichiometry inside lipoprotein Nanodiscs^{81,283,418}; see §2.2.3.2) and proteomics tools to identify post-translational modifications and protein isoforms. A set of scoring algorithms to evaluate the plausibility of the reconstructed spectrum and peak assignments is available in UniDec.^{436,437} Batch processing capabilities to facilitate, e.g., adduct binding kinetics and thermodynamics measurements have been added in a modified version of UniDec called “MetaUniDec”.⁴³⁸ Marty also introduced a tunable “SoftMax” function to reduce the likelihood of producing artifactual peaks at multiples (i.e., harmonics) of true peaks in the zero-charge spectrum (see **Figure 7**).⁴³⁹ UniDec and MetaUniDec are both freely

available open-source Python programs, and a recent preprint manuscript describes all of UniDec's features in depth.¹⁶⁷

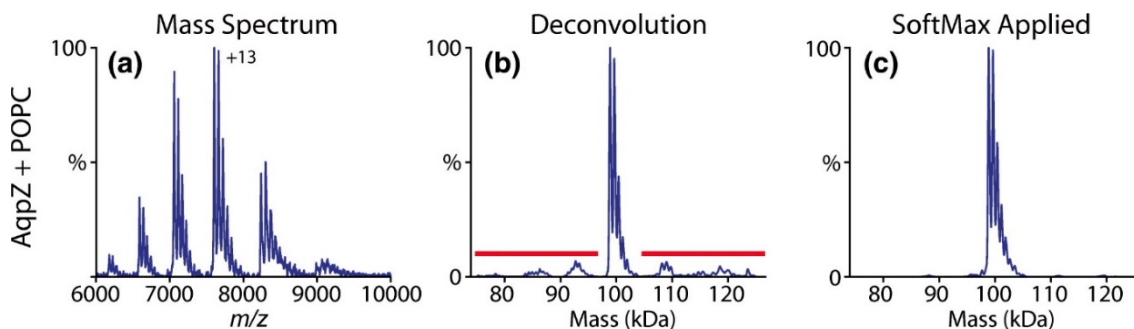


Figure 7. Native mass spectrum of aquaporin Z (AqpZ) with bound palmitoylcholine (POPC) lipids (A), corresponding zero-charge mass spectrum from UniDec showing artefactual “satellite” peaks (B), and zero-charge mass spectrum after application of UniDec’s SoftMax function to suppress satellite peaks (C). Reprinted in part with permission from ref. 439. © 2019 American Society for Mass Spectrometry.

Expanding the capabilities of their Byonic peptide and protein identification software originally introduced to the market primarily for use in proteomics in 2011,⁴⁴⁰ Bern and coworkers at Protein Metrics, Inc. separately developed a new program, Protein Metrics Intact⁴⁴¹ (“PMI Intact”) that also utilizes Bayesian inference. The heart of the PMI Intact algorithm is a matrix of intensity values that are a function of both m/z and assigned charge state and are iteratively corrected by comparing the simulated m/z spectrum obtained from the matrix with the experimental m/z spectrum. PMI Intact identifies candidate charge states for an experimental spectrum using a “parsimonious algorithm” that attempts to explain all zero-charge mass spectrum data with as few charge states as possible.⁴⁴¹ Peak-sharpening algorithms are subsequently used on the deconvolved data to resolve remaining overlapped features in the zero-charge spectrum. PMI includes a “comb filter” to identify peak series equally spaced in m/z , such as those arising from polydisperse adduction of a subunit, which can greatly improve analysis of

mass spectra representing samples of this type, including those of great interest in the biopharmaceutical industry^{331,332} such as highly disperse antibody-drug conjugates.^{84,95,188,337,442-445} PMI is coded and compiled in C++ for increased speed, has batch processing capabilities, allows the user to easily select different liquid chromatography-MS (LC-MS) retention data to analyze, and can be used to automatically assign peaks based on protein sequence data or other user-supplied information. It is also vendor-neutral and can produce user-friendly, customizable reports for non-MS users, features important for its use in industry.³³¹ Users can also input expected mass differences (arising, e.g., from known ligand masses) to bias charge state assignments toward those consistent with these mass differences.⁸⁴ **Figure 8** shows a comparison of results from PMI and other deconvolution algorithms (Agilent's PMod, two implementations of MaxEnt, iFAMS, and UniDec) for a 40 kDa PEGylated protein.³³⁷ This example illustrates the superior performance of more sophisticated and recent deconvolution algorithms which utilize Bayesian (UniDec, PMI Intact) or Fourier Transform (iFAMS, see §2.1.9) over earlier tools, as indicated by their faithful reproduction of the reference mass distribution observed for the singly-charged ions using MALDI-MS.

2.1.8. Game-Theoretic Approach: AutoMass

Assigning mass and charge to peaks in native mass spectra for charge state distributions of different ions at their “boundaries”, i.e., at the extreme high m/z end of one distribution where it overlaps with the extreme low m/z end of a different distribution, can be especially problematic. This can occur, for example, when two different stoichiometries of a complex are present in the ion population, or for different symmetries of a viral

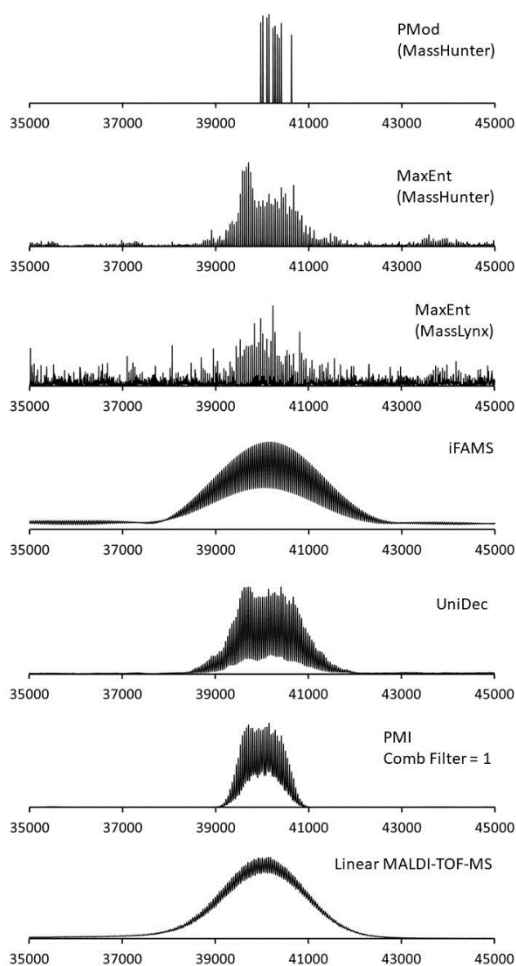


Figure 8. Comparison of deconvolution of ESI mass spectra for PEGylated granulocyte colony stimulating factor protein using different deconvolution algorithms (top 6 traces) and MALDI-TOF 1+ charge state mass spectrum (bottom trace). Reprinted with permission from ref. 337. © 2019 American Chemical Society.

capsid. Peak assignments in boundary regions can be very challenging due to the presence of “overassigned” peaks (i.e., peaks consistent with more than one mass and charge assignment) and low-intensity peaks. Peng and coworkers introduced AutoMass⁴⁴⁶ to combat this challenge and also to achieve accurate mass and charge assignments with minimal input from the user, building off ideas introduced in their earlier tool for the same purpose, LeastMass.⁴⁴⁷ AutoMass treats charge and mass assignment of the peaks in a mass spectrum as “competitors” in a zero-sum game and seeks a game theoretic solution that simultaneously minimizes the maximum “loss” for mass assignment (the standard deviation of the m/z discrepancy for observed peaks given a particular set of m/z assignments) and maximizes the minimum “loss” for charge assignment (the shift in charge for the observed peaks given a particular set of m/z assignments). AutoMass applies this algorithm after smoothing, Gaussian baseline subtraction, and thresholding of the mass spectrum. In this manner, the boundaries between peak distributions can be determined automatically, enabling peak

assignment for mass spectra containing many tens of overlapped peaks. Peng and coworkers demonstrated application of AutoMass to assignment of intact 3-4 MDa hepatitis B viral capsids with T=3 and T=4 symmetries and also to the tens of products with different protein stoichiometries produced upon collision-induced dissociation (CID) of isolated T=3 and T=4 ions.⁴⁴⁶

2.1.9. Fourier Transform Approaches: iFAMS

Many analytes of interest in native MS, or in ESI-MS more generally, differ primarily in the polydispersity of one or more constituent subunits. For example, long-chain homopolymers and copolymers contain many identical monomer subunits in varying stoichiometry, and challenging samples such as lipoprotein Nanodiscs or detergent micelles containing membrane proteins are polydisperse in the number of constituent lipid detergent molecules. In these and many other cases, the ESI mass spectrum often contains tens or even hundreds of overlapped peaks due to the charge distribution and polydisperse subunit distribution. However, the regular spacing between peaks in the mass spectrum for a given charge state due to the varying number of repeated subunits forms a pattern with a “frequency” that can be analyzed using Fourier Transform (FT). In 2004, Prebyl and Cook introduced the use of FT to analyze electrosprayed polymer mass spectra,⁴⁴⁸ noting that a much simpler set of peaks is present in the Fourier spectrum than in the mass spectrum itself, with each peak occurring at some integer multiple of the reciprocal of the monomer mass (its characteristic frequency, $1/m_s$, where m_s is the monomer/subunit mass). This provided a straightforward way of measuring the subunit mass (from the spacing of the Fourier spectrum) and

determining which charge states may be present in the ion population (from the integer multiples of the characteristic frequency at which a peak is present).

Cleary and Prell expanded this concept in 2016 to analysis of Nanodiscs, heavily metal ion-adducted native proteins, and polymers, producing an open-source Python program called iFAMS (interactive Fourier-Transform Analysis for Mass Spectrometry).⁷¹ This program automates computation of the FT of an input mass spectrum (by treating it as a composite of three functions, see **Figure 9**),¹⁸³ identification of Fourier-domain peaks, and determination of the subunit mass and charge states in the ion population. Signal for individual charge states in the Fourier spectrum can be readily extracted and inverse Fourier-Transformed to reconstruct individual charge-state-specific mass spectra as well as a zero-charge spectrum in iFAMS (as compared with other deconvolution methods in **Figure 8**).³³⁷ One disadvantage of using FT for some samples is that the ion population may not be sufficiently polydisperse to yield well-resolved peaks in the Fourier domain, although this can be mitigated somewhat by using harmonic peaks,¹⁸³ which are spaced more widely (see **Figure 10**). Another disadvantage is the possibility for two or more types of ion to have overlapping Fourier-domain frequencies, e.g., two heavily sodiated proteins of different masses but similar charge states.

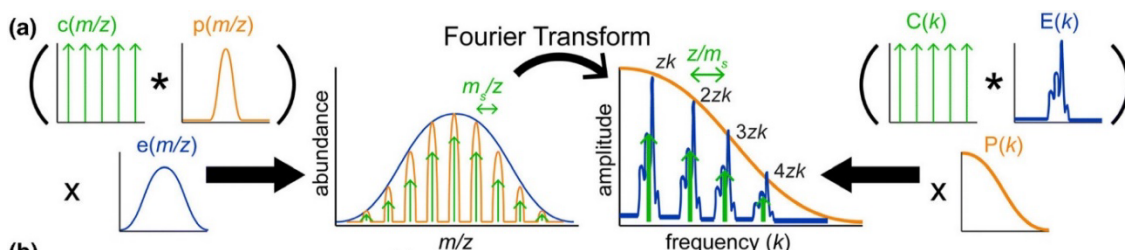


Figure 9. Schematic of iFAMS Fourier Transform-based algorithm, showing decomposition of mass spectrum into “comb”, “peak shape”, and “peak envelope” functions (left) and their corresponding functions in the Fourier spectrum (right). * indicates convolution, and \times indicates pointwise multiplication. Reprinted in part with permission from ref. 183. © 2018 American Society for Mass Spectrometry.

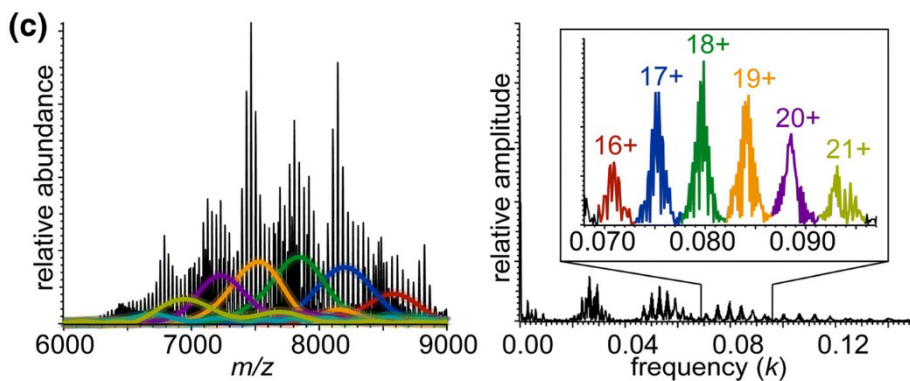


Figure 10. Deconvolution of native mass spectrum of dimyristoylphosphatidylcholine MSP1D1 Nanodiscs using iFAMS Fourier Transform-based algorithm (left), and corresponding Fourier spectrum (right), illustrating the use of higher-harmonic data (inset). Colored traces in mass spectrum correspond to reconstructed peak envelope functions for the charge states indicated with the same color in the inset. Reprinted in part with permission from ref. 183. © 2018 American Society for Mass Spectrometry.

To address these problems, Cleary and Prell introduced the use of Gábor Transform (GT),⁴⁴⁹ which is a type of “windowed” or “short-time” Fourier Transform in which the intensities of “local” frequencies in the mass spectrum are plotted against the mass spectrum itself, into iFAMS.⁴⁵⁰ GT and FT analysis with iFAMS of heterogeneous mass spectra of α -hemolysin complexes in detergent micelles enabled separation of the overlapped frequency signals of two oligomeric states, as well as determination of detergent stoichiometries and reconstruction of zero-charge mass spectra,⁷⁵ and iFAMS has also been used to characterize functionalized polymer constructs for protein conjugation.⁴⁵¹ In many cases, GT can readily overcome pitfalls of FT analysis due to separation of frequency signal from different types of ions according to their m/z . Another advantage is that salt cluster ions, which typically increase in mass as their charge state increases, can be distinguished at a glance from native biomolecular ions, which typically change little in mass over their charge state envelope and give rise to a “negatively chirped” GT signal (see §2.4.2.3).⁴⁵⁰ Similar to FT, a disadvantage of GT is

that low polydispersity samples may give rise to overlapped GT signals for different charge states, although even the isotope pattern may be sufficient for GT analysis in mass spectra where isotopes are resolved. Both FT and GT analysis can serve as ideal “notch filters”, dispensing with nearly all chemical noise as well as white noise, though windowing artifacts can sometimes show up as “ringing” near the baseline of reconstructed spectra.¹⁸³ Further capabilities of FT analysis for distinguishing between different compositional heterogeneity types⁶⁰ are discussed in §2.4.1.3.

2.1.10. MetaOdysseus

Some metals of physiological and human health relevance (e.g., zinc and platinum) have complex isotope patterns compared to those of common organic atoms, thus it is important for the study of metalloproteins and other metal-containing analytes to develop deconvolution algorithms that can handle these challenging isotope patterns. In 2021 Peris-Díaz, Krężel, and coworkers published the most recent of the deconvolution algorithms reviewed here: MetaOdysseus,⁴³⁷ a software suite written in R. MetaOdysseus can be used for analysis of native, bottom-up, and native top-down mass spectra. After spectra are smoothed with one of three included algorithms, convolution with a Mexican hat wavelet can optionally be performed to help identify peaks. The three main features of MetaOdysseus are charge state deconvolution, mass assignment, and statistical scoring. Two algorithms can be used for charge state deconvolution: 1) an algorithm similar to that of ZSCORE³⁸¹ (see §2.1.3) for peak assignment for high-resolution, low-charge mass spectra, and 2) an “onion-peeling” algorithm based on fitting simulated spectra to experiment and which can account for peak broadening often observed in native MS due to adducts. Mass assignment is achieved through cross-correlation with a

generated expected mass pattern based on the amino acid sequence of the protein of interest as well as a library of common labeling reagents and metal isotope distributions. MetaOdysseus incorporates the UniScore⁴³⁶ scoring schemes developed by Marty which can be used to evaluate results from deconvolution and mass assignment.

2.2. Data Reduction

2.2.1. Monomer Mass

In many chemical applications, it may sometimes be necessary to determine the accurate masses of repeated subunits in polydisperse samples, i.e., the sample components whose stoichiometry varies in the sample. This can be especially important when samples are prepared from mixing reagents with similar masses or when bulk average measurements fail to properly distinguish successfully made products from leftover reagents, conditions which apply to lipid Nanodiscs, polymers, antibodies, and other biotherapeutics.^{60,95,177,184,337,338,452,453} Several approaches have been demonstrated to address this challenge.

2.2.1.1. FT Methods. Prebyl and Cook noted in their 2004 Fourier Transform-based algorithm for analyzing electrospray mass spectra of polymers that the characteristic spacing between fundamental peaks in the Fourier spectrum (which represent the charge states present) is the inverse of the monomer mass.⁴⁴⁸ From simulated spectra of polydisperse 40-kDa polymers with a charge state distribution spanning 15-22+ and exact monomer mass of 160.0 Da, they found that the accuracy of the monomer mass determined from peak spacing in the Fourier spectrum decreases with S/N of the mass spectrum. However, reasonable agreement (7% error) is achieved even for a very low S/N of 5:1 and with very poor resolution of the mass spectrum, which

exhibits a high, curved baseline due to the overlapping tails of tens of adjacent peaks. Applying their method to ESI spectra of sodium poly(styrenesulfonate) with a nominal average mass of 4.6 kDa, they determined a monomer mass 1.2% lower than the expected monomer mass. However, they were able to confidently assign all of the charge states present in the ion population and attributed some of the monomer mass inaccuracy to substitutions of protons with sodium ions during ESI that could be mitigated by adjusting the pH of the ESI solution (to 0.1-0.3% monomer mass error).

Cleary and Prell demonstrated automated determination of subunit mass from nESI mass spectra using a similar algorithm in iFAMS for sodiated and potassiated ubiquitin, long-chain poly(ethylene glycol), and lipoprotein Nanodisc samples.⁷¹ They found typically less than 0.2% root mean squared deviation of determined subunit masses from their known exact masses for the metal adducts, ethylene glycol monomer unit, and Nanodisc phospholipids. The precision of the monomer adduct mass for poly(ethylene glycol) was sufficient to distinguish the Fourier spectrum signal from that potentially arising from sodium metal adduction.

2.2.1.2. “Double FT”. Because fundamental peaks in the Fourier spectrum are spaced by the reciprocal of the repeated subunit mass, another approach to determining the subunit mass is to apply another (forward) Fourier Transform to the Fourier spectrum itself. This results in a “double FT spectrum” in which a peak is expected at the mass of the subunit. Marty demonstrated that the mass of the phospholipid subunit in Nanodiscs can be recovered in this way without directly analyzing the initial Fourier spectrum (see **Figure 11**).⁴⁵³ This method was also recently employed to distinguish mixtures of poorly-resolved lipid head groups attached to protein ions.⁴⁵⁴

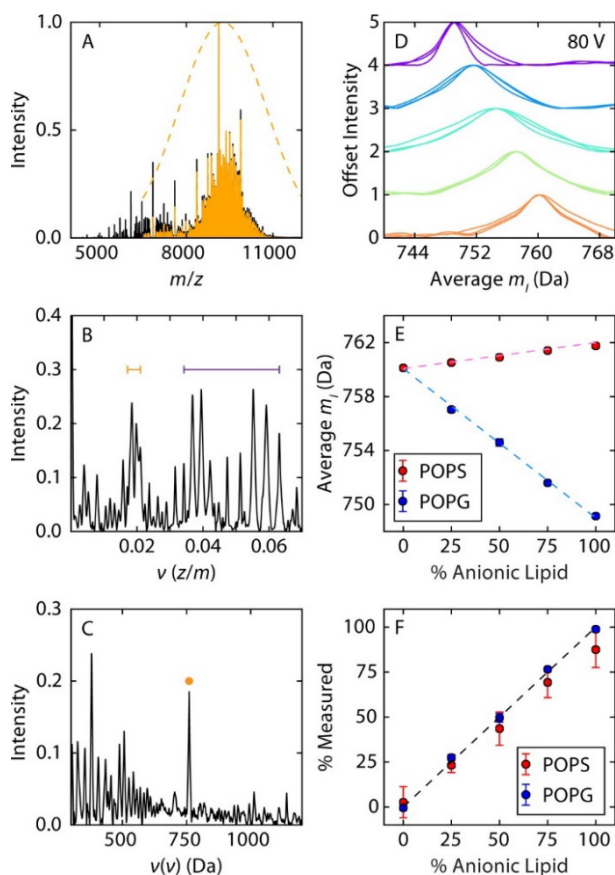


Figure 11. UniDec-based “double FT” analysis of native mass spectrum of Nanodiscs containing mixtures of POPC and either PO-phosphatidylserine (POPS) or PO-phosphatidylglycerol (POPG) lipids. Example pure POPC Nanodisc native mass spectrum (A), corresponding Fourier spectrum (B) and “double FT” spectrum (C), revealing apparent average lipid mass (yellow dot). Measured apparent average lipid masses for different bulk lipid compositions (D, E) and reconstructed Nanodisc lipid composition versus bulk lipid composition (F). Reprinted with permission from ref. 453. © 2016 American Chemical Society.

The double FT spectrum can be similar in appearance to the spectra

produced by Fenn’s deconvolution method¹⁸² (see §2.1.2), but with the major peaks at multiples of the repeated subunit rather than the total ion mass. However, a large baseline is often present in the double FT spectrum, and numerous other signals can be present, potentially making the method difficult to use when mass spectral resolution is too low. Intriguingly, this method can also be used to approximate the bulk fraction of two different types of lipids in mixed-lipid Nanodiscs (see §2.4.1.2 and 2.4.1.3). Further discussion of samples this type of analysis is well-suited for, as well as of potential caveats, is included in §2.4.1.3.

2.2.2. Base Mass or “De-adducting” Measurements

For many samples, the complementary problem to determination of accurate monomer/repeated subunit masses (§2.2.1), i.e., measurement of the “base mass,” or

mass conserved across many or all members of a polydisperse ion population, may be of interest. For example, in studying ligand-bound proteins, non-specific adduction of sodium and potassium or other common metal ions may obfuscate the relative abundances of other proteoforms or of ligands bound to the protein. Recently-introduced methods computationally remove these nuisance adducts to reveal the underlying base masses of interest (e.g., the abundance distribution of a protein and its ligand-bound complexes).

2.2.2.1. SWARM. Klassen and coworkers introduced the SWARM (“Sliding Window Adduct Removal Method”) algorithm in 2019 to effectively remove patterns of adducts from mass spectra and reveal more clearly the peaks belonging to base masses of interest.⁴⁵⁵ This is achieved by first smoothing the experimental spectrum, with optional baseline subtraction. It is assumed that the user knows the mass of the protein and ligands in the sample and is interested primarily in determining the relative abundances of different ligand states. It is further assumed that identical non-specific adduction occurs for each base mass. A region of the mass spectrum is then selected to represent the pattern of non-specific adducts expected for each base mass in the ion population. This region must be well-separated from peaks associated with other base masses; often a region from the native mass spectrum of the ligand-free protein is used. Within the selected region, the low- m/z side of the base mass peak is ignored, and the remaining portion is called the “template window” (see **Figure 12**).⁴⁵⁵ The template window is then scaled vertically and horizontally according to the pre-assigned charge state and abundance of each target base mass in the spectrum and slid over to the base mass peak m/z value. The resulting scaled and translated template is subtracted from the smoothed

mass spectrum, and this process is repeated for all target base masses. The resulting SWARM-processed spectrum thus reveals the abundances of each base mass with non-specific adducts removed. Klassen and coworkers originally demonstrated the utility of this algorithm in studying equilibrium and kinetics between ligand states of carbonic anhydrase, lysozyme, and the C-terminal portion of human galectin-3 with glycan ligands in the presence of non-specific sodium and potassium adducts.⁴⁵⁵ They recently showed the facility with which the abundances of a library of glycans attached to CUPRA linkers can be determined from highly-overlapped mass spectra and also demonstrated utility for quantifying weak protein-glycan interactions.^{456,457} Marty and coworkers applied a similar algorithm to deconvolve base masses of interest for zinc- and lipid-bound rhodopsin.⁵⁷

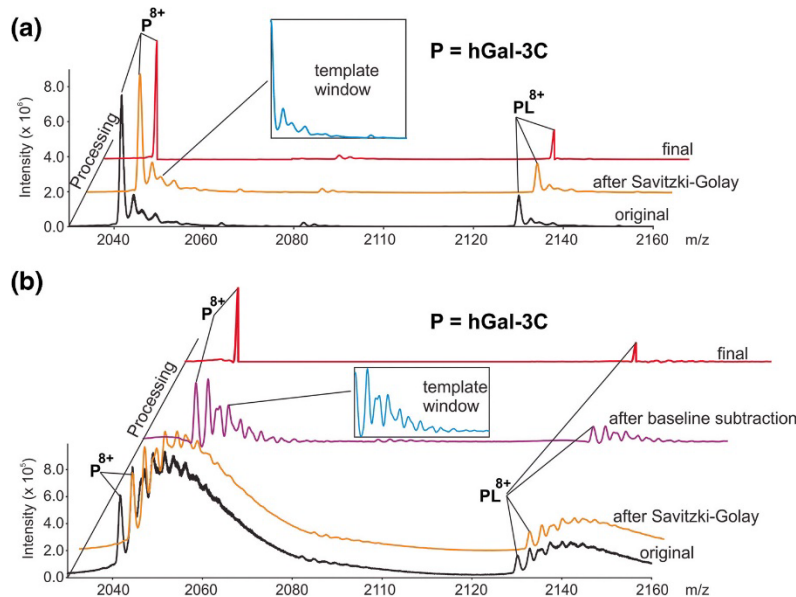


Figure 12. Native mass spectrum of human galectin-3 C-terminal domain without (A) and with (B) extensive sodium adduction (black traces), and final de-adducted base mass spectra from application of SWARM (red traces). Blue insets illustrate de-adducting template that includes oligosaccharide and sodium adduct profiles. Reprinted with permission from ref. 455. © 2019 American Society for Mass Spectrometry.

2.2.3. Mass Defect Analysis

In their FT-based analysis of ESI-MS of polymers described above (§2.2.1.1),⁴⁴⁸ Prebyl and Cook also pointed out that, in principle, the phase information in the Fourier spectrum could be used to determine the average total mass of the end groups on polymers (plus the mass of any non-covalent adducts) *modulo* the monomer mass. This procedure would effectively be analogous to Kendrick Mass Defect⁴⁵⁸ analysis common in polymer mass spectrometry as well as to Macromolecular Mass Defect^{81,165} analysis in native MS, both described below.

2.2.3.1. Kendrick Mass Defect Analysis. In 1963 Kendrick introduced a method for characterizing polymer mass spectra based on the difference in mass defect between an ion and a chosen molecular fragment (e.g., a monomer).⁴⁵⁸ Part of the original motivation for this method was to reduce the size of mass spectral datasets for more efficient storage and although the method is not typically used in its original form in native MS, it illustrates key concepts that are used in the related Macromolecular Mass Defect method, which has utility in native MS (§2.2.3.2). First, a molecular fragment of interest is chosen, typically one present in varying stoichiometry within the analyte population. The “Kendrick mass” of each analyte ion is defined as the product of its measured accurate mass and the nominal (nearest-integer) mass of the molecular fragment, divided by the exact mass of the molecular fragment. The “Kendrick mass defect” is then defined as the nominal mass of an analyte minus its Kendrick mass. Thus, if an analyte has a mass that is an exact multiple of the molecular fragment mass, it will have a Kendrick mass defect of exactly 0. Typically, the Kendrick mass defects of each analyte in an ion population are plotted against their Kendrick masses. In such a plot,

analytes belonging to a “family,” such as linear polymers with the same end groups but differing monomer numbers, will fall along horizontal lines corresponding to the same total end group mass. Data falling along lines of non-zero slope can indicate the presence of analytes with a different repeated subunit other than the chosen molecular fragment. Kendrick mass defect analysis has become a major tool in polymer analysis for the ease with which researchers can make judgments about sample composition from visual analysis of the plot, and it has also been adapted for native ESI-MS investigation of polymers, gangliosides, and other analytes.⁴⁵⁹⁻⁴⁶³ For example, the number of different horizontal groupings in the Kendrick mass defect plot can reveal how many different combinations of end groups are present. This is analogous to modular arithmetic, in which numbers are considered equivalent if they have the same remainder after division by a chosen natural number. Kendrick mass analysis readily reveals which “remainders” are present in the polymer ion population as well as what the mass of the end groups are in a given ion, *modulo* the chosen molecular fragment mass. Although it is therefore possible for different combinations of end groups to yield the same Kendrick mass defect, the researcher can often make unique assignments for a given Kendrick mass defect based on additional information about the sample.

2.2.3.2. Macromolecular Mass Defect Analysis. Marty extended the ideas of Kendrick mass analysis to the study of polydisperse native biomolecular ion complexes, in particular, lipoprotein Nanodiscs containing varying numbers of lipids and embedded membrane proteins.^{81,165,418,464} In this case, the molecular fragment mass used in the “macromolecular mass defect” (MMD) analysis is the known molecular mass of the lipid.¹⁶⁵ After the native mass spectrum is deconvolved to a zero-charge mass spectrum,

it is computationally divided into strips starting and ending at consecutive integer multiples of the lipid mass. The strips are then overlaid and the intensities summed to produce a plot of intensity versus MMD, the x-axis of which is simply the remainder obtained upon dividing each ion's mass by the mass of the lipid (as shown in **Figure 13**). This method has the advantage of providing a global-average distribution of the MMD over all lipidation states, effectively increasing the S/N of each MMD. MMD analysis is available in UniDec, with options for making 2-dimensional plots of MMD versus mass and applying Richardson-Lucy peak sharpening to assist in determining MMD values. Marty and coworkers illustrated that this method can be extremely useful for determining peptide and small membrane protein incorporation into Nanodiscs as a function of bulk peptide/protein composition in the Nanodisc assembly mixture (see **Figure 13**), which can reveal stability and specificity (i.e., preference for particular oligomeric states and/or lipid interactions) of the inserted molecules in lipid environments of varying compositions.^{81,418,453,464}

2.2.4. Modeling Complex Topologies

Reconciling observed masses for protein complexes with reasonable complex stoichiometries and topologies is important in determining quaternary structure using data from native IM-MS,^{48,115,135,136,138-140,200,201,212,224,304,465-478} surface-induced dissociation (SID),^{58,86,120,464,479-485} and complementary methods.^{50,58,77,86,107,113,115,258,286,288,292,479,486-488} SOMMS,⁶⁶ CHAMP,³⁹⁵ and SUMMIT⁷³ include algorithms for this purpose and are described below. Although a detailed analysis of these and other quaternary structure modeling programs is beyond the scope of this review,^{50,118,465,472,482,486,489,490} possible

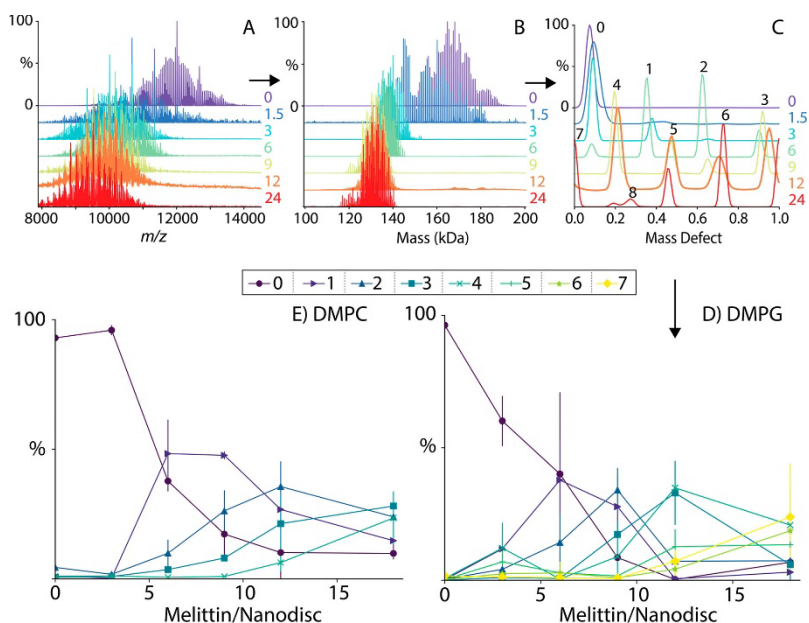


Figure 13. Native mass spectra of charge-reduced Nanodisc-embedded melittin for different bulk melittin:Nanodisc concentrations (A), corresponding zero-charge spectra deconvolved using UniDec (B), MMD profiles reconstructed using MetaUniDec and sharpened with the Richardson-Lucy algorithm with peak label numbers indicating stoichiometry of incorporated melittin (C), and variation of melittin incorporation as a function of bulk melittin:Nanodisc concentration for DMPG and DMPC lipids (D, E). Reprinted with permission from ref. 81. © 2019 American Chemical Society.

structures determined from these programs can provide tight constraints for modeling atomistic structures and interpreting complementary information from other structural methods. We briefly highlight these capabilities below.

2.2.4.1. SOMMS. In addition to its mass spectrum deconvolution algorithm, SOMMS⁶⁶ (see also §2.1.4) can be useful in analyzing multi-protein complexes with two or more different types of protein subunits by calculating hypothetical spectra *a priori* based on combinations of known subunit masses and user-input charge state ranges. SOMMS performs best with high-quality prior measurements of the subunit masses and may not be optimal for identifying unknown components or for analyzing experimental mass spectra in which many unknown contaminant ions are present.

2.2.4.2. CHAMP. Benesch and coworkers introduced an algorithm, CHAMP³⁹⁵ (Calculating Heterogeneous Assembly and Mass spectra of Proteins), that shares similarities with SOMMS⁶⁶ and uses a more sophisticated approach than previous efforts off which it builds^{63,72,491} to charge state distribution assignment as well as a χ^2 -based optimization algorithm for the reconstructed mass spectrum. Empirical relationships between mass and the native charge state envelope as well as a mass adjustment factor based on the estimated surface area of each putative complex are used to more realistically predict m/z distributions based on user input. A three-stage optimization algorithm based on the χ^2 statistic for the difference between the reconstructed and experimental mass spectra is used to tune the fitting parameters; this three-stage optimization was found to avoid local-minimum “traps” in the fitting parameter surface and converge faster than a simpler steepest-descent approach.³⁹⁵ High-quality fits of calculated spectra to poorly resolved mass spectra representing very polydisperse ion populations, such as oligomers of small heat shock proteins³⁹⁵ and α B-crystallins,⁴⁹² and to investigate selectivity of lipid binding to membrane proteins were obtained using CHAMP.^{55,492} Like SOMMS, CHAMP performs best when the user can supply as much input information about the component proteins as possible.

2.2.4.3. SUMMIT. Taking a structure-based approach to elucidating heterogeneous multi-protein complexes, in 2008 Robinson and coworkers introduced SUMMIT (SUMming Masses for Interaction Topology) to generate protein interaction networks and, in some cases, atomic model structures.⁷³ This program uses a multi-technique approach in which subcomplexes are deliberately formed using solution-phase chemical cross-linking,^{493,494} gas-phase dissociation of the intact complex and

subcomplexes, and gel electrophoresis. Both native and denaturing MS are used to assign the identities and masses of the subunits, and overlapping information for different subcomplexes is used to generate a “protein interaction network,” which is a map of likely subunit interfaces.^{73,74,490,495-503} The interaction network can be used along with other computational approaches, such as homology modeling, to build 3-dimensional models of the intact complex that are consistent with the experimental data (see **Figure 14**). In addition to other uses of SUMMIT to reveal the architecture and interactions of subunits within complexes,^{74,490,495-503} the Robinson group has demonstrated the utility of this powerful combined approach for assigning the 3-dimensional structure of the 19S proteasome lid, which contains 9 distinct protein subunits, and the yeast exosome complex, which contains 10 distinct subunits. A major advantage of this method is that the number of subcomplexes with overlapping information is maximized, vastly reducing the number of possible structures consistent with all of the structural data.

2.3. Instrumental and Experimental Approaches

2.3.1. Charge Detection of Single Particles

Especially for very large ions approaching the MDa size range, native ESI mass spectra can exhibit very poor resolution due to adduction of buffer salts and other small cosolute molecules in addition to heterogeneity resulting from the presence of multiple isoforms.^{379,504} The resolving power and sensitivity of TOF, Orbitrap, and FTICR instruments tend to decrease at very high m/z due to a number of instrumental factors⁵⁰⁵ including space-charge repulsion, further complicating mass spectral analysis.⁵⁰⁶ An experimental alternative to (nearly) simultaneous detection of multiple ions per scan, as is the case for these instrument types, is charge detection mass spectrometry (CDMS), in

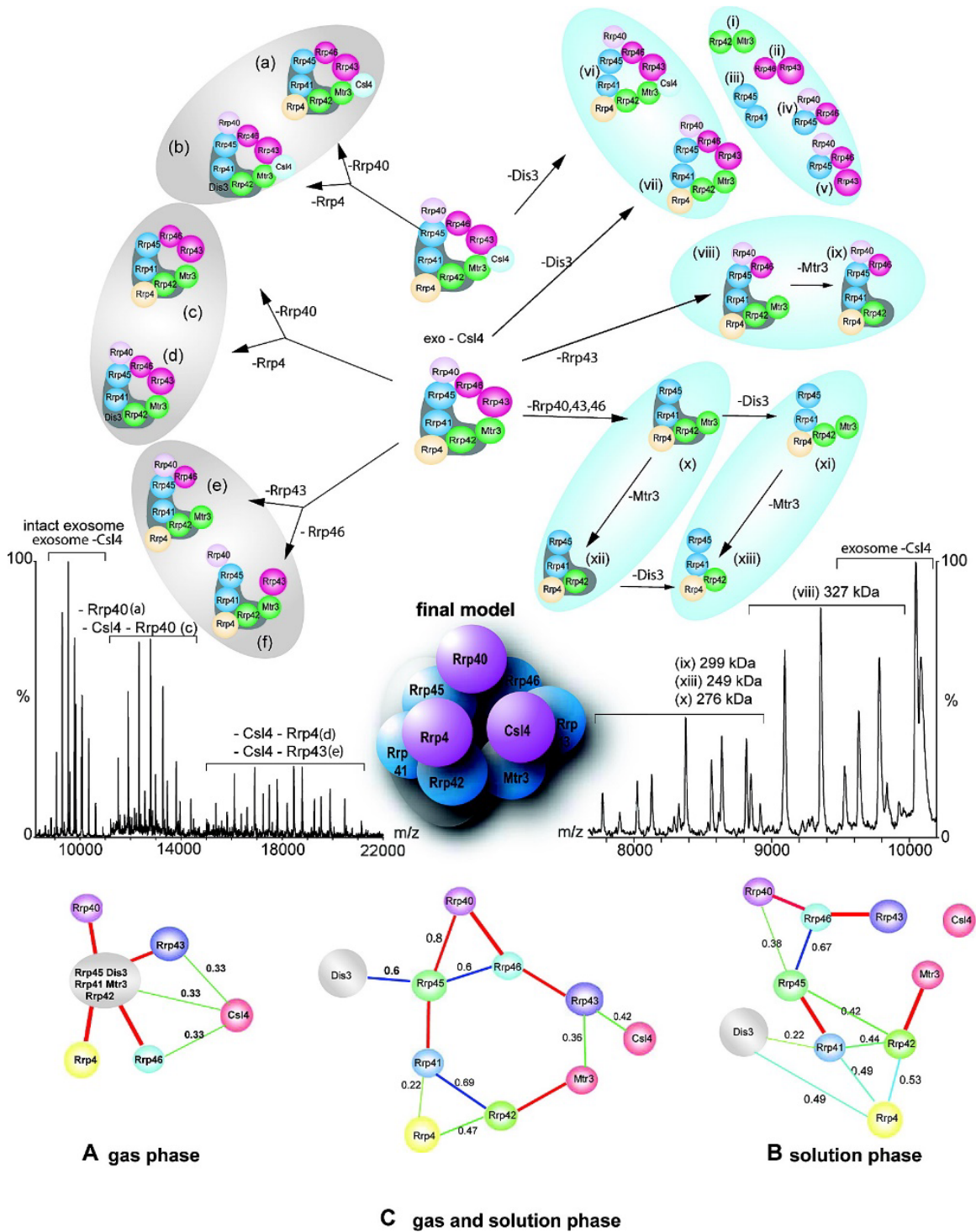


Figure 14. Representative native mass spectra of intact yeast exosome and its subcomplexes formed in solution or generated by collision-induced dissociation (middle), interaction networks generated by SUMMIT from native MS and solution-phase data (bottom, A-C), subcomplex map (top), and final proposed 3-dimensional model topology of the intact exosome (center). Reprinted with permission from ref. 73. © 2008 American Chemical Society.

which individual ions are trapped and their accurate masses measured one at a time or in very small groups.^{125,506} Initially introduced by Benner in the mid-1990s,^{507,508} innovative work done to increase speed and sensitivity⁵⁰⁹⁻⁵¹⁴ and, more recently, to enable performance of these experiments in Orbitrap instruments,¹⁵⁶ has made CDMS an exciting addition to the arsenal of native MS techniques that aims to circumvent many of these challenges of conventional biomolecular ESI-MS. We provide a brief overview of CDMS innovation and recent exciting applications to challenging, heterogeneous samples below and encourage interested readers to the many in-depth reviews and landmark publications available in the literature.^{100,123,156,176,177,268,508-511,513-521}

2.3.1.1. Benner Trap. Improving on earlier instrumentation for determining masses of aerosol and cosmic dust particles,^{522,523} Benner designed a mass spectrometer consisting of an ESI source, an electrostatic ion gate, and two electrostatic ion mirrors on either side of a cylindrical inductive pick-up electrode.^{507,508} The pick-up electrode is connected to a field-effect transistor assembly that transmits signal to an external amplifier and detector. Single ions that pass through the gate and trigger a response in the detector assembly are trapped by rapidly switching on the ion mirrors, which cause the ion to oscillate back and forth repeatedly through the pick-up electrode (on the order of tens of passes in a few milliseconds). Each time the ion exits or enters the pick-up electrode, a characteristic spike and dip in the voltage on the pick-up electrode are digitally recorded. By adjusting the potentials on the ion mirrors, only ions within a certain range of kinetic energies are trapped, enabling kinetic energy selection. Because the magnitude of the voltage spikes on the detector is proportional to the charge of the ion, and the time required for the ion to traverse the pick-up electrode is related to its m/z ,

the detector read-out can be used to determine both the charge state and the mass of the single trapped ion. The mass distribution for a sample can be reconstructed by superimposing results from many such individual measurements. Benner initially illustrated the use of CDMS to measure the mass and charge of the pBR322 plasmid (2.88 MDa) carrying ~690 charges in positive ion mode.⁵⁰⁷ This technology was soon applied to the analysis of viruses and viral capsids²⁶⁸ and large, heterogeneous DNA samples.^{521,524}

Jarrold^{100,125,176,513,517-520,525-527} and, separately, Williams^{510-512,528-530} later showed how FT analysis of the detector signal can be used to rapidly assign ion mass and charge, even when a small number of ions are simultaneously trapped. The incorporation of multiple pick-up electrodes arranged in a row results in faster signal acquisition and greater sensitivity. In addition, ion kinetic energy uncertainty can be reduced to ~0.45% using a hemispherical electrostatic energy selector prior to trapping,⁵²⁵ and the ratio of the time ions spend outside and inside the pick-up electrodes can also be used to more accurately determine ion kinetic energy.⁵²⁹ Jarrold and coworkers demonstrated detection of pyruvate kinase aggregates up to 40-mers (2.43 MDa) using CDMS and noted that the larger aggregates are typically 5-6% more massive than predicted simply based on the native tetramer mass, indicating significant adduction of salts, solvents, and other cosolutes at this size.⁵²⁰ Plots of the measured m/z of these ions versus their mass illustrate that, even in the absence of space-charge repulsion and other effects common to conventional ESI-MS, the mass spectrum would exhibit extreme overlap of ion signals.⁵²⁰ Williams has used CDMS to track solvent evaporation from multi-MDa ions produced by ESI and as a method for determining their collision cross sections from CDMS

measurements,⁵³⁰ a finding with promising implications in the future study of very large biomolecular complexes.

2.3.1.2. CDMS in Orbitrap Instruments. Recently, Kelleher^{132,531-533} and Heck and Makarov¹⁵⁶ demonstrated that CDMS can be performed in modified Orbitrap instruments. For these experiments, only a few (~100) ions are trapped in the Orbitrap per scan. Their transient signals are collected, and the charge of each ion is deduced from the current it induces on the detection electrodes as measured against a calibration curve. This results in simultaneous measurement of m/z and charge (see **Figure 15**) and greatly improves mass accuracy due to the reduction in space-charge repulsion owing to the small number of trapped ions. Kelleher showed that this method can drastically improve identification of 0-30 kDa proteoforms from extremely complex mixtures, such as fractions of human cell extracts, even using direct infusion ESI.⁵³¹ This method can be extremely useful in distinguishing otherwise overlapping m/z signals for different oligomers of the same species, as shown for immunoglobulin-M in **Figure 15**, and for very large complexes, such as Adeno-associated virus capsids with (4.91 MDa) and without (3.74 MDa) genome cargo.¹⁵⁶

2.3.2. Cutting-Edge IM-MS Instrumentation

Ion mobility separation is a technique that can be integrated into mass spectrometer instruments to provide complementary information through separation of ions based on size and shape,¹³⁸ and IM-MS instruments have been commercially available since 2004.¹⁹¹ In addition to providing some structural information via collision cross section (CCS) measurements, which can be useful for characterizing structural heterogeneity, for distinguishing between different possible conformations, and for

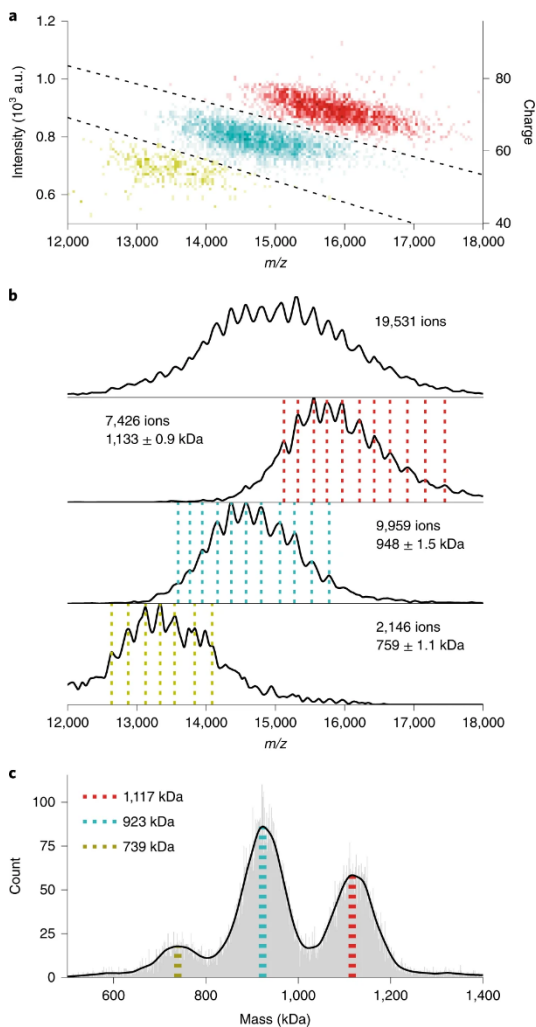


Figure 15. Two-dimensional histogram of single-ion signals measured using Orbitrap CDMS of immunoglobulin-M oligomers (A), m/z of histograms of single-particle centroids illustrating m/z overlap (B), and corresponding mass histograms (C). Reprinted with permission from ref. 156. © 2020 Springer Nature America, Inc.

classifying ions (see §2.4.2.1-2.4.2.2), IM-MS can serve as a filter to enable isolation of heterogeneous species which may overlap in the mass spectral domain,^{135,471} as illustrated in the literature.^{68,69,75,277,470,474,534-544} We direct readers to many excellent reviews on the principles and history of IM-MS and aim to provide an overview of exciting innovation in this field to improve resolution and separation capabilities, a critical

development as samples amenable to study with native MS become increasingly more complex.^{89,126,135,136,138-140,200,466,471,474,475,477,545-550}

Beyond conventional drift-tube IM separation,⁵⁵¹ in which resolving power increases with the square root of drift tube length and presents rapidly diminishing returns in instrument design, a number of promising alternative IM technologies have been introduced and rapidly developed over the last two decades. Improved IM separation and S/N can be helpful in studying heterogeneous mixtures because analytes with identical m/z that are not separated in the mass spectrometry step can in many cases

be separated by IM based on shape and size. The resulting mobility-selected mass spectra are often better resolved and simpler than the full mass spectrum, resulting in more facile assignment of peaks. However, while IM resolving power in commercial instruments can be relatively high for small ions, such as peptides, lipids, and oligonucleotides (typically ~50-300 CCS/ Δ CCS with many currently available instruments⁵⁴⁶), resolving power for larger proteins and biomolecular complexes is often substantially lower. Much recent effort has gone into developing instrumentation to address this challenge while minimizing signal loss and ion heating/unfolding for native ions.

In Traveling Wave Ion Mobility (TWIM) instruments,^{545,547} such as Waters' Synapt series,^{192,193} a high degree of ion separation (up to ~40:1 for small biomolecules and somewhat less for native proteins)¹⁹⁰ using a relatively short (on the order of ~10-25 cm) IM cell can be achieved. Waters' recently-introduced Cyclic Ion Mobility cell design¹⁸⁹ effectively turns the TWIM cell into a circular path, in which multi-pass separations and much higher resolution are possible (~750 for isobaric 491-Da peptides in 100 passes around the cyclic cell; see **Figure 16**), although at present only a few results for native protein complexes have been published.^{189,202,552-554} Separation of the reverse-sequence peptides as shown in **Figure 16** represents an important milestone for the utility of IM-based separation of isobaric heterogeneous analytes. Because they have the exact same mass and amino acid composition, differences in their mobility should ultimately be due solely to conformational differences. This and other key work done to achieve separation of isomers and mixtures of small molecules^{195,549,555-563} provide an exciting glimpse to the future separation of larger, heterogeneous samples with continued improvements to IM-MS instrumentation, though these capabilities have utility even now

as native MS expands to the investigation of endogenous small molecule ligands bound to biomolecular complexes.^{91,93}

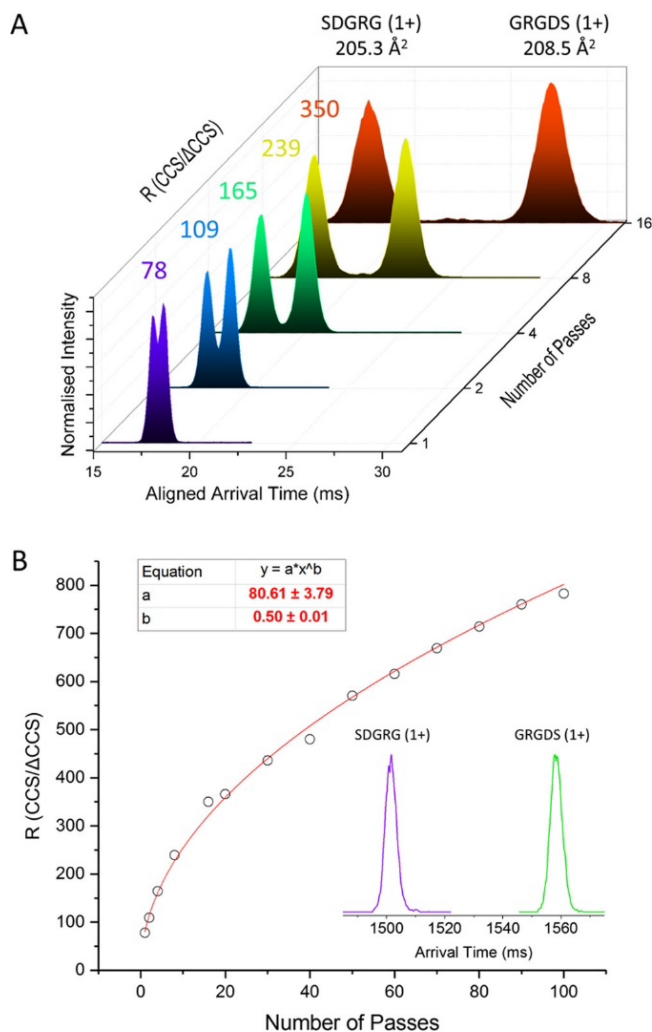


Figure 16. Arrival time distribution of reverse-sequence peptides SDGRG and GRGDS as a function of number of passes around cyclic TWIM cell (A) and corresponding plot of IM resolution as a function of number of passes (inset corresponds to arrival time distribution after 100 passes). Reprinted with permission from ref. 189. © 2019 American Chemical Society.

Trapped Ion Mobility Spectrometry (TIMS)⁵⁴⁸ devices,^{127,198,535,548,564-568} such as those present in Bruker's timsTOF series,^{565,569} are a recent addition to the native IM-MS arsenal, building upon development of this technique in 2011 by Park, Fernandez-Lima, and coworkers.^{197,564} These TIMS mass spectrometers offer the advantage of performing

many different types of tandem experiments online after IM separation. IM resolving power up to ~400:1 is possible on these instruments for small molecules,⁵⁷⁰ and “microheterogeneity” (multiple conformations of a protein for a single mass and charge state) has been observed using TIMS.⁵³⁵ More recently, Bleiholder and coworkers have introduced a setup utilizing two TIMS cells (tandem TIMS)¹²⁷ which enables collisional activation of mobility-selected ions and subsequent mobility-based structural analysis of their new conformations and/or fragments, expanding native MS capabilities in structural biology.⁷⁹

Although integrated IM separation is not yet available commercially for Orbitrap instruments from ThermoFisher Scientific, prototype instruments coupling drift-tube IM to Orbitrap mass analyzers have recently been demonstrated.^{152,155,199,571} Due to the relatively slow scan rate of the Orbitrap, sensitivity and resolution can be poor if ion packets are introduced into the drift tube only after all ions from the previous scan have exited the drift tube (amounting to a small duty cycle). To increase the duty cycle, FT methods,⁵⁷²⁻⁵⁷⁵ in which many packets of ions are released into the drift tube in rapid succession using precisely-controlled gating at a single or chirped frequency, have been introduced by Clowers, Laganowsky, and Russell (see **Figure 17**).^{152,573,576,577} This combination of the superior resolution and activation capabilities of the Orbitrap with additional separation of ions in the mobility dimension represents an exciting new development in the field of native MS toward analyzing large, extremely polydisperse samples. Advantages and disadvantages of these gating methods have been compared to other high-duty cycle gating methods, such as Hadamard Transform.⁵⁷⁸

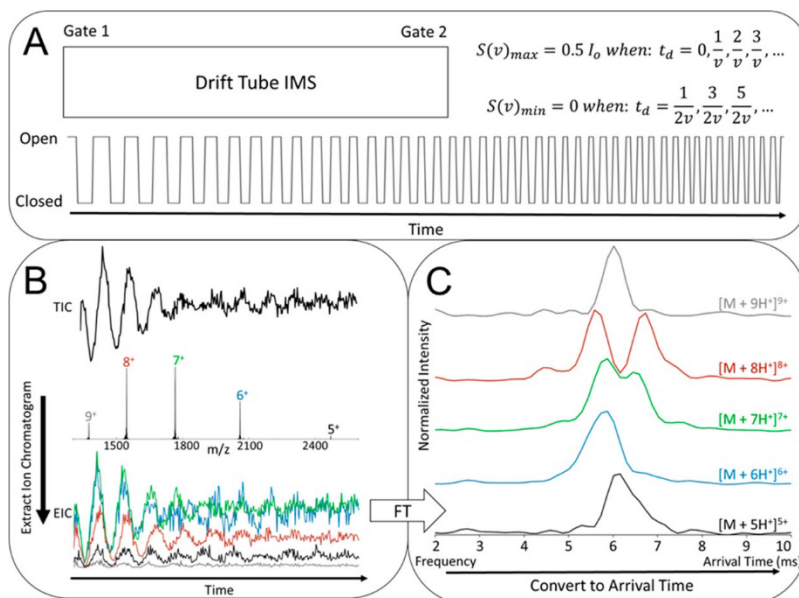


Figure 17. Schematic of entrance and exit gate synchronous chirped pulsing for FT-drift tube ion mobility-MS experiments (A). FT-IM-MS data for native cytochrome C obtained on a prototype FT-IM-Orbitrap instrument (B) and Fourier Transform of extracted ion chromatograms from FT-IM-MS data converted to arrival time distributions (C). Reprinted with permission from ref. 152. © 2018 American Chemical Society.

Very high sensitivity can be achieved in prototype IM-MS instruments based on Structures for Lossless Ion Manipulations (SLIM) developed by Richard Smith,^{194,196,579,580} printed circuit board ion optics with small cross sectional areas that maximize ion transmission. IM separation for native-like protein ions in a ~46 cm SLIM-TOF instrument was found to have a resolution of ~13-42, with CCSs nearly identical to those measured using drift-tube MS.¹⁹⁴ In these development-stage instruments, effective drift tube path lengths of ~540 m based on multiple passes around a serpentine SLIM board have resulted in resolving power of >1,800:1, although trapping times for the ions can be so long that substantial unfolding and even chemical reactions with trace reactive background gases often occur on the timescale of the separation.⁵⁷⁹ Ever-increasing complexity of samples could lead to not only signal overlap in *m/z* but also in ion

mobility, thus improved separation in more dimensions than m/z may be very advantageous.

2.3.3. Ion Reactions for Improved Separation

A common problem in native MS for complex samples is that nESI-generated ions of different charge states can sometimes overlap at the same m/z . Since the early days of native MS, researchers have utilized various methods to manipulate the charge states of ions with minimal perturbation to their native-like structures and thus shift their signal in m/z to facilitate analysis.⁵⁸¹⁻⁵⁹⁰ Increasing charge states can move mass spectral peaks to lower m/z , where instrument resolving power, trapping, and transmission efficiencies are often higher. Decreasing charge states (as in Charge Reduction Electrospray Mass Spectrometry developed more than 20 years ago by Lloyd Smith and coworkers^{587,589,590}) can be advantageous because the spacing between mass spectral peaks increases, reducing peak overlap. These effects on charge state can be achieved through addition of chemical reagents to sample solutions and through gas-phase ion/ion reactions performed in the instrument. In this section, we describe recent developments in this area, made possible by early pioneering work utilizing ion/ion reactions, supercharging reagents, superbases and proton sponges, α -particle emitters, and corona discharge for charge manipulation.^{452,582-597}

2.3.3.1. Charge Manipulation. Native Supercharging ESI, a modification of denaturing supercharging electrospray ionization, uses small, polar chemical additives with high boiling points to encourage attachment of unusually high numbers of charges to native-like ions during the ESI droplet evaporation process.^{595,598-600} In most cases, this results in extensive unfolding of the ions, even to the point that nearly linear structures

are produced.^{205,206,211,594,598,601-610} However, in some cases, such as ions with very strong noncovalent interactions, less unfolding is observed,⁵⁹⁵ and native stoichiometries are preserved, as for anthrax lethal toxin ((PA₆₃)₈(LF_N)₄, ~630 kDa) in its pore form.⁵⁹⁸ Many reagents have shown excellent supercharging properties, including some that are very economical.^{206,283,594,609,611} In addition to moving mass spectral peaks into *m/z* regions with higher resolving power, supercharging reagents can improve the efficiency of top-down dissociation methods, such as CID and electron capture/transfer dissociation (ECD, ETD).^{131,595,612-614}

Manipulation of peaks to shift the opposite direction in *m/z* and thus spread out overlapped peaks can be done via charge reduction, which dates back to work done to measure gas-phase basicities of reagents and the addition of superbases and proton sponges to samples.^{452,587,589-592} Numerous experiments have demonstrated charge reduction of native biomolecular complexes upon addition of strong bases or their salts,^{204,584,615} such as triethylammonium salts,^{178,204,616-618} trimethylamine N-oxide (TMAO),⁶¹⁹ polyamines,⁵⁷⁶ and imidazole derivatives,^{426,593} to native ESI buffers. Laganowsky showed that charge reduction can be especially useful in revealing multiple lipid adduction states for membrane proteins embedded in lipid-detergent micelles which were not accessible without addition of TMAO (see **Figure 18**).⁶¹⁹ In addition to separating overlapping peaks in native mass spectra, charge reduction can also improve the ability of methods such as SID to maintain compact ion structures upon dissociation, useful for determining quaternary structure and subunit interactions in complexes.^{119,221,485,620,621}

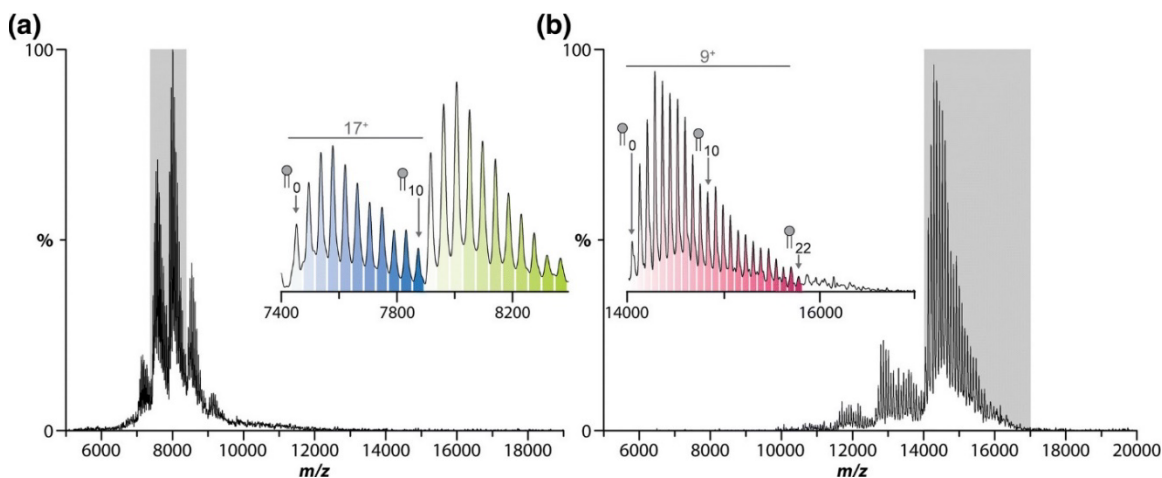


Figure 18. Native mass spectrum of *Escherichia coli* ammonia channel B trimers with PO-phosphatidylethanolamine adducts and no TMAO (A) and with TMAO (B), illustrating charge reduction by TMAO and associated increase in the number of observable lipid adducts. Reprinted with permission from ref. 619. © 2019 American Society for Mass Spectrometry.

2.3.3.2. Ion/Ion Reactions. Gas-phase ion/ion reactions^{121,583} performed inside the mass spectrometer are another common route to simplify otherwise complicated mass spectra. Building upon the use of corona discharge in ESI pioneered by Lloyd Smith,^{587,591} Cation to Anion Proton Transfer Reactions (CAPTR), introduced by Bush, is a method for reducing the charge of native protein cations in the gas phase by reacting them with small reagent anions that abstract protons.^{622,623} The reagent anions are produced from flowing fluorocarbons through a corona discharge in the ion source, after which they are trapped inside the instrument. The polarity of the ion source is rapidly switched to enable introduction of native protein ions produced by ESI, and these ions are combined with the reagent anions, to which they transfer protons, thereby reducing their charge state (see **Figure 19**). This method (as well as charge reduction and manipulation in general) can facilitate analysis of heterogeneous samples, as illustrated for the overlapped peak in the native mass spectrum in **Figure 19A** corresponding to charge states of two different proteins and subsequent separation of each species' peaks with

CAPTR in **Figure 19D**. Advantages of CAPTR for native biomolecular complexes can be similar to those of charge reduction reagents. A similar effect on charge states in native mass spectra can be obtained using a form of ETD, in which the multiply-charged protein ions capture an electron produced by a cathode or transferred from a radical anion reagent in the gas phase without subsequent dissociation (“ETnoD” or nondissociative electron transfer), as illustrated by results from the Barran and Sobott groups.^{130,298,624} Kaltashov and coworkers have also utilized transfer of electrons from ETD reagents (such as fluoranthrene radical anions) to protein ions isolated in small m/z windows to reduce mass spectral complexity and spread the resulting reduced charge states along the m/z axis (“limited charge reduction”).^{59,179,625}

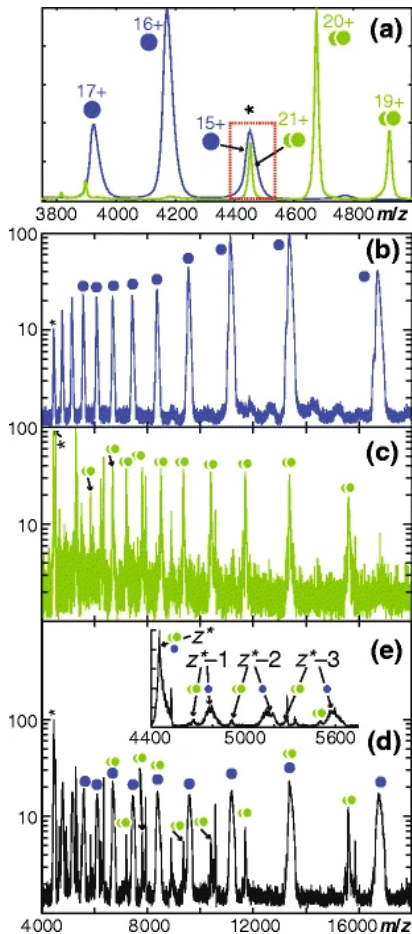


Figure 19. Native mass spectrum of bovine serum albumin (BSA, blue) and yeast enolase dimer (green) (A), CAPTR of BSA15+ in the absence of enolase (B) and enolase21+ in the absence of BSA (C), and CAPTR of BSA15+/enolase21+ peak (D,E) from the red box in (A). Reprinted with permission from ref. 622. © 2015 American Society for Mass Spectrometry.

In 2020 McLuckey, a long-time innovator in gas-phase ion/ion chemistry,^{121,581-583,597,626} introduced a method similar to CAPTR, but instead using a modified source in which two electrospray sources are used, one in positive ion mode (for the ion of interest) and the other in negative ion mode.⁶²⁷ The anionic reagent is a protein ion with multiple negative charges, such as (insulin chain A)⁵⁻⁶⁻ or (holomyoglobin)^{~10-}, which, due to its physical size and large negative

charge, has a large adduction cross section for recombination with the positively-charged native biomolecular ion of interest. This process can result in multiple adductions of the reagent protein to the ion of interest, reducing its net charge and producing a characteristic train of peaks at high m/z that can be used to identify it and determine its charge state based on the known mass of the reagent protein (see **Figure 20**).⁶²² Additionally, proton transfer charge reduction capabilities are now possible on commercial instruments, such as ThermoFisher Scientific's Orbitrap Eclipse Tribrid mass spectrometer,⁶²⁸ and we refer interested readers to a recent review covering the latest developments in gas-phase ion/ion reactions in MS.¹²¹

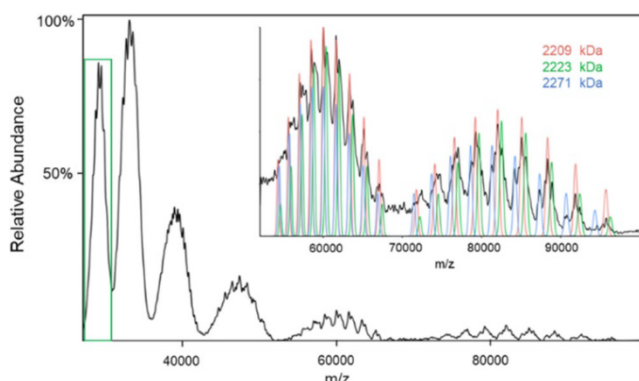


Figure 20. Post-ion attachment mass spectrum of *E. coli* 70S ribosome-related subunits showing charge reduction upon gas-phase attachment of holo-myoglobin₁₀₋ and associated resolution of non-isobaric components of the native ion distribution (green box). Reprinted with permission from ref. 627. © 2020 American Chemical Society.

2.4. Global Approaches to Heterogeneity

2.4.1. Average Composition

In some cases of extreme compositional heterogeneity, such as that in random copolymers or mixed-lipid Nanodiscs,^{60,168,169,453,629,630} it may be very difficult, even with the above state-of-the-art methods, to determine the complete mass and stoichiometry distributions for the entire ion population. However, a number of methods have been

introduced to determine global average composition information for these types of samples.

2.4.1.1. Inference from Fragmentation Data. Although Prebyl and Cook hinted at the possibility of using FT-based analysis methods to determine the monomer ratio of copolymers in the original article describing their FT-based algorithm (see §2.2.1.1),⁴⁴⁸ ultimately they demonstrated an alternative method relying on CID.^{631,632} In this method, it is assumed that the monomer composition of the end regions of the polymer ions is representative of the composition of the polymers as a whole. CID is used to fragment the polymer ion population formed using electrospray ionization, and low-mass fragment ions produced by this process are assigned based on the known monomer masses. The ratio of the total intensity of low-mass ions associated with each monomer is calculated and assumed to represent the global average composition of the copolymer sample. These authors examined the accuracy and precision of this approach at various collision voltages, including whether it is better to use only intact monomer fragments versus include secondary fragments.⁶³¹ Intriguingly, for ~20 kDa poly(styrene sulfonate)-co-(maleic acid) samples, in which the styrene sulfonate (SS) monomers are significantly more acidic than the maleic acid (MA) monomers, observed fragment ratios were typically a factor of at least 3 times the monomer ratios provided by the manufacturer. The authors attributed this to a difference in ionization efficiency between ions with unusually high SS content and those with low SS content owing to the high acidity of this monomer. While the accuracy and precision of the method can be excellent, a calibration curve is necessary to reconcile the bias of the method toward the higher-acidity monomer.⁶³² Importantly, recent work on the gas-phase behavior of lipids has

demonstrated that deducing the average composition of such polydisperse analytes as membrane proteins and lipid Nanodiscs from observed lipid loss upon activation can be unreliable.^{165,283,454}

2.4.1.2. “Double FT” Approach. FT-based methods have enabled analysis of average composition directly from mass spectra of intact large ions, instead of relying on fragmentation data. As described above in §2.2.1.2, the “double FT” approach can be used to approximate the composition of Nanodiscs containing two different types of lipid. Marty illustrated use of this method to determine the composition of Nanodiscs formed from MSP1D1(–) and binary mixtures of palmitoylcholine (POPC) and either PO-phosphatidylserine (POPS) or PO-phosphatidylglycerol (POPG).⁴⁵³ Overall, excellent agreement was observed between the double FT-based lipid composition and the bulk lipid composition used to assemble the Nanodiscs. For these determinations, it was assumed that the average lipid mass found by double FT of the mass spectrum is a simple bulk population-weighted average of the lipid monomer masses. Double FT was recently used to determine the identity and relative abundances of lipid head groups adducted to native proteins and found excellent agreement with expected masses as well as abundances anticipated from the appearance of the raw mass spectra.⁴⁵⁴

2.4.1.3. Distinguishing Compositional Heterogeneity Types Using FT-Based Methods. Cleary and Prell showed that FT-based approaches, such as those implemented in iFAMS, can be used not only to characterize the bulk composition of ion populations formed from two types of subunits, but also to reveal what type of heterogeneity is present in the sample (see **Figure 21**).⁶⁰ They introduced a classification scheme for

different common types of sample heterogeneity: “superpositions”/simple mixtures (Class I), mixtures satisfying a “mean-proportional-variance condition” (Class II), and mixtures following a multinomial subunit distribution (Class III). Class I includes mixtures of analytes that contain exclusively one type of subunit, such as a mixture of homopolymers or single-lipid Nanodiscs. Class II includes analytes for which incorporation of different subunits is essentially random, and the distribution of the entire population is well described by a convolution of separate distributions, one for each type of subunit, as may be the case for Nanodiscs made from pre-mixed non-interacting lipids or for random copolymers. Class III includes ion populations for which the incorporation of a particular type of subunit follows a multinomial distribution, such as different isotopes of a particular atom in an ion or different protein isoforms into a protein complex whose stability is not affected by the identity of the isoform.

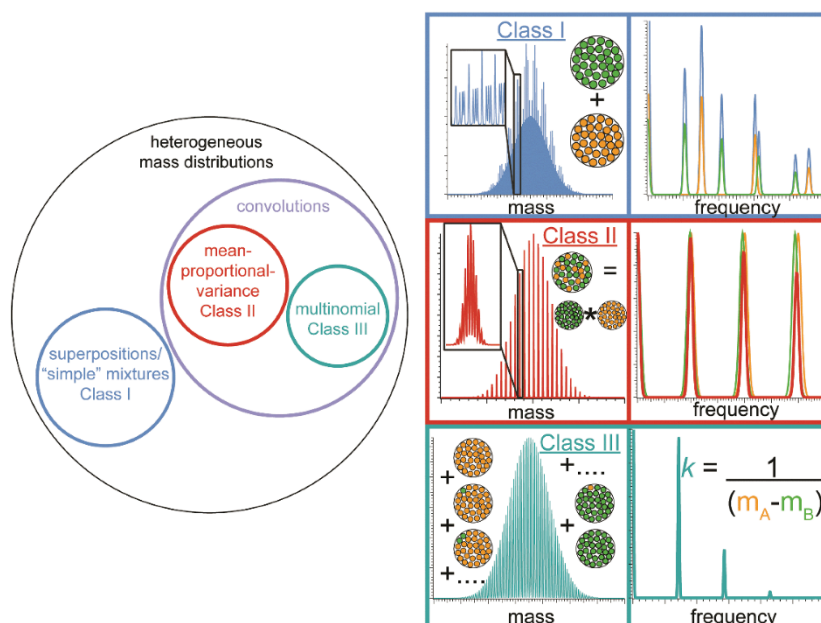


Figure 21. Schematic of different classes of compositional heterogeneity for analyte mixtures (left) and representative mass spectra and corresponding Fourier spectra for model ion populations representing each heterogeneity class. Reprinted with permission from ref. 60. © 2020 Royal Society of Chemistry.

Class I and II populations can often be clearly distinguished by their corresponding Fourier spectra, even when the bulk compositions of the mixtures are identical. This work also provided mathematical justification for Marty's "double FT" approach⁴⁵³ (see §2.4.1.2) in analyzing binary phospholipid Nanodiscs. For the double FT approach to work, the mean number of each subunit type incorporated into the ion population must be proportional to the variance in the distribution for that subunit across the whole population (the "mean-proportional-variance condition").⁶⁰ Under other conditions, the result from the double FT approach can be inaccurate. Fortunately, the mean-proportional-variance condition likely holds for many common types of assembly mechanisms for copolymers, mixed-detergent micelles, Nanodiscs, and other membrane mimetics.

The FT approach of iFAMS can also be used to infer information about the assembly mechanism for heterogeneous ion populations based on their apparent membership in the various classes described above. For example, from their Class II FT spectra, it was deduced that phospholipids incorporate into Nanodiscs without extensive equilibration of their composition after Nanodisc assembly is arrested by complete removal of detergent,^{633,634} in agreement with other experiments showing that lipid exchange between fully-formed Nanodiscs is very slow.^{629,635,636} This distinction, which is only possible through analysis of the Class behavior of the FT spectra because extensive equilibration would result in no change in bulk composition, illustrates the utility of compositional analysis even for poorly-resolved heterogeneous ion populations.

2.4.2. Assigning Biomolecular Ions to Chemical and Structural Class

For some samples, complete analysis of their mass spectra to achieve the level of detailed interpretation in many of the aforementioned strategies may not be possible. However, various features, including charge state, CCS, and/or Fourier frequency information, can still enable a coarse-grained level of characterization of the ion's chemical or structural class, which we detail below.

2.4.2.1. Small Biomolecular Ions. Although calling the structures of small biomolecular ions “native-like” may be inappropriate in many cases (for example, isolated phospholipid ions may have structures rather different from those when they are packed into cell membranes *in vivo*), structural classification and prediction based on electrospray IM-MS data provide key insights into how this approach might be used more generally for larger native biomolecular ions in the future. This type of classification could be particularly relevant for heterogeneous biomolecular complexes involving many small molecules (either bound or free in clusters) for which the identities are unknown and/or for which there are coincident masses. Because IM separation in the low-field limit reflects the “size” (CCS) to charge ratio of ions,⁶³⁷ some approaches for classifying ions according to their chemical structure take advantage of different typical densities belonging to each class. For example, over a wide range of masses, lipids tend to have lower densities (thus higher CCS) in the gas phase than do nearly isobaric carbohydrates, which tend to have high density owing to their very high number of internal hydrogen bonds.⁶³⁸⁻⁶⁴² Peptides tend to fall somewhere in between, and small drug-like molecules tend to be lower in mass than the other three classes, yet span a wider range of CCS/*z* ratio (see **Figure 22**).⁶⁴¹⁻⁶⁴³ McLean^{641,642} and Xu^{640,643} have demonstrated reliable and

reproducible classification of lipids, sugars and polysaccharides, nucleotides, peptides, and small drug-like molecules into different regions within electrospray ion mobility-mass spectra, with CCS measured in nitrogen on both drift-tube and traveling-wave type ion mobility-mass spectrometers. Subclassification of phospholipids according to head group type has also been demonstrated, although isobaric lipids with different head groups types often differ in CCS by only a few percent,⁶⁴⁴ illustrating the necessity of increased separation and resolving power as described in §2.3.2. Zhu,⁶³⁹ McLean,^{641,642} Baker,⁶³⁸ and Xu⁶⁴⁰ have introduced efforts to build large, publicly available online compendia of CCS information for metabolites to improve database- and Machine Learning-based prediction of CCS using structural information as well as prediction of structure (from biomolecule type to more detailed Lewis structure) using IM-MS data. In combination with gas-phase isolation and fragmentation, remarkably detailed structures can be predicted using these approaches. This foundational work toward classification of small molecules using IM-MS data holds great promise with future interpretation of increasingly complex, larger, and heterogeneous samples, especially as IM-MS instrumentation continues to improve and native IM-MS is applied to investigate endogenous and/or unknown bound small molecules and ligands (see §2.3.2).^{87,91,93,322}

2.4.2.2. Classification of Large Biomolecular Ion Conformation Using Native IM-MS Data. Quantitative correlations of mass with charge state^{205,208,255,645-650} and with CCS^{201,205,207,209} have long been noted in IM-MS research. Based on a simplistic picture of the electrospray process, the charge state for globular ions is expected to follow a mass^{1/2} dependence due to the Rayleigh criterion for fission of charge droplets (the “Charge Residue Model”).^{180,646,651} By contrast, extended, quasi-linear structures⁵⁹²

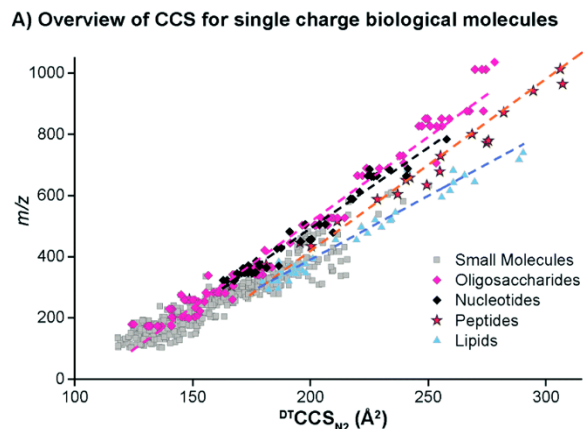


Figure 22. Composite nitrogen drift tube IM-MS data for singly-charged biological molecules illustrating separation into different m/z vs. CCS regions according to structure type. Reprinted in part with permission from ref. 638. © 2017 Royal Society of Chemistry.

should follow the relationship $[(z-1) \ln(z-1)] \propto \text{mass}$, where z is the charge of the ion.²⁰⁵

Structures in between these extremes, such as mostly globular native protein ions with unfolded or disordered regions, may follow intermediate behavior (see **Figure 23**).²⁰⁸

Likewise, CCS is expected to scale with $\text{mass}^{2/3}$ for globular ions^{201,205,207,209} and mass^1 for quasi-linear structures.^{205,206} Because solvent accessible surface area (SASA) can be

computed very quickly by many molecular visualization and dynamics programs, some researchers have used SASA for modeled protein structures in place of experimental or computed CCS values.^{208,210,650} Empirical mass scaling exponents for charge, CCS, and

SASA have been measured for a wide variety of proteins with structures ranging from intrinsically disordered or semi-disordered to compact globular. Using these expected

scaling relationships, it is often possible to assign protein and protein complex ions (even with the same m/z) to different structural classes by examining IM-MS data. This simple approach can be very useful in determining whether a given set of solution and/or

instrumental conditions produces a structurally homogeneous vs. heterogeneous ion population, and whether these structures are likely compact, partially unfolded, or

extensively unfolded, especially important in cases where native MS reveal species not previously identified by other structural methods.^{68,75,99,156,652} Oligomers can also be classed into linear, compact, and other topologies based on expected CCS scaling with mass, even for samples containing mixtures of these topologies.^{208,210}

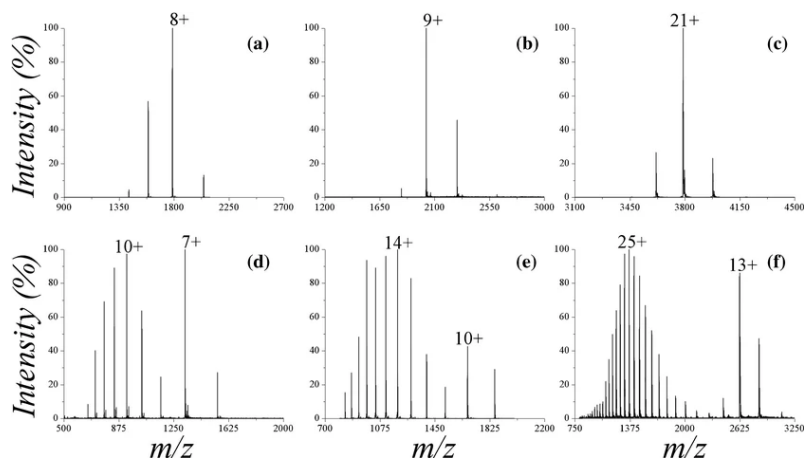


Figure 23. Representative native mass spectra of globular proteins (A: chicken-egg lysozyme, B: bovine β -lactoglobulin, C: human transferrin) and intrinsically disordered proteins (IDPs; D: Sic1-KID from *Saccharomyces cerevisiae* residues 215-284, E: human stathmin-4, F: murine ataxin-3 residues 1-291), illustrating relatively low charge states for globular proteins and multimodal distributions for IDPs. Reprinted with permission from ref. 208. © 2017 American Society for Mass Spectrometry.

2.4.2.3. Gábor-Transform Isolation of Biomolecular Ion Signal from High-

Salt Background Signal. One limitation in the use of native MS in structural biology is the reliance upon volatile buffer salts such as ammonium acetate rather than those which more closely resemble physiological conditions, due to the tendency of nonvolatile salts to complicate mass spectra and suppress ionization of the analyte of interest.^{230,231,597,653} Efforts to circumvent these challenges include the use of submicron emitter tips^{228,457,654-656} as well as improvements to data analysis methods (see SWARM, §2.2.2.1). Gábor Transform (see §2.1.9) of highly congested native mass spectra in iFAMS was used to characterize the masses of monomeric protein ions electrosprayed from buffers

containing a relatively high concentration of salt (100 mM NaCl in Tris or HEPES buffer).⁴⁵⁰ Despite signal from large salt cluster ions dominating the mass spectrum, GT enabled isolation of signal arising from the protein. As illustrated in **Figure 24**, signal from protein ions (which tend to follow a negatively chirped pattern) can be visually distinguished in the GT spectrogram from interfering/overlapping salt cluster signal (which appear as horizontal stripes or positively chirped patterns). This difference arises from the essentially constant mass of the protein ions as a function of charge state, whereas the charge state of salt cluster ions and clusters of small molecules such as lipids tends to increase with mass. By the same reasoning, protein ions of similar m/z but different masses can in principle be readily distinguished in GT spectra upon visual inspection due to their different chirp patterns, as was demonstrated for α -hemolysin hexameric and heptameric complexes which were overlapped in both the FT spectrum and the mass spectrum.⁷⁵ As seen in **Figure 24**, higher charge states (indicative of some unfolding) can often be easier to detect in a high salt cluster background than fully-folded native ions of lower charge states, but the chirp pattern established by these higher-signal peaks can facilitate visual identification of lower-signal native peaks.⁴⁵⁰

3. Conclusions and Outlook

3.1. Current State of the Field

Above we have provided an overview of past and state-of-the-art approaches toward overcoming the problem of heterogeneity in native MS, with a specific focus on strategies which enable preservation of inherent heterogeneity of samples important for understanding biological structure and function and aim to facilitate analysis and interpretation. Initial efforts in this area focused on accurate assignment of charge states

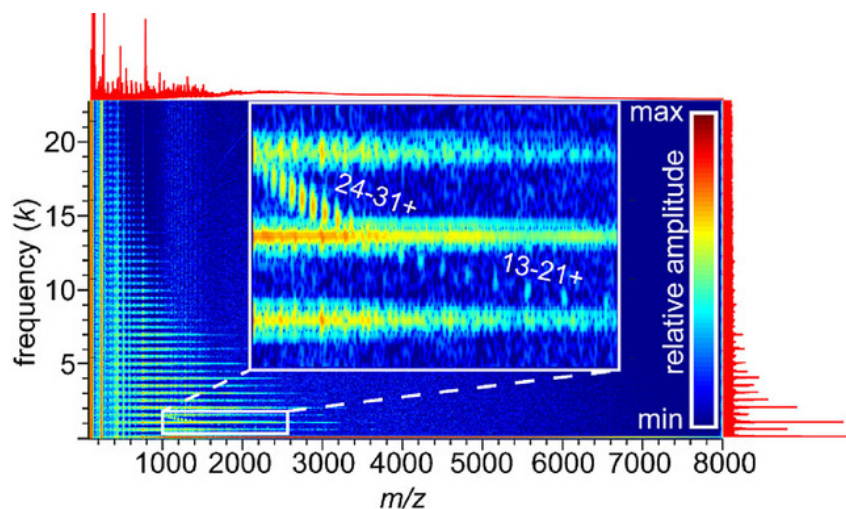


Figure 24. Mass spectrum of native-like anthrax toxin Lethal Factor N-terminal domain electrosprayed from Tris/sodium chloride buffer, (top red trace), corresponding Fourier spectrum (right red trace), and Gabor spectrogram (heat map), illustrating separation of negatively-chirped protein signal (labeled according to charge state in inset) and sodium chloride clusters (horizontal bands). Note that cluster ion and protein ions signals are strongly overlapped in both m/z and frequency but are easy to identify in the Gabor spectrogram. Reprinted with permission from ref. 450. © 2019 Wiley-VCH Verlag GmbH & Co.

and masses to relatively simple native mass spectra representing few ions and with ample resolution of individual charge states.^{249,657-663} Of course, as instrumentation rapidly improved and landmark achievements were made, samples of ever-increasing complexity have become routine to investigate with this powerful technique.

Today, it is possible to analyze mass spectra representing highly polydisperse ion populations, with broad charge state distributions and tens or even hundreds of overlapping peaks, and researchers have a plentiful buffet of programs and algorithms from which to select. Automation and batch processing has continued to improve to the point that some published articles in the field of native MS now reflect many tens to hundreds of individual mass spectra^{283,418,629} that might be effectively hopeless to analyze by hand, an improvement that parallels software development in “omics” fields.^{664,665} Adjuvant strategies for separating complex ion mixtures using chemical reactions or

labeling during the electrospray process or within the mass spectrometer have further expanded the range of challenging samples that can be addressed. Deconvolution approaches now span the range from game theory to Bayesian inference to Fourier/Gábor Transform methods from signal processing theory. This plethora of “orthogonal” deconvolution methods offers the promise of cross-validation, although to date this has been rarely implemented in the literature.^{337,371} Furthermore, for the past 25 years or so, the use of volatile salt “buffers”⁶⁶⁶ (such as ammonium acetate) has been nearly universal in native IM-MS due to the adverse effects of salt adduction when using more physiologically-relevant buffers (Tris, HEPES, phosphate buffers, etc.). Modern deconvolution methods, including Gábor Transform and SWARM, as well as the recent use of submicron nESI emitters^{228,229,457,653-656} may finally liberate native IM-MS from dependence on volatile salts and artifacts arising from their use.⁶⁶⁶ Other current efforts toward better understanding of detergent/lipid properties and their influence on membrane protein behavior, as well as engineered and tailored membrane scaffold proteins and lipids for Nanodisc construction and other membrane mimetics, also present exciting avenues for the future of native MS.^{162,163,168,419,667-671}

Additionally, continual improvements and innovation to instrumentation, including increasing mass resolution and separation capabilities and implementing various techniques including ion/ion reaction capabilities into high-performing mass analyzer instrument platforms, demonstrates the rapid, ever-evolving state of this field. Thanks to these advancements, native MS investigation of extremely large, heterogeneous samples, such as intact viral capsids, multimeric protein complexes, and membrane proteins, is now in many laboratories routine. Recent work in combining

native MS with other techniques, such as cryo-electron microscopy (cryo-EM) and omics approaches,^{46,91,103,672-675} and in analyzing samples directly from native environments, lipid vesicles, and/or crude cell lysates^{83,87,106,158-161,425,670,676-680} constitutes the very exciting, hybrid future of structural biology and of the role of native MS within it.^{82,150}

3.2. Remaining Challenges

3.2.1. Recalcitrant Features of Heterogeneity

Despite major improvements in theory, software, sample preparation, and instrumentation, it remains very challenging to quantitate heterogeneous mixtures with very different component intensities, although solving this problem would be highly beneficial for drug development, fundamental biochemistry, and related fields. For example, this problem arises when large and small peaks overlap in the mass spectrum or Fourier/Gábor spectrum, in which case it can be extremely challenging to decide whether the small peak is present. Curiously, resolution generally improves in Fourier/Gábor spectra with higher polydispersity in the corresponding mass spectrum. Thus the complementarity of this method with other methods operating on the m/z domain suggests that combining both approaches may provide an optimal path forward in mixture quantitation. For both types of approach, however, it is still very challenging in general to analyze polydisperse multi-subunit ion populations if the subunit masses are not near-multiples of one another.

Another outstanding question pervading native IM-MS is whether measured ion abundances do in fact quantitatively reflect those present in solution, let alone under what conditions native-like ions may be relevant for understanding structure and function. Recent results⁶⁵³ using submicron nESI emitters indicate that biomolecular ions formed

from solutions containing higher concentrations of physiological salts (such as sodium chloride) can be stabilized in more compact conformations, consistent with what has long been known about effects on protein stability from different ions first described by Hofmeister in 1888.^{681,682} Thus experimental methods which enable ionization of biomolecules from physiological buffers^{228,229,653,654} and deconvolution methods^{450,455} that can eliminate remaining background salt cluster signal and/or accurately account for salt adduction to biomolecular ions will be especially important for approaching this question for heterogeneous mixtures.

3.2.2. Is There a “Complexity Limit” in Native Mass Spectrometry?

All of the data analysis methods described in our review are ultimately limited by the resolution of the mass spectra, which typically decreases as the ion population grows more heterogeneous.⁵⁰⁴ Although the resolving power and sensitivity of modern mass spectrometers continue to improve, researchers will inevitably need to understand yet larger, more complex and heterogeneous samples. It is therefore imperative to continue developing methods that anticipate these future advances or which can work together synergistically to combat the problem. For example, many current deconvolution methods can be and are regularly used without the luxury of isotopic resolution, which somewhat paradoxically can simplify the deconvolution process and interpretation of the resulting data. How will these algorithms perform if and when much higher resolution is readily available? It is plausible that unique assignments of peaks for complex isotope distributions of overlapped ions representing different species will be very challenging within the m/z domain, and high m/z resolution may lead to extensive harmonic overlap in FT/GT approaches, complicating deconvolution. Perhaps methods like SWARM could

be combined with Bayesian, game theoretical, or FT/GT methods, for example, to first “de-isotope” the mass spectrum before further processing. Alternatively, charge manipulation or CDMS methods might be combined with deconvolution approaches to handle highly heterogeneous samples that suffer from space-charge repulsion or other resolution-reducing phenomena that occur with conventional mass spectrometry instrumentation. Continued investigation of these theoretical challenges in advance of improvements in instrumental resolution is therefore highly desirable.

3.2.3. Education Barriers

The variety of methods described in this review for approaching heterogeneous native samples with IM-MS is both exciting and daunting. Are there now too many options to choose from when deconvolving a complex mass spectrum? How should a researcher go about deciding which one to use? Many of the deconvolution methods here involve a substantial dose of mathematics, probability theory, signal processing, and facility with programming that many researchers may not have encountered in their training. Thus developers in this field face a major challenge of educating potential users on both theoretical aspects of how these approaches work as well as their practical use. A number of the data analysis tools described in this review have been made deliberately open-source so that users around the world can adapt the code to their own purposes, but doing so can be very intimidating for many new users. Fortunately, modern software sharing platforms, such as GitHub and GitLab, online science communities like Zenodo, and video sharing platforms (YouTube, Vimeo, and many others) offer researchers new and innovative ways to share their developments with others in ways beyond the written page, including through step-by-step video tutorials. Workshops at conferences aimed at

training new users on the theory and best practices for using these programs are increasingly common. It is our view that increased training of undergraduate and graduate students in practical scientific programming and modern data analysis methods will be highly beneficial in preparing the next generation of scientists to use these methods to their full potential. In parallel, we recommend that developers of these methods make a concerted effort to use online tools such as those mentioned above to lower the barrier for access to these powerful programs. Several good models for these recommendations exist already in both industry and academia. Protein Metrics Inc., for example, hosts regular user meetings and webinars for their software, which includes PMI Intact discussed here, as well as other tools for omics research.^{440,441} The National Resource for Native MS-Guided Structural Biology,⁶⁸³ funded by the National Institutes of Health since 2018, hosts regular workshops led by algorithm developers, instrumentation innovators, and technique pioneers with a goal to educate potential users.

3.3. Future Strategies and Best Practices

In our view, future advances to overcome the heterogeneity problem in native MS should embrace and preserve the inherent heterogeneity of samples rather than requiring researchers to mitigate it or make samples more homogenous, as was typically the focus of early efforts and much related discussion in the literature to date. Sustained growth of native MS as a tool in structural biology in many ways depends upon this strategy, as these heterogeneous features, such as bound small molecules, multiple coexisting stoichiometries, etc., continue to be revealed as important for understanding biological structure and function. Specifically with regard to optimal deconvolution methods, critical, necessary features include: ease and flexibility/customization of use (both

practically and with regard to different kinds of samples/information amenable), availability of resources and education materials for users including both practical and theoretical aspects as well as cautions about potential artifacts, ability to output information in formats digestible for both native MS experts and novices, compatibility with different mass spectrometer platforms and data types, and minimal requirements for user input which may ultimately bias results and lead to errors. Ease of interpretation is especially important for integration of these tools into industry settings, in addition to rigorous validation and automation of these methods.³³¹ We also envision a future in which multiple different tools can be integrated onto the same platform to provide complementary and/or supporting information, including development of field-wide scoring metrics, which has been the focus of some recent efforts already.^{436,684,685}

Based on our above analysis, we believe that a number of strategies exist that can be immediately undertaken to address the challenges outlined in §3.2. For example, streamlining existing software programs based on user feedback will greatly increase their widespread utility and application, thus continued conference and online workshops aimed at training users on and improving software through direct interaction will be very useful.⁶⁸³ Convergence on a small number of universal data formats amenable to multiple software platforms will provide a path towards improved reproducibility and cross-platform validation, as will inclusion of metadata needed for reproduction of analysis results in public data repositories.³⁰⁴ Continued development of cross-platform validation methods (such as comparing results from “orthogonal” approaches, e.g., Bayesian and FT/GT methods, or even feeding them into each other^{183,337,371}) and standardization of quality scores^{436,437} for results produced from them will help users identify artifacts and

better characterize uncertainties. For example, FT/GT methods can greatly facilitate identification of charge states for distinct, highly overlapped peaks in mass spectra,⁷⁵ thus inputting the range of charge states thereby identified may greatly reduce artifacts of other deconvolution methods that perform best when the charge state range is confined to correct values. Experimental and instrumental improvements possible in the near future include development of robust inlet-based separation beyond liquid chromatography (such as capillary zone electrophoresis³¹⁹⁻³²¹), next-generation nESI tip design (including reliable production of submicron emitters^{90,228,229,457,653,654,656} and theta-glass emitters for rapid mixing of samples during the ESI process⁶⁸⁶⁻⁶⁸⁸), and more efficient in-source desolvation.^{108,379}

In the more distant future, we also envision theoretical and instrument developments that reveal new types of information in native IM-MS data. For example, field alignment of biomolecular ions in IM-MS instruments may be used to separate ions based on structural differences not easily observed in experiments on current low-field IM-MS instruments.²⁰⁰ Further theoretical investigation into the relationship between observed heterogeneity/polydispersity and assembly mechanisms and kinetics may reveal information that is very challenging to deduce by other means.^{60,629} Continued improvement in modeling of dissociation, unfolding, and labeling kinetics and energetics will also allow researchers to design experimental protocols that can unveil subtle structural details and possibly differences not resolved by conventional native IM-MS.^{97,114,116,221,288,301,468,472,530,612,622,623,689-699} Finally, using the data analysis tools described in this review, streamlining the interface between native IM-MS and complementary state-of-the-art structural methods, such as cryo-EM and coherent

diffractive imaging, will likely provide unprecedented insight into composition, structure, and behavior of highly heterogeneous biomolecular systems.

Bridge

In this chapter, historical and state-of-the-art strategies to interpret information obtained with native mass spectrometry for heterogeneous biomolecular samples were reviewed. While these algorithm-based, instrumental, and experimental approaches focused specifically on information contained within the mass spectral domain, the next chapter surveys computational efforts to understand gas-phase protein ion structure, requisite for interpreting the information contained within the ion mobility domain. The following chapter also describes a comparative study of the performance of multiple molecular dynamics force fields in recapitulating gas-phase protein structure for use in combination with ion mobility experiments. In addition to providing new insight into robust features of gas-phase protein ion compaction, the resulting validated molecular dynamics simulation protocol serves to establish a quantitative benchmark with which to interpret ion mobility experimental data.

CHAPTER III
COMPUTATIONAL INSIGHTS INTO COMPACTION OF GAS-PHASE PROTEIN
AND PROTEIN COMPLEX IONS IN NATIVE ION MOBILITY-MASS
SPECTROMETRY

Includes co-authored material reprinted with permission from:

Rolland, A.D.; Prell, J.S. Computational Insights into Compaction of Gas-Phase Protein and Protein Complex Ions in Native Ion Mobility-Mass Spectrometry. *TrAC Trends Anal. Chem.* 2019, *116*, 282-291. © 2019 Elsevier Ltd.

1. Introduction

Native ion mobility-mass spectrometry (IM-MS) is an exciting and rapidly growing field of analytical chemistry with a central goal of learning about condensed-phase properties of biomolecules and biomolecular complexes by exploiting the high sensitivity, chemical specificity, and rapidity of gas-phase techniques.^{138,139,255} In native IM-MS, ion shape and size measurements made using IMS are performed in tandem with mass and charge measurement. Because flexible ions, such as polymers or biomolecules, of identical mass and charge can adopt different shapes under different conditions, the IM and MS steps can provide somewhat orthogonal information about an ion's properties. The measurements are not completely orthogonal in all cases, however, as an ion's size (measured in IMS as its collision cross section, CCS, which is akin to its orientationally-averaged "shadow") tends to increase with mass, albeit with different scaling laws for different classes of shapes, e.g., linear versus globular ions.⁶⁴⁹ Native IM-MS almost universally uses nanoelectrospray ionization (nESI) to transfer ions from aqueous buffer solutions into the gas phase, as the small size of the nESI capillaries helps to avoid artefactual oligomer formation induced by in-droplet condensation, and nESI conditions

can be controlled to minimize heating and structural changes of the complexes upon transfer into the instrument.^{255,700,701}

At the heart of native IM-MS is a long-standing question: to what extent and under what conditions are condensed-phase properties preserved upon transfer into the gas phase?⁷⁰² This question ranges in scope from coarse-grained properties such as native oligomeric state and subunit stoichiometry down to atomistic properties such as the number and location of hydrogen bonds, salt bridges, and coordination of particular functional groups. Although a great wealth of information about condensed phase properties of biomolecules has already been learned from native IM-MS, the answer to this question is far from complete and remains a subject of much current research. This review aims to survey the state of the art concerning changes in condensed-phase structure of globular proteins and protein complexes upon transfer to the gas phase using gentle nESI conditions, focusing on experimental native IM-MS and computational modeling approaches.

2. What are “Native” nESI Conditions?

The low-pressure gas-phase environment of a mass spectrometer (and of most IM instrumentation used in native IM-MS) differs significantly from the aqueous condensed phase in a number of important ways. The relative permittivity is close to 1 (some experiments suggest a slightly higher effective relative permittivity for protein ions owing to the polarizability of various functional groups),⁷⁰³ which intrinsically increases charge-charge and many charge-dipole interaction energies. This difference, and the absence of solvent molecules to favorably solvate them, might be expected to drive “self-solvation” of charged groups by interacting with nearby oppositely-charged or polar

groups. With the effects of water solvent also absent in the gas phase, one might anticipate that gas-phase biomolecular ion structure would differ strongly from condensed-phase structure, with self-solvation driving large-scale rearrangement or even “inversion” of condensed-phase structure.⁷⁰²

How, then, can structures resembling those in the condensed phase be preserved upon ionization and transfer to the gas phase? While small- or even large-scale rearrangements may be thermodynamically favorable, energy barriers for these rearrangements can be intrinsically quite high and may increase further relative to analogous condensed-phase rearrangements due to the absence of solvent and the low relative permittivity of the gas-phase environment. Because high barriers typically require high activation energy or long timescales to overcome, structures resembling those in the condensed phase can become kinetically trapped upon transfer to the gas phase on the millisecond timescale of native IM-MS experiments (see **Figure 25**).⁷⁰⁴⁻⁷⁰⁶

Gas-phase techniques that probe detailed ion structure, including infrared photodissociation spectroscopy,⁷⁰⁷ indicate that “memory” of solution-phase structure, such as charge sites in small dibasic organic ions,⁷⁰⁸ can sometimes be preserved in the gas phase under suitably gentle ionization and transfer conditions. Deliberate heating of biomolecular ions in the gas phase via energetic collisions with background gas, by contrast, can cause extensive unfolding driven by electrostatic repulsion of charge sites (“Collision Induced Unfolding”, CIU),^{114,693} which has been used to infer structural information about proteins and protein complexes.¹¹⁴

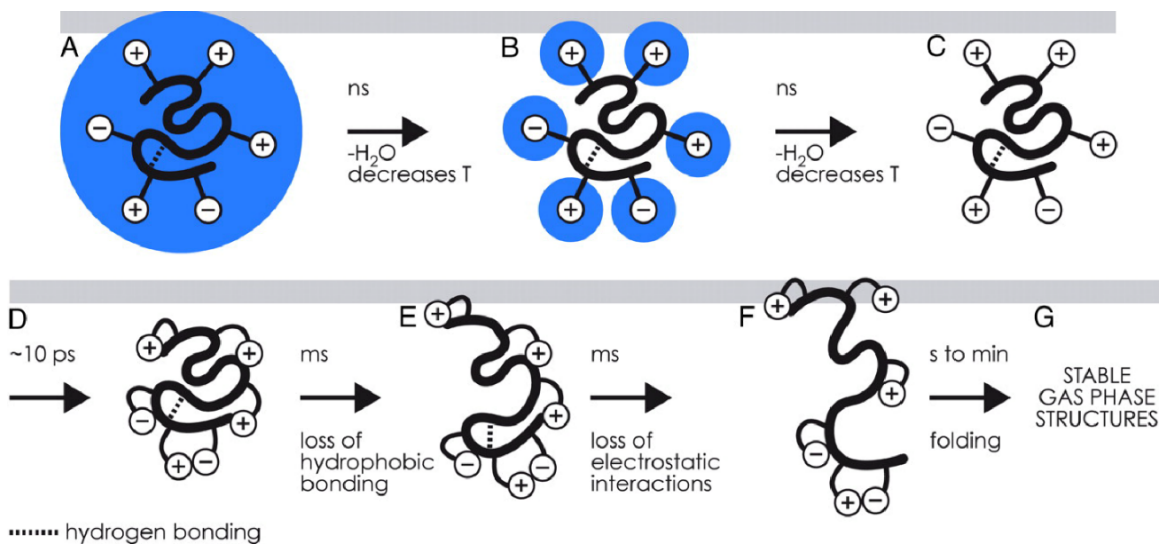


Figure 25. (A-D) Depiction of charging and self-solvation of charge sites (+ and – symbols) for globular protein ions during evaporation of the nanoelectrospray droplet on the nanosecond to picosecond timescale and (E-G) subsequent structural rearrangement and unfolding at longer timescales. Reprinted with permission from ref. 704. © 2008 National Academy of the Sciences.

Native IM-MS instrumentation offers a number of observables that can be measured to assess whether ions have likely retained native-like structures. Much evidence indicates that globular biomolecules typically adopt a gas-phase charge just below the “Rayleigh limit” charge for an aqueous droplet with the same volume as the biomolecule.^{648,649} The “Charged Residue Model” (CRM) states that charges originally at the surface of this end-stage droplet are then deposited onto the protein, determining its charge state distribution,^{646,651} which is relatively low and narrow as compared to denatured or intrinsically disordered protein ions.²²⁴ Conversely, several authors have shown a correlation between observed charge states of protein ions in native MS and the solvent-accessible surface area of their condensed-phase structures.^{648,649} Similarly, experimental CCS for globular protein ions typically scales as roughly the two-thirds power of mass, as expected for roughly spherical objects of similar density (see **Figure 26**).^{205,207,649,709}

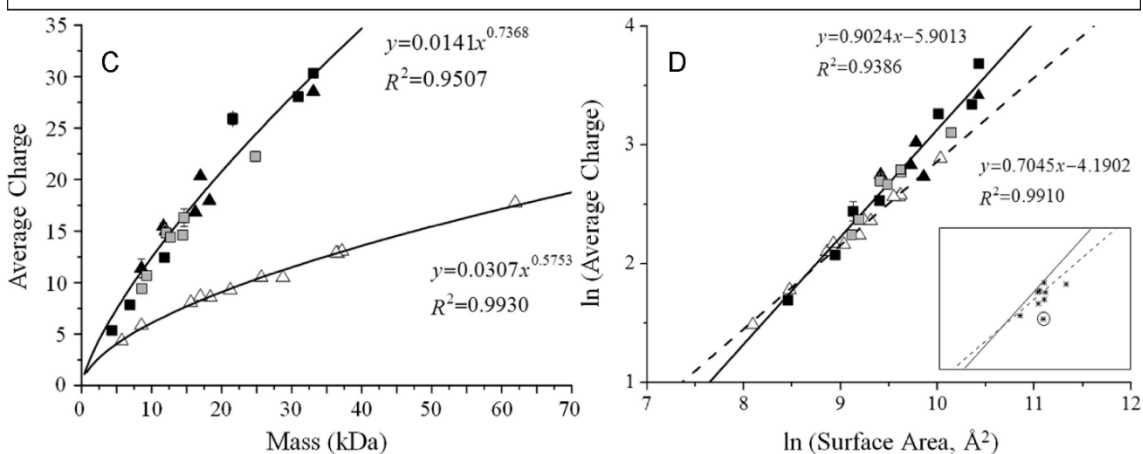
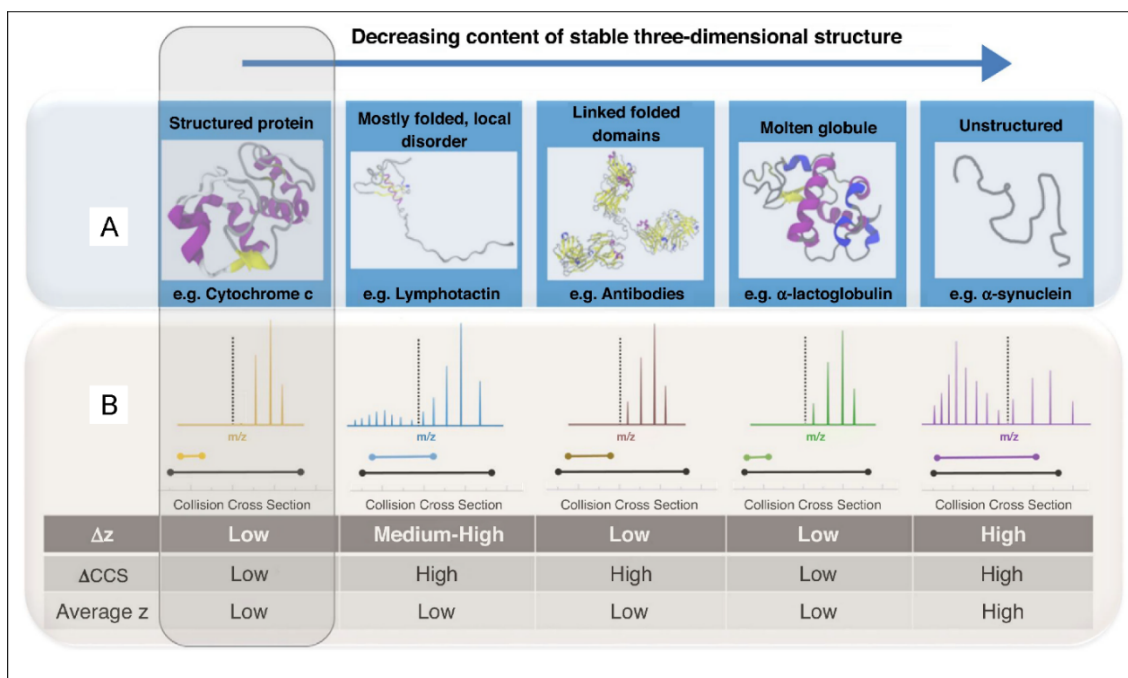


Figure 26. (A) Schematic illustration of condensed-phase protein structure types and (B) typical charge state and CCS distributions in IM-MS experiments. (C) Average charge states for protein ions formed under non-denaturing (native) conditions (open triangles) and denaturing conditions (all other symbols) as a function of mass and (D) relationships between average charge state and condensed-phase surface area for the same ions. A, B reprinted with permission from ref. 709. © 2018 Elsevier Ltd. C, D reprinted with permission from ref. 649. © 2011 American Chemical Society.

In the remainder of this review, we focus on the use of computational simulations and IM-MS data to understand the degree of compaction and structural rearrangement

undergone by native-like, globular protein ions upon transfer to the gas phase from solution.

3. What Happens to Folded Protein Ions Upon Transfer to the Gas Phase?

As described above, charging slightly below the Rayleigh limit is typically observed for many globular protein and protein complexes upon native nESI, but CCSs measured by IM-MS are often smaller than those predicted using condensed-phase structures drawn from x-ray crystallography or NMR experiments or from condensed-phase MD simulations.²²⁴ This difference in the CCS predicted for condensed-phase structures versus experimental native IM-MS values varies from ~0-20% for globular proteins and protein complexes ranging in mass from 2.8 kDa (melittin) to 336 kDa (glutamate dehydrogenase hexamer) (see **Figure 27**). This gas-phase compaction effect has long been attributed to “self-solvation” of charged and polar sidechains at the surface of the ion.^{704,710,711} IM-MS studies of polyalanine peptide ions indicate that self-solvation of the N-terminal charge on protonated ions of these peptides results in destruction of most α -helical content, illustrating the dramatic effects of self-solvation possible in the gas phase.⁷¹²

Simulations of gas-phase compaction of globular protein and protein complex ions have been undertaken through a variety of molecular dynamics (MD) approaches and with a range of force fields (FF).^{221,300,476,534,705,711-734} These approaches, along with examples from the literature, are summarized in **Table 1**. A recent review by Konermann discusses other MD simulation parameters and their impact on results.⁷³⁵ With simulated

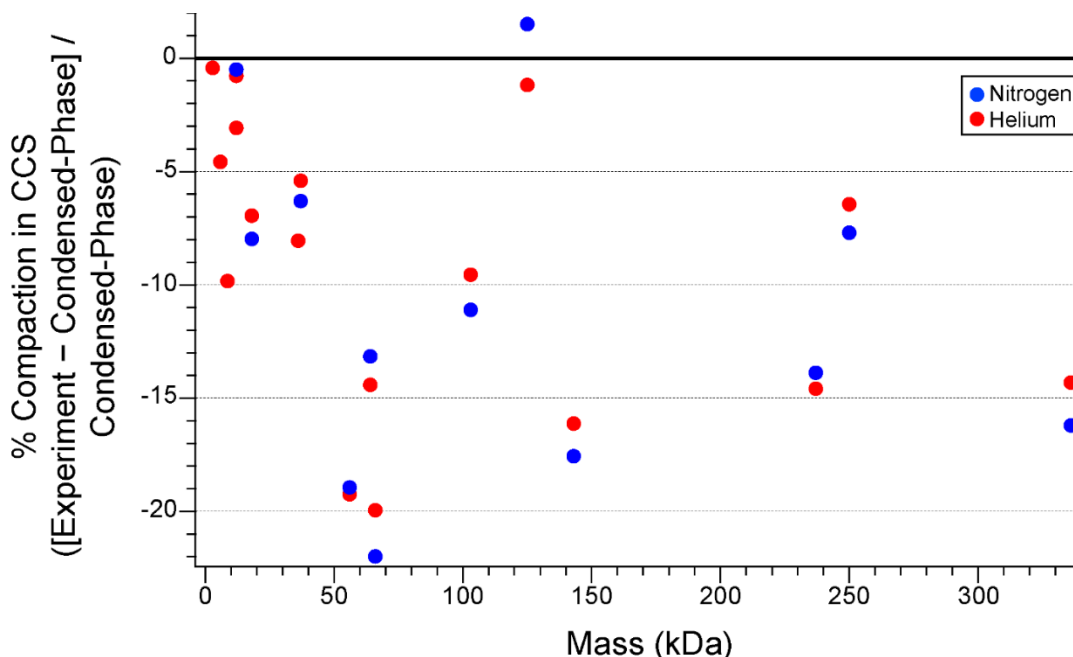


Figure 27. Plot of fractional compaction of protein and protein complex ions produced by nESI under native conditions measured by IM-MS in He or N₂ buffer gas as compared to CCSs for condensed-phase structures computed using Collidoscope.²¹⁴ Experimental CCSs from ref. 201 and 203. Protein Data Bank identifiers for all protein structures are listed in Figure 28.

structures in hand, ion CCSs in the relevant IM-MS buffer gas can be predicted using a variety of computational tools with tradeoffs in physical realism and computational expense. Reference 637 provides an overview of these CCS calculation tools, including their advantages and disadvantages, and the most common widely-used tools are summarized in **Table 2**.

A number of FFs have been developed for widespread use in both condensed-phase and vacuum MD simulations. These include the AMBER, OPLS-AA, CHARMM, and GROMOS FF families, which are optimized to reproduce experimental thermodynamics or results from quantum mechanical computations on small prototypical molecules (see **Table 1**).^{736,737} Because MD is by nature only an approximation of quantum mechanics, each FF has unique tradeoffs in physical realism and computational

Table 1. Overview of Types of Theory Used to Simulate Gas-Phase Protein Ions.

Type of Theory	Important Features	References
“Beads on a String”	Coarse-grained; amino acids represented as beads with no explicit accounting for atomistic structure	205,738
Molecular Dynamics	AMBER	Atomistic; partial charges based on gas-phase electrostatics computed with QM
	OPLS	Atomistic (united-atom also available); partial charges empirically optimized to experimental liquid vaporization and density data
	CHARMM	Atomistic (united-atom also available); polarizable variants available; partial charges based on small-molecule-water interactions computed using QM
	GROMOS	United-atom; solvated and vacuum variants available; partial charges based on experimental vaporization, density, and solvation free energy data
	MOIL	Atomistic; based on AMBER and OPLS
	Martini	Coarse-grained; parametrized based on experimental thermodynamics, including lipid bilayer properties
	ESFF	Atomistic; partial charges derived from ab initio computation of electronegativity and hardness
Quantum Mechanics	Atomistic; rigorous accounting of polarization, hydrogen-bonding, and electron density; extremely computationally demanding for large biomolecules	721,742,743
Quantum Mechanics/ Molecular Mechanics (QM/MM)	Multi-scale; Dynamics and conformational space explored with MD; local details (such as atomic coordinates, hydrogen bonding, electron density of a small region) computed with QM	713

efficiency. For example, the AMBER and CHARMM FF families use partial charges based on gas-phase electrostatics and aqueous solvation energies computed with quantum mechanics, respectively, but both of these FFs are known to have bias toward high helical

Table 2. Overview of Programs for Computing Collision Cross Sections of Gas-Phase Ions.

Computation Suite	Method	Scattering Type	Explicit Trajectories	Temperature/ Charge State-Dependent	3D Geometry-Dependent	Buffer gases
MOBCAL ²²⁰	PA	–	–	– / –	–	He
	PA*	–	–	– / –	+	He
	EHSS	elastic	+	– / –	+	He
	TM	elastic	+	+ / +	+	He
WebPSA ²¹³	PSA*	–	–	+ / +	+	He/N ₂
LCPA ⁷⁴⁴	LCPA	–	–	+ / +	+	He/N ₂
Sigma ⁷⁴⁵ , CCSCalc ⁷⁴⁶ , IMPACT ²⁰⁷	PA*	–	–	– / –	+	He
EHSSRot ⁷⁴⁷	EHSS	elastic	+	+ / –	+	He
IMoS ⁷⁴⁸	PA	–	–	– / –	–	He/N ₂ /
	(D)TM	elastic (inelastic)	+	+ / +	+	Ar/CO ₂ /air
	EHSS (TDHSS)	elastic (inelastic)	+	+ / +	+	
Collidoscope ²¹⁴ , HPCCS ⁷⁴⁹ , MobCal-MPI ⁷⁵⁰	TM	elastic	+	+ / +	+	He/N ₂

Features present (+) or absent (–) in various CCS calculation tools. Methods in bold type use 2-dimensional projections rather than explicit 3-dimensional scattering for CCS computations. Asterisks (*) indicate that a geometry-dependent “shape factor” is used to partially account for 3-dimensional scattering. PA = Projection Approximation, EHSS = Exact Hard Spheres Scattering, PSA = Projected Superposition Approximation, LCPA = Local Collision Probability Approximation, TM = Trajectory Method, D indicates inclusion of diffuse scattering (see ref. 637). Adapted with permission from ref. 214. © 2017 American Society for Mass Spectrometry.

content in condensed-phase protein simulations.⁷³⁷ GROMOS and OPLS-AA are optimized to reproduce experimental liquid vaporization and density data but have a known bias toward high β -sheet content (GROMOS more so than OPLS-AA).⁷³⁷

Reference 751 compares results from ten different FFs for solution-phase MD simulations of peptides.

MD simulations vary in physical realism and accuracy. However, nearly universally, these simulations predict compaction of globular protein and protein complex ions, in qualitative agreement with native IM-MS experiments. Few studies to date have directly compared results from multiple FFs for the same ions^{718,721,724} or over multiple different ions,^{221,300} thus we present an overview of some important case studies.

3.1. Ubiquitin

Ubiquitin (8.6 kDa) has long been a “fruit fly” of native IM-MS research, as it is a typical small, globular protein with known condensed-phase native structure^{752,753} and solution-phase unfolding behavior.⁷⁵⁴ Studies comparing ubiquitin ion structure predicted with MD simulations to native IM-MS experiments illustrate the power of using MD simulations to interpret experimental data while also providing important caveats.^{717,719,724} Chen and Russell studied temperature-dependent unfolding of ubiquitin ions in water (to simulate heating inside the nESI droplet) and in vacuum using an AMBER FF, comparing the MD results to IM-MS data from Clemmer⁷⁵⁵ and Bowers.⁴⁶⁹ Aqueous ubiquitin⁶⁺ ions were found to retain structures similar to the starting crystal structure up to ~375 K in simulations, with extensive unfolding at higher temperatures that resulted in loss of most helical content. By contrast, ubiquitin⁶⁺ ions in vacuum MD compacted to a small degree (~3%, with a CCS of ~950 Å²) with accompanying loss of secondary structure, but significant unfolding was not observed for temperatures below 600 K. Above 600 K, a large number of energetically-competitive structures were predicted, with a correspondingly wide spread in CCSs.⁷¹⁷

Structural effects of non-volatile salts on compaction and unfolding of ubiquitin have also been investigated with MD and experiment. Starting with folded structures

embedded in aqueous nanodrops containing 16 sodium ions, McAllister et al. used a CHARMM FF to simulate charging and desiccation of ubiquitin⁶⁺ (with sodium ion adducts as the source of charge rather than protons).⁷²⁹ Both the final charge of the protein and the predicted CCS were found to agree with experimentally measured values, within uncertainty, and were found to be consistent with the CRM and kinetic trapping of native-like structure. Further CHARMM simulations by Bartman et al. indicate that common biological metal ion adducts (such as Na⁺ and Ca²⁺) can form multidentate interactions with polar groups in ubiquitin⁶⁺ that make it resistant to gas-phase unfolding,⁷⁵⁶ a result echoed by a report from Wagner et al. that chloride anion adducts can have a similar effect.⁷⁵⁷ Bartman et al. caution that the MD-predicted structures for activated, metal-adducted ubiquitin⁶⁺ have structures bearing little resemblance to the crystal structure, despite similar calculated and experimental CCSs.⁷⁵⁶

Radical-Directed Dissociation experiments by Ly and Julian on ubiquitin ions formed from denaturing solutions were used to provide experimentally measured distance constraints for MD simulations of ion structure.⁷²³ Intriguingly, they found that constrained ubiquitin 4+ and 6+ charge states adopted structures in OPLS-AA MD simulations that differ significantly from the crystal structure and from unconstrained simulated structures, even though they possess CCSs within the range of those measured experimentally. These results provide an important additional caveat to interpreting MD-simulated structures with CCSs consistent with experimental values as definitive evidence that MD structures do in fact represent the experimental ion population, even when they are compact.

3.2. Cytochrome *c*

Cytochrome *c* (12 kDa), which contains a covalently-bound heme group, is another “fruit fly” of IM-MS and has served as a benchmark for gas-phase MD simulations of relevance to native IM-MS.^{704,705,726,732} Steinberg et al. performed MD simulations of solvent evaporation from and gas-phase collapse of native cytochrome *c*,^{705,732} building off of earlier CHARMM MD and IM-MS work by Jarrold.⁷²⁶ Using the MOIL FF (a hybrid of AMBER and OPLS FFs), Steinberg et al. found that cytochrome *c*⁶⁺, starting with its aqueous NMR structure and surrounded by 182 water molecules cools rapidly via loss of some, but not all, water molecules over a period of ~100 ps.⁷³² Little significant change in the structure of the protein was observed in any case, and the authors concluded that evaporative cooling prevents complete desolvation or restructuring of the ion in the absence of collisions or absorption of blackbody radiation on the picosecond timescale. A subsequent constant-energy MOIL FF study, starting with a completely desolvated cytochrome *c*⁷⁺ ion, predicted a number of structural changes.⁷⁰⁵ Charged sidechains were observed to self-solvate within 0-20 ps, and the typical number of salt bridges (SBs) was found to increase over ~10 ps from 6 to 17.2. The average number of hydrogen bonds (HBs) involving positively-charged sidechains increased dramatically from 0 to 11.7 on a similar timescale, but the number of HBs involving negatively-charged sidechains increased only slightly from 5 to 6.3. Charged sidechains moved to decrease the net dipole by ~1/3 during the first 10 ps. No significant breaking of non-covalent bonds was observed during the 4.2 ns simulations, and thus the final structure possessed a similar backbone conformation to the aqueous NMR structure. The

MD-predicted integrity of the folded structure was found consistent with experimental native electron capture dissociation experiments.⁷⁰⁵

Fascinating IM-MS experiments by Warnke et al., in which charged lysine sidechains of cytochrome *c* were capped with large crown ether ligands during the nESI process, indicate that self-solvation of charged sidechains in ordinary native IM-MS may actually prevent some collapse of ion structure.⁷¹⁰ Native charge states of cytochrome *c*⁷⁻⁸⁺ adopted successively lower CCSs as the number of adducted crown ethers increased from 1 to 5, despite the large size of the ligands. The authors interpreted these results to mean that, in the absence of self-solvation of charged surface residues by polar groups on the protein, the interior of the ion collapses significantly on transfer to the gas phase.

3.3. Retention and Loss of Condensed-Phase Structure in Peptides and Small Proteins

Melittin (2.8 kDa) is a 26-amino acid membrane protein from bee venom, with a condensed-phase structure consisting of two α -helices joined by a proline “kink”.⁷¹⁴ This structure is known to be more stable in less polar condensed-phase environments (e.g., methanol⁷³⁹ or lipid membranes⁷⁵⁸) than in water. Contrasting with results for singly protonated polyalanine peptides with 3-20 amino acids⁷¹² and for Trp-cage¹⁺ (2.2 kDa),⁷²⁵ melittin³⁺ formed from acidified 1:1 water:methanol was found with a combination of mass-analyzed ion kinetic energy (MIKE) experiments and CHARMM FF MD to retain its helical structure in the gas phase.⁷¹¹ The authors attributed the retention of structure to the “highly oriented network of hydrogen bonds along the polypeptide backbone” and noted that, with no water surrounding the ions to compete with self-solvation, the intrinsic H-bond network is left undisturbed. Florance et al. performed AMBER FF MD

simulated annealing computations between 0 and 800 K to identify structure families consistent with IM-MS data for melittin³⁻⁴⁺ formed by nESI from aqueous solutions containing 0-100% methanol.⁷¹⁴ Computed CCSs correlated with the number (1-3) of α -helical regions in the simulated structures. The MD results supported assignment of a range of partially helical structures to the ions, and the authors noted that there was “slight evidence for solvent memory,” with more helical structures being formed in higher-fraction methanol solutions.

Further support for retention of native-like folds in small, globular native protein ions comes from infrared multiple-photon dissociation spectroscopy results for gas-phase myoglobin (16.7 kDa) and β -lactoglobulin (18 kDa) ions. Seo et al. report that myoglobin⁸⁺ and β -lactoglobulin⁸⁺ ions retain their highly α -helix- and β -sheet-rich structures, respectively, upon nESI.⁷⁵⁹ Driven by repulsion between positively-charged sidechains, β -lactoglobulin ions with higher charge states adopt progressively greater α -helix content. Such studies are expected in the future to provide important targets for MD simulations and assist in interpretation of IM-MS data.

3.4. Protein Complexes

Larger proteins and protein complexes, which contain many more degrees of freedom than peptides and small proteins, can be considerably more computationally expensive to simulate with MD and often intractable with high-level QM computations. Ruotolo et al. demonstrated a simple coarse-grained approach to study gas-phase collapse of *trp* RNA-binding attenuation protein (TRAP) 11-mer assemblies (~90 kDa), in which each protein in the assembly is treated as a sphere.⁷⁶⁰ Their simulations indicated that lower native charge states of the assemblies have experimental CCSs consistent with

retention of planar ring structures, but higher native charge states collapse ~14% to close-packed, roughly spherical assemblies, with some evidence for additional partially compacted structures. These results illustrate the sensitivity with which native IM-MS can be used to study large-scale gas-phase structural rearrangement, even with simple computational models.

OPLS-AA FF MD simulations in combination with native IM-MS experiments by Hall et al. further examined desolvation-induced compaction as well as gas-phase collision-induced compaction of serum amyloid P component pentamer (SAP, 125 kDa), avidin tetramer (64 kDa), transthyretin tetramer (TTR, 56 kDa), and TRAP 11-mer.²²¹ Under minimal activation conditions, SAP¹⁸⁻³⁰⁺ assemblies were found to have experimental CCSs slightly larger (~70 nm²) than those computed for 300 K 18+ ions with native-like ring structures (~68 nm²). Low charge states were predicted by MD to collapse up to ~7% by elimination of the ring's central cavity upon heating by several hundred K, qualitatively consistent with observed ~10% compaction of these charge states upon collisional activation in IM-MS experiments.

Friemann et al. studied changes in detergent micelle-embedded transmembrane protein β -barrel regions using a GROMOS FF and found that the micelle shields the transmembrane region from structural collapse upon transfer to vacuum.⁷⁴⁰ By contrast, hairpin loops extending outside the micelle were found to collapse. They concluded that membrane proteins embedded in micelles are “not very sensitive to the vacuum environment,” a property that may prove highly beneficial in studying their condensed-phase structures using gas-phase measurements. The Robinson group has explored lipid binding to native membrane protein complexes embedded in detergent micelles and

“Nanodisc” lipid bilayers and compared them to MD simulations to identify lipid binding preferences.^{164,165,741} In their experiments, all but a few lipids are stripped from the native protein ions to reveal those that closely associate with the protein. The remarkable agreement between simulated and experimentally determined lipid binding preferences, which have been extended to quantitative measurements of lipid binding thermodynamics by the Laganowsky group,^{119,173,761} provides indirect evidence that tightly bound lipids do not move significantly during nESI or the gas-phase stripping process.

3.5. Explicit Modeling of nESI Droplet Evaporation and Ion Charging Process

During the last decade or so, efforts to accurately simulate desiccation of biomolecules within ESI droplets and concomitant acquisition of charge have been undertaken by several groups.^{300,722,729,730,735,740,762-765} In addition to the aforementioned simulations by Steinberg et al.,⁷³² the Konermann and Consta groups have applied MD simulations to charged droplets containing biomolecules to learn about ionization mechanisms, ion compaction upon desiccation, and heating-induced unfolding and dissociation. These computations can be especially sensitive to choice of water model, treatment of electrostatics, temperature control, and simulation length, among other user-determined variables.⁷³⁵ These simulations provide insight into native charge distributions of proteins and protein complexes produced by nESI,⁷²⁹ droplet evaporation dynamics,⁷⁶³⁻⁷⁶⁵ as well as the role of charge hopping and charge-charge repulsion in both the ionization and collision-induced dissociation processes.³⁰⁰

4. Comparison of MD Results with Different Force Fields for Ion Compaction Upon Transfer to Vacuum

As discussed above, electrostatics, hydrogen bonding, and other local molecular properties and interactions can play cooperative or competitive roles in determining both solution and gas-phase structure for proteins and protein ions. Because MD FFs differ in their treatment of these properties and interactions,⁷³⁶ different FFs may in principle lead to different conclusions about both local and global protein ion structure even if computed CCSs are similar. Despite the wealth of information about gas-phase native-like protein ions gained from the comparison of MD and experimental IM-MS results discussed above, results from different FFs have only rarely been compared for the same ions, and typically only for one or perhaps a small number of separate proteins. One advantage of comparing results from different FFs is that biases of specific FFs as well as commonalities can be identified. To contribute to this discussion, we present here a brief comparison of vacuum MD ion compaction results for 5 different common FFs (AMBER94,⁷⁶⁶ OPLS-AA/L,⁷⁶⁷ CHARMM27,^{768,769} GROMOS96 43a2,⁷⁷⁰ and GROMOS96 54b7⁷⁷¹) and 17 different natively-charged proteins with well-characterized experimental CCSs in helium and nitrogen that serve as calibration standards for native IM-MS experiments.^{201,203}

4.1. MD Simulation Method

Initial structure for all 17 proteins were taken from the Protein Data Bank (PDB) structures indicated in **Figure 28A**, with any missing residues appended using PyMol. All MD simulations were conducted with GROMACS v. 2016.4. After a brief (1 ns) relaxation of any added residues in explicit water solvent, all water molecules were

deleted, and low-energy protomers for these structures with native charge states were identified using the Charge Placement algorithm in Collidoscope, leaving SB structures from the MD simulations intact.²¹⁴ Subsequent fixed-charge-site vacuum MD simulations for the protonated ions consisted of a short vacuum relaxation step followed by a 5 ns production run at 300 K with a Berendsen thermostat. CCSs for typical final structures were computed using He or N₂ buffer gas in Collidoscope with the Trajectory Method. Variations of this procedure were conducted for alcohol dehydrogenase tetramer to assess the sensitivity of the results to vacuum simulation length (5, 50, and 500 ns) and velocity seeding, and GROMOS96 43a2 heat ramp studies (from 300 to 600 K in 25 K increments every 5 ns) were conducted for melittin, insulin monomer, and ubiquitin. These variant methods were found to result in only minor differences (typically no more than ~1%) in computed CCSs from the above-described method, with the exception of the heat ramp studies, which predicted up to 4% variability of the CCS between 300 and 600 K.

4.2. Maximal Degree of Compaction Predicted from MD Simulations

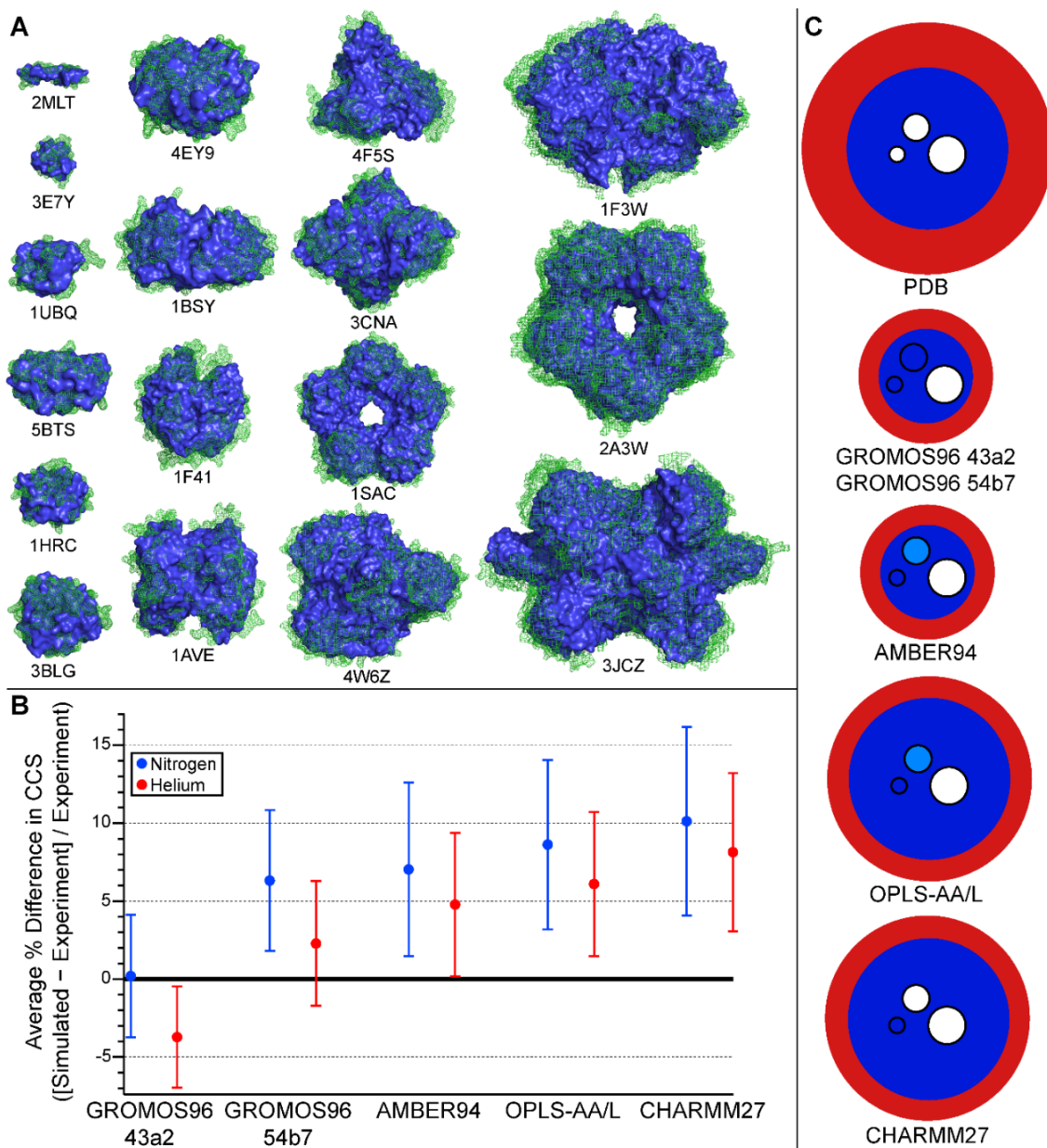
All five FFs tested produced structures that were on average compacted relative to the PDB structures, as measured by computed CCS. The GROMOS FFs resulted in the greatest global compaction relative to the PDB structures (up to 20%), whereas the other three force fields compacted ions only up to 9-10% (see **Table 3**). To provide a coarse-grained picture of ion compaction, ion “surface” was defined as the set of all residues with at least 30% water solvent accessibility as determined with SwissPDBViewer, and the remainder of the ion was defined as the “interior”. At the global structural level, all five FFs compacted the ion surface relative to the PDB structure, resulting in a smaller number of surface residues and a larger number of polar contacts involving charged

residues initially at the surface. However, there were notable differences in the degree to which the interior of the ions were compacted by each FF (see **Table 3** and **Figure 28**), as determined by using the computed CCS of the interior as a measure of its size. Thus, differences in global compaction for the five FFs were largely attributed to the extent of compaction of the interior of the ions.

4.3. Changes in Secondary Structure and Number of Hydrogen Bonds and Salt Bridges

All five FFs resulted in minor loss of α -helical content (up to 7% for OPLS-AA/L) and very minor loss of β -sheet content (up to 2% for AMBER94). These results were largely consistent with known tendencies of these FFs (see above).⁷³⁷ Using Marklund's algorithm for determining the "maximum possible" number of hydrogen bonds for each ion (NHB_{max})⁷⁷² and PyMol to determine the number of hydrogen bonds actually present in each structure (NHB), NHB/NHB_{max} was found on the whole to

Figure 28. (A) Structures of protein and protein complex ions from Figure 27 before (green mesh) and after (blue solid) MD simulation of gas-phase compaction using GROMOS96 43a2 FF (see text). Protonated ions simulated (with Protein Data Bank identifiers indicated below structures) are melittin⁴⁺ (2MLT), insulin³⁺ (3E7Y), ubiquitin⁵⁺ (1UBQ), insulin dimer⁵⁺ (5BTS), cytochrome *c*⁷⁺ (1HRC), β -lactoglobulin monomer⁷⁺ (3BLG), insulin hexamer¹⁰⁺ (4EY9), transthyretin tetramer¹⁵⁺ (1F41), avidin tetramer¹⁶⁺ (1AVE), bovine serum albumin¹⁵⁺ (4F5S), concanavalin A tetramer²¹⁺ (3CNA), serum amyloid P component pentamer²⁴⁺ (1SAC), alcohol dehydrogenase tetramer²⁴⁺ (4W6Z), pyruvate kinase tetramer³²⁺ (1F3W), serum amyloid P component decamer³³⁺ (2A3W), glutamate dehydrogenase hexamer⁴⁰⁺ (3JCZ). (B) Plot of average percent difference between experimental CCS data from ref. ²⁰¹ and ²⁰³ and CCSs computed for MD-compacted ions shown in A using Collidoscope for each of the 5 FFs tested (see text). (C) Schematic depiction of typical degree of surface (red) and interior (dark blue) compaction predicted by MD simulations using 5 different FFs for ions represented in A and B. Embedded circles represent the typical size (small: 5-12 Å diameter, medium: 12-25 Å, and large: ≥ 25 Å) of cavities in the ions that are fully eliminated (dark blue), sometimes eliminated (light blue), or not eliminated (white) during the MD simulations.








increase for each FF in vacuum, with the greatest increase for the GROMOS FFs. By contrast, the change in the number of SBs (determined using PyMol) increased among the five FFs but exhibited no clear dependence on mass.

4.4. Collapse of Cavities and Grooves

Many of the proteins and protein complexes studied here possess sizeable cavities or grooves in their condensed-phase structures. The largest cavities (~ 25 Å in diameter)

Table 3. Summary of Results from MD Simulations of Ion Compaction on Transfer to Gas Phase.

Force Field	Global	Surface	Interior	Secondary Structure	Cavities/ Grooves	Non-covalent Interactions				
	Maximum % Compaction ^a (He/N ₂)	Mean Change in Number of Surface Residues	Mean Number Polar Contacts for Charged Sidechains (1.3 for condensed- phase structures)	Mean Change in Interior CCS, He	Mean Change in Interior CCS, N ₂	Mean Change in α - Helical Content	Mean Change in β - Sheet Content	Diameter 5- 12 Å → 25 Å	Mean Number of HB (% NHB _{max})	Mean Number of SBs (8 for condensed- phase structures)
GROMOS96 43a2	20/18	-42%	4.1	-1.2%	-6.3%	-4.1%	-0.1%		49	9
GROMOS96 54b7	14/12	-28%	1.5	+0.3%	-2.0%	-1.6%	-1.8%		49	12
AMBER94	10/10	-28%	3.7	+2.9%	-1.1%	-0.9%	-2.1%		48	15
OPLS-AA/L	9/9	-25%	3.7	+2.0%	-0.4%	-6.8%	-1.0%		44	11
CHARMM27	9/9	-20%	3.7	+3.6%	+1.0%	-2.7%	-0.1%		45	14

^a Maximum % compaction refers to largest % compaction as measured by computed CCS (condensed-phase – collapsed)/condensed-phase among all 17 protein and protein complex ions studied (see Figure 28). Methods for determining number of non-covalent interactions described in text. Shading of cavities same as in Figure 28.

were not completely collapsed at the end of the simulations by any of the FFs, whereas all FFs resulted in collapse of small cavities and grooves with diameters ranging from ~5-12 Å. For cavities and grooves with diameters in between these extremes (in β -lactoglobulin dimer and concanavalin A tetramer), significant differences were observed between the FFs. The GROMOS FFs collapsed these intermediate-sized cavities, whereas CHARMM27 collapsed neither, and AMBER94 and OPLS-AA/L completely collapsed only one of the two cavities. Taken together with the results described above, this assessment of gas-phase collapse leads to the schematic depiction of compaction represented in **Figure 28C** for the ions investigated with these five FFs.

4.5. Comparison of MD Results to Native IM-MS CCS Data

A comparison of average differences in computed and experimental CCSs in both He and N₂ buffer gas is shown in **Figure 28B**. Both GROMOS FFs outperformed the others in these simple simulations in reproducing experimental CCSs in both buffer gases. As seen in **Figure 28B**, the average difference in CCSs between simulated structures and experiment was $0 \pm 4\%$ and $-4 \pm 3\%$ for GROMOS96 43a2 in N₂ and He buffer gas, respectively. Results from GROMOS96 54b7 were slightly better for He buffer gas ($2 \pm 4\%$), especially for ions below ~36 kDa in mass. The other three FFs (AMBER94, OPLS-AA/L, and CHARMM27) resulted in less average compaction, with the average difference between simulation and experiment being more than one standard deviation away from 0 (see **Figure 28B**). These trends were confirmed by MD simulation of three additional native-like membrane protein complex ions (multi-antimicrobial extrusion protein, 50 kDa; aquaporin Z tetramer, 99 kDa; and ammonia channel B trimer, 127 kDa),⁷⁷³ which have an average He CCS difference of $0 \pm 4\%$ between simulation

and experiment using GROMOS96 43a2 and somewhat higher differences for the other FFs. Based on the results from this simple and relatively low-expense computational method, we recommend use of GROMOS96 43a2 for similar simulations to predict experimental CCSs in N₂ or He buffer gas. We anticipate that slight reparametrization of He Lennard-Jones parameters in Collidoscope (and other CCS calculation programs that use the same parameters, including MOBCAL²²⁰) based on these results may further improve accuracy of He CCS prediction in native IM-MS.²¹⁴

5. Summary and Outlook

As the above survey of the literature shows, the last two decades of research into the structure of biomolecular ions upon transfer from solution into the gas phase indicates that many ions can retain native-like structure, including secondary structure, upon native nESI through the timescale of IM-MS experiments. Although important exceptions, especially for smaller ions such as peptides, indicate that conversion to more stable gas-phase structures with accompanying loss of native-like structure can sometimes occur, the vast majority of results are very promising for native IM-MS work aimed at inferring solution-phase structure from gas-phase data. Both IM-MS data and MD simulations using a variety of FFs indicate that native-like ions compact by several percent upon desiccation and self-solvation of charge sites, although detailed results can be discrepant between FFs. This highlights the need for comparison between FFs in MD simulations, and we hope that the example given in section 3 of this review illustrates a path forward for more reliable interpretation of IM-MS data by use of MD simulation results.

Very recent advances in interpretation of IM-MS data, including simulation of entire experimental CCS distributions,⁴⁶⁷ are likely to provide a more complete, holistic

picture of ion structure by simultaneously matching large sets of data for individual ions rather than single CCS values. Combining these approaches with structural “fingerprinting” via collision-induced unfolding¹¹⁴ as well as with H/D exchange experiments,⁷³⁴ novel dissociation methods,⁴⁸⁵ ion spectroscopy,^{707,742} and other experimental methods should provide yet more structural constraints for MD simulations. The recent inclusion of nanoscale water droplet environments^{730,763} and mobile charges³⁰⁰ in MD simulations represents a step forward in realism, and more accurate parametrization of water models for nanoscale droplets is expected to provide unparalleled insight into native ion compaction and structure.

Bridge

Here, a force field molecular dynamics simulation protocol is validated on a set of 17 native proteins with literature collision cross-section values and shown to robustly produce structures for which computed CCSs are within 4% of experiment. The next chapter builds upon this study by applying this MD simulation protocol to investigate the relationship between structure and charge of gas-phase ions, a fundamental question in the field of native ion mobility-mass spectrometry. The following study provides more detailed insight into features of gas-phase compaction as it relates to protein ions in general as well as to those belonging to the same native charge state distribution.

CHAPTER IV

INVESTIGATION OF CHARGE-STATE-DEPENDENT COMPACTION OF
PROTEIN IONS WITH NATIVE ION MOBILITY-MASS SPECTROMETRY AND
THEORY

Includes co-authored material reprinted with permission from:

Rolland, A.D.; Biberic, L.S.; Prell, J.S. Investigation of Charge-State-Dependent Compaction of Protein Ions with Native Ion Mobility-Mass Spectrometry and Theory. *J. Am. Soc. Mass Spectrom.* 2022, 33, 369-381. © 2022 American Chemical Society.

1. Introduction

Native-like protein ions formed by electrospray ionization often exhibit an approximately Gaussian distribution of charge states in the mass spectrum,¹⁸² consistent with stochastic charging during the electrospray process.^{104,180,181} Higher charge states beyond the native charge state distribution (CSD) typically indicate a significant degree of unfolding,^{205,208,649,774-776} as measured with complementary ion mobility (IM) experiments. However, many researchers anticipate this relationship—that higher charge indicates partial unfolding—extends to the native charge state distribution, interpreting the lowest charge state as corresponding to the most “native-like” structure. In mass spectrometry (MS) experiments which require isolation of a single charge state, such as in collision-induced dissociation/unfolding and tandem MS, mass spectrometrists must decide which charge state(s) to select for further study. Though it is commonly accepted that protein ion structure likely varies to some degree across the CSD,⁷⁷⁷ the magnitude of these structural differences and their influence on gas-phase behavior remain poorly understood. For example, in collision-induced unfolding (CIU) experiments,¹¹⁴ CIU fingerprints, in which collision cross-section (CCS) of an ion is plotted against the

collision voltage used to unfold it, have often been observed to vary among different charge states of the same protein (and transition voltages do not simply scale with charge state).^{114,620,693,694,778} Whether this is due to differences in charge or structure or both remains to be determined. CCS measurements made in native ion mobility-mass spectrometry (IM-MS) experiments¹³⁷⁻¹³⁹ provide information on the overall size and shape of ions and enable some insight into the charge-structure relationship.^{221,468,696,730,774,777,779} However, investigation of protein structure using native IM-MS is complicated by the well-documented observation that protein ions typically compact to some extent in the gas phase, as compared to condensed-phase (e.g., X-ray crystal, NMR, or cryo-EM) structures.^{215,222,224,225} As evidenced through comparison of experimental CCSs with those computed for condensed-phase structure coordinate files,²²⁴ many proteins compact by more than 10% (including small proteins such as ubiquitin, an 8.6-kDa monomer) and some compact by as much as ~20-30% (such as transthyretin and bovine serum albumin, 56 and 66 kDa, respectively).²¹⁵ While the lowest charge state from a protein ion native charge state distribution does often represent the most compact structure, the term “native-like” can be somewhat context-dependent based on what aspects of native structure are under discussion.^{221,774}

According to Dole’s “Charge Residue Model” (CRM),^{180,646,651} ion charge (z) should scale approximately with $\text{mass}^{1/2}$ for ions of fixed density and globular shape, and experimental evidence supports this.^{205,255,648,649} The general relationship between CCS and quasi-globular protein ion mass can also be derived from first principles based on geometry. For hard spheres of fixed density (and ignoring charge), CCS should increase as $\text{mass}^{2/3}$.^{201,205,207,209} Taken together, it follows that CCS should scale roughly as $z^{4/3}$ for

fixed-density hard spheres, ignoring charge entirely (i.e., charge exerts no forces and simply follows the CRM; see **Appendix**). Examination of well-established experimental drift tube CCS values, which do not require external calibration²⁰¹ and thus have relatively small calibration uncertainties compared to other methods,^{222,780} for a set of 17 protein cations widely used as IM-MS calibrants^{201,203} generally supports these relationships between CCS with charge state and mass (**Figure 29**). As shown in these plots, the expected scaling of CCS with $z^{4/3}$ and $\text{mass}^{2/3}$ most closely applies to the most abundant native charge states and to the average CCS from individual protein ion native CSDs. (Including uncertainties of one standard deviation, the overall fits for both helium and nitrogen CCS data sets, respectively, very closely follow the expected power laws, with charge exponents of 1.23 ± 0.07 and 1.2 ± 0.1 and mass exponents of 0.71 ± 0.02 and 0.66 ± 0.03 . Fits to exact 4/3- and 2/3-power laws for each of these, respectively, can be found in **Appendix Figure S1**.) By contrast, CCS remains almost constant across each protein's CSD (**Figure 29**), an observation reported previously by Bush and coworkers for cations, anions, and charge-reduced cations of the same protein species over a wide range of charge states.⁷⁷⁹ Closer inspection of each individual protein native charge state distribution reveals small but measurable differences in CCS (see **Appendix Figure S2** for inset version of this plot to illustrate trends for small proteins). This observation itself indicates that protein ion structure does vary across native CSDs. However, the role of charge in affecting CCS and the details of the structural differences between ions of the same protein but different charge remain unclear.

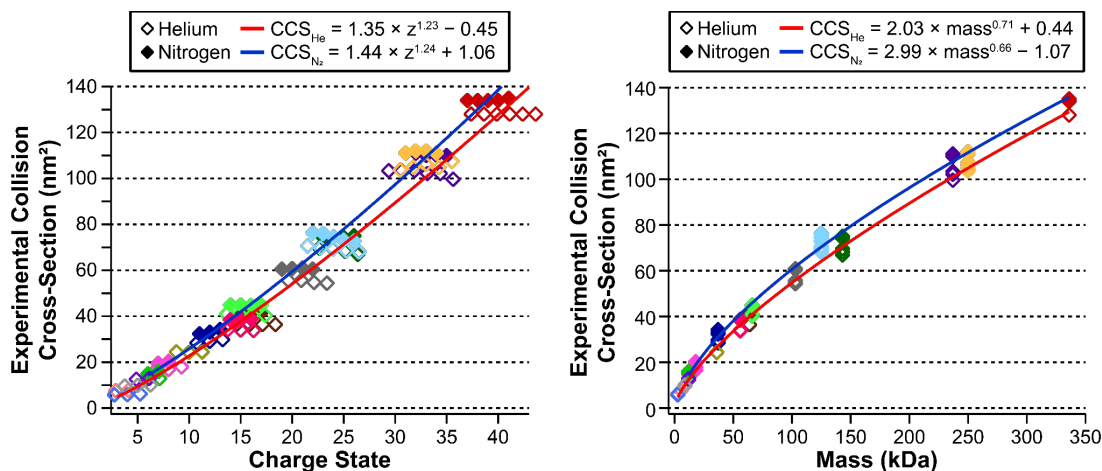


Figure 29. Plot of experimental drift tube CCS values versus charge state (left) and mass (right) for 17-protein IM-MS calibrant data set.^{201,203} Each color represents a different protein. Shaded and open markers represent CCSs measured in nitrogen or helium buffer gas, respectively. Trendlines represent CCS fits to power laws and are colored according to buffer gas identity as in legend.

Additionally, these differences are observed from a more coarse-grained view of global protein ion size and shape, and straightforward methods to probe finer structural details of native protein ions in the gas phase remain elusive. Molecular dynamics (MD) simulations offer a method by which to shed light on these unresolved questions regarding gas-phase protein ion structure.^{215,300,476,705,706,710-712,714-719,722,725,729,735,772,781,782}

We recently reported a simple *in vacuo* force field MD protocol²¹⁵ for simulating experimental gas-phase protein compaction to enable relatively fast calculation²¹⁴ of accurate, reliable theoretical CCS values for native protein ions (**Appendix Table S1**). This study represents the most wide-scale comparison of the performance of different force fields in the context of gas-phase protein ion structure to date, with one simulation performed for each protein (ranging in mass from 2.8 to 336 kDa) using each of 5 different force fields for a total of 85 simulations. Validated on a set of drift tube CCS values for 17 protein cations commonly used to calibrate IM-MS experiments,^{201,203} the method accurately captures the extent of gas-phase compaction that protein ions undergo

experimentally, producing structures for which the theoretical CCSs differ on average from experiment by only $0\pm 4\%$ (with nitrogen buffer gas) and $-1\pm 3\%$ to $-2\pm 3\%$ (with helium buffer gas for smaller and larger proteins, respectively).²¹⁵ The most important finding from this previous work is that all five force fields on average compacted structures both globally and at the surface of the proteins while largely retaining higher-order structure. These results are consistent with theoretical and experimental work in the literature indicating collapse of surface residue side chains in self-solvation and gas-phase protein compaction.^{704-706,710,712,772} Additionally, hydration has been shown to affect competition for hydrogen bond formation on many small ions, indicating the potential to alter these processes.⁷⁸³⁻⁷⁸⁶ Experiments utilizing spectroscopy and, separately, unfolding/dissociation provide evidence of preservation of secondary and higher-order structure into the gas phase.^{58,77,113,116,221,479,759,760} While theoretical results using force fields developed for use with water models and optimized on small molecules should not be over-interpreted,^{736,787} structural features that are predicted robustly across many force fields and supported by other work can reasonably provide some insight into gas-phase protein ion structure and the role of charge.

Here, we utilized this established simulation protocol to examine in detail structural variation across native protein ion charge state distributions. We selected three proteins from the set of 17 native protein IM-MS calibrants as a case study: β -lactoglobulin (BLG; 18 kDa monomer), concanavalin A (ConA; 103 kDa tetramer), and glutamate dehydrogenase (GDH; 336 kDa hexamer).^{201,203} These proteins represent a wide range of masses, charge states, CCS values (measured in both helium and nitrogen buffer gas), oligomeric states, and structural features (**Appendix Figure S3**). For each,

we identified up to five stable charge configurations for each native charge state using the charge placement algorithm in Collidoscope, performed *in vacuo* molecular dynamics simulations of each charge conformer, and computed the CCSs of the simulated structures using the Trajectory Method.²¹⁴ We then further analyzed structural features and changes in each simulated charge conformer, as well as in the original 17-protein data set,²¹⁵ in order to determine any structural trends with respect to charge state both globally and in the context of individual protein native CSDs. Results from this investigation of structural variation across charge states and the contributions of charge in affecting CCS provide useful insight for mass spectrometrists' interpretation of structural information from unfolding/dissociation experiments, as well as for the use and development of molecular dynamics simulations with which to investigate gas-phase protein behavior.

2. Experimental Section

2.1. Molecular Dynamics Simulations, Charge Placement, and Collision Cross-Section Calculations

Three proteins were selected from a set of 17 native-like protein ions with experimental drift tube ion mobility data:^{201,203} β -lactoglobulin (BLG; 18 kDa monomer), concanavalin A (ConA; 103 kDa tetramer), and glutamate dehydrogenase (GDH; 336 kDa hexamer). All experimental IM-MS data used here was previously reported. Experimental conditions can be found in references 201 and 203; we note that activation conditions were minimized for all of these native IM-MS calibrant protein ions to ensure reproducibility. The following condensed-phase structure coordinate PDB files were used for simulation: 3BLG (β -lactoglobulin), 3CNA (concanavalin A), and 3JCZ (glutamate

dehydrogenase). Residues missing from the full sequence were added to the GDH (3JCZ) structure in PyMOL, and this modified structure was briefly (1 ns) relaxed via molecular dynamics simulation with water to ensure more reasonable folding of these added segments. The resulting structure (with water molecules removed) was used as the starting structure for all subsequent work.

The charge placement algorithm in Collidoscope²¹⁴ was used to identify stable configurations for each charge state included in the experimental native protein ion IM-MS database. This was repeated five times for each charge state of each protein. *In vacuo* molecular dynamics simulations were performed with the GROMACS 2016.6 molecular dynamics package as previously described.²¹⁵ Briefly, topology files were generated with charges assigned according to each unique charge configuration identified with Collidoscope.²¹⁴ All structure coordinate files were simulated with the GROMOS96 43a2 force field,⁷⁷⁰ and the BLG charge conformers for which there was experimental data reported in helium buffer gas were simulated using the GROMOS96 54b7 force field⁷⁷¹ (due to GROMOS96 54b7 performing better for small proteins in helium; see **Appendix Table S2**). A brief energy minimization step was performed first, followed by a 5 ns NTV-ensemble production run at 300 K with a modified Berendsen thermostat. (Previous results indicate that longer production runs up to 500 ns do not typically result in additional measurable structural differences.²¹⁵)

Collision cross-sections were computed for all structures (unsimulated and simulated) using the Lennard-Jones 6-12-4 parameters for either helium or nitrogen buffer gas as implemented in the Trajectory Method in Collidoscope²¹⁴ with the original number of charges, unless otherwise noted (see below; CCS values listed in **Appendix**

Table S3). (Throughout the text, we refer to the original condensed-phase starting structures as “unsimulated” and to the vacuum MD-compacted structures as “simulated”.) Experimental CCS values for comparison were obtained from the literature set of 17 native-like protein ion IM-MS calibrants (see **Appendix Table S1** for complete list of protein identities, masses, and starting PDB IDs).^{201,203}

2.2. CCS Calculations for Identical Structures Varying Only in Charge

The CCS of each smallest-CCS and largest-CCS structure resulting from the above-described simulations of BLG, ConA, and GDH charge conformers was recalculated using the Trajectory Method in Collidoscope²¹⁴ using both the lowest and highest native charge state for each protein in both buffer gases. The resulting CCS values (reported in **Appendix Table S4**) were used to represent extremes of the CCS range expected if native charge state distributions corresponded to identical protein ion structures varying only in charge state.

2.3. Projection Approximation CCS Calculations

To represent the size of protein ions in the absence of charge-dipole interactions, Projection Approximation CCSs were calculated using IMoS for unsimulated and simulated structure coordinate files containing no explicit charges (**Appendix Table S5**).^{217,748,788}

2.4. Analysis of Structural Features

Full details of how all structural features (listed in **Appendix Table S6**) were determined and analyzed, including principal component analyses, are available in the **Appendix**. All structural feature analysis presented in this work, both for the set of 3

proteins simulated for the first time here and the set of 17 native-like protein IM-MS calibrants with which the protocol was previously developed,²¹⁵ represents new results.

3. Results and Discussion

3.1. Experimental Trends in Collision Cross-Section with Charge for Globular Protein Ions

As shown for the set of 17 native-like protein ion IM-MS calibrants in **Figure 29**,^{201,203} while the $z^{4/3}$ power law derived from first principles generally holds empirically for the CCS of most-abundant charge states, the trend in CCS across individual protein ion native CSDs is nearly flat. This observation indicates that different native charge states of the same protein ion do not simply “expand” or “compact” to respect the CRM (which would indicate large changes in density), and it is known that charge state does affect long-range ion-dipole interactions that contribute to charge scattering and thus can potentially alter CCS.^{220,776} The assumptions inherent to simplistic derivation of power-law relationships of CCS to charge and mass from CRM and geometry—fixed ion density, charge-independent CCS, and fixed structure across the charge state distribution—predict a perfectly flat trend in CCS across individual native CSDs (see **Appendix**). The measurable (albeit small, on the order of ~2%) differences in the CCSs across native CSDs (**Appendix Figure S2**) indicate that at least one of these assumptions must be invalid. Either 1) density varies to some small extent across the native charge state distribution, 2) charge exerts sufficient forces to alter CCS, or 3) protein ion structure varies.

Computation of the volumes of simulated charge conformer structures (described in detail in a later section) for individual protein ion native charge state distributions

reveals only minimal variation in density (**Appendix Table S7**).⁷⁸⁹ Packing density, the ratio of the van der Waals volume to the total volume, varies less than 1% across all charge states for each of the proteins regardless of size (0.9% deviation for BLG, 18 kDa, and 0.3% deviation for GDH, 336 kDa). Examination of density determined as the ratio of protein mass over volume yields similar results. The plot of experimental drift tube CCS values^{201,203} as a function of mass in **Figure 29** further shows very little change in density with mass. Thus we conclude that the first assumption—that density is essentially fixed across the native CSD—generally holds true, narrowing focus to investigation of the other two assumptions, which regard the role of charge and possible structural variation.

The “global” trend in CCS across all 17 proteins depicted in **Figure 29** has a slope of $\sim 3.2\text{-}3.4 \text{ nm}^2/\text{charge}$ (using local linear fits for the most-abundant native charge states) using CCSs measured in helium or nitrogen buffer gas, respectively.^{201,203} As determined through linear regression, the experimental CCSs of smaller proteins across their individual CSDs tend to exhibit slightly more positive trends with respect to charge state, in contrast to larger proteins, which either exhibit a negative local slope or do not strongly correlate with charge state (**Appendix Table S8**). Regardless, among proteins with at least three native charge states, all local slopes were of magnitude equal to or less than $1 \text{ nm}^2/\text{charge}$, with the majority less than $0.5 \text{ nm}^2/\text{charge}$, considerably less drastic than compared to the “global” trend.⁷⁷⁹

Overall, the trends observed between experimental drift tube CCS and charge state suggest that ions of the same protein identity but different charge states do not adopt identical structures in the gas phase. However, despite the very slight changes in CCS

with respect to charge state, we also cannot rule out the other remaining assumption—that charge does not affect CCS—from these observations alone. Both long-range and short-range interactions can affect CCS. Long-range charge-dipole interactions should typically increase CCS with increasing charge state,⁷⁷⁶ owing to increased long-range scattering, at least for identical ion structures.²²⁰ Thus, as previously noted by Robinson, Bush, and others,^{221,468,696,774,790,791} charge-dipole interactions should in principle have a relatively greater influence on the CCS of smaller proteins than larger proteins containing more residues and multiple subunits, as evidenced by their slight increases in CCS with increasing charge (**Appendix Figure S2**). If structure does vary across native CSDs, several key questions remain: 1) How large are the effects of structural differences on CCS? 2) What structural features cause these effects? 3) Are these effects monotonic with charge? Teasing apart the reason for experimental CCS deviation from the expected relationship from first principles—whether it be due to variation of structure across native charge state distributions or due to significant contributions of charge to CCS—requires further investigation into the role of charge in gas-phase protein structure, for which we draw upon experiment and theory.

3.2. Global Trends in Protein Ion Structural Features with Charge State

To help assess the role of structure and charge state on CCS trends across native CSDs, we first investigated possible global trends by re-analyzing the original 17-protein data set in greater detail.²¹⁵ In our previous systematic comparison of the results of *in vacuo* simulation of each of the 17 proteins in the IM-MS database,^{201,203} we examined structural changes predicted by each of the five force fields tested in order to identify both robust and force field-specific trends. This was based on the average change for

each structural feature across all 17 proteins, for which only one charge state was investigated. Here, we re-analyze these simulated structures to identify possible trends with charge. Because this original data set encompasses a wide range of charge states from 17 different proteins, trends derived from the full data set are less likely to be heavily skewed by unique features of a single protein.

Features analyzed (see **Appendix Table S6** for full list and analysis details) included those related to size (CCS, compaction, percent difference with respect to experiment, and RMSD as compared to the initial condensed-phase structure used for the simulations) and measures of how compaction varies for solvent-accessible residues at the “surface” of the protein versus the remaining set of buried residues in the “interior” (interior CCS, number of surface residues, number of polar contacts involving charged side chains at the surface, and number of hydrogen bonds involving surface residues). We also analyzed non-covalent interactions (number of hydrogen bonds and salt bridges) and secondary structure content (number of residues with α -helical or β -strand geometry as determined in PyMOL). Among the five FFs tested in our original study, most resulted in the same general changes to these structural features with differences only in magnitude or the extent of the change.²¹⁵ For example, all five FFs caused structures to compact both globally and at the surface, as determined by comparison of the CCS, number of “surface” residues, and number of polar contacts involving charged side chains before and after simulation (**Figure 30**). Non-covalent interactions increased on average relative to initial structures for ions simulated with each of the five FFs, while secondary structure content decreased very slightly on average, with more loss of α -helical structure than β -strand.

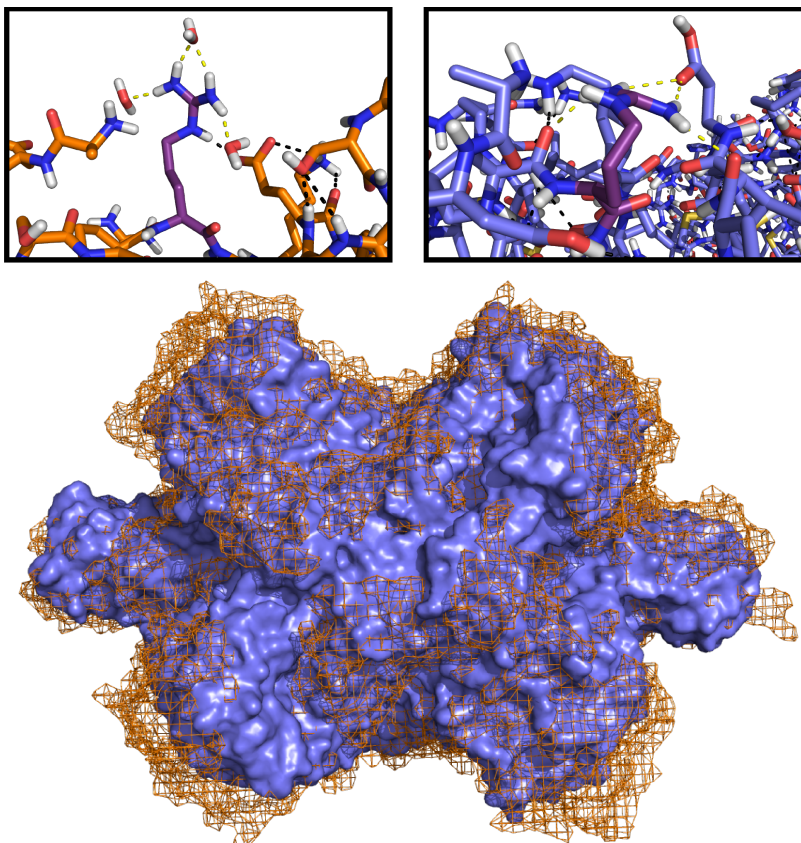


Figure 30. Example of typical compaction with overlaid structures of a GDH 42+ charge conformer before (unsimulated cryo-EM structure, orange mesh) and after *in vacuo* molecular dynamics simulation (blue solid). Panels above show initial hydrogen bond formation for ARG338 (purple, charged site) with water in the condensed-phase structure and subsequent collapse to form interactions with other residues after simulation in absence of solvent, with yellow dotted lines representing the polar contacts involving the side chain amine groups. All other polar contacts involving side chains are indicated with black dotted lines for both structures.

Linear regression analysis performed here of each of these metrics against charge state revealed significant (Pearson $R^2 > 0.9$) correlations with CCS, number of hydrogen bonds, number of surface hydrogen bonds, number of surface residues, interior CCS, and number of polar contacts involving charged residues, and all of these exhibited positive slopes (**Figure 31** and **Appendix Figures S4-S5**). CCSs and surface hydrogen bonds (which should scale roughly with surface area) for these simulated structures are fit to a $z^{A/3}$ power law as expected for global trends. The total number of hydrogen bonds should

correlate to volume, which scales with z^2 , and is fit accordingly. While the total number of salt bridges, RMSD, and secondary structure content also increased with increasing charge state, these trends did not have significant R^2 values (**Appendix Figures S4-S5**). The global linear trend in CCS as a function of charge state identified here for simulated structures (with derivative values of ~ 3.1 nm²/charge and ~ 3.4 nm²/charge for helium and nitrogen buffer gas, respectively) matched well to that observed for the experimental drift tube CCS measurements described above (~ 3.2 - 3.4 nm²/charge).

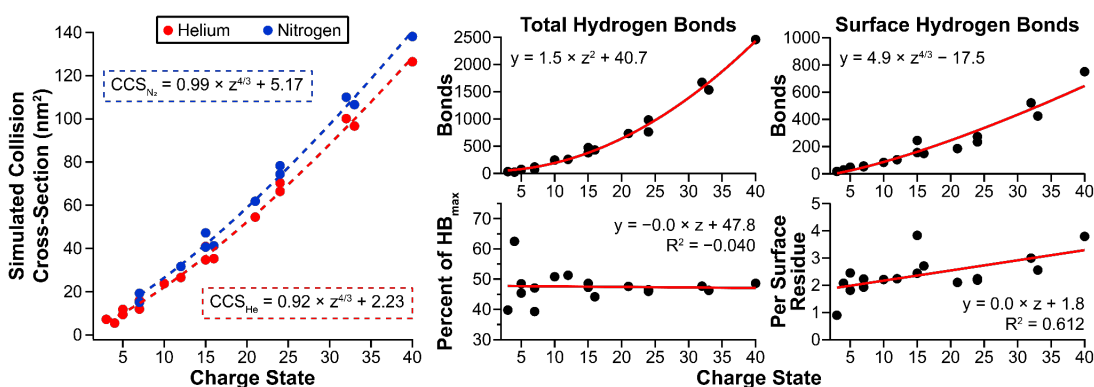


Figure 31. Structural feature trends as a function of charge state for the original data set of simulations of 17 IM-MS calibrant proteins using one central charge state for each. CCS, total number of hydrogen bonds, and surface hydrogen bonds all exhibit power law relationships with increasing charge. Normalization of these metrics to the specific features of each protein before simulation (percent of maximum number of hydrogen bonds⁷⁷² and number of hydrogen bonds per surface residue) results in effectively flat trends.

Further analysis of the above types of structural features as normalized metrics (with structural features represented as either a percent change relative to the unsimulated structure or a proportion relative to the maximum possible number of interactions⁷⁷² or number of features per residue) yielded trends with no additional significant correlation coefficients (**Appendix Figures S4-S5**). However, the slopes for many of these trends in structural changes relative to their respective unsimulated starting structures as a function of charge state were near zero, indicating structural features or changes that are

effectively constant (slopes of approximately $\pm 0.1\%$ relative change/charge) across this wide range of protein charge states (**Appendix Figures S4-S5**). Several of these were related to non-covalent interactions: percent of maximum number of hydrogen bonds, percent change in number of hydrogen bonds, number of hydrogen bonds per surface residue, number of polar contacts per charged residue, and percent of maximum number of salt bridges (**Appendix Figure S4**). Percent change in secondary structure also exhibited a flat trend with respect to charge state for this 17-protein data set. That the relative changes in each of these features is constant across this wide range of charge states, each representing a different protein ranging in mass from 2.8 kDa to 336 kDa, suggests that the GROMOS96 43a2 force field⁷⁷⁰ robustly predicts these typical changes regardless of the particular protein, a result that is useful in interpreting structural information from simulation results. Because this force field also outperforms others tested for recapitulating experimentally observed gas-phase compaction of native protein ions,²¹⁵ the parameters associated with these types of interactions represent a good starting point for future optimization of existing or new force fields or more sophisticated computations for gas-phase purposes in the future. As collapse of side chains at the surface of proteins is the dominant feature of gas-phase compaction, it may be possible to capture more detailed aspects of compaction in the future by focusing more computationally-expensive methods, such as quantum mechanical simulations, on the protein ion surface.

Other trends for normalized (i.e., percent change or percent of maximum) metrics with respect to charge state which had neither a significant (> 0.9) R^2 value or effectively zero slope are also included in **Appendix Figures S4-S5**. Briefly, we note that the

percent change in each of the following features exhibited positive, although not strong, trends: surface hydrogen bonds, polar contacts involving charged side chains, and salt bridges. By comparison, the percent change in surface residues and “interior CCS” decreased (i.e., became more negative) with increasing charge, indicating “smoother” surfaces for larger gas-phase protein ions due to large decreases in solvent-accessibility of surface residues. Overall, findings from these linear regression analyses are consistent with the general conclusion that larger protein ions form more new non-covalent interactions during *in vacuo* MD simulation than do smaller protein ions and thus are able to compact to a greater extent.

3.3. Trends in Structural Features Across Protein Native Charge State Distributions

Having established global trends in structure with respect to charge, we analyzed BLG, ConA, and GDH in greater detail, separately simulating compaction for each charge state in their native charge state distributions. These ions were chosen because they span a wide range of masses, charge states, and oligomeric states (BLG monomer: 18 kDa, 7-9+; ConA tetramer: 103 kDa, 19-23+; GDH hexamer: 336 kDa, 37-43+), and there is no significant homology between them (**Appendix Figure S3**). BLG consists of a small β -barrel with short segments of helical structure. The condensed-phase structure of ConA contains no α -helical secondary structure and is primarily composed of β -sheets with a gap at the center of its four-subunit interface. GDH features a much larger subunit interface involving all C-termini at its center and is mostly α -helical, though each subunit also contains multiple β -sheets. Drift tube CCSs for these three protein ions are also available for both helium and nitrogen buffer gas,^{201,203} and these experimental values range from $\sim 17 \text{ nm}^2$ to $\sim 135 \text{ nm}^2$. (Monomeric BLG is the smallest protein for which

CCS measurements in both gases are reported, and GDH is the largest protein of the 17 in the IM-MS calibrant data set, which excludes GroEL.^{201,203})

Analysis of individual protein CSDs removes effects of mass differences and allows for closer examination of the specific role of charge in influencing features of gas-phase structure. We identified up to five high-stability charge configurations for each experimental charge state of all three proteins using the Collidoscope charge placement algorithm.²¹⁴ We then performed an *in vacuo* MD simulation on the condensed-phase structures of these three proteins for each stable charge configuration identified. As before, CCSs were computed using the Trajectory Method in Collidoscope (**Appendix Table S3**),²¹⁴ and structural features of both the unsimulated and simulated structures were analyzed using PyMOL.

For the structural analysis above and in our previous simulation study, we utilized only the most abundant charge state from each protein's distribution for simulation and CCS calculation. To ensure that the accuracy of the protocol is not limited to this charge state, we first checked its accuracy and precision for all of the native charge states for the three test proteins with available consensus CCS. As shown in **Figure 32**, all 24 computed average CCSs (and all 49 total computed CCSs for individual structures) fell well within the expected range of performance with only one exception—the single CCS value for BLG 9+ in helium. We thus concluded that the simulation protocol is accurate across the native charge state distributions for these ions.

We also note that these simulation results, especially for the larger proteins ConA and GDH, do not exhibit a monotonically increasing relationship between CCS and charge state (**Appendix Figure S6**), indicating that the lowest charge state from a native

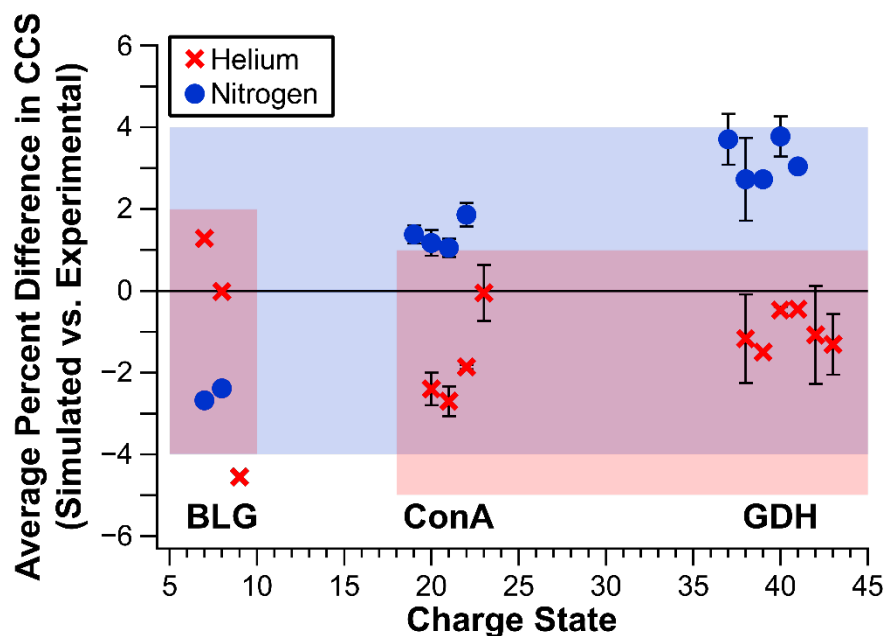


Figure 32. Average percent difference between experimental drift tube^{201,203} and simulated CCS for BLG, ConA, and GDH charge state conformations. Error bars represent 1 standard deviation. Symbols and coloring represent different buffer gases as indicated in legend. Shaded areas span the established range of accuracy and precision with the utilized MD simulation protocol for nitrogen buffer gas ($0\pm 4\%$) and helium buffer gas ($-1\pm 3\%$ and $-2\pm 3\%$ for lower charge states and higher charge states, respectively).

protein ion distribution does not necessarily correspond to the most compact structure. CCSs for individual simulated charge conformer structures for each protein were very similar to each other, with less than 1% standard deviation for ConA and GDH in both gases and for BLG in helium (**Appendix Table S3**). This value was slightly higher for BLG structures in nitrogen buffer gas ($\sim 3\%$), though this is likely due to only one stable configuration being identified for each of the two charge states.

Linear regression analysis of structural features across individual protein ion CSDs for the three proteins investigated here, however, did not yield any significantly different findings from the global study described above. In general, the only linear trends with apparently strong correlation coefficients were for BLG (**Figure 33** and

Appendix Figures S7-S8), though these are not to be over-interpreted as they originate from fitting a set of just three data points due to identification of only one stable charge configuration for each charge state. While most trends for the two larger proteins ConA and GDH were effectively flat with respect to charge state (**Appendix Figures S9-S11**), structural changes related to surface hydrogen bonds, surface residues, and salt bridges exhibited the clearest trends with charge state for BLG (**Figure 33**). For all of these trends, increasing charge state correlated with fewer interactions or smaller percent increases in the number of these interactions. That is, the BLG 9+ structure formed fewer hydrogen bonds involving surface residues and salt bridges than did the 7+ structure, indicating competition between Coulomb repulsion of the charge sites and self-solvation of charges that is generally a major feature of gas-phase compaction.^{704,705,710,712,772} Interestingly, this trend for BLG contrasts with the *global* decrease in surface residues retained relative to the unsimulated condensed-phase structure (i.e., increased surface “smoothing” as exemplified in **Figure 30**) described above as a function of protein mass.

Structural changes that were consistent across the entire native CSD for both ConA and GDH include those related to hydrogen bonding and non-covalent interactions (percent of maximum number of hydrogen bonds, percent change in total number of hydrogen bonds, number of hydrogen bonds per surface residue, number of polar contacts per charged residue, and percent of maximum number of salt bridges), as well as RMSD (relative to condensed-phase structure coordinate file) and percent change in secondary structure (**Appendix Figures S9-S11**).

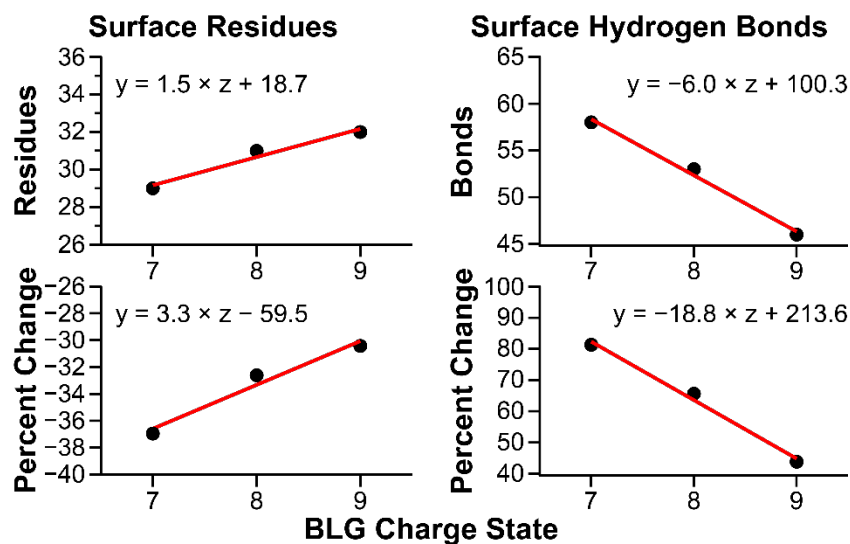


Figure 33. Relatively strong correlations of surface residues and surface hydrogen bonds with charge state for BLG as determined with linear regression analysis. For each of these two structural features, the top plot shows the trend for the total number of surface residues and surface hydrogen bonds, while the bottom plots represent percent change relative to the unsimulated starting structure.

3.4. Expected Collision Cross-Section Trends for Identical Structures Varying Only in Charge

To further investigate the role of both long-range and short-range interactions in determining CCS, we decoupled the influence of charge-dipole and gas-phase compaction by two different methods using the simulated protomer structures of BLG, ConA, and GDH. With the first of these methods, we tested the possibility that the ions represented by a charge state distribution have identical structure (other than that of the protonated residues) and varied only in charge. As described above, charge-dipole interactions between the ions and the buffer gas should result in larger CCSs for higher charge states.^{220,776} To more fully capture the variation in CCSs expected, we identified the simulated charge conformer structure with the smallest computed CCS and that with the largest computed CCS for each protein in each buffer gas and re-computed each corresponding structure's CCS with the lowest and highest charge states from the

distribution (**Appendix Table S4**). As shown in **Figure 34**, the variation in CCS over the native CSD assuming identical structure is minimal. In helium buffer gas, the largest variation by far in CCS expected between the lowest and highest charge state is 0.28 nm^2 for GDH, with all other ranges $\sim 0.1 \text{ nm}^2$ or less. These absolute differences correspond to differences in CCS below 0.5%. Similarly, in nitrogen buffer gas, the largest variation (again for identical structures of GDH) is $\sim 1 \text{ nm}^2$, with all percent differences in CCS

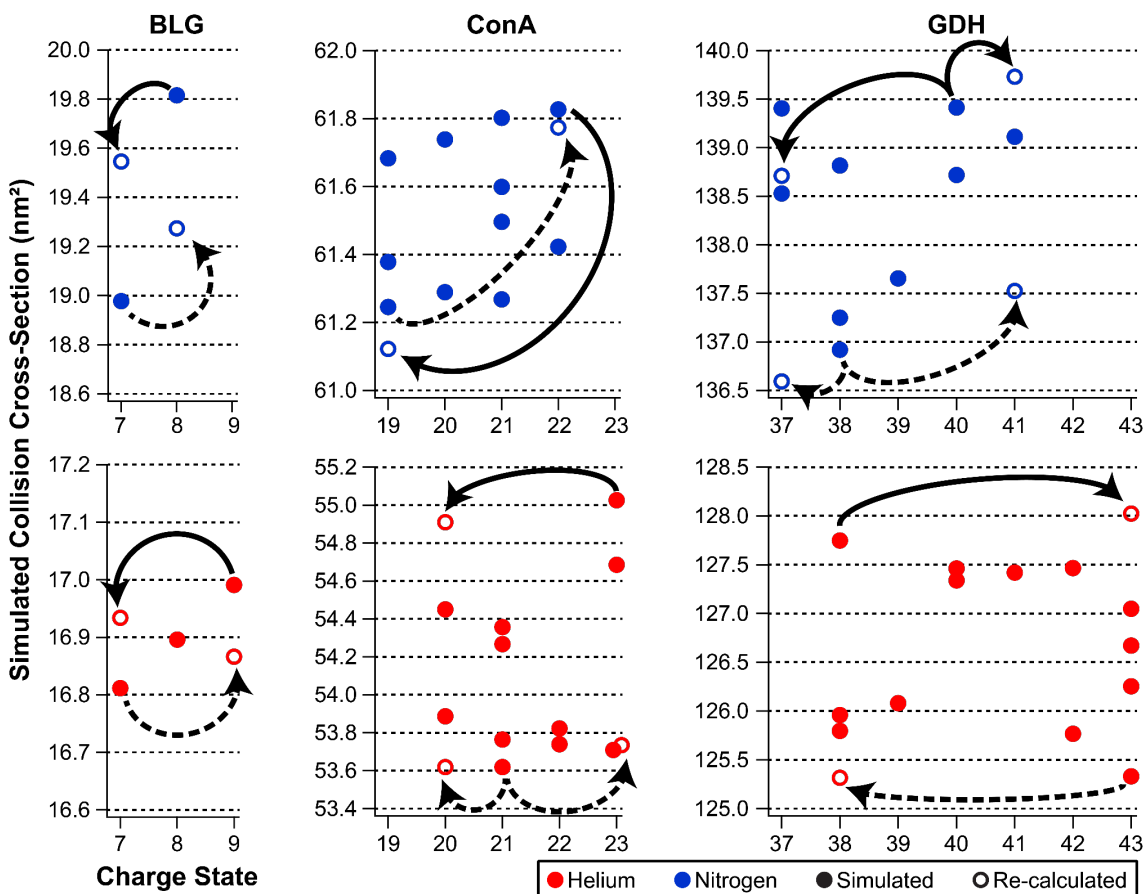


Figure 34. Plots of computed CCSs for individual simulated charge conformers of BLG, ConA, and GDH against charge state (filled circles), with CCS values re-calculated assuming identical protein ion structure for each distribution (open circles). Arrows highlight relevant comparisons, either from the largest-CCS structure (solid arrow) or from the smallest-CCS structure (dotted arrow) to re-calculated CCSs at the lowest and highest charge states, respectively. Filled points from which two arrows originate (ConA helium and GDH nitrogen plots) indicate this structure was either the smallest or largest CCS but had not been simulated with either of the charge state extremes originally. Blue and red coloring correspond to values computed with nitrogen (top row) and helium buffer gas parameters (bottom row), respectively.

~1.6% or less. (Note that the scale used for CCS values on the y-axis differs in each plot and that the difference after re-calculation of ConA CCSs in nitrogen buffer gas is much smaller than for GDH.) Thus, for these ions with essentially fixed structure across the native CSD, the difference in CCS arising from charge effects is below current experimental uncertainty and effectively unmeasurable. These results suggest that contributions of long-range charge-dipole effects alone cannot account for the variation in CCS observed across individual protein ion native CSDs, consistent with previous findings.⁶⁹⁶ The inability of a single structure to explain the full range of experimental CCSs is also consistent with the hypothesis that protein ion CSDs arise from a distribution of multiple solution-phase folded states.⁷⁹²

To further confirm that charges do not exert significant forces to alter CCS, we performed a separate set of calculations to remove contributions of charge-dipole interactions from the computation of CCSs of the simulated structures. Charge is accounted for in Trajectory Method (TM) calculations through explicit inclusion of both long- and short-range scattering effects.^{214,220,637} We thus performed an additional set of CCS computations on the simulated structures using the Projection Approximation (PA) method, which does not model charge-dependent interactions, in IMoS (**Appendix Table S5**).^{217,748,788} The resulting (charge-ignorant) PA CCSs qualitatively mimic the trends observed with the TM, as shown in **Figure 35** where both are plotted as percent differences in CCS relative to the condensed-phase, unsimulated structure. Although there are systematic shifts in the PA computed CCSs relative to those from the TM due to the well-understood differences in accuracy of the two methods,⁶³⁷ the PA results confirm

that variation in CCS for the simulated structures reported here is not merely a result of accounting for long-range charge-dipole interactions in the CCS computation itself.

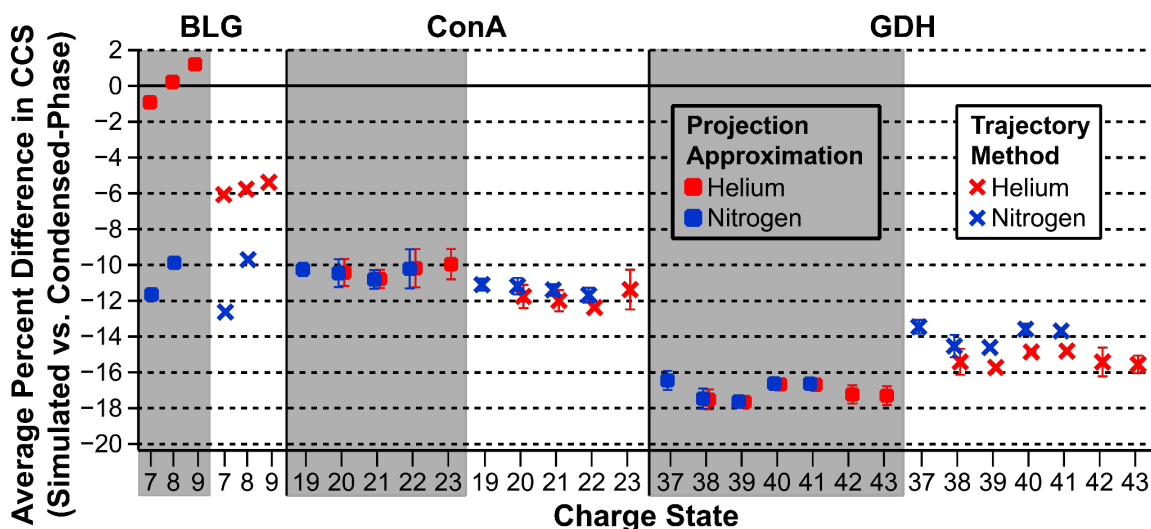


Figure 35. Average percent difference in CCS for simulated charge conformers of BLG, ConA, and GDH in both buffer gases (color indicated in legend). Values are calculated using the difference between CCSs for the simulated and unsimulated structures, relative to the unsimulated structure. Trajectory Method calculations with Collidoscope and Projection Approximation calculations with IMoS represented by symbols indicated in legend. To provide further clarity, the full set of PA CCSs is shown first for each protein with a grey background, with the full set of TM CCSs adjacent.

Of note, the greatest percent difference in CCS relative to the condensed-phase structure for BLG is observed for the lowest charge state (**Figure 35** and **Appendix Table S3**), with the smallest percent difference in CCS seen for the highest charge state. Further, as discussed above, BLG CCSs follow a positive trend with increasing charge state. For BLG and other small proteins for which the extent of possible compaction is limited and for which charge density and the proportion of surface residues is greater, experiment and these simulation results together indicate increasing charges can often lead to Coulombic repulsion that preferentially stabilizes larger structures. This finding (specific to the one small protein studied here) is consistent with a common observation in the literature whereby the lowest charge states are the most compact (i.e., have the

smallest CCS). However, it is important to note that this structure is the most compacted and different from the condensed-phase structure, and labeling such structures as the most “native-like”, based solely on their CCS, can be somewhat misleading. While experiment reveals that the 7+ structure has a smaller CCS than does the 9+ structure, these results illustrate unique insight from computational chemistry that the higher-charged ion is indeed “larger” than the lower-charged ion.

3.5. Principal Component Analyses of Structural Features

Because linear regression analysis of the individual structural features as a function of charge did not yield any new significant trends, we sought to determine whether some combination of these features might be more meaningful in explaining the observed trends in CCS than each feature alone. Other IM-MS researchers have used sophisticated machine learning and PA CCS computations on condensed-phase structures to analyze ion mobility results for very large data sets.^{793,794} Here, we use principal component analysis (PCA) and TM computations for MD-compacted structures, owing to the relatively small data set, for which more advanced machine learning approaches might be inappropriate or extremely time-consuming. We selected one metric from each of the 7 different categories of features (hydrogen bonds, surface hydrogen bonds, surface residues, polar contacts involving charged side chains, salt bridges, α -helical and β -strand secondary structure content), expressed as a percent change relative to the original unsimulated structure so that all features would be on the same protein-normalized scale. PCA of the charge state averages of these 7 features revealed that almost all of the variation could be explained by the first two principal components alone (66.0% and

25.0%, respectively, for a total of 91.0%). Replotting these data along the first two principal components shows clustering determined by protein identity (**Figure 36**).

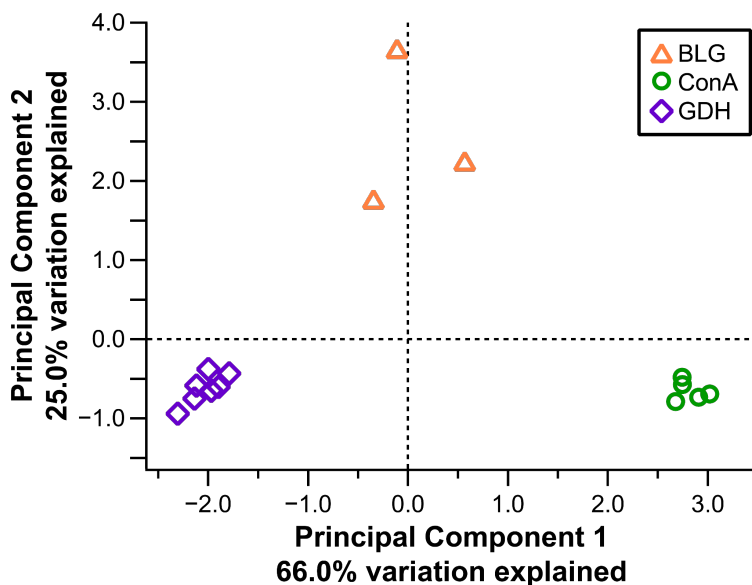


Figure 36. Principal component analysis of BLG, ConA, and GDH structural features, with the average for each charge state plotted according to the first two principal components and proteins represented by colors/symbols as indicated in legend.

However, while all three proteins are well separated along the first principal component, ConA and GDH fall onto the same region along the second principal component axis (**Figure 36**). The eigenvectors of the first principal component are evenly weighted with a coefficient ± 0.37 - 0.44 for all features except for percent change in the number of surface residues (0.17 , **Appendix Table S9**). This latter feature then dominates the second principal component (coefficient of 0.69), for which ConA and GDH have similar values and are clearly separated from BLG. These two larger proteins show similar behavior for this feature, with an average decrease in the number of surface residues of ~ 50 - 56% , but differ drastically by all other metrics studied. By comparison, the average decrease in the number of surface residues for BLG is considerably lower at ~ 30 - 37% . These differences lend further support to our general conclusion that smaller

proteins' tendency toward increasing CCS with increasing charge state—indicative of long-range charge-dipole interactions predominating—can be rationalized by their minimal ability to undergo significant surface compaction, which is a robust, major contributor to global gas-phase compaction for larger protein ions.^{215,704,710,772} We also note that of these three proteins, ConA is unique in that its condensed-phase, unsimulated structure contains no α -helical residues (**Appendix Figure S3**). The differences in the first two principal components suggest that, in these simulations, percent change in the number of surface residues and α -helical secondary structure content are not strongly linked.

We also performed PCA on our original 17-protein data set with these same 7 features, both with the aggregated data and with each individual force field (see **Appendix Tables S10-S12 and Extended Methods**). Importantly, the two major principal components in the aggregated data set, which together account for 56.9% of the variation, do not distinctly separate these data according to force field (**Appendix Figure S12**). These axes are dominated primarily by features related to hydrogen bonding, surface residues, and polar contacts with charged side chains (**Appendix Table S10**), similar to PCA results for charge conformers of the 3 proteins described above. PCA of these data for individual force fields reveal a high degree of similarity, with the two GROMOS96 force fields^{770,771} and, separately, CHARMM27^{768,769} and OPLS-AA/L⁷⁶⁷ being most similar to one another and AMBER94⁷⁶⁶ sharing commonalities with each of these pairs (**Appendix Tables S11-S12**). These results are consistent with the findings in our original study and further suggest that a major explanation for differences in structural features and performance for gas-phase investigations among the force fields is

due to the greater extent to which GROMOS-simulated structures form new hydrogen bonds and surface interactions on the timescale used in this protocol.²¹⁵ We note that compaction at the surface is to be expected given the relatively short (5 ns) production runs for these simulations, although the interior regions of most protein structures simulated with GROMOS FFs in the previous study also decreased in size (CCS) (**Appendix Figure S5**). Extending the production run timescale to 50 ns and 500 ns did not result in significant additional structural changes or performance with respect to comparison to literature CCS values.²¹⁵ We attribute this to the accelerated dynamics possible with united-atom FFs such as the GROMOS FFs used, which additionally offers advantages in reducing computational expense while enabling a high degree of accuracy and precision in comparison to experimental IM-MS data.

4. Conclusions

Small but measurable differences in experimental CCS across individual native protein ion CSDs^{201,203} provide an initial indicator that the structures of gas-phase ion charge conformers are not identical and that charge may contribute to CCS. Deviations from the expected trend cannot be explained by varying density of ions across their native CSDs, as supported both by experimental trends in CCS with charge state and by MD simulations indicating essentially fixed density across CSDs (**Appendix Table S7**). The greater tendency of smaller proteins to exhibit positive slopes in CCS across their native CSDs suggests their structures and CCSs are more sensitive to charge than larger proteins, as evidenced by results described throughout. Many small monomeric proteins, such as BLG (studied here), have minimal interior regions and lack cavities and grooves, resulting in a reduced ability to compact in the gas phase. Experimental and theoretical

work reported here, as well as many examples of previous work in the literature,^{215,704,705,710,712,772} indicate self-solvation is a major feature of gas-phase protein ion structure and compaction (**Figure 30**).

CCSs for simulated structures of BLG, ConA, and GDH were very similar to each other, with less than 1% standard deviation for all values of each protein, except for the two structures of BLG for nitrogen buffer gas (3% standard deviation; **Appendix Table S3**). Our results thus suggest that structural differences can impart a small but measurable effect on CCS, though this effect is not necessarily monotonic with charge (**Appendix Figure S6**). Differences in compaction across charge state are supported by computation of PA CCS values (**Figure 35**), and long-range charge-dipole interactions do alter CCS, but to a minimal extent that is effectively unmeasurable with most current native IM instrumentation and cannot explain experimental CCS variation (**Figure 34**).⁶⁹⁶ This result, as well as those described below, supports a model whereby compaction occurs after or simultaneously with charging of the ion, and results in structure varying across native CSDs. Compaction is affected by charge, with charged residues (and residues at the surface generally) collapsing to self-solvate by forming new hydrogen bonds and other non-covalent interactions, ultimately resulting in subtle structural differences between charge states. By contrast, the opposite scenario (in which compaction occurs first, followed by charging) should result in essentially the same compacted structure initially, especially as protons are likely somewhat mobile during the final stages of ion desolvation and migrate to relatively stable charge sites.^{722,777,784} The overall effect of compaction occurring prior to charging would be a slight monotonic increase in CCS with charge state, which is unsupported by experiment and simulations. Further, it is

reasonable to expect that the energy released by formation of many (tens to hundreds of) new hydrogen bonds would exceed the small concomitant increase in Coulombic energy upon compaction. Together these findings support previous work showing that CCS need not correspond one-to-one with native protein ion structure and that peaks in IM spectra often represent multiple different conformations of protein ions with indistinguishable CCS.^{790,795} The MD protocol utilized here,²¹⁵ with which we were able to identify several competing protomers for each charge state that had different structures, may also be useful when integrated into ongoing efforts to model experimental arrival time distributions, especially when combined with more extensive solution MD modeling prior to vacuum MD.²¹⁶ Because CCSs for cationic, anionic, and charge-reduced cationic protein ions of the same species have been found to vary to a small extent,⁷⁷⁹ we also anticipate investigation of how structure may vary across native CSDs obtained with negative polarity and in comparison with their positive polarity counterparts, which are often higher in charge than for negative polarity, as a future application of this protocol.

Overall, results presented from experiment and theory provide evidence that gas-phase protein ion structure varies, albeit to a small extent, across native charge state distributions. Trends (or lack thereof) in structural features across CSDs identified here (**Figures 31, 33**) can better inform researchers performing experiments which require isolation of a single charge state and rationalize differences in gas-phase behavior observed in CIU. Simulated protein charge conformers reported in the present work, as well as simulated structures in our previous work, all retain much higher-order structure and similarity to their corresponding original condensed-phase structure coordinate files. This result warrants optimism for the use of native IM-MS in studying protein structure,

and other evidence also supports the finding that (globular) protein ions preserve much of their solution-phase structures in the gas phase.^{469,711,714,759,772} However, we would caution the native IM-MS community against interpreting the lowest charge state from a native distribution or the native ion with the smallest CCS to be the most “native-like” simply because it is the most compact. Results from literature drift tube CCS values^{201,203} and from simulations of protomers here illustrate that CCS does not vary with charge state “trivially” due to long-range ion-dipole interactions. As shown for the small protein BLG (**Figure 35**), the most compact structure can also be the most different from the “native” condensed-phase structure, as shown by experimental and theoretical results together.

The primary explanation for gas-phase compaction identified here—extensive formation of new hydrogen bonds and non-covalent interactions—is not a novel finding,^{704-706,711,759,772,781} but results presented here show that “smoothing out” of the ion surface and collapse of cavities/grooves upon compaction (as exemplified in **Figure 30**) can subtly depend on charge state. This appears to be a general phenomenon applying to biomolecules beyond just proteins, as similar findings of gas-phase compaction and self-solvation by hydrogen bond formation have been reported for nucleic acids as well.⁷⁹⁶ The general ability of our MD simulation protocol,²¹⁵ in which charges are added to condensed-phase structures before a gas-phase production run, to recapitulate both general and detailed trends with charge state suggests that charging occurs before or along with final compaction of the protein ion, as described above. Detailed structure changes upon ion desolvation are then largely determined by charge state and compaction—through self-solvation and formation of new interactions for surface

residues with other parts of the protein to replace those in many cases originally fulfilled by solvent interactions.^{704-706,710,712,772} Results from cryogenic IM-MS studies of different hydrated peptides and small ions by Russell and coworkers include examples where solvation with increasing numbers of water molecules can lead to different effects on CCS and structural changes.⁷⁸⁶ Separately, results from Williams and Russell provide evidence that even a small extent of hydration can screen electrostatic interactions and their effects on structure.^{783,784,797} In the context of this work, we posit that formation of new hydrogen bonds after charging and concomitant with compaction and surface “smoothing”—as evidenced by our simulations—is a major part of the desolvation process. Dissociating a water molecule requires a considerable amount of thermal energy (often ~40 kJ/mol), which could be offset by the formation of new hydrogen bonds. While the smallest protein studied here formed only ~14 new hydrogen bonds on average through simulation, this number was much higher for both ConA and GDH (~270 and ~200 on average, respectively), and the energy gained would be sufficient to dislodge more than many water molecules for these latter cases. Results from this work not only provide new insight into the relationship of gas-phase protein ion structure and charge that will be useful for interpretation of structural information from native IM-MS experiments, but also highlight the important role for formation of new hydrogen bonds between protein functional groups in aiding desolvation and determining final protein ion structure and CCS.

Bridge

The previous chapters have introduced advances in interpreting native ion mobility-mass spectrometric analysis of heterogeneous biomolecular ions and featured

the validation of computational methods to improve fundamental understanding of gas-phase protein ion structure. This force field molecular dynamics simulation procedure enabled, for the first time, quantitative comparison between experimental and simulated structural data with known accuracy and precision, representing the first major goal of this dissertation. The following chapters apply these computational approaches with native ion mobility-mass spectrometry experimentation to the study of heterogeneous protein complexes which have proved challenging to investigate with other state-of-the-art methods, revealing new features important for understanding their structure and function which were not previously accessible. The next chapter describes the native IM-MS characterization of a pore-forming membrane protein toxin formed in various membrane-like conditions and the use of gas-phase dissociation to characterize these complexes.

CHAPTER V
SYMMETRIC DISSOCIATION OF OLIGOMERIC COMPLEXES OF CYTOLYSIN A
UPON COLLISIONAL ACTIVATION IN DIFFERENT MASS SPECTROMETER
PLATFORMS

While the material included here is primarily my own work, Jesse W. Wilson and Sophie R. Harvey assisted with sample preparation and data collection. Vicki H. Wysocki and James S. Prell contributed to experimental design and interpretation. This work will be the basis of a manuscript to be submitted in the future, with the above named as co-authors.

1. Introduction

Native electrospray ionization mass spectrometry (ESI-MS) is a powerful tool for studying biomolecules and offers several advantages for analytes such as membrane proteins and other heterogeneous complexes.^{41,42,44,47,49,52,53,136,137,157,179,338,798} Many membrane proteins require a membrane-like environment (e.g., including the presence of lipids and/or detergents) for stability, making them often challenging samples to work with. For membrane proteins and their complexes that are too large (> ~20 kDa) for detailed study with NMR spectroscopy, detailed condensed-phase structural determination methods are further limited to those solution conditions which prove suitable for crystallization and/or immobilization. This can restrict experimental design and could exclude some membrane proteins from study by these methods.^{28,29,31,32,35,36,38} By contrast, in native ESI-MS experiments, analytes can often be transferred intact within

a small membrane-like environment (such as a detergent micelle, lipoprotein nanodisc, bicelle, or other membrane mimic) directly from solution into the gas phase.^{44,169,273,670,799} This confers flexibility in conditions that can be used, in addition to the benefits of having minimal sample requirements and being very fast, with collection of a dataset taking only seconds to minutes. The high mass accuracy and sensitivity of native ESI-MS also enable unambiguous determination of complex stoichiometries, including subunit composition and the number and identity of ligands or small molecules bound.^{52,57,90,91,93,94,99,174,186,338,347,629,800}

Since Robinson and coworkers first demonstrated that addition of detergent at twice its critical micelle concentration to membrane protein samples was often sufficient to stabilize them and enable their study with native MS,²⁷⁰ many researchers have utilized this technique²⁷¹ to uncover new details of membrane proteins. In some cases this has resulted in identifying new structures or oligomeric forms that were not previously observed with traditional condensed-phase structural determination methods and the membrane mimics amenable to them. More recently, there have been studies reporting variation in protein behavior and structure, including oligomeric state, depending on the detergent or lipid environment used.^{37,55,64,65,75,163,186,667,668,671} This illustrates the importance of detergent/lipid selection in membrane protein studies but also highlights the range of solution conditions that can be explored with native MS.

1.1. Cytolysin A Oligomeric Pore Complexes

Native IM-MS is thus well-suited for the study of biomolecules for which there is evidence of structural or functional dependence on environment. Cytolysin A (ClyA) is a 34.5 kDa α -pore-forming toxin⁸⁰¹ found in pathogenic strains of *Escherichia coli*^{802,803}

and *Salmonella enterica*⁸⁰⁴ that has drawn interest in bionanotechnological applications,⁸⁰⁵⁻⁸¹⁵ but many details of its assembly and characteristics of its final oligomeric pore complex remain unresolved.⁸¹⁶⁻⁸²⁸ Pore-forming toxins are a subclass of membrane proteins, with their initially soluble monomers undergoing conformational transitions to form oligomeric membrane-inserted pore complexes in membrane-like environments.⁸²⁹⁻⁸³² Reports in the literature identifying the oligomeric state of the final pore complex formed by ClyA are conflicting, and the ability to form arc-like pores and prepore complexes has also been debated.^{810,818,825,833-838} In early electron microscopy experiments, predominantly octamers as well as a small population of hexamers were identified, with the authors interpreting their data to indicate ClyA possesses some degree of conformational variability.⁸³⁸ Separately, others reported in the same year that ClyA formed tridecameric pore complexes in their electron microscopy experiments.⁸³⁴ Later, an X-ray crystal structure of a dodecameric pore complex was solved,⁸³⁷ while most recently cryogenic electron microscopy has been used to determine the structure of dodecameric, tridecameric, and tetradecameric complexes.⁸³⁶ These experiments were all conducted under different conditions, including the presence of different detergents. Given these discrepancies, we sought to utilize the advantages of native MS to characterize the oligomeric complexes formed by ClyA in different detergents.

1.2. Gas-Phase Dissociation Techniques

Because these types of membrane protein samples are necessarily prepared in membrane-like environments, relatively high levels of activation are often employed within the mass spectrometer to dislodge lipid, detergent, salt, and other adducts.^{44,70,93,142,171,270,271,397,798,800,839} This is because heterogeneous samples yield

congested mass spectra, arising from overlapping signals of ions varying not only in charge but also in number and identity of bound ligands. However, as we described recently in a comprehensive review on this topic, many state-of-the-art deconvolution algorithms, computational tools, and instrumental and experimental strategies are now available to combat this challenge.¹⁵⁷ This is especially important for analytes for which sources of heterogeneity are physiologically relevant and thus need to be preserved in the complex. It has also recently been shown that these sometimes harsh conditions may cause unintentional lipid rearrangements,^{282,454} which can affect structural interpretation of native MS data. Together, this has led to a shift in the direction of the field to seek and prioritize softer conditions in experimental and instrumental design.

Once the total mass of the intact protein complex has been determined, adjuvant unfolding and dissociation experiments within the mass spectrometer are a valuable tool can be valuable for determining further structural information.^{107-110,113,114,116,117,142} This is most commonly done with collision-induced dissociation (CID), in which analyte ions undergo collisions with neutral gas molecules in specific regions of the instrument. CID characteristically results in an unfolded monomer accounting for approximately half of the original charge and the corresponding (n-1)-mer ion with the rest of the original charge.^{113,114,239,840,841} This can be useful for confirming the subunit stoichiometry of a complex based on the identity of the ejected monomer and the mass of the remaining complex.^{61,73,77,99,113,446} However, CID of large protein complexes typically does not provide much additional structural information. Surface-induced dissociation (SID) experiments, in which ions undergo a single collision with a solid surface, are much more informative in this respect.^{58,117,485,620,842} The product ions formed from SID have been

shown to reflect quaternary structure in pioneering work from Wysocki and coworkers.^{58,86,88,120,479,480,843-845} Complexes usually dissociate in SID along their weakest protein-protein interface, allowing researchers to infer details of their higher order structure by studying the product ions. Further differences between these two dissociation methods include their timescales and energetics.^{689,693,694,846-852} SID activation occurs on the picosecond timescale, and the ions produced remain compact during the course of a full native MS experiment.^{88,851,853} CID involves hundreds or thousands of low-energy collisions with gas, resulting in a slow (hundreds of microseconds) heating process, while SID is more efficient, requiring a single, high-energy collision event with a surface.^{693,846,854} It is currently speculated that SID, which raises the temperature of the ion much more quickly than does CID, causes symmetric dissociation by accessing thermal, high-energy pathways that are not kinetically accessible in CID. However, some experiment indicate that SID often involves at least some non-thermal (i.e., mechanical) interaction with the surface.^{846,855} Despite the rich information that can be gleaned from SID, instrument modification to install the surface device is required, and transmission efficiency can often be reduced in these experiments.⁸⁵⁶⁻⁸⁶³ Intriguingly, a small number of native protein complexes have been reported to undergo symmetric dissociation or otherwise follow atypical CID pathways when activated by methods other than SID, including CID and ultraviolet photodissociation (UVPD).^{151,153,288,620,864-871} Some trends and shared structural features have been noted for these (e.g., interface area, salt bridges, charge state, intramolecular disulfide bonds),^{221,472,620,841,866,871-876} but these do not hold true for all protein complexes. This atypical behavior is poorly understood and invites

further investigation, especially in pursuit of a unified understanding of gas-phase dissociation by these common, but very different, techniques.

Here, we have utilized the advantages of native ion mobility-mass spectrometry to characterize complexes formed by ClyA in a variety of detergents. We found that collisional activation of ClyA oligomers produced not only canonical CID products—monomers and (n-1)-mers—but also symmetric dissociation product ions (e.g., dissociation of octamer into tetramers). This result was consistent regardless of detergent or initial oligomeric state and was reproducible on both a time-of-flight instrument and an Orbitrap mass spectrometer, under a variety of different activation conditions throughout the different regions of these two mass spectrometer platforms. Using the relative ratio of symmetric and asymmetric dissociation products detected as a guide, we speculate on the conditions needed to access SID-like dissociation pathways in commercial instruments without requiring modification or trading off transmission efficiency. We conclude by drawing upon experimental and theoretical work in the literature to understand the energy barriers associated with these different gas-phase dissociation pathways.^{840,877-888}

2. Methods

2.1. Cytolysin A Expression and Purification

A glycerol stock of competent BL21 (DE3) cells containing a plasmid encoding Cytolysin A (ClyA) with a C-terminal hexa-histidine tag (pClyAwt-CHis6) was a generous gift from Dr. Min Chen (University of Massachusetts Amherst). ClyA was expressed and purified according to previously published methods.⁸⁰⁶ Briefly, this glycerol stock was used to inoculate a starter culture of 10 mL LB with 100 µg/mL ampicillin, which was allowed to grow overnight at +37 °C on a shaking platform at 180

rpm. This starter culture was then added to 250 mL LB with the same concentration of ampicillin in a large Fernbach flask the next day to use for expression. This culture was incubated at +37 °C with shaking at 180 rpm until the OD600 was within the range of 0.5-0.65 (approximately one hour). The culture was cooled on ice, and then IPTG was added to achieve a final concentration of 0.5 mM to induce protein expression. Protein expression was done overnight (total of 16 h) at +15 °C with shaking at 180 rpm. Cells were harvested via centrifugation at 3100 x g for approximately 10 min at +4 °C. Cell pellets were resuspended in 15 mL of 50 mM Tris-HCl, pH 8.0, 1 mM EDTA, frozen, and stored at -20 °C until purification.

To lyse thawed cells, PMSF was added to a final concentration of 0.5 mM, and the mixture was sonicated, followed by addition of MgCl₂ to a final concentration of 10 mM. Clarified lysate was obtained after centrifugation for 20 min at 20,000 x g and filtration of the supernatant through a 0.22- μ m membrane. Initial affinity purification was done using a HisPrep FF16/10 Ni-NTA resin column on an AKTA Prime Plus FPLC System (GE Healthcare). The column was equilibrated with Buffer A (150 mM NaCl, 50 mM Tris-HCl, pH 8) prior to loading the clarified lysate onto the column. Buffer A1 (150 mM NaCl, 50 mM Tris-HCl, 50 mM imidazole) was used to wash the column, and ClyA was eluted with Buffer A2 (150 mM NaCl, 50 mM Tris-HCl, 150 mM imidazole). Fractions containing the protein of interest were pooled and dialyzed in tubing with a molecular weight cutoff of 6-8 kDa against 150 mM NaCl, 50 mM Tris-HCl, 5 mM EDTA overnight at +4 °C with constant stirring. The dialyzed sample was centrifugally concentrated using a 10 kDa cutoff filter to a total volume of a few milliliters. This sample was then further purified by size exclusion chromatography directly in 200 mM

ammonium acetate, pH 7.50. Pooled fractions containing ClyA were centrifugally concentrated as above (final concentration 26.8 μM), aliquoted, flash-frozen in liquid nitrogen, and stored at $-80\text{ }^{\circ}\text{C}$ until further use.

2.2. Screening Detergents for ClyA Oligomerization

To test which detergents were capable of inducing ClyA oligomerization, an initial screening was conducted using a panel of different detergents. A stock solution of each detergent prepared in 200 mM ammonium acetate, pH 7.50, at 10 times the critical micelle concentration (CMC) was added to a small volume of ClyA and further diluted as needed with the same buffer to create a mixed sample with a total volume of 50 μL , final detergent concentration equivalent to 2x the CMC, and final ClyA concentration of $\sim 10\text{ }\mu\text{M}$. These samples were incubated at $+4\text{ }^{\circ}\text{C}$ overnight and then analyzed with both BN- and SDS-PAGE. Samples for which these gels indicated formation of higher molecular weight species were selected for further study.

2.3. Native Mass Spectrometry of ClyA

ClyA-detergent samples were analyzed using native electrospray ionization ion mobility-mass spectrometry. Most native MS experiments were performed on a Waters Synapt G2-Si ion mobility time-of-flight mass spectrometer equipped with a nanoelectrospray ionization source. Additional data were collected on a ThermoFisher Q Exactive UHMR Orbitrap mass spectrometer. A small volume of sample ($\sim 3\text{-}5\text{ }\mu\text{L}$) was loaded into a borosilicate glass capillary (i.d. 0.78 mm) that had been pulled to a fine tip ($\sim 1\text{-}2\text{ }\mu\text{m}$ in diameter). A platinum wire was placed in electrical contact with the sample solution, and electrospray was initiated by applying a voltage of $\sim +1.0\text{ kV}$ and thereafter lowered to just above the threshold voltage needed to maintain ionization and detection

(typically +0.7-1.0 kV). Instrumental parameters are specified in the text. Dissociation experiments were performed by increasing collisional activation in different regions of the two mass spectrometer platforms, and surface-induced dissociation experiments were performed using an SID device installed in these instruments. Mass spectra were analyzed using UniDec.¹⁷¹

3. Results and Discussion

3.1. Detergent-Induced Oligomerization of ClyA

Several detergents—differing in class, molecular weight, critical micelle concentration, and other physical and chemical properties—did not result in oligomerization or instead caused ClyA aggregation and thus were unsuitable for further study (n-tetradecylphosphocholine, tetraethylene glycol monoethyl ether, and n-dodecyl-N,N-dimethylamine-N-oxide). Interestingly, we found that in n-octyl-beta-D-glucopyranoside (OG), ClyA formed complexes ~111,262 Da in mass. This could correspond reasonably to a ClyA trimer (103,344 Da) with an excess mass equivalent to 27 molecules of OG (m.w. of 229 Da). By comparison, OG was used in early EM experiments that identified octameric and hexameric complexes of ClyA.⁸³⁸

Two of the detergents tested resulted in formation of large oligomeric complexes of ClyA and thus were chosen for further study: n-dodecyl-beta-D-maltopyranoside (DDM) and octaethylene glycol monododecyl ether (C12E8). Adapting previously reported methods for inducing ClyA oligomerization with DDM detergent,⁸³⁷ all ClyA-detergent samples were incubated at +4 °C overnight before native ESI-MS analysis. Both ClyA and detergent stock solutions were prepared in 200 mM ammonium acetate,

pH 7.50, to avoid requiring buffer exchange or other perturbations after the components were mixed.

The resulting distributions of oligomeric complexes formed in these detergents were mostly similar. We identified octameric complexes in both, and this oligomeric state was typically the most abundant of the larger species. One major difference was that well-resolved dodecameric complexes could routinely be detected from C12E8 preparations, while in DDM, complexes larger than octamers (i.e., decamers and dodecamers) were only present at very low abundances when detected at all. This could be partially attributed to differences in the detergent in native ESI-MS experiments.^{64,162,271,282,420,454,667,668,671,889} While glycol ether detergents can be rather easily dissociated from protein complex ions, DDM clusters produce broad distributions in the mass spectrum that routinely stretch into the m/z range where complex ions appear, obscuring signals of interest. Even for ion populations well outside of this range, heterogeneity arising from detection of ions with not only different charges but also different numbers of bound DDM molecules creates a very congested mass spectrum. Comparatively, DDM requires higher levels of collisional activation to sufficiently resolve the peaks of interest in the mass spectrum (**Figure 37**).⁴²⁰

3.2. Symmetric Dissociation Observed upon Collisional Activation

In performing CID experiments on ClyA oligomeric complexes to generate better-resolved, cleaner spectra and to confirm the putative identity of the complexes, we observed other product ions beyond the highly-charged monomer and remaining (n-1)-mer that canonically result from CID of a protein complex ion (**Figure 37**). Octameric complexes, which were the primary species studied due to being formed in the presence

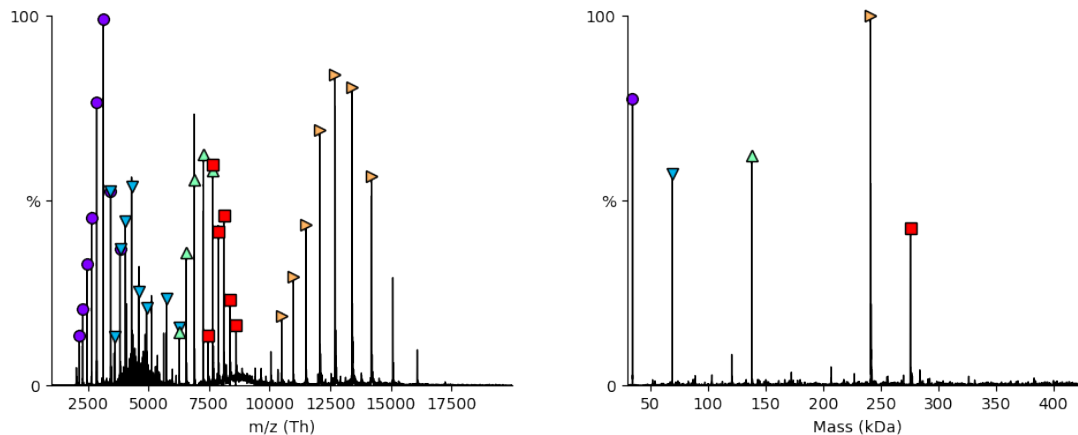


Figure 37. ClyA octameric complexes (red squares) formed in DDM dissociate symmetrically into tetramers (mint triangles) as well as into canonical CID products: monomers (purple circles) and heptamers (orange triangles). Left: Mass spectrum of ClyA-DDM sample acquired on a ThermoFisher Orbitrap instrument with activation restricted to the source region (IST 200 V, HCD 0 V), analyzed and annotated to show the distribution of each oligomeric species with UniDec. Right: Normalized relative intensities of the identified peaks corresponding to each oligomeric species, determined with UniDec. Dimers are also labeled with blue triangles.

of both DDM and C12E8, produced tetrameric ions upon increased collisional activation. The charge state distributions of these overlapped, with the tetramer charge being half that of the octamer, indicative of symmetric dissociation—a result typically observed for SID and sparingly reported for collisional activation of protein complexes in the literature. This was also true of the dodecameric complexes (both those formed in C12E8 and those representing soluble oligomers separated from ClyA monomer with size exclusion chromatography) and the small populations of decameric ions when detected, resulting in symmetric dissociation into hexamers and pentamers, respectively, with roughly half the number of charges of the original complex. This often was discernible from the appearance of the mass spectrum alone; instead of resembling an approximately Gaussian distribution of charge states, these series would exhibit a pattern with the intensity of alternating peaks being higher than expected for a Gaussian. Because the

original intact complex is a dimer of the dissociation product, the even-charge-state peaks of the former overlap with peaks corresponding to the latter.

We found this pattern of symmetric dissociation to be reproducible not just for different oligomeric states formed in various solution conditions but also across mass spectrometer platforms. Native mass spectra of ClyA complexes were acquired on both a Waters Synapt G2-Si ion mobility time-of-flight mass spectrometer (**Figure 38**) and a ThermoFisher Orbitrap instrument (**Figure 37**). Differences in the extent of typical ion activation used in these instruments are well-established. Pertinently, while symmetric dissociation was observed on both instruments, the abundance of these product ions relative to those produced by asymmetrical dissociation (i.e., unfolded monomer and (n-1)-mer) varied. Furthermore, while heptameric product ions from CID of octamer were readily observed, the corresponding 9-mer and 11-mer product ions were not always observed upon CID of decameric and dodecameric ions. Taken together, these findings indicated that in these experiments for ClyA specifically, symmetric dissociation was a competitive mechanism on CID timescales. While other instances of symmetric dissociation upon collisional activation have been reported (albeit sparingly) in the literature,^{153,864-866,868,870,871,876} the study of several oligomeric complexes of the same protein on multiple mass spectrometer platforms—with varying activation capabilities in different instrument regions—in this study presented a unique opportunity to investigate this phenomenon in detail.

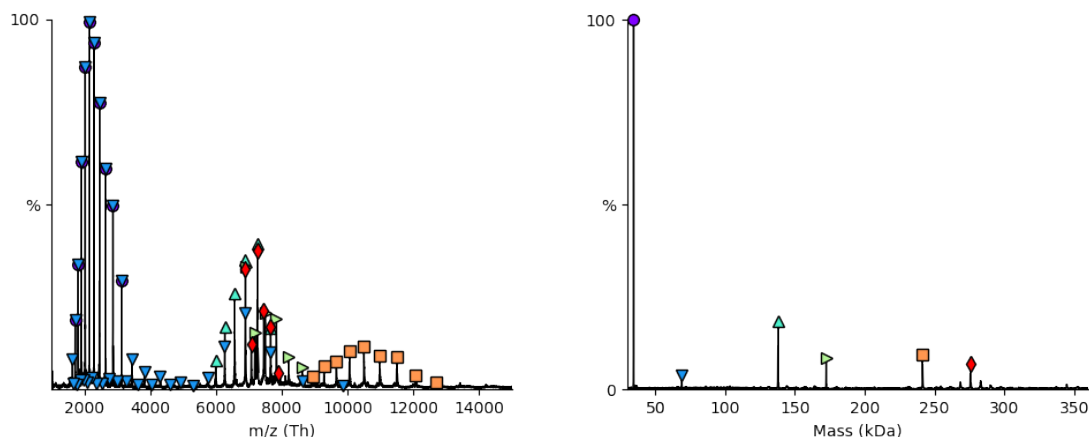


Figure 38. Dissociation of ClyA octameric complexes (red diamonds) formed in DDM into both symmetric and asymmetric product ions upon activation primarily in the trap region of a Waters time-of-flight mass spectrometer (source temperature 150°C, sample cone CE 25 V, trap CE 200 V). Left: Mass spectrum analyzed and annotated with UniDec, where monomers are represented by purple circles, dimers blue triangles, tetramers teal triangles, pentamers light green triangles, and heptamers orange squares. Right: Relative abundances of the peaks corresponding to each oligomeric species, plotted according to their mass.

3.3. Surface-Induced Dissociation Supports Quaternary Structure Involving Equal Subunit Interfaces

As both types of instruments were equipped with SID devices, we also performed SID experiments as a point of comparison and to better understand the quaternary structure of these complex ions. For both detergents, SID of octameric complexes ($n = 8$) resulted in product ions of all possible oligomeric states ($n = 1$ to 7) that in combination could reproduce an octamer (shown for the ThermoFisher Orbitrap instrument in **Figure 39**). SID has been shown to produce ions that reflect the quaternary structure of the original complex, with dissociation occurring along the weakest interface.⁸⁴³ Solved structures of ClyA oligomeric pore complexes resemble barrels composed of rods of long, extracellular α -helices arranged in a ring-like conformation.^{836,837} The symmetry of these structures dictates that the interfaces between subunits are identical, thus all

possible combinations of oligomeric subunits would be equally likely to result from SID, in agreement with experiment. These SID experimental results support the conclusion that the octameric ClyA ions resemble symmetrical pore-like structures.

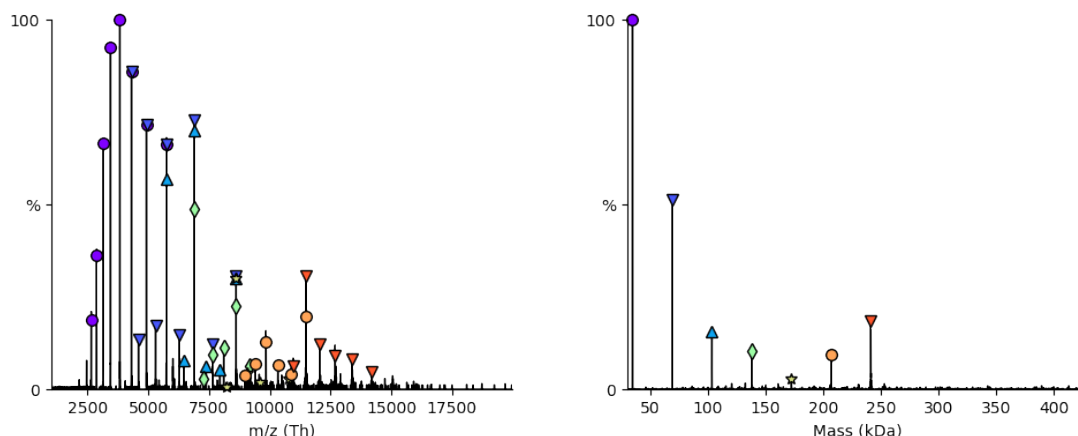


Figure 39. Surface-induced dissociation of octameric ClyA complexes formed in C12E8 detergent result in all possible product ions from monomers to heptamers, analyzed using UniDec. Left: Mass spectrum acquired on a ThermoFisher Orbitrap instrument with SID (145 V) of ions isolated in the range of 8200-8850 m/z . Oligomeric ClyA species indicated according to the following color/symbol combinations: monomers (purple circles), dimers (blue triangles), trimers (light blue triangles), tetramers (mint diamonds), pentamers (tan stars), hexamers (orange circles), and heptamers (red triangles). Right: Relative abundances of the peaks associated with each SID product oligomer.

3.4. Correlating Dissociation Pathway with Collisional Activation in Different Instrument Regions for ClyA Octamers

Among native mass spectrometrists who study membrane proteins, there has been recent, growing interest in using softer conditions to avoid unintended structural effects caused by high levels of activation and choice of detergent/lipid which can affect interpretation of results. Consideration of instrument design and study of activation in different regions of mass spectrometer platforms is thus important within this context. While CID and SID have well-established differences with respect to the energy, number, and activation timescale of their respective dissociation events, the observation of both

symmetric and asymmetric dissociation products of ClyA indicate its potential to act as a “thermometer ion” for tuning activation throughout the mass spectrometer instrument.⁸⁹⁰⁻

⁸⁹² This finding represents a possible bridge between these different methods of dissociation, with symmetric dissociation being a competitive mechanism on CID timescales. Accessing more SID-like dissociation without requiring instrument modification—and the associated reduction in transmission efficiency—with collisional activation would be very valuable.

While the two mass spectrometer platforms used here—a Waters Synapt G2-Si time-of-flight instrument and a ThermoFisher Q Exactive Orbitrap UHMR instrument—have different designs and activation capabilities, some regions are analogous to each other in how they are used in native MS study of membrane protein complexes. Desolvation is commonly achieved in the source region by increasing the collisional energy of the sample cone¹⁰⁸ (Synapt) or in-source trapping (IST, Orbitrap). Further activation—to aid in desolvation and removal of adducts, or to perform dissociation experiments—is achieved in the collision cell in both instruments, which are the trap collision cell (Synapt) and the higher-energy C-trap dissociation cell (HCD, Orbitrap).²⁶¹

To begin to assess the conditions under which these two dissociation pathways remain competitive, we investigated the differences in the ratio of the two types of dissociation product ions detected when collisional activation was largely confined to either the source region or the collision cell—or both—on each mass spectrometer platform. For the octamer, these two populations include canonical CID products (highly-charged monomer and heptamers lower in charge) and the SID-like tetramer ions.

On the ThermoFisher Orbitrap instrument, high activation of ClyA-DDM octamers with in-source trapping of 200 V and no activation in the HCD cell resulted in the CID products predominating (**Figure 37**). The heptameric and monomeric CID product ions are the most abundant species here (100% and ~75% relative abundance, respectively), while the tetrameric ions formed upon symmetric dissociation are detected at approximately 60% abundance relative to the heptamer. In contrast, activation in the source region of the Waters Synapt instrument (with a small-aperture cone and sample cone CE of 100 V) supplemented with a low trap collision energy of 25 V was not sufficient to result in dissociation of ClyA octamers formed in DDM. Under these conditions, the most abundant species detected was octamer.

When activation was largely constrained to the collision cell, tetrameric species were detected at a greater abundance than were heptameric ions on both instruments. Both of these species were more abundant than the octamers, although ClyA monomers were most abundant overall. These mass spectra of ClyA oligomers in DDM were acquired with the collision cell CE set to 125 V and minimal activation in the source region (25 V) on both instruments. The heptameric CID product ion peaks were ~25% and ~50% as abundant as those of the tetrameric ions on the Orbitrap and Synapt instruments, respectively. We also note that a population of decameric ions was detected at low abundances under these conditions on both instruments. This can be seen in the spectra acquired under these conditions on the Synapt in **Figure 38**; although the decameric population is not denoted with a symbol, pentamers resulting from symmetric dissociation of decamers are present at an appreciable abundance. As was the case under a wide variety of instrumental parameters, nonameric CID product ions were not

observed. Thus, while both typical (loss of unfolded monomer) and atypical (loss of compact oligomers) collisional dissociation pathways are accessible for octameric ions under these conditions, symmetric dissociation appears to be favored for the larger decameric ions.

As a final point of comparison, mass spectra were also acquired with activation in both the source region and collision cell in each platform. These collisional energy settings were IST 100 V and HCD 150 V for the Orbitrap (**Figure 40**) and sample cone 200 V and trap 100 V for the Synapt. This produced a similar result as described immediately above for activation in the collision cell—tetrameric product ions were more abundant than heptamers. Although monomeric product ions were still detected with high abundance, peaks corresponding to the CID heptamer products were much less intense than the tetramer symmetric dissociation products (<10% and ~15% for the Orbitrap and Synapt, respectively).

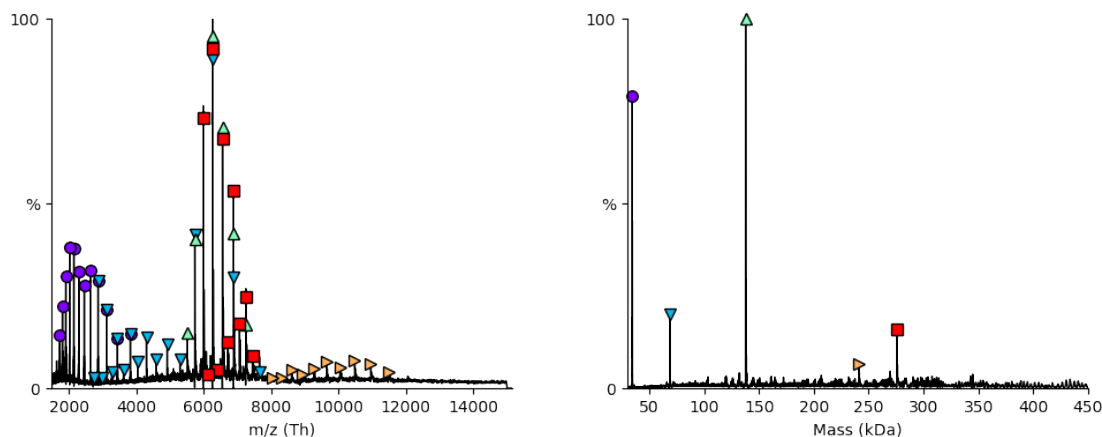


Figure 40. Dissociation of octamers of ClyA (red squares) formed in DDM with activation in both the source and collision cell regions of a ThermoFisher Orbitrap UHMR instrument (IST 100 V, HCD 150 V). Left: Mass spectrum analyzed with UniDec, annotated as follows: monomers (purple circles), dimers (blue triangles), tetramers (mint triangles), heptamers (orange triangles), and octamers (red squares). Right: Relative abundances of the peaks associated with each species, plotted according to their mass.

3.5. Larger ClyA Oligomers Only Followed Symmetric Dissociation Pathways

For the larger oligomeric complexes of ClyA (decamers and dodecamers), the product ions detected were almost exclusively from symmetric dissociation regardless of the collisional energy or instrument region. With moderate activation in both the source and trap regions of the Waters instrument (small-aperture¹⁰⁸ sample cone CE 100 V, trap CE 50 V), we detected hexamer ions formed from dodecamers. On the Orbitrap mass spectrometer, high activation in the source region (in-source trapping 250 V) followed by moderate activation in the collision cell (HCD 50 V) also resulted in symmetric dissociation. As described above for activation in the collision cell only (**Figure 38**), the only dissociation products observed for decameric ions were pentamers.

We rationalize these findings by positing that the thermochemical barrier for symmetric dissociation is likely comparable regardless of oligomeric state, owing to the subunit interfaces being equal in area.⁸⁴³ By contrast, asymmetric charge partitioning in CID is thought to proceed by thermally activated “hopping” of protons between basic sites at the ion surface concomitant with unfolding of the monomer that eventually dissociates; as these protons must find their way onto the unfolding monomer for CID to proceed, the entropy barrier for this process likely increases with the number of subunits in the complex. The relationship between charge state and mass is well-established for globular, native-like proteins in native ESI MS, with charge scaling approximately with the square root of the protein ion mass.^{180,205,646,649,651} However, the surface area of the protein, which can serve as a proxy for the number of basic sites that could potentially be charged here, should scale approximately as $n^{2/3}$, where n is the number of subunits.^{208,210,650} Thus, the number of possible charge sites will quickly outgrow the

number of charges with increasing oligomeric state. Migration of a sufficient number of charges onto a single subunit (typically ~40-50% of the total charge of the intact complex) in order for CID to occur should thus be entropically disfavored. For smaller oligomeric complexes, energy released by unfolding the monomeric subunit is likely sufficient to offset this entropic penalty. This will be the same regardless of oligomeric state because they share the same monomeric subunit, but for larger ClyA oligomers the entropic barrier likely remains too high to overcome which leads to symmetric dissociation being favored.

More tangibly, we can crudely estimate and compare the differences in the entropic penalty associated with moving charges onto a single subunit in CID for an octamer and a dodecamer by calculating the logarithm of the number of microstates possible in each scenario. Based on native mass spectra of ClyA acquired with minimal collisional activation, charge states of 40+ and 50+ are reasonable for intact octamer and dodecamer, respectively. Unfolded monomeric subunits in dissociation experiments typically had a charge state of 16+, which would require complementary (n-1)-mer CID products of 24+ heptamer and 34+ 11-mer. This allows comparison of the entropic energy of equally distributing charges among all subunits (5+ and ~4+, respectively, for the octamer and dodecamer) against putting 16 charges on a single subunit and the remaining charge on the other subunits for both oligomeric states. In this simplistic estimation and assuming standard temperature of 298 K, accumulating 16 charges on a single subunit would have an entropic penalty of -47.4 kJ/mol for the octamer and -52.8 kJ/mol for the dodecamer.

This explanation is supported by SID results illustrating that these symmetric complexes can dissociate along any of the subunit interfaces because the area of each subunit interface is equal, as calculated with PISA. By comparison, in CID, a high number of charges must migrate onto the same subunit in order for an unfolded monomer to be ejected. The rate of this process can reasonably be expected to differ for an ion containing only eight subunits compared to one with twelve, with the latter having ~1.5 times as many possible charge sites as the former. Relatedly, others have speculated that charge migration, concomitant with monomer unfolding in CID, is likely slower for precursor ions with a higher initial charge state,⁸⁷¹ as would be the case for ClyA dodecameric ions here. Our results are also consistent with theoretical investigation into the energy barriers associated with gas-phase dissociation. Thachuk and coworkers posit that dissociation pathways are controlled by the balance between inter- and intramolecular Coulomb energy.⁸⁸¹⁻⁸⁸³ For multimeric complexes with charges distributed symmetrically, which is energetically favored over asymmetric charge partitioning, intermolecular repulsion will dominate, lowering the barrier for dissociation. Although dodecameric ClyA ions have a higher number of charges than do octamers, the fractional occupancy of charge sites is lower (both overall and per subunit), which should reasonably result in stable charge configurations that minimize Coulomb repulsion. This is supported by results from Thachuk and coworkers showing that the relative potential energy rises more steeply for higher-charged ions as charge partitioning among subunits becomes more asymmetric.⁸⁸¹ This is also in line with foundational investigation into the nature of asymmetric charge partitioning for homodimers by Williams and coworkers.^{840,877,878} They demonstrated for cytochrome c and disulfide-reduced α -

lactalbumin homodimers that higher charge states tended to dissociate symmetrically, while lower-charged ions exhibited asymmetric dissociation typical of CID,^{840,878} and the importance of charge state has been reported to influence the dissociation pathway of other protein complexes as well.^{221,300,620,866,871,874,876,879,893-895} By contrast, octameric ClyA complexes have more charges per subunit, which will increase intramolecular repulsion and serve to lower the barrier to unfolding.

These early studies by Williams and coworkers also demonstrated that subunit conformation and flexibility play a major role in determining the gas-phase dissociation pathway.^{840,878} When heterodimers of these ions were prepared such that one subunit was oxidized and the other reduced, asymmetric dissociation was observed, with the disulfide-reduced subunit—i.e., the one with more conformational flexibility—taking a disproportionate amount of the original charge. Intramolecular disulfide bonds, cross-linking, salt bridges, and other interactions will increase the barrier to unfolding relative to dissociation. Because ClyA contains no disulfide bonds and the interfaces between subunits are of equal area and strength, we conclude that the differences in dissociation pathways products observed for ClyA octamers and dodecamers here results from the enhanced stability of symmetric charge distribution in the latter and the ability of unfolding a monomeric subunit to offset the entropic penalty associated with charge migration for the former.

4. Conclusions

Here, we have described the observation of ClyA accessing both typical and atypical collision-induced dissociation pathways simultaneously. This result was consistent across two different mass spectrometer platforms. Differences in the ratios of

CID heptameric product ions and SID-like tetrameric product ions formed from collisional dissociation of ClyA octameric complexes were correlated to activation in different regions of these two instruments. Interestingly, tetramers were more abundant than heptameric ions in all conditions studied here, with the sole exception of spectra acquired with activation constrained to the source region of the Orbitrap instrument (**Figure 37**). These initial findings will serve as the foundation for future work toward systematic study of the dissociation pathways of ClyA. Quantification the entropy and enthalpy of these different dissociation processes and investigation of dissociation rates as a function of energy will provide novel insight into gas-phase dissociation of protein complexes in native ESI-MS.^{693,694} When paired with simulations of the effective temperature experienced by the ion throughout the different regions of these instruments, ClyA has the potential to serve as a thermometer ion to tune levels of activation.

The ability of ClyA to form pore-like complexes of multiple oligomeric states also may provide insight into the energy barriers for these different dissociation pathways. While ClyA octameric complexes were able to access both typical and atypical dissociation pathways, the larger decameric and dodecameric complexes appeared to preferentially follow symmetric dissociation pathways. In the context of previous experimental and theoretical work,^{840,878,881-883} we interpret these results to indicate differences in the entropic energy barrier associated with migration of a large number of charges onto a single subunit.

Detailed investigation of protein ions that are able to access more structurally informative SID-like pathways is very valuable to the field of native MS. While SID can inform quaternary structure and subunit connectivity of complexes, these experiments

require instrument modification and can be associated with a reduction in transmission efficiency. In addition to results for ClyA described here, tryptophan synthase has also been previously reported to exhibit both typical and atypical dissociation pathways simultaneously.⁸⁷¹ While some of the proteins for which atypical CID behavior has been reported are similar to ClyA (e.g., the symmetric ring-like/toroidal protein complexes peroxiredoxin⁸⁷⁰ and stable protein I⁸⁶⁶), there are many properties that vary among these proteins. Further study of possible correlations of differences in CID behavior with structure, interfacial area, charge state, and interactions that reduce conformational flexibility will also be important for improved understanding of the determinants of gas-phase protein ion dissociation and for interpreting ion structure from CID behavior.

Bridge

In addition to the study of dissociation pathways in different mass spectrometer platforms, native ion mobility-mass spectrometry experiments combined here with the computational approach described in earlier chapters revealed differences in the oligomeric state of complexes assembled by a pore-forming toxin across various membrane-like environmental conditions. This highlights the technique's advantages of easily-changed solution conditions and high mass accuracy and sensitivity together with the structural interpretation made possible by combining ion mobility with computational methods. The next chapter further expands the wealth of information possible with these methods through investigation of another challenging heterogeneous biomolecular system, complexes formed by a trio of β -crystallin eye lens protein isoforms.

CHAPTER VI
NATIVE ION MOBILITY-MASS SPECTROMETRY REVEALS COMPOSITION
AND TOPOLOGY OF HETEROOLIGOMERIC COMPLEXES FORMED
BY EYE LENS β -CRYSTALLIN PROTEIN ISOFORMS

While the material included here is primarily my own work, Takumi Takata and Micah T. Donor assisted with sample preparation and data collection. James S. Prell and Kirsten J. Lampi contributed to experimental design and interpretation. This work will form the basis of a manuscript to be submitted in the future, with the above named as co-authors.

1. Introduction

Long-lived proteins in humans, which can last days to years without degradation or turnover, are implicated in numerous diseases.⁸⁹⁶⁻⁹⁰² Chemical modifications to and/or aggregation of these proteins can disrupt their normal protein-protein interactions and structure crucial to healthy processes.^{896,903-924} One example of this is the transparency of the eye lens, which is maintained by a family of structural and refractive proteins called crystallins that are present in an increasing concentration gradient from the outer layer to the center of the lens.⁹²⁵⁻⁹³⁶ Aggregation of crystallin proteins disrupts normal eye lens transparency and results in formation of cataracts, a major cause of blindness around the world.⁹³⁷ Evidence suggests that aggregation is caused by modifications that crystallins accumulate during aging,^{918,938,939} but detailed characterization of the role of these modifications in disease and their effects on crystallin structure and behavior remains challenging to obtain.⁹⁴⁰

These eye lens crystallins are of multiple types— α , β and γ —each with their own set of many isoforms.^{928,941} Of these three, α -crystallins occur as very large aggregates and share similarities to small heat shock proteins.⁹⁴² By comparison, β and γ crystallin proteins share many structural similarities with each other, namely two double Greek key motifs in each of the N- and C-terminal domains which are connected by a flexible linker region.^{925,927,929,931-933,935} β -crystallin monomers, which are the focus of the present work, are relatively small, approximately 20-30 kDa in mass, and readily oligomerize with each other in the eye lens.⁹³⁴ At the center of the lens, the crystallin protein concentration can be as much as ~400-500 mg/mL or greater.⁹⁴³⁻⁹⁴⁵ However, this high solubility makes crystallization—and thus study of their structure with X-ray crystallography—difficult, and their low mass also prohibits the use of cryo-electron microscopy.⁸⁹⁶ As such, nuclear magnetic resonance (NMR) has been the primary technique for high-resolution studies of crystallin structure and dynamics to date.⁹⁴⁶

Despite these challenges, a handful of X-ray crystal structures of human β -crystallins have been solved, including a dimer of truncated β B1 and of β B2 monomer, as well as of trimeric β A3 (PDB ID: 3QK3) and dimeric β A4 (PDB ID: 3LWK).^{935,947} Results from NMR study of human β B2 support formation of a dimer in solution exhibiting a face-en-face dimer, similar to that of the truncated β B1 dimer structure.⁹⁴⁸ In these structures, the linker region connecting the N- and C-terminal domains is bent, allowing a compact structure. By contrast, the X-ray crystal structure of β B2 is domain-swapped, with the linker in an extended conformation. Interestingly, the truncated β B1 dimer structure very closely matches half of the lattice tetramer of bovine β B2 crystallin.⁹³² This observation has led some to question whether the domain-swapped

structure with an elongated linker might instead be representative of the unit cell and ultimately caused by crystallization conditions.^{948,949} While reports on the nature of the linker structure and of the subunit interface are conflicting, the importance of dimerization has been a consistent finding.

In contrast to the wealth of information on crystallin monomers and dimers, details of the higher-order structures present in the eye lens remain elusive. Light scattering experiments have been used to characterize larger-scale physical properties of crystallin complexes and how they change as a function of changing conditions, and when coupled with size exclusion chromatography (SEC), have revealed the presence of high molecular weight aggregates.^{913,915,918,950,951} However, these methods do not have sufficient resolution to determine in detail the distribution of oligomeric states, masses, or subunit compositions with respect to the many different crystallin isoforms. These gaps in knowledge together underlie the long-standing questions in this field of how (wild-type) crystallin diversity plays a role in establishing the refractive index gradient across the lens required for maintaining transparency and how disruption of normal crystallin complex formation results in cataracts.⁹⁵²⁻⁹⁵⁴ Answering these questions is necessary for understanding the normal structural and chemical behavior of crystallins and how modifications to long-lived proteins result in aggregation and disease, critical information for designing therapeutic remedies.^{955,956}

Native electrospray ionization ion mobility-mass spectrometry (ESI-IM-MS) is a powerful technique for studying biomolecules, including heterogeneous complexes composed of nearly-isobaric protein subunits not easily distinguished by chromatography or other structural methods.^{42,43,47,48,50,137,139,226} With nano-ESI, analytes are gently

ionized and transferred from buffered aqueous solution into the gas phase.^{105,227} This can preserve non-covalent interactions and allow study of biomolecular complexes ranging widely in mass and from solution conditions that can be easily changed. The high mass accuracy and sensitivity of this technique enables routine measurement of subunit masses with sub-Da precision and, as a result, unambiguous determination of subunit composition from complex masses, especially with adjuvant dissociation experiments within the mass spectrometer.¹⁰⁷ Ion mobility spectrometry further provides orthogonal information, separating ions which can overlap extensively in the mass spectral domain based on their size/shape.^{128,135,136,138} The measured ion mobility cell drift times can be converted into collision cross-sections (CCSs), representing the rotationally-averaged silhouette of ions and somewhat akin to surface area, to provide some structural information. Comparison of experimental CCSs to those computed for condensed-phase structure coordinate files can be used to distinguish between different possible topologies. Owing to the benefits of this technique, native IM-MS has been used previously to study the much larger α -crystallin aggregates.^{63,171,491,492,957}

Here, we demonstrate the advantages of using native IM-MS to characterize β -crystallin complexes. Focusing on three wildtype β -crystallins (β B1, β B2, and β A3), we provide novel insight into the normal behavior of these critical eye lens proteins. The distributions of homo- and hetero-oligomeric complexes, including their exact subunit compositions, formed are identified, revealing the importance of dimerization to serve as a building block for complex formation. Guided by previous studies indicating crystallins' preference to form heterodimers over homodimers, we investigated the kinetics of formation of β B1/ β A3 and β B2/ β A3 heterodimers, finding the former to occur

approximately three times slower than the latter. Ion mobility measurements combined with a large set of model structures with various subunit arrangements indicate these complexes adopt very compact topologies. Although these experiments are performed at protein concentrations lower than those found in mature lenses *in vivo*, results presented here are nevertheless consistent with tight packing of crystallin oligomers necessary to achieve such high protein concentrations at the center of the eye lens. This study serves not only as a benchmark for establishing wildtype crystallin behavior, from which we can begin to unravel the role of crystallin diversity in maintaining stable, tightly-packed oligomeric structures and establishing the refractive gradient across the lens, but also as a test-bed for investigating the toxic aggregation of other long-lived proteins responsible for many diseases.

2. Methods

2.1. Protein Expression and Purification

Crystallins were expressed and purified as previously reported.^{915,920,958} Briefly, recombinant proteins were expressed in *Escherichia coli* strain BL21 (DE3) or BL21 (DE3) p*LysS* (Invitrogen, Waltham, MA). Cells were grown to an optical density of 0.4 at 600 nm after an overnight culture and induced with 1 mM IPTG for 4 hours at +37°C with constant shaking. Cells were harvested by centrifugation and lysed by repeated freeze/thaw cycles in the chromatographic buffer used for the first step of purification for each protein containing protease inhibitors, lysozyme, DNase I, RNase A, and MgCl₂.

For β B1, cell lysates were applied to a SP Sepharose Fast Flow (Amersham Pharmacia Biotech, Piscataway, NJ) equilibrated in 13.2 mM sodium phosphate, 23 mM KCl, 0.16 mM EDTA, and 1 mM DTT. For β B2, cell lysates were applied to a

MacroPrep DEAE anion exchange column matrix (BioRad, Hercules, CA) equilibrated in Tris buffer (pH 8.0) for the first step followed by DEAE Fast Flow anion exchange column matrix (Amersham Pharmacia Biotech) equilibrated in Tris buffer (pH 7.4) for the second step. Both Tris buffers contained 20 mM Tris, 1 mM EGTA, 0.16 mM EDTA, and 1 mM DTT. For β A3, cell lysates were applied to a DEAE Fast Flow anion exchange column equilibrated in a 50 mM Tris buffer (pH 7.8), 2 mM EDTA, and 1 mM DTT followed by a SP Sepharose cation exchange column equilibrated in a 20 mM MES buffer (pH 5.6), 2 mM EDTA, and 1 mM DTT.

Each protein was eluted with a 0-500 mM NaCl gradient. Fractions containing protein of interest were checked by electrophoresis, pooled, and concentrated and their masses confirmed by mass spectrometry. All proteins were estimated to be greater than 90% pure by these methods. Proteins were aliquoted and stored at -80°C . Upon thawing proteins were buffer-exchanged into the appropriate buffer for experiments described below.

2.2. Native Electrospray Ionization-Ion Mobility Mass Spectrometry Experiments

All native ion mobility-mass spectrometry experiments were performed on a Waters Synapt G2-Si ion mobility-mass spectrometer with a nano-electrospray ionization source. 50 μL aliquots of individual crystallin isoform protein samples were exchanged into 200 mM ammonium acetate, pH 7.5, using Micro Bio-SpinTM 6 columns (Bio-Rad Laboratories, Inc.) prior to mass spectrometric analysis. Samples were diluted as needed with additional 200 mM ammonium acetate, pH 7.5. A small volume (\sim 3-5 μL) of buffer-exchanged protein sample was loaded into a borosilicate glass capillary pulled to a fine (\sim 1-2 μm i.d.) tip, and electrospray was initiated by applying a voltage to a platinum wire

in electrical contact with the sample. Prior to data collection, a mass calibration profile was generated based on clusters of cesium iodide.

For all experiments, the capillary voltage was maintained just above the threshold needed to generate sufficient ionization and detection, typically +0.7-1.0 kV, and the sample cone and transfer collision energy were operated at 25 V and 5 V, respectively. For accurate mass determination and homooligomer dilution series experiments, spectra were generated as the sum of scans over 5 minutes and were collected with a trap collision energy of 10 V and trap gas flow of 7 mL/min. For ion mobility-mass spectra collected to measure collision cross-sections in nitrogen buffer gas, tri-wave height and velocity settings were: 300 m/s and 2 V (trap), 500 m/s and 16 V (IMS), and 100 m/s and 2 V (transfer). Ion mobility-mass spectra were acquired under identical instrumental settings for the following proteins used for calibration according to established procedures: cytochrome c, β -lactoglobulin, transthyretin, avidin, bovine serum albumin, concanavalin A, alcohol dehydrogenase, and pyruvate kinase.^{201,203}

2.3. Homo-Oligomer Formation as a Function of Concentration

We investigated the oligomeric distribution of complexes formed by each crystallin isoform on its own as a function of protein concentration over a dilution series of 11.5 μ M, 1.5 μ M, 575 nM, 288 nM, and 144 nM (equivalent to concentrations of approximately 267-321 μ g/mL, 35-42 μ g/mL, 13-16 μ g/mL, 7-8 μ g/mL, and 3-4 μ g/mL, respectively, depending on the specific isoform which vary in mass \sim 2-5 kDa from one another). The sensitivity of native MS instruments allows investigation of these low protein concentrations, at which these crystallins remain soluble and do not aggregate, preventing protein loss during the course of the experiments.

2.4. Kinetics of Heterodimer Formation

To measure the kinetics of formation of heterodimers, 11.5 μM βA3 (289 $\mu\text{g/mL}$) was mixed in equimolar amounts with βB1 (321 $\mu\text{g/mL}$) or βB2 (267 $\mu\text{g/mL}$) in a tube placed on a heating block at +37°C, which yields a total protein concentration of 11.5 μM in the final mixed sample. A small aliquot was immediately removed for mass spectrometry analysis. The sample continued to incubate, and additional small volumes were removed periodically over a period of 3 hours. These spectra were acquired with ion mobility mode to enable distinction between possibly overlapping peaks of oligomers using the same tri-wave settings as above except for the IMS wave height and velocity (550 m/s and 20 V). The trap collision energy and trap gas flow were 15 V and 5 mL/min, respectively, and spectra were acquired for 10 min. As above for the homooligomer dilution series experiments, this concentration was chosen to avoid aggregation. Protein loss did not occur over the time course of these experiments, as determined by visual inspection of sample tubes and monitoring for changes in the total ion chromatograms and ion signal intensity.

2.5. Analysis of Ion Species Abundance

Mass spectral peak areas were calculated by using a built-in integration feature in Igor Pro. Detected abundances were then determined by summing these values for the native charge state peaks for each ion species present in each mass spectrum. Homooligomer abundances from the dilution series experiments were normalized relative to the detected abundance of the monomer population in each spectrum. For the kinetics experiments, the heterodimer abundance is reported as a fraction of the total detected abundance of the dimer population in each spectrum to monitor the relative increase in

heterodimers over homodimers initially present upon mixing the two isoforms together. Analyzing the proportion of heterodimers as a function of incubation time, we report both inverse rate constants yielded from approximation by pseudo-first-order kinetics and half-lives from treating heterodimer formation as a second-order kinetics reaction.

2.6. Generation of Model Structures, Molecular Dynamics Simulations, and Collision Cross-Section Calculations

An X-ray crystal structure of monomeric β -crystallin B2 (PDB ID: 1YTQ)⁹⁴⁷ was used as a template for all model structures, which were created manually in PyMol. Model structures were built to represent a wide array of possible subunit arrangements for each oligomeric state detected in the native IM-MS experiments. For each oligomer, a single charge state from the native charge state distribution detected experimentally was selected for all simulation and computational work. A stable configuration of the appropriate number of charges chosen for each oligomeric state was then determined for each model structure using the charge placement algorithm in Collidoscope.²¹⁴ Topology files were generated for model structures to match these charge configurations. An in vacuo molecular dynamics (MD) simulation of each of these structure coordinate files was performed in GROMACS with the GROMOS96 43a2 force field using a previously-described protocol validated to robustly produce simulated structures with computed CCSs on average $0 \pm 4\%$ different from literature IM-MS data for a set of protein calibrants.²¹⁵ Collision cross-sections were computed for the model structure coordinate files after MD simulation using the Trajectory Method with nitrogen buffer gas in Collidoscope. Experimental CCS measurements were then compared to these computed values for the model structures representing a variety of topologies.

The β B2 structure (PDB: 1YTQ) used here is of the domain-swapped conformation with an extended linker region,⁹⁴⁷ in contrast to other findings supporting a face-en-face dimer conformation with a bent linker.^{935,948} This structure was selected to use as a template here rather than the truncated β B1 face-en-face dimer (PDB: 1OKI) because a considerably higher percentage of the residues in the amino acid sequence are resolved. Given the features of gas-phase protein ion compaction we have reported previously^{215,223} and that the extended linker here is compacted upon simulation, we expect that results from MD simulation of model structures built from a face-en-face template structure would be similar.

3. Results and Discussion

3.1. β -Crystallin Isoforms β B2 and β A3 Readily Homo-Oligomerize, While β B1 is Primarily Monomeric

We first acquired a mass spectrum of each of the three β -crystallin isoforms after mass calibration, used to determine an average accurate mass from multiple charge states with sub-Da precision. As shown in **Table 4**, these measured masses compare well to the expected mass calculated based on each isoform amino acid sequence, with mass differences of less than 1 Da for all three. The accuracy confirms the identity and purity of each sample, and the precision of these measurements enable not only easy distinction between the isoforms but also unambiguous determination of complex stoichiometries and subunit compositions based on their mass. This is critical for detailed characterization of the higher-order structures formed by crystallins, as the diversity of subunit types and isoforms within this protein family complicate interpretation of subunit composition from complex masses determined using techniques with low mass

resolution. Because the masses of all crystallin isoform subunits, which can combine in many different possible stoichiometries to form oligomeric complexes, differ by a few kDa from each other at most, it can be almost impossible to assign a specific subunit composition to a single complex mass measured with less precision in traditional biophysical techniques, including native gel electrophoresis, SEC-MALS, and analytical ultracentrifugation. The presence of multiple complex stoichiometries close in mass complicates this even further, with the resulting broad distribution of overlapping masses preventing more detailed interpretation. Even considering only the three β -crystallin isoforms studied here, the range of the six different possible homo- and hetero-dimer masses is less than 10 kDa. Thus, very accurate mass measurements possible with native MS are required to access more detailed information about the complexes formed by these proteins.

Table 4. Measured accurate monomer mass of each of the three β -crystallin isoforms, with the mass expected based on amino acid sequence for comparison.

β-Crystallin Isoform	Charge states	Sequence mass (Da)	Measured mass (average \pm S.D., Da)
β B1	12-16+	27892.21	27892.3 \pm 0.4
β B2	7-10+	23248.74	23249.7 \pm 0.6
β A3	8-10+	25149.94	25150.6 \pm 0.2

To begin this characterization of β -crystallin complexes, we first sought to determine the distribution of homo-oligomers formed by each of the three isoforms. Native mass spectra were acquired for each over a range of protein concentrations from 11.5 μ M to 144 nM. In addition to enabling study of oligomer formation as a function of concentration and benchmarking K_D values, dilution series can also reveal whether detected oligomers are non-specific, formed by chance in the evaporating electrosprayed droplet due to high protein concentration rather than formed natively in solution. As

described in detail previously, the abundances of spurious complexes would resemble a Poisson distribution of oligomeric states, with each possible oligomer number detected and the relative abundances changing in accordance with decreasing protein concentration.^{99,701} At concentrations below 1 μM , monomers have the highest calculated Poisson probability, thus any oligomers present at these low concentrations are assigned as native.⁹⁹

Of the five different protein concentrations used in the dilution series, three are well below this threshold, and the second highest concentration is 1.15 μM . A homodimer population was present for each isoform over the entire range of protein concentrations, which we conclude are not artifacts of the electrospray process. Although homodimers were the largest oligomer detected for βB1 , homotetramers of both βB2 and βA3 , as well as homohexamers βA3 , of were also present at 11.5 μM . The small βA3 tetramer population persisted through most dilutions. Other than monomers, only even-numbered oligomeric complexes were detected for all three isoforms, a finding that itself suggests these are not spurious.

This underscores the importance of dimerization in maintaining crystallin stability and, relatedly, eye lens transparency. The lack of any odd-numbered oligomers provides evidence that dimers are the building blocks from which higher-order crystallin complexes are formed, with assembly proceeding via dimerization followed by additions of dimer subunits. This in turn suggests that disruption of dimer formation could be a key feature of aggregation and cataract formation. These results are consistent with results from other methods in the literature which demonstrate the functional importance of dimers. Analysis of human eye lens samples has also revealed a predominant population

of dimers, and many crystallins have been found to preferentially exist as dimers.^{913,915,920,922,927,934,935,958,959}

However, these native MS experiments revealed a distinct difference between β B1 compared to the other two isoforms with respect to dimerization. While homodimers of β B2 and β A3 were readily detected at each protein concentration of the dilution series, β B1 was predominantly monomeric even at 11.5 μ M. Homo-dimers of β B1 were detected but at a much lower abundance relative to that of the monomer, and this decreased significantly upon each successive dilution. By contrast, both β B2 and β A3 formed homo-dimers predominantly, with the detected abundance being several times that of each respective monomer (**Figure 41**). This finding for β B1 contrasts other reports which find it, like many other crystallin isoforms, to exist primarily as a homodimer, but these experiments were performed using much higher protein concentrations.^{913,920,959}

Together, these results suggest that either β B1 may play a different role in the formation of multi-crystallin complexes than that played by β A3 and β B2, or that the K_D for dimerization of β B1 is much weaker. The β B1 has an elongated N-terminal region compared to the other two isoforms and is the largest in mass. Perhaps this creates difficulties in homo-oligomerization due to steric clashes, as there is a considerable population of β B1 present in the β -high molecular weight fractions isolated from human lens samples.^{920,930,932,960}

Regardless, it appears that crystallin oligomerization is concentration-dependent. Both β A3 and β B2 readily dimerize and form higher-order oligomers at higher concentrations (**Figure 42**), and it seems reasonable to expect that this finding would be repeated for β B1 if analyzed at higher concentrations than those used in the dilution

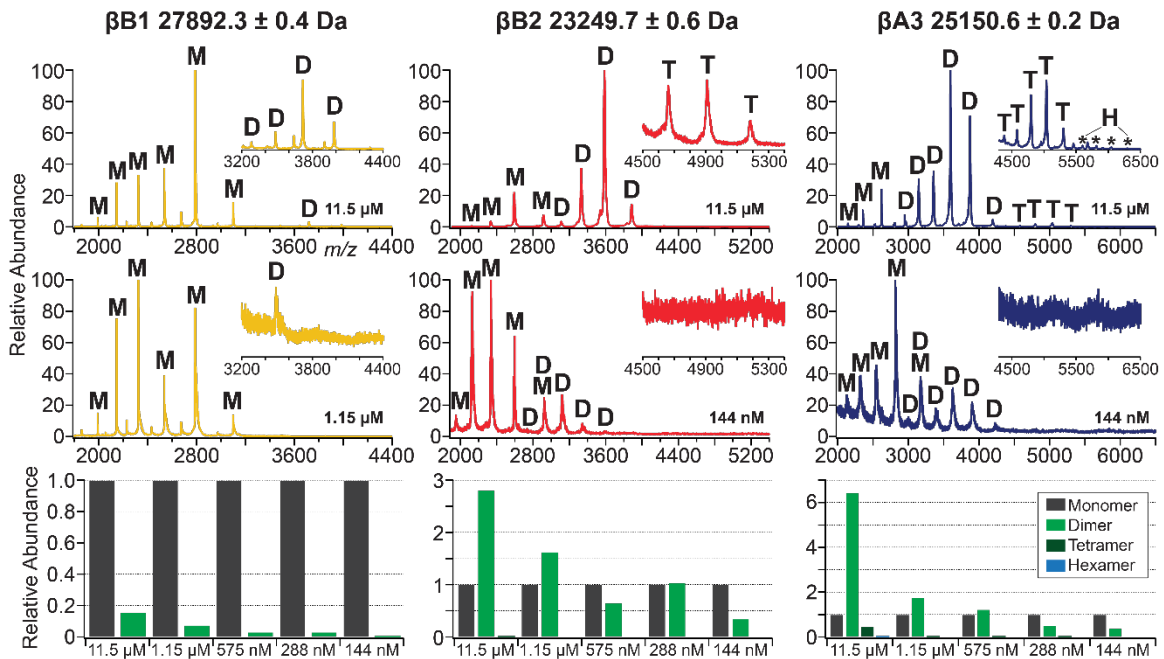


Figure 41. Native mass spectra acquired for a dilution series of individual β -crystallin isoforms and relative abundances of homo-oligomers detected. The native mass spectrum of each protein as labeled is shown for the highest protein concentration used (11.5 μM , top row) and a lower protein concentration (1.15 μM or 144 nM as labeled in figure, middle row) selected to illustrate disappearance of peaks corresponding to dimers. The detected abundance of each homo-oligomeric species is plotted in the bottom row, with abundances for each protein at each concentration relative to that of the monomer.

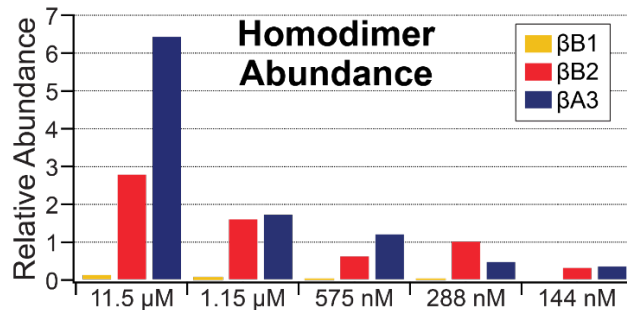


Figure 42. Homodimer abundance for each of the three β -crystallin isoforms at each protein concentration studied, relative to each isoform monomer abundance.

series. Concentration-dependent oligomerization of these β -crystallin isoforms may play a physiologically significant role *in vivo* in establishing the refractive gradient across the lens.^{913,922,931,932,952,959} Protein concentration increases from the outer layer inward toward the center of the eye lens, where it can reach upwards of 400-500 mg/mL. Such high

concentrations must require tight packing of crystallin proteins into stable oligomeric structural arrangements, which, according to a wealth of evidence, is mediated by dimerization.

3.2. β -Crystallin Isoform β A3 Forms Heterodimers with β B2 with a Greater Rate than with β B1

Having characterized the homo-oligomerization of each β -crystallin isoform individually, we next investigated formation of heterooligomeric complexes involving β A3 with either β B1 or β B2. Despite the masses of each of these isoforms differing only by a few kDa, the high mass accuracy afforded by native mass spectrometry enables distinguishing between these subunits and their possible combinations into oligomeric complexes. In native mass spectra acquired for equimolar mixtures of β A3/ β B1 and β A3/ β B2, homooligomeric and heterooligomeric complexes could be distinguished from each other easily. We observed formation of the same hetero-oligomeric complexes by β A3 with both β B1 and β B2: heterodimers, heterotetramers, and heterohexamers. While these data were not collected over a dilution series, given the above-described results together with these observations, we expect that heterooligomerization (and crystallin oligomerization generally) is also concentration-dependent with a role in maintaining the refractive gradient across the eye and lens transparency.

Most crystallin isoforms have been reported to predominantly be dimeric *in vitro*, and there is a preponderance of evidence highlighting the functional relevance of dimer formation.^{913,915,918,920,958} Results from native mass spectrometry experiments for homooligomers and heterooligomers of the three β -crystallin isoforms studied here clearly illustrate that oligomerization into higher-order structures involves addition of

dimer subunits. Modifications such as deamidation, which is hypothesized to be an impetus for aggregation and subsequent cataract formation, have been shown to disrupt crystallin dimer structure and stability, resulting in aggregation.^{915,921,938,950,951,961}

Previous reports have also indicated that when multiple crystallin subunit types are present, heterodimers are preferentially formed over homodimers.^{922,959} Given the importance of the dimer in crystallin structure, interactions, and stability, we next sought to characterize heterodimer formation.

Because β B2 has a much higher propensity to dimerize while β B1 is predominantly monomeric at the concentration ranges used in this study, we anticipated possible differences in the formation of heterodimers by each of these isoforms with β A3. Thus, we performed experiments to monitor heterodimer formation over time and to allow study of their kinetics of formation. β -crystallin isoform β A3 was mixed in equimolar amounts with either β B1 or β B2 and allowed to incubate at physiological temperature, and we removed small aliquots at regular intervals over a period of three hours for analysis with native mass spectrometry. We then quantified the detected abundance of each species of dimer present and analyzed the increase in the heterodimer population over the time course to investigate their kinetics of formation.

Differences are readily apparent upon comparison of mass spectra acquired for each sample immediately after mixing the two isoforms (**Figure 43**). Homodimers of both isoforms are present in each but with noticeable differences in relative abundance. As expected from the characterization of homo-oligomers above, β B1 homodimers are detected at a much lower abundance relative to the β A3 homodimers in the same sample, while β B2 homodimers are present at levels comparable to β A3 homodimers.

Additionally, peaks corresponding to β B2/ β A3 heterodimers are already clearly present, while β B1/ β A3 heterodimer peaks—if present at all—are below the noise baseline. (Due to the similar charge states and sizes of these proteins, as well as structural similarities, these differences in relative abundance are unlikely to originate from large differences in ionization efficiency between these proteins.)

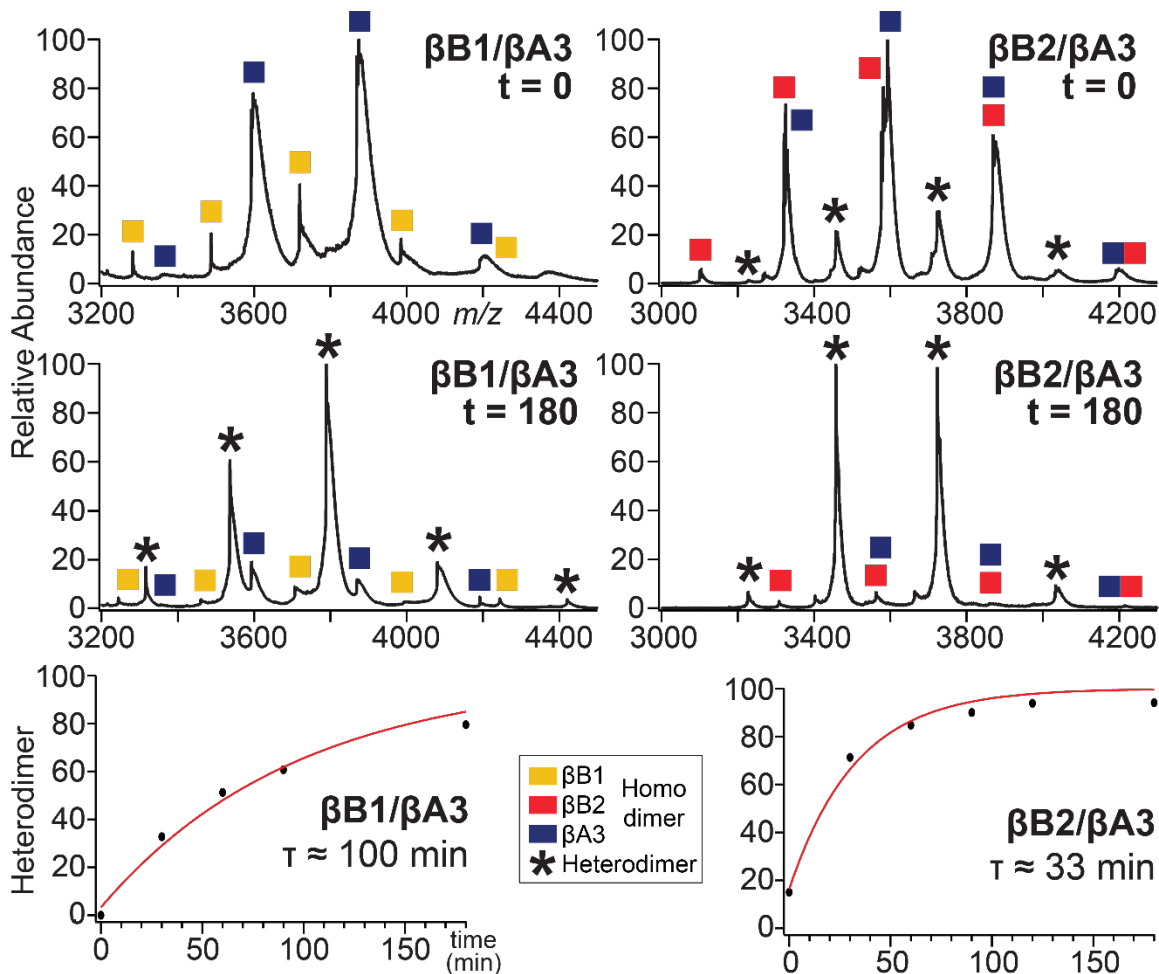


Figure 43. Native mass spectra of equimolar mixtures of β -crystallin β A3 with either β B1 (left) or β B2 (right) acquired to investigate the formation kinetics of heterodimers. The native mass spectra shown in the top row were acquired for a small aliquot removed immediately upon mixing the sample ($t = 0$ min), while the middle row shows the native mass spectrum for the same samples after 3 hours ($t = 180$ min). Peaks corresponding to homo- and heterodimers are labeled according to the legend. Plots in the bottom row illustrate differences in the formation of β B1/ β A3 and β B2/ β A3 heterodimers. The proportion of the total detected dimer abundance corresponding to the heterodimer is plotted as a function of time. Approximation by pseudo-first-order kinetics produces exponential fits with inverse rate constants (τ) labeled on each plot.

For both mixtures, the heterodimer is detected at an abundance greater than that of the homodimer by the end of the time course, consistent with previous reports of preferential heterodimer formation. Plotting the proportion of heterodimer as a function of time illustrates a clear difference in the rates at which these two different heterodimers form. While the fraction of $\beta\text{B1}/\beta\text{A3}$ heterodimers grows slowly, only reaching equivalent detected abundance with the homodimers after almost an hour, $\beta\text{B2}/\beta\text{A3}$ heterodimers rapidly form and dominate the population of dimers (**Figure 43**).

We determined the rate constant for the formation of each species of heterodimer with approximation by pseudo-first-order kinetics. These exponential fits revealed that $\beta\text{B2}/\beta\text{A3}$ heterodimers form ~ 3 times as fast as $\beta\text{B1}/\beta\text{A3}$ heterodimers, with inverse rate constants of ~ 33 min and ~ 100 min, respectively. (More accurate treatment with second-order kinetics requires precise determination of initial dimer and monomer populations, which is very challenging due to potentially different ionization efficiencies of these species. In any case, these observed difference in formation kinetics should be qualitatively robust.)

These results support models whereby crystallins preferentially form heterodimers over homodimers, with almost the entire detected dimer ion population in each mixture corresponding to heterodimers at the end of the time course.^{919,958} The above observation that βB1 was predominantly monomeric at a protein concentration of $11.5 \mu\text{M}$ with a homodimer population low in abundance is an interesting contrast with results from these heterodimer kinetics experiments which were also conducted at a total protein concentration of $11.5 \mu\text{M}$, with the concentration of βB1 being half this after mixing with equimolar βA3 . Although there are differences to consider with respect to incubation

time and temperature between the two sets of experiments, these results appear to indicate that β B1 has a greater tendency to oligomerize when in the presence of another crystallin isoform than on its own. This suggests that a possible functional explanation for (or perhaps result of) the extensive diversity of crystallin proteins found in the eye lens is to increase the propensity of dimer/oligomer formation, necessary to form tightly-packed, stable structures in the eye lens critical for lens transparency, protection against UV light, and other processes.^{919,932,934}

3.3. β -Crystallin Oligomeric Complexes Adopt Compact Topologies

The above experiments have highlighted the advantage of the high mass accuracy and sensitivity in native MS to uncover the oligomeric states and subunit compositions of crystallin complexes. Given that a crucial aspect of the biology of crystallin proteins is the concentration gradient they establish across the eye lens, reaching very high concentrations at the center of the lens, it is important to also characterize the structure of crystallin complexes. Native mass spectrometers equipped with ion mobility cells thus offer additional advantages for study of these polydisperse proteins, enabling accurate mass determination and structural information within the same instrument.

In addition to unambiguous determination of mass and stoichiometry obtained with native mass spectrometry, online ion mobility spectrometry measurements provide further information on ion size/shape through measurement of collision cross-section (CCS). Comparison of experimental CCS to those computed for condensed-phase structure coordinate files can be used to confirm or exclude conformations or topologies. We previously developed and validated a force field molecular dynamics simulation protocol that reliably produces structures with computed CCSs within $0\pm 4\%$ of

experiment for a wide range of native-like protein/protein complex masses and native charge state distributions.^{215,223} To provide new insight into the possible conformations adopted by these β -crystallin oligomeric complexes, we generated model structures with various topologies in PyMol to simulate with this protocol and then compare to experimental CCS measurements. Although crystal structures have not been solved for all isoforms, it is reasonable to expect a high degree of similarity, thus we used an X-ray crystal structure of β -crystallin β B2 (PDB ID 1YTQ) as a template for all model structures (**Figure 44**).

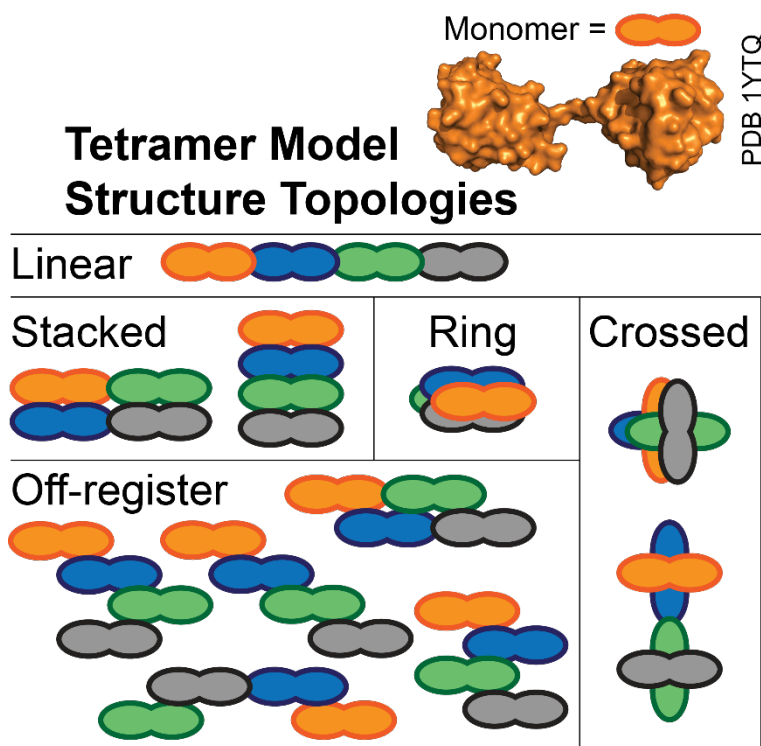


Figure 44. Example illustrations of the various topologies of model structures for comparison with experimental ion mobility data, divided into categories. X-ray crystal structure of β -crystallin β B2 monomer (PDB ID: 1YTQ) is shown in surface representation in orange in the top right. Examples of model structure categories with various subunit arrangements are shown for tetramers.

Comparison of the computed CCSs of these structures after MD simulation with experimental values for β -crystallin species supports very compact topologies for these

complexes (**Figure 45**). It is clear that β -crystallin complexes do not resemble the most extended of these model subunit arrangements (“linear”), which have CCSs $\geq 30\%$ larger than experimental measurements for all oligomers larger than dimers. The same is true of other topologies with smaller interfaces between subunits (e.g., those in the “off-register” category). By contrast, for each oligomeric state, there are a few model structures with computed CCSs that are well within the established range of accuracy and precision ($0\pm 4\%$) highlighted in green in **Figure 45**. Each of these falls into either the “crossed” or “ring” categories, both of which are used to describe structures with significant contact and overlap between subunits and thus are physically the smallest structures. While we cannot use these data to determine exactly the arrangement of subunits in the β -crystallin complexes detected with native mass spectrometry, these results strongly support compact topologies instead of linear, “stacked”, and off-register topologies.

This is in agreement with expectations given that a very high number of crystallin proteins must fit within the spatial constraints at the center of the eye lens to achieve the high concentrations found there. Some reports in the literature indicate that heterodimers can be more compact than their respective homodimer counterparts.^{913,919,948} This would suggest an additional role of crystallin diversity in establishing the refractive gradient and maintaining transparency. In this view, not only would the existence of many different subunit types and isoforms help drive complex formation, as evidenced by preferential heterodimer formation, but also adopt more compact structures required to physically fit all the crystallin molecules necessary to achieve the ~ 400 - 500 mg/mL concentration at the center of the eye lens. While the CCSs of these small crystallin oligomers studied here are too close to one another to make this interpretation, it is not inconceivable that it

would be possible to distinguish between higher-order oligomers on the basis of their ion mobility data or in an ion mobility-mass spectrometer with lower experimental error.

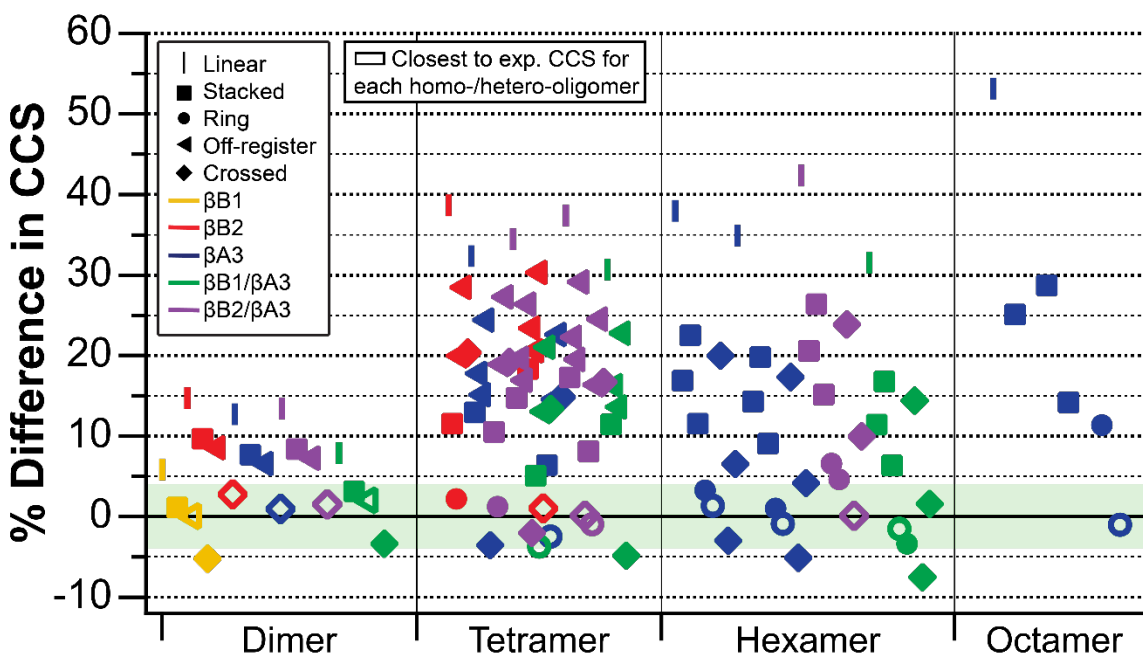


Figure 45. Comparison between experimental collision cross-section for each detected oligomeric species of β -crystallin proteins and those computed for simulated model structures of various topologies. Percent differences were calculated as (computed CCS – experimental CCS) / experimental CCS. The established range of accuracy and precision of the simulation protocol ($0 \pm 4\%$) is represented by a green bar. Colors and shapes of symbols correspond to model structure categories and protein species as shown in the legend. For each homo- or hetero-oligomer, the unfilled symbol corresponds to the model structure CCS closest to experiment.

4. Conclusions

Overall, the results reported here highlight powerful advantages offered by native IM-MS in accessing detailed information about biomolecular complexes which can be more challenging with other biophysical techniques. The accuracy and precision of mass measurements made here for these three β -crystallin isoforms revealed the distribution of homo- and hetero-oligomeric complexes formed, including unambiguous identification of their stoichiometries despite the subunits being very similar in mass. In addition to the structural information that can be obtained with ion mobility, the use of native IM-MS to

investigate kinetics of complex formation represents an exciting addition the structural biologists' toolkit.

These native IM-MS results underscore the importance of the dimer in crystallin structure and function. Formation of oligomeric complexes proceeds via addition of dimer subunits in a concentration-dependent manner, and these adopt very compact topologies. While all three were capable of homodimerization to varying extents at the low μM to nM concentration range tested here, although βB1 was primarily monomeric, dimer formation was elevated when two isoforms were present due to preferential heterodimerization. In the case of βA3 , at higher concentrations, a significant portion was no longer a dimer but instead a tetramer. This matches what is found in the isolated β -high molecular weight fractions from lens homogenates. We interpret these findings together to suggest that the diversity of the crystallin family of proteins plays a critical role in increasing dimerization via heterodimers, with the dimer subunit being the key building block with which to assemble larger oligomers and that this subunit exchange occurs rapidly in solution.

This study of wildtype crystallin isoforms establishes a baseline understanding of the details of complexes they form in normal, healthy functioning of the human eye lens. Having demonstrated the utility of native IM-MS in providing novel insight into the nature of these protein complexes, future efforts will focus investigation on modified and truncated crystallin variants believed to have a role in disruption of wildtype behavior and interactions resulting in aggregation and disease. For example, accumulation of deamidations has been shown to disrupt dimerization, leading to aggregation without significant rearrangement of the structure.⁹²² With the advantages of native IM-MS,

examining changes to features uncovered here for deamidated crystallin mutants would provide a path forward for understanding how and why modifications to crystallins accumulated during aging cause aggregation. This information could lead to development of better therapeutic remedies against aggregation not just of cataracts but of many other long-lived proteins implicated in disease.

CHAPTER VII

OUTLOOK

Native ion mobility-mass spectrometry has seen rapid growth as a tool in structural biology in the relatively short history of this field. This technique offers many advantages for the study of heterogeneous, challenging biomolecular samples, with its high mass accuracy and sensitivity allowing unambiguous determination of the composition and stoichiometry of large complexes, as well as benefits in sample and time requirements. For many types of samples, native MS can be used to uncover details relevant to structure and function that are very challenging to access with other traditional biophysical and structural techniques. Innovation in instrumentation, experimental design, and data analysis tools and strategies continually push the boundaries of what can be studied with this powerful technique. The work described in this dissertation serves to highlight the possibilities of native IM-MS but also to underscore the importance of detailed investigation into fundamental aspects of this method.

As was the common theme of Chapters II and III, the current most pressing issue that could slow the growth of native IM-MS in the study of biomolecules is not acquisition of high-quality data for complex samples but rather our ability to interpret the data, both in the mass spectral domain and from ion mobility. In Chapter II, the focus was on the problem of heterogeneity in this field, which can lead to incredibly complicated, congested mass spectra from which no useful information can be gleaned. The state-of-the-art computational, instrumental, and experimental strategies covered in this chapter are necessary in the study of heterogeneous, challenging biomolecules, especially as

more evidence accumulates that the sources of heterogeneity—e.g., lipids, small molecules, co-existence of multiple conformations and stoichiometries—are essential to biological relevance. As instrument design continues to improve and the technique is applied to ever-increasingly complex samples, researchers must be trained in not just the use of these tools but also the principles behind them to interpret results correctly and avoid potential artifacts.

In Chapter III, I introduced a similar drawback within this field—our ability to interpret the structural information contained in ion mobility data. This requires investigation into features of gas-phase protein behavior to establish a solid framework of knowledge from which to draw conclusions about structure from native IM-MS data. In addition to reviewing the state-of-the-art computational efforts related to this problem, the comparison of multiple molecular dynamics force fields for use in native IM-MS solves a significant problem with our ability to interpret ion mobility data. The validation of the simulation protocol from this study to establish its accuracy and precision for a large set of proteins is a necessary first step to making comparisons between gas-phase experimental measurements to calculations done for condensed-phase structures quantitative and more meaningful.

Identifying robust features of gas-phase protein ion compaction shared among these force fields, all of which were optimized differently for small molecules, allowed subsequent investigation into the relationship between charge and structure in Chapter IV. For interpretations of structure and differences in gas-phase behavior, better understanding of the effects of charge state is required. Some of the findings in this chapter serve to caution researchers in taking the ion species with the smallest collision

cross-section to be the most “native-like.” This is representative of a broader theme contained within the chapters of this dissertation, namely that more detailed investigation and understanding of fundamental aspects of native IM-MS are needed in order to best inform researchers in their interpretations of this data. In Chapter V, characterization of the complexes formed by the α -pore-forming toxin Cytolysin A in different detergents leads to a more focused investigation of the different activation conditions commonly employed in these kinds of studies. Accumulating evidence underscores the possibility of unintended effects to structural features, stemming from choice of detergent/lipid environment and instrumental parameters and conditions used to generate well-resolved, interpretable native IM-MS spectra of membrane proteins and other heterogeneous biomolecules.

Application of native IM-MS to characterize the oligomeric assemblies of membrane proteins in Chapter V and of crystallin isoforms in Chapter VI highlight the rich information that can be obtained with this technique and of the additional structural detail possible when ion mobility data comparisons are made quantitative. Native IM-MS is able to fill in crucial details not accessible by other methods, such as identifying the exact subunit compositions of these protein complexes relevant to human health. The complementarity of the information provided by native IM-MS with that from more traditional biophysical techniques has positioned this technique well for continued use in investigating biological questions.

APPENDIX

SUPPLEMENTAL INFORMATION FOR CHAPTER IV

1. Extended Methods

1.1. Analysis of Structural Features

A complete list of structural features analyzed is shown in **Table S6**. Features of structure coordinate files were analyzed with the molecular visualization program PyMOL unless otherwise noted. Root mean square deviation (RMSD) in atomic structure was calculated for simulated structures relative to the original, unsimulated coordinate file. Polar contacts involving side chains were visualized using the corresponding built-in feature in PyMOL. Hydrogen bonds were identified using a command to find pairs of hydrogen bond donors and acceptors within a cut-off distance of 3.5 Å and angle of 30°. Salt bridges were identified using the same Python command for pairs of oxygen atoms (from acidic residue side chains or the C-terminal residue in a chain) and nitrogen atoms (from basic residue side chains or the N-terminal residue in a chain) within a cut-off distance of 3.0 Å. HB_{\max} and SB_{\max} , the maximum number of possible hydrogen bonds and salt bridges, respectively, were calculated using previously-reported methods and based on amino acid composition.⁷⁷² Numbers of residues with either α -helical or β -sheet secondary structure were determined based on PyMOL's criteria for proper geometries. Swiss-PdbViewer was used to select all residues with 30% or greater solvent accessibility, referred to as "surface residues". The remaining set of residues are referred to as "interior residues". To assess compaction of residues not located at the surface, CCSs of structure "interiors" were computed for each protein using the set of residues

identified as interior for the original, unsimulated structure. Similarly, comparisons between unsimulated and simulated structures involving surface residues are based on the set of surface residues identified for the unsimulated structure. “Interior” CCS calculations were done using the Trajectory Method in Collidoscope with one charge placed at the center of mass.²¹⁴

Percent difference in CCS was computed as $[(\text{simulated CCS}) - (\text{experimental CCS})] / (\text{experimental CCS}) * 100\%$. Compaction was calculated as $[(\text{simulated CCS}) - (\text{unsimulated CCS})] / (\text{unsimulated CCS}) * 100\%$. All features reported as a percent change between unsimulated and simulated structures were likewise calculated in this manner, except secondary structure. Percent change in secondary structure content was instead defined relative to the total number of residues to avoid instances of division by zero.

Total volume, void volume, van der Waals volume, and packing density were computed with ProteinVolume for each simulated structure coordinate file using default values for volume probe radius (starting size 0.08 Å, ending probe size 0.02 Å) and minimum distance between surface probes (0.1 Å).⁷⁸⁹ Packing density is calculated as the ratio of the van der Waals volume to the total volume.

1.2. Principal Component Analyses of Structural Features

Seven structural features were selected for inclusion in principal component analyses, with one from each major category (listed in **Table S6**) and all expressed as percent changes to normalize each to the particular features of each starting condensed-phase structure (see **Table S6**). These percent changes between simulated and condensed-phase structures were for: hydrogen bonds, surface hydrogen bonds, surface residues,

polar contacts, salt bridges, and secondary structure content (both α -helical and β -strand, separately). PCAs were performed in Python with scikit-learn. Data for each feature were standardized prior to PCA by subtracting the mean and scaling to unit variance. Seven separate PCAs were performed: one with data from simulated charge conformers of β -lactoglobulin, concanavalin A, and glutamate dehydrogenase (using averages for each native charge state); one with an aggregate dataset containing structural features for each of the 17 native-like IM-MS calibrant protein ions^{201,203} simulated with the same central/most-abundant native charge state with each of 5 force fields (for a total of 85 observations),²¹⁵ and for the structural features of each of the 17 native-like IM-MS calibrant protein ions simulated with each force field separately (for a total of 5 separate PCAs).

1.3. Relationship Between CCS and Charge from First Principles

For approximately spherical ions of fixed density, volume (V) and density (ρ) can be written as follows, where R is the radius of the ion and N_A is Avogadro's number:

$$V = \frac{4}{3}\pi * R^3 \quad \text{Eq. 1}$$

$$\rho = \frac{mass}{N_A * V} \quad \text{Eq. 2}$$

where the molar mass of the ion is used.

The radius of the ion (R) depends, in principle, on the average collision cross-section (Ω_{avg}) and radius of the gas (r_{gas}):

$$R = \sqrt{\frac{\Omega_{avg}}{\pi}} - r_{gas} \quad \text{Eq. 3}$$

Combining equations 1 and 2 yields:

$$\rho * N_A * 4 * \pi * R^3 = 3 * mass \quad \text{Eq. 4}$$

Substituting equation 3 into equation 4:

$$\rho * N_A * 4 * \pi * \left(\sqrt{\frac{\Omega}{\pi}} - r_{gas} \right)^3 = 3 * mass \quad \text{Eq. 5}$$

where r_{gas} is very small relative to R .

This can be simplified to the following relationship between CCS and mass:

$$\Omega \propto mass^{2/3} \quad \text{Eq. 6}$$

According to the Rayleigh limit for charged droplet fission, charge (Z_R) depends on elementary charge (e), surface tension of the solvent (γ), relative permittivity (ϵ_0), and the radius (R):

$$Z_R = 8 * \pi * e * \sqrt{\gamma * \epsilon_0 * R^3} \quad \text{Eq. 7}$$

Combining equations 7 and 4 yields:

$$Z_R = 8 * \pi * e * \left(\gamma * \epsilon_0 * \frac{3 * mass}{\rho * N_A * 4 * \pi} \right)^{\frac{1}{2}} \quad \text{Eq. 8}$$

This can be simplified to the following relationship between charge and mass:

$$Z_R \propto mass^{1/2} \quad \text{Eq. 9}$$

Taking the expected scaling of mass with CCS and charge (equations 6 and 9) produces a $Z^{4/3}$ power law:

$$\Omega \propto Z^{4/3} \quad \text{Eq. 10}$$

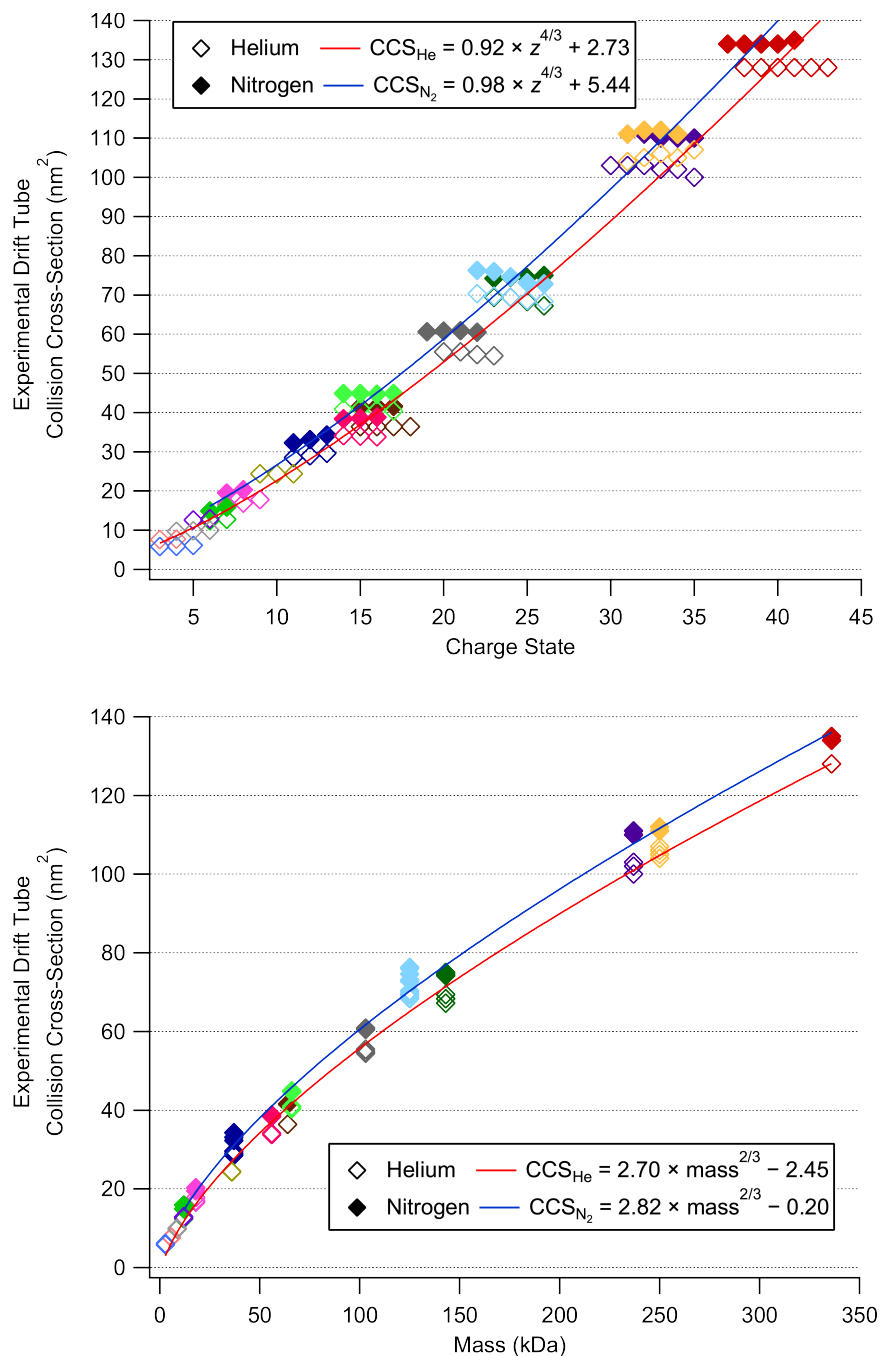


Figure S1. Plots of experimental drift tube collision cross-sections^{201,203} of 17 native-like proteins against charge state (top) and mass (bottom). CCS data is fit to a 4/3-power law with respect to charge (top) and to a 2/3-power law with respect to mass (bottom). Colors represent different protein species. Data and fits for CCSs measured in helium or nitrogen buffer gas represented as indicated in legend.

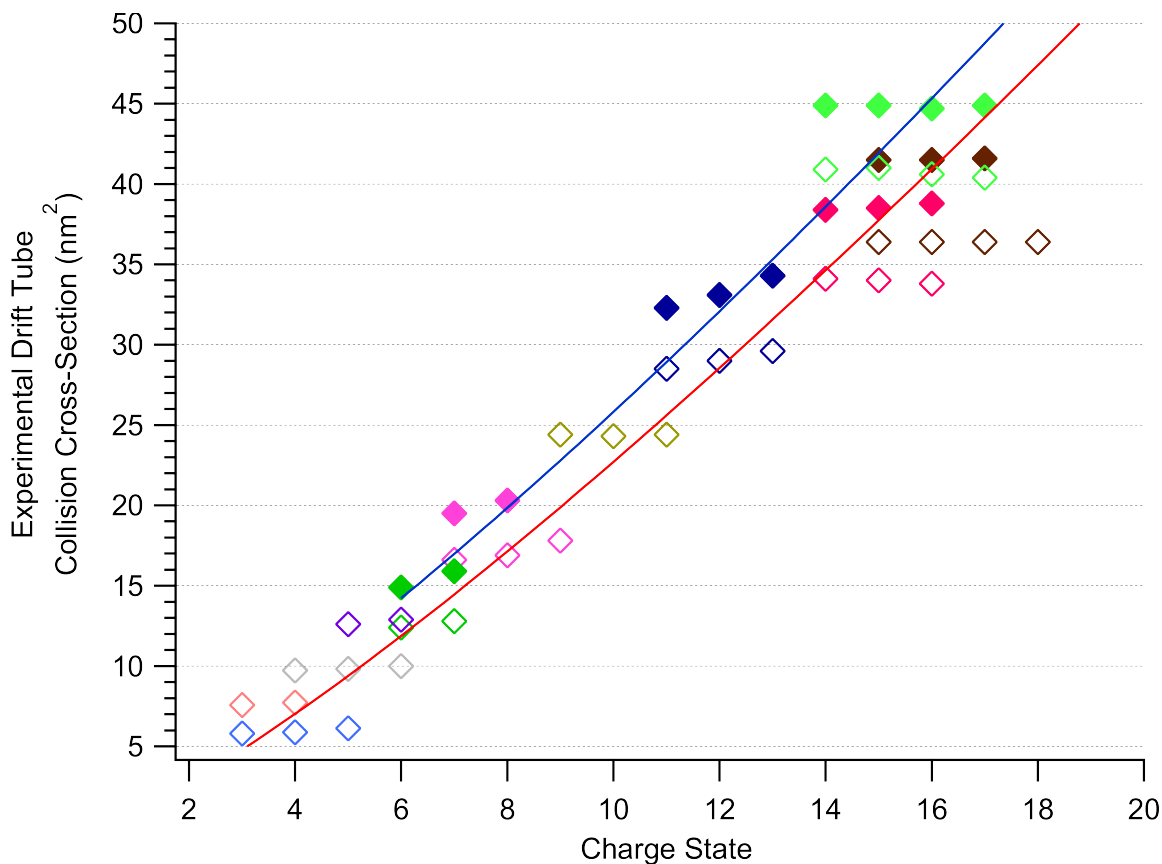
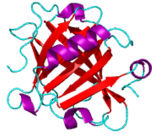
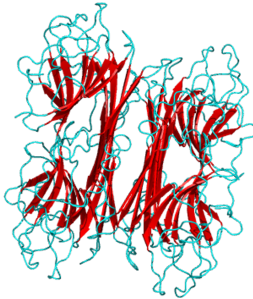


Figure S2. Plot of experimental drift tube collision cross-section^{201,203} against charge state. Zoomed-in version of left panel of Figure 1 in main text to show trends for smaller proteins more clearly. Different protein species represented by different colors. Open and filled symbols correspond to measurements made in helium and nitrogen buffer gas, respectively. Trendlines shown are the same as in Figure 1.

β -lactoglobulin (BLG)
18 kDa monomer, 7-9+
PDB ID: 3BLG



concanavalin A (ConA)
103 kDa tetramer, 19-23+
PDB ID: 3CNA



glutamate dehydrogenase (GDH)
336 kDa hexamer, 37-43+
PDB ID: 3JCZ

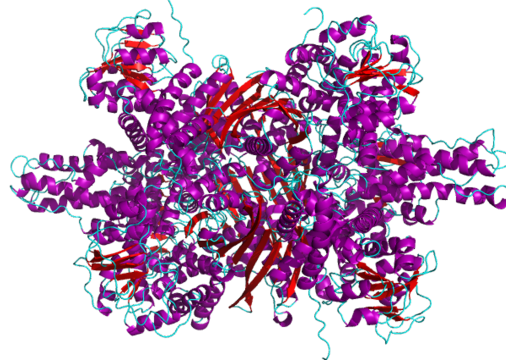


Figure S3. Condensed-phase structures of β -lactoglobulin, concanavalin A, and glutamate dehydrogenase used in simulations of charge conformers, shown to scale. Protein identity, mass, oligomeric state, charge states, and PDB identifier indicated above each structure. Structures are colored according to secondary structure to illustrate differences: helix (purple), strand (red), coil/loop (cyan).

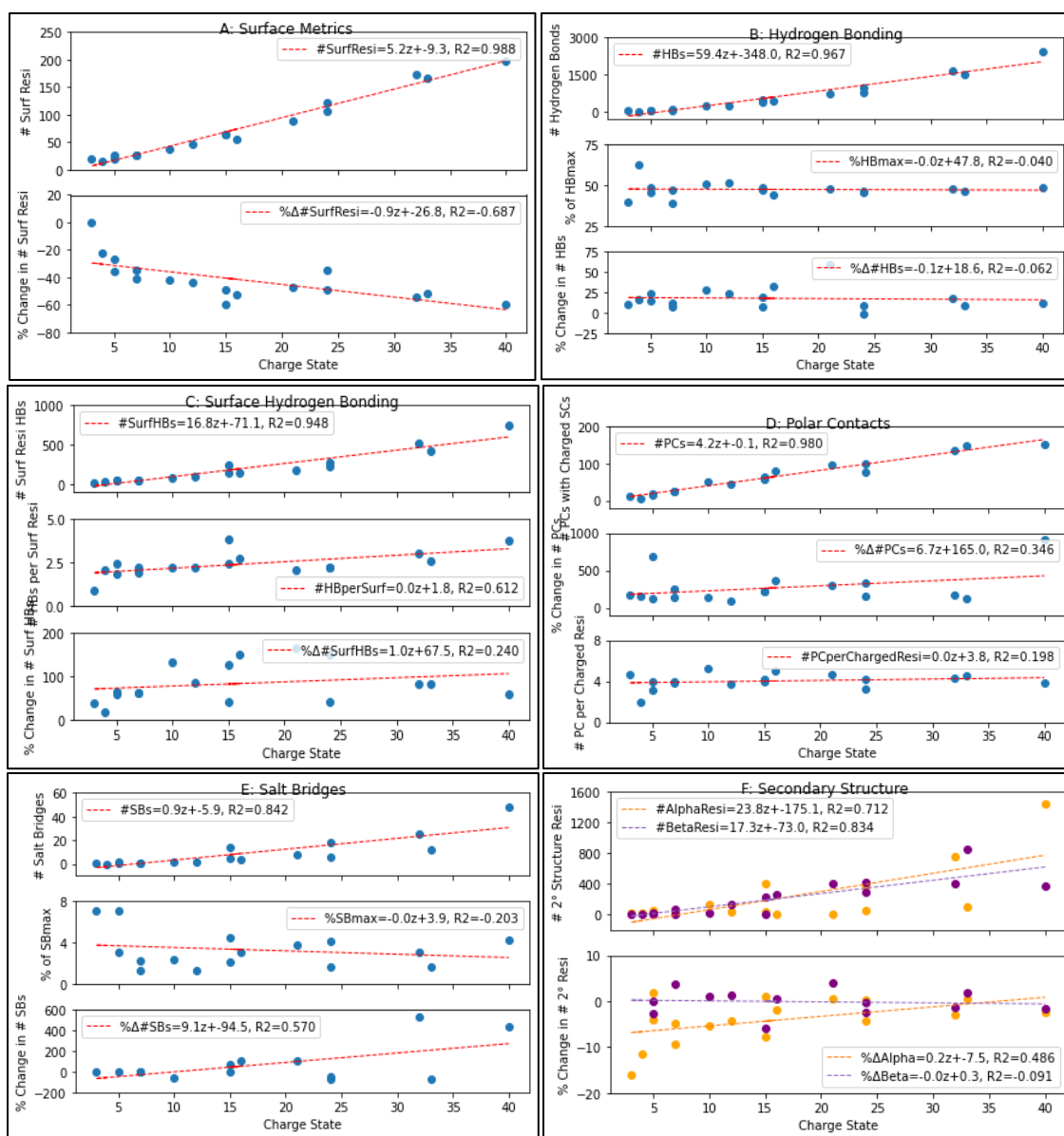


Figure S4. Linear regression plots for structural features for set of 17 IM-MS calibrant protein simulated structures²¹⁵ against charge state. Each datapoint corresponds to a different protein. Each legend indicates linear trendlines with corresponding R^2 value and any relevant color representation. Structural features are grouped by category, as in Table S6: (A) surface, (B) hydrogen bonding, (C) surface hydrogen bonding, (D) polar contacts, (E) salt bridges, and (F) secondary structure.

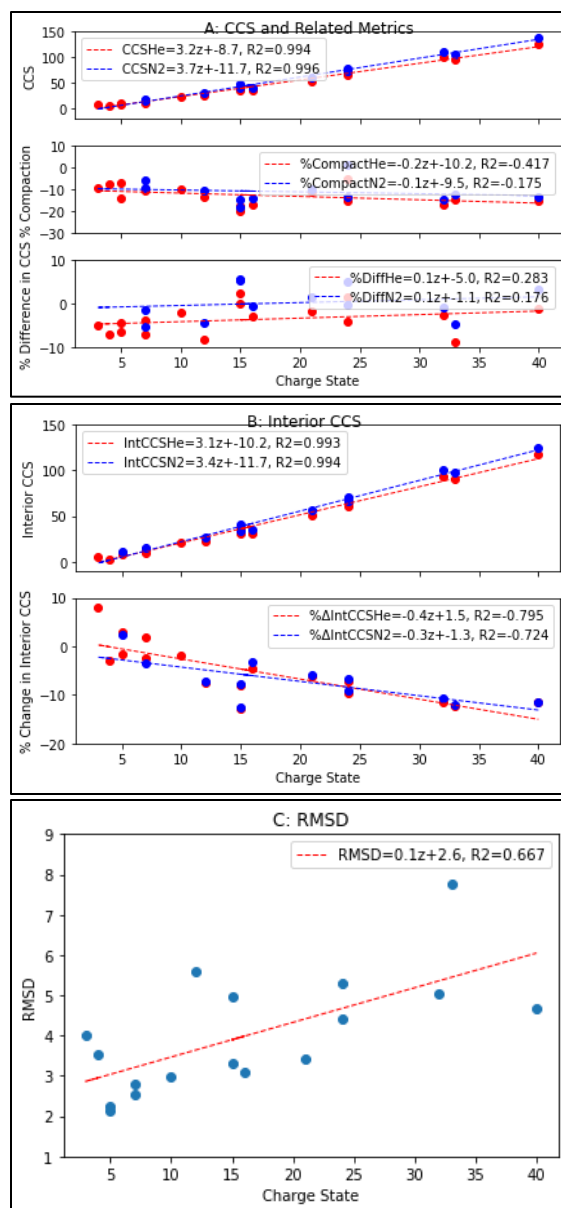


Figure S5. Linear regression plots for features related to size for set of 17 IM-MS calibrant protein simulated structures²¹⁵ against charge state. Each datapoint corresponds to a different protein. Each legend indicates linear trendlines with corresponding R^2 value and any relevant color representation. Structural features are grouped by category, as in Table S6: (A) CCS, (B) interior, and (C) RMSD.

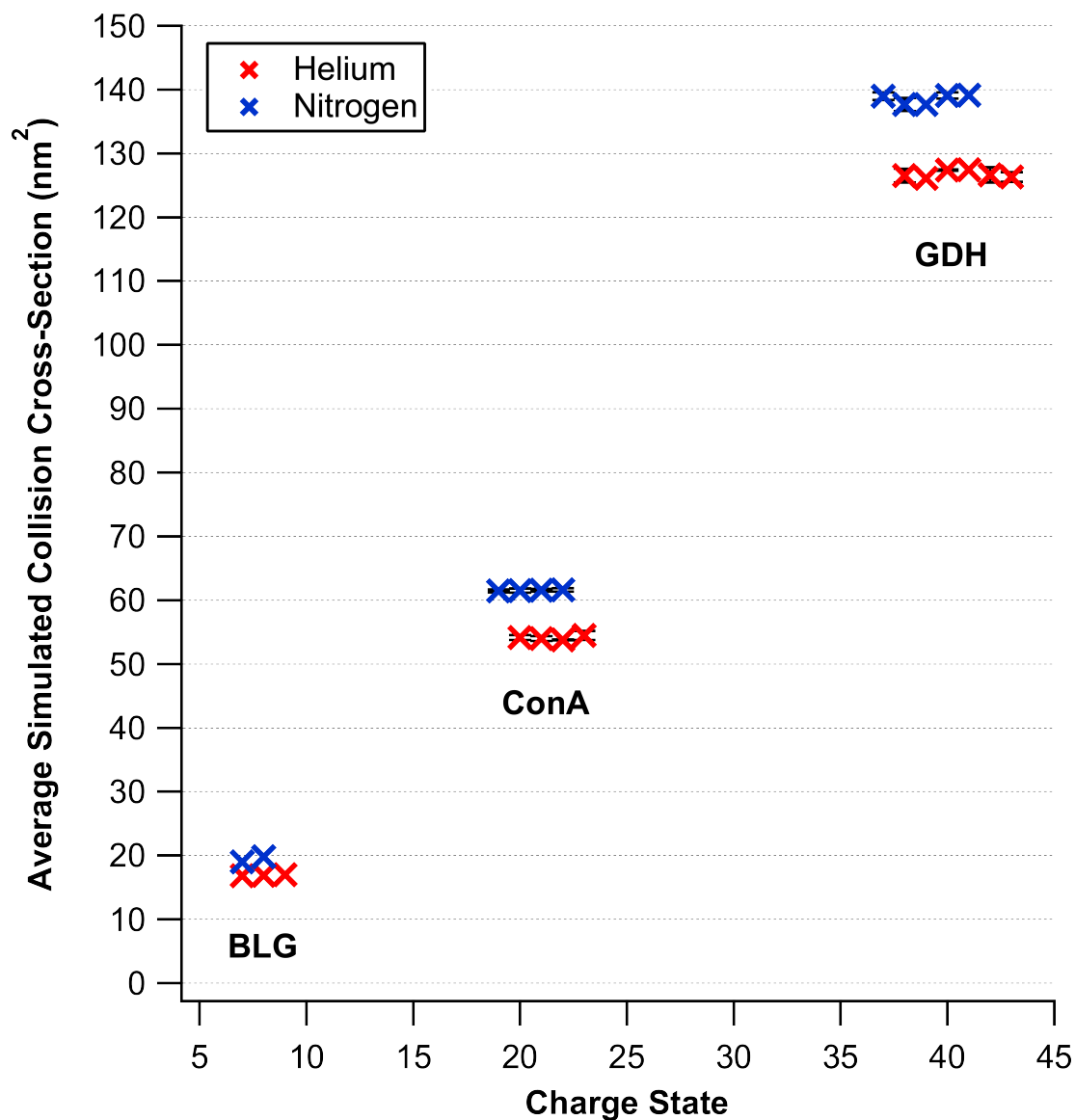


Figure S6. Plot of collision cross-sections computed for simulated charge conformers of β -lactoglobulin, concanavalin A, and glutamate dehydrogenase. Datapoints represent the average for each charge state. Black error bars underneath represent 1 standard deviation. Helium and nitrogen buffer gas represented by red and blue, respectively.

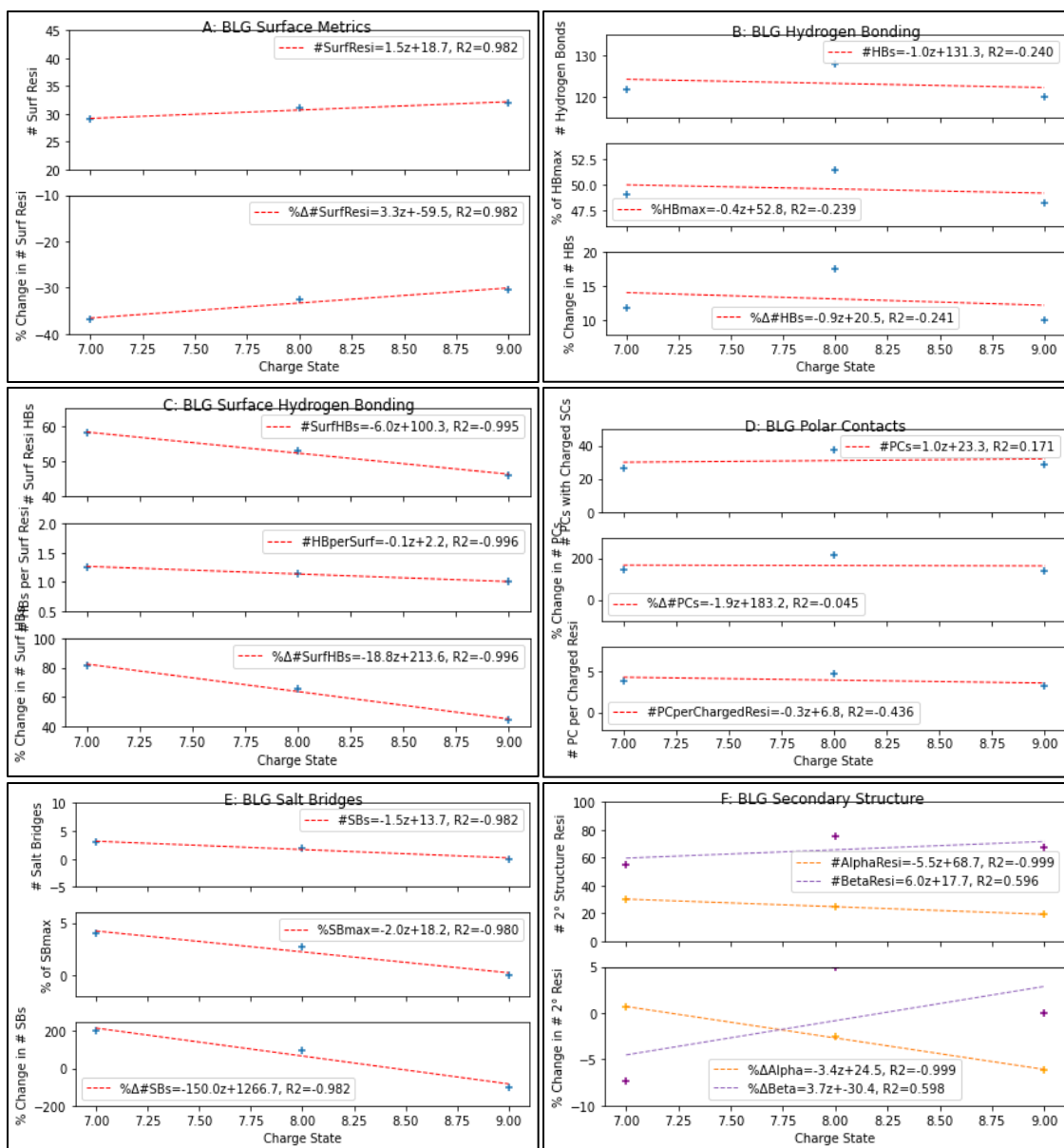


Figure S7. Linear regression plots for structural features for β -lactoglobulin simulated structures against charge state. Each legend indicates linear trendlines with corresponding R^2 value and any relevant color representation. Structural features are grouped by category, as in Table S6: (A) surface, (B) hydrogen bonding, (C) surface hydrogen bonding, (D) polar contacts, (E) salt bridges, and (F) secondary structure.

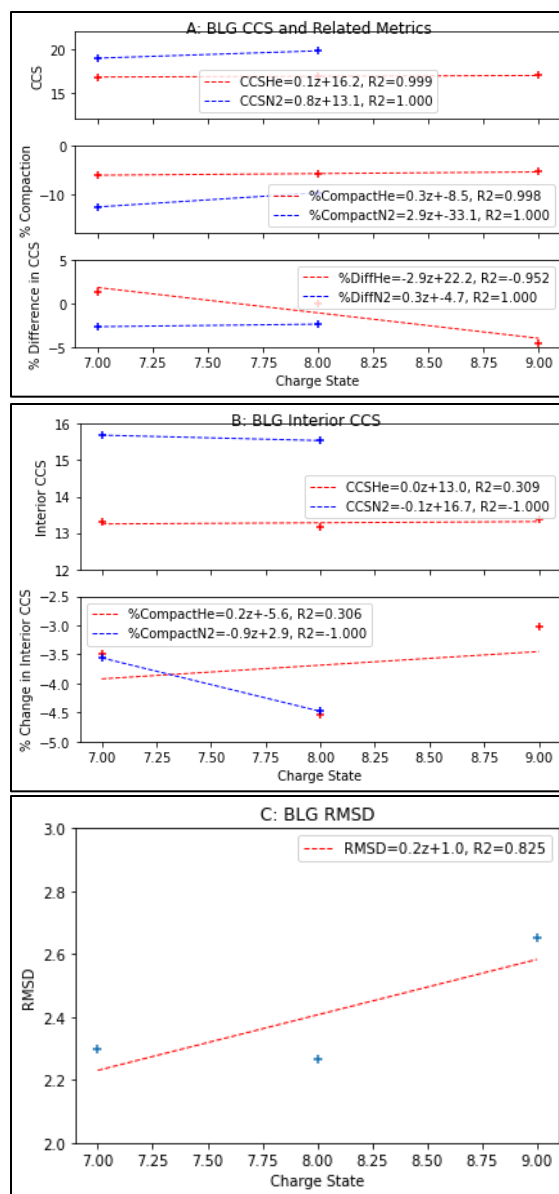


Figure S8. Linear regression plots for features related to size for β -lactoglobulin simulated structures against charge state. Each legend indicates linear trendlines with corresponding R^2 value and any relevant color representation. Structural features are grouped by category, as in Table S6: (A) CCS, (B) interior, and (C) RMSD.

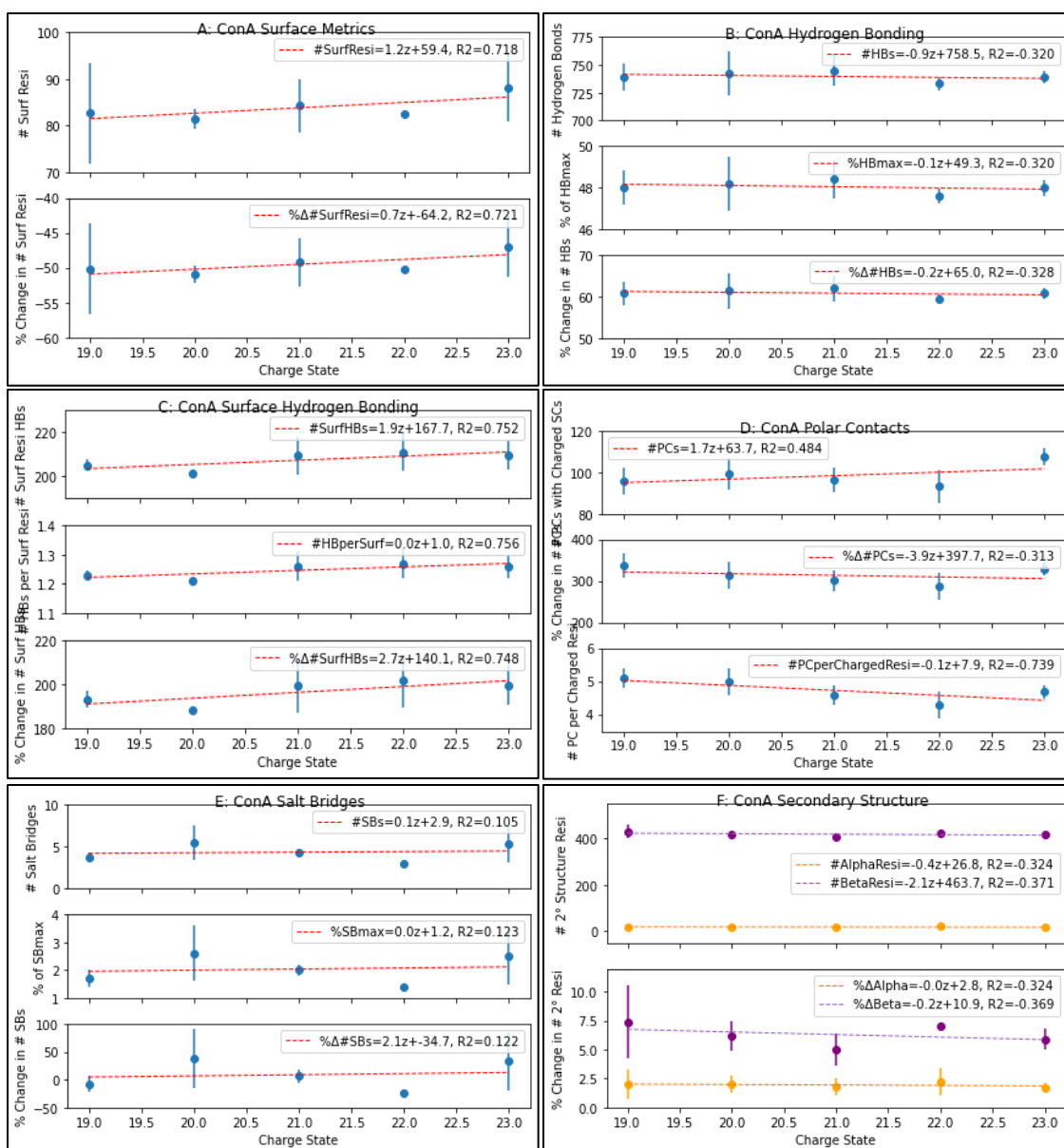


Figure S9. Linear regression plots for structural features for simulated charge conformers of concavalin A against charge state. Circles represent the average value for each charge state, and error bars represent 1 standard deviation. Each legend indicates linear trendlines with corresponding R^2 value and any relevant color representation. Structural features are grouped by category, as in Table S6: (A) surface, (B) hydrogen bonding, (C), surface hydrogen bonding, (D) polar contacts, (E) salt bridges, and (F) secondary structure.

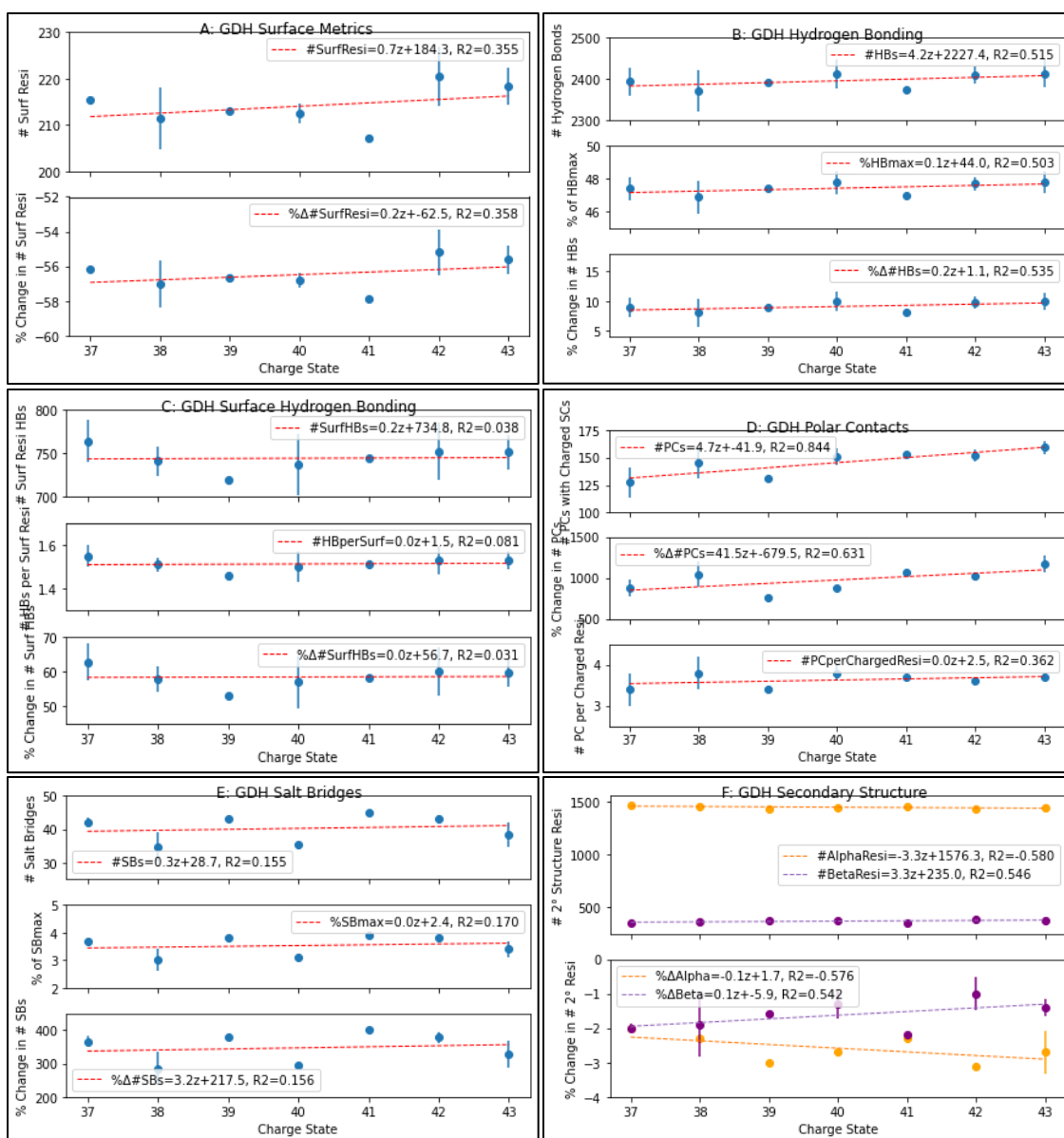


Figure S10. Linear regression plots for structural features for simulated charge conformers of glutamate dehydrogenase against charge state. Circles represent the average value for each charge state, and error bars represent 1 standard deviation. Each legend indicates linear trendlines with corresponding R^2 value and any relevant color representation. Structural features are grouped by category, as in Table S6: (A) surface, (B) hydrogen bonding, (C), surface hydrogen bonding, (D) polar contacts, (E) salt bridges, and (F) secondary structure.

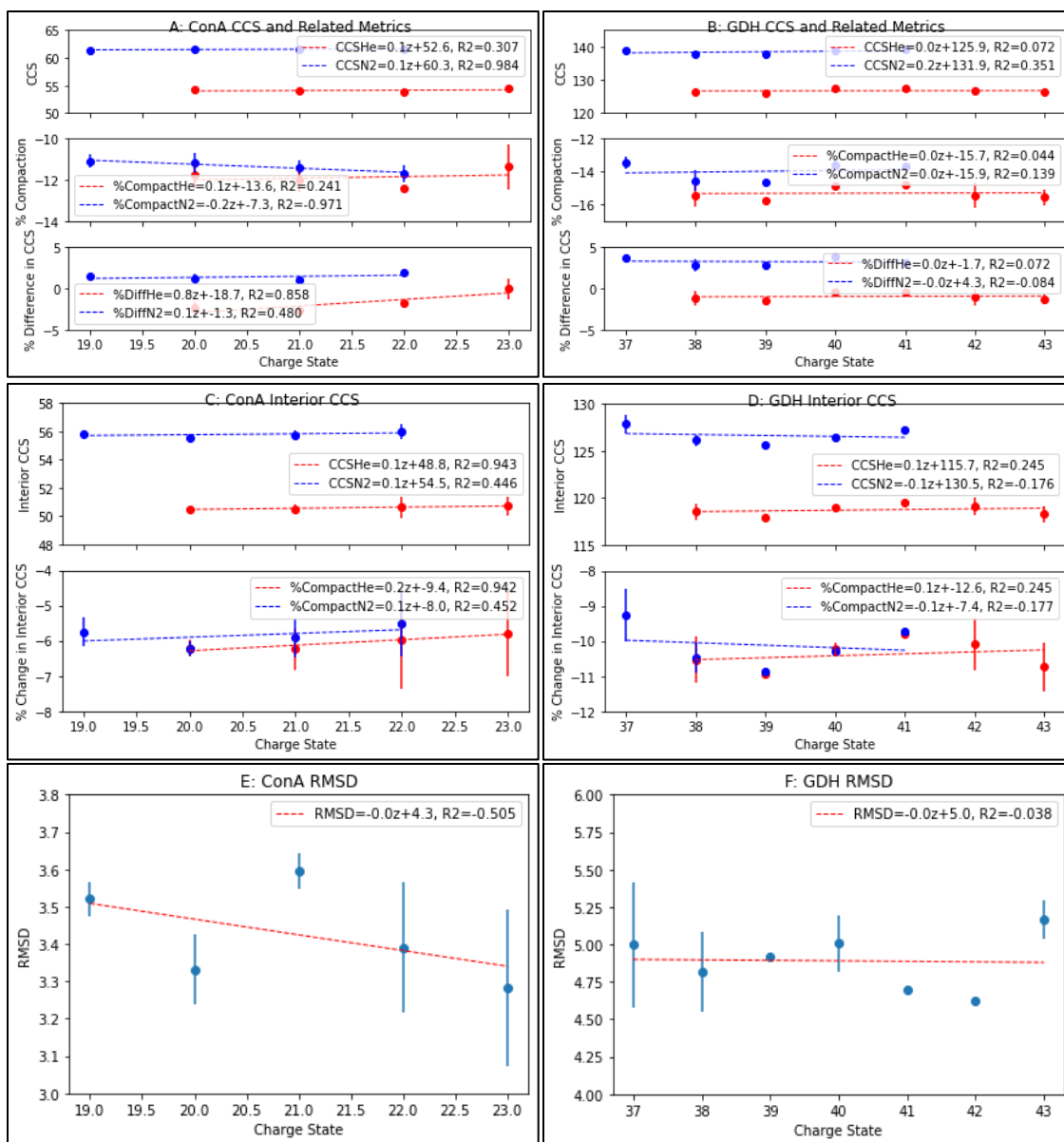


Figure S11. Linear regression plots for features related to size for simulated charge conformers of concanavalin A (A,C,E) and glutamate dehydrogenase (B,D,F) against charge state. Circles represent the average value for each charge state, and error bars represent 1 standard deviation. Each legend indicates linear trendlines with corresponding R^2 value and any relevant color representation. Structural features are grouped by category, as in Table S6: (A,B) CCS, (C,D) interior, and (E,F) RMSD.

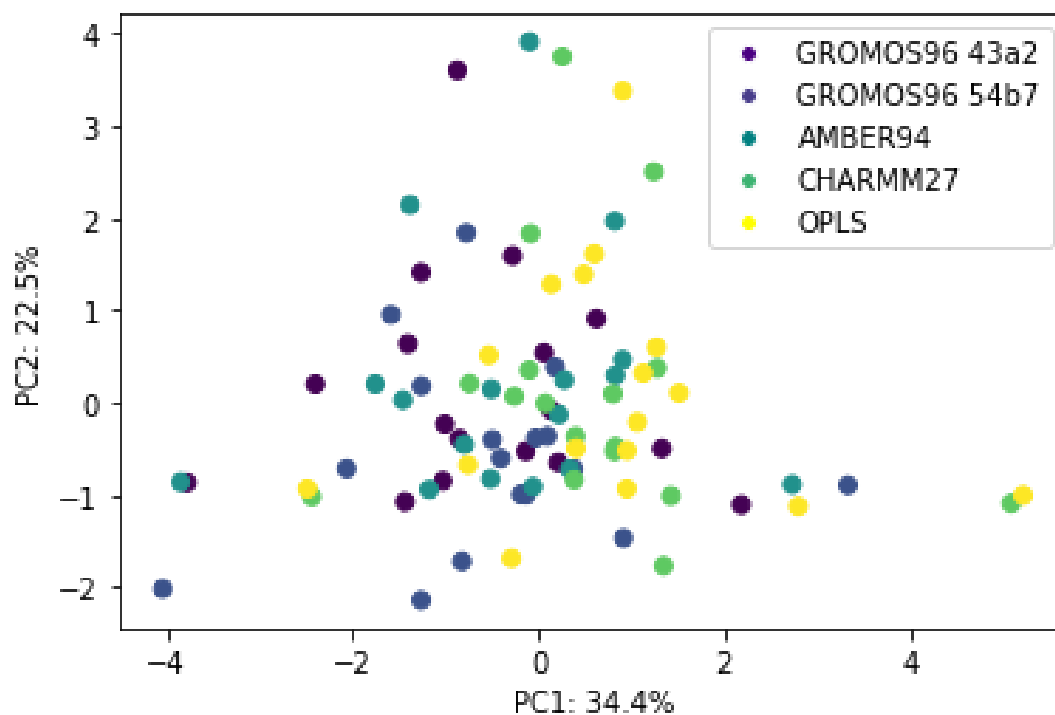


Figure S12. Aggregate dataset of 17 native-like IM-MS calibrant protein structures simulated with each of 5 force fields²¹⁵ recast along the first and second principal components. Principal component analysis was performed using 7 structural features (see main text, Table S6). Different colors represent structures simulated with different force fields as indicated in the legend.

Table S1. Set of 17 native-like protein IM-MS calibrants used. PDB ID and charge listed refer to those used for simulations in comparison of five force fields. Computed CCS for structure of each protein simulated with each force field shown.²¹⁵ Experimental CCS values can be found in references 201 and 203.

Protein	Mass (kDa)	PDB ID	Charge	GROMOS 96 43a2	GROMOS 96 54b7	AMBER 94	CHARMM 27	OPLS- AA/L
Collision Cross-Section (nm²) of Simulated Structure, Helium Buffer Gas (N = 17)								
melittin	2.8	2MLT	4	5.46372	5.6924	5.9308	5.8973	6.0653
insulin monomer	5.8	3E7Y	3	7.17816	7.8361	7.8991	8.1085	7.9332
ubiquitin	8.6	1UBQ	5	9.38348	9.7480	10.2729	10.6874	10.2718
insulin dimer	12	5BTS	5	11.7872	12.4790	12.5606	13.5957	12.4499
cytochrome c	12	1HRC	7	11.9043	12.2791	12.5234	12.6442	12.7413
β -lactoglobulin monomer	18	3BLG	7	15.9403	16.7038	17.1996	17.5373	17.6061
insulin hexamer	36	4EY9	10	23.7543	25.0160	25.3254	26.0380	25.8338
β -lactoglobulin dimer	37	1BSY	12	26.5718	28.1043	28.7246	30.0221	29.4932
transthyretin	56	1F41	15	34.7568	36.6754	38.6330	39.9923	38.2549
avidin	64	1AVE	16	35.2721	38.8205	38.3177	39.7234	39.1418
bovine serum albumin	66	4F5S	15	40.9374	44.0715	46.0574	46.8515	46.9623
concanavalin A	103	3CNA	21	54.5647	57.6440	57.5025	60.2895	59.7130
serum amyloid P pentamer	125	1SAC	24	66.4227	71.5942	73.1727	75.8189	73.0422
alcohol dehydrogenase	143	4W6Z	24	70.3632	74.0836	77.5249	79.9436	78.3593
pyruvate kinase	237	1F3W	32	100.113	106.7590	108.5900	113.0180	111.5760
serum amyloid P decamer	250	2A3W	33	96.6701	104.1660	106.9830	108.8680	106.4960
glutamate dehydrogenase	336	3JCZ	40	126.407	135.6320	139.0410	144.1080	140.3300
Collision Cross-Section (nm²) of Simulated Structure, Nitrogen Buffer Gas (N = 12)								
cytochrome c	12	1HRC	7	15.0375	15.4984	15.4378	15.5558	15.5691
β -lactoglobulin monomer	18	3BLG	7	19.2235	20.4830	20.2804	20.7366	21.0024
β -lactoglobulin dimer	37	1BSY	12	31.6442	33.4082	33.5079	34.8284	34.0663
transthyretin	56	1F41	15	40.6392	42.3945	43.9816	45.5135	43.6485
avidin	64	1AVE	16	41.2033	44.6065	43.5191	44.9723	44.5324
bovine serum albumin	66	4F5S	15	47.2238	50.5585	51.5917	52.3480	52.3746
concanavalin A	103	3CNA	21	61.8522	65.3986	64.3994	66.7328	66.6827
serum amyloid P pentamer	125	1SAC	24	74.4047	80.1278	80.3291	83.3871	80.6132
alcohol dehydrogenase	143	4W6Z	24	78.2537	82.4892	84.6393	87.0484	86.0058
pyruvate kinase	237	1F3W	32	109.971	116.7560	117.5470	122.1790	120.9210
serum amyloid P decamer	250	2A3W	33	106.578	113.6990	115.9900	117.7040	115.8170
glutamate dehydrogenase	336	3JCZ	40	138.083	147.4770	149.6270	154.9110	150.4350

Table S2. Comparison of performance of GROMOS96 43a2 and GROMOS96 54b7 in recapitulating experimental native protein ion compaction. Percent difference in CCS between simulated structure and to experimental drift tube measurement shown for both force fields. For each protein, the percent difference closest to zero (closest to experiment) is shaded in green. The thick line between data for β -lactoglobulin dimer and transthyretin represents the threshold in protein size above which GROMOS96 54b7 generally performs better and below which GROMOS96 43a2 performs better.

Protein	Mass (kDa)	Percent Difference in CCS Relative to Experiment	
		GROMOS96 43a2 ⁷⁷⁰	GROMOS96 54b7 ⁷⁷¹
melittin	2.8	-7.0796	-3.1905
insulin monomer	5.8	-5.1762	3.5147
ubiquitin	8.6	-4.5424	-0.8345
insulin dimer	12	-6.4508	-0.9603
cytochrome c	12	-6.9977	-4.0695
β -lactoglobulin monomer	18	-3.9741	0.6253
insulin hexamer	36	-2.2457	2.9465
β -lactoglobulin dimer	37	-8.3731	-3.0886
transthyretin	56	2.2259	7.8688
avidin	64	-3.0986	6.6497
bovine serum albumin	66	-0.1527	7.4915
concanavalin A	103	-1.6852	3.8631
serum amyloid P pentamer	125	-4.1519	3.3105
alcohol dehydrogenase	143	1.3879	6.7487
pyruvate kinase	237	-2.8029	3.6495
serum amyloid P decamer	250	-8.8018	-1.7302
glutamate dehydrogenase	336	-1.2445	5.9625

Table S3. Computed CCSs for each simulated charge conformer. Percent difference in CCS is relative to the experimental drift tube CCS value.^{201,203} Bolded CCS values indicate average \pm standard deviation for all charge conformers of each protein, with percent deviation below this in parentheses. Bolded percent difference in CCS values indicate average over all charge conformers of each protein. Blacked-out cells indicate that experimental CCS values are not reported for that charge state in that buffer gas. Values for β -lactoglobulin in helium correspond to structures simulated with GROMOS96 54b7, and all others are with GROMOS96 43a2.

Charge	Conformer ID	Helium Buffer Gas		Nitrogen Buffer Gas	
		CCS (nm ²)	% Diff. in CCS	CCS (nm ²)	% Diff. in CCS
β-lactoglobulin		16.90 \pm 0.09 (0.53%)	-1.10	19.4 \pm 0.6 (3.1%)	-2.53
7	A	16.8117	1.28	18.9774	-2.68
8	A	16.8960	-0.02	19.8149	-2.39
9	A	16.9908	-4.55		
concanavalin A		54.1 \pm 0.5 (0.9%)	-1.77	61.5 \pm 0.2 (0.4%)	1.31
19	A			61.2454	1.07
	B			61.6832	1.79
	E			61.3782	1.28
20	A	53.8862	-2.91	61.2890	0.80
	C	54.4500	-1.89	61.7384	1.54
21	A	53.7644	-3.13	61.2682	0.60
	B	54.3570	-2.06	61.5992	1.15
	D	54.2665	-2.22	61.8024	1.48
	E	53.6185	-3.39	61.4958	0.98
22	A	53.7395	-1.94	61.4230	1.53
	B	53.8223	-1.78	61.8270	2.19
23	A	53.7090	-1.45		
	B	55.0251	0.96		
	E	54.6853	0.34		
glutamate dehydrogenase		126.6 \pm 0.8 (0.6%)	-1.06	138.4 \pm 0.9 (0.7%)	3.22
37	A			139.406	4.03
	C			138.529	3.38
38	A	127.748	-0.20	138.816	3.59
	B	125.959	-1.59	136.919	2.18
	E	125.797	-1.72	137.249	2.42
39	A	126.080	-1.50	137.654	2.73
40	A	127.461	-0.42	138.718	3.52
	D	127.338	-0.52	139.414	4.04
41	A	127.419	-0.45	139.113	3.05
42	A	125.767	-1.74		
	E	127.465	-0.42		
43	A	125.331	-2.09		
	C	126.671	-1.04		
	D	127.048	-0.74		
	E	126.254	-1.36		

Table S4. Re-calculated CCSs at native charge state distribution extremes assuming identical structure. For each protein, the simulated charge conformer structure with the smallest and largest CCS in the original set of simulations is listed with its computed CCS. Re-calculated CCS values correspond to the CCS of each structure upon re-calculation with the lowest and highest charge states from each protein's native charge state distribution. Blue text indicates that re-calculated CCS is the same as originally calculated (due to the selected charge conformer structure already having either the lowest or highest charge state).

Helium Buffer Gas				Nitrogen Buffer Gas			
Original Charge & Conformer ID	Original Simulated CCS	Re-Calculated CCS		Original Charge & Conformer ID	Original Simulated CCS	Re-Calculated CCS	
		Lowest z	Highest z			Lowest z	Highest z
BLG		7+	9+	BLG		7+	8+
7+ A	16.8117	16.8117	16.8664	7+ A	18.9774	18.9774	19.2739
9+ A	16.9908	16.9337	16.9908	8+ A	19.8149	19.5455	19.8149
ConA		20+	23+	ConA		19+	22+
21+ E	53.6185	53.6191	53.7311	19+ A	61.2454	61.2454	61.7740
23+ B	55.0251	54.9091	55.0251	22+ B	61.8270	61.1220	61.8270
GDH		38+	43+	GDH		37+	41+
43+ A	125.331	125.316	125.331	38+ B	136.919	136.594	137.525
38+ A	127.748	127.748	128.024	40+ D	139.414	138.710	139.732

Table S5. CCSs computed for each simulated charge conformer structure with the Projection Approximation (PA) in IMoS,^{217,748,788} along with its corresponding percent difference in CCS (between the simulated and condensed-phase structure). Values for β -lactoglobulin in helium are from simulations with GROMOS96 54b7,⁷⁷¹ and all others are with GROMOS96 43a2.⁷⁷⁰ PA does not model ion-dipole or other electrostatic interactions related to ion charge state, so the resulting CCSs are “charge-ignorant.” Bolded CCSs listed for each protein correspond to the average computed PA CCS for all simulated charge conformers.

Charge State	Conformer ID	PA CCS in Helium	% Diff. in CCS	PA CCS in Nitrogen	% Diff. in CCS
β-lactoglobulin		14.2922		14.8014	
7	A	14.1611	-0.92	13.0767	-11.65
8	A	14.3231	0.22	13.3393	-9.88
9	A	14.4647	1.21		
concanavalin A		46.5008		47.5034	
19	A			42.4457	-10.65
	B			42.7983	-9.90
	E			42.6563	-10.20
20	A	41.4061	-10.96	42.2763	-11.00
	C	41.8991	-9.90	42.7977	-9.91
21	A	41.3825	-11.01	42.2588	-11.04
	B	41.6490	-10.43	42.5431	-10.44
	D	41.7158	-10.29	42.5985	-10.33
	E	41.2027	-11.39	42.0701	-11.44
22	A	42.1173	-9.43	43.0169	-9.44
	B	41.4143	-10.94	42.2830	-10.99
23	A	41.4159	-10.93		
	B	42.1173	-9.43		
	E	42.0740	-9.52		
glutamate dehydrogenase		114.5460		116.2093	
37	A			97.5290	-16.07
	C			96.6498	-16.83
38	A	95.2290	-16.86	96.6675	-16.82
	B	94.0871	-17.86	95.5187	-17.80
	E	94.1293	-17.82	95.5377	-17.79
39	A	94.3230	-17.65	95.7247	-17.63
40	A	95.5580	-16.58	96.9946	-16.53
	D	95.3357	-16.77	96.7813	-16.72
41	A	95.4275	-16.69	96.8820	-16.63
42	A	94.3846	-17.60		
	E	95.2169	-16.87		
43	A	93.9565	-17.97		
	C	95.2056	-16.88		
	D	95.2026	-16.89		
	E	94.5397	-17.47		

Table S6. List of structural features analyzed and details of how features were determined for structure coordinate files, grouped according to general category. Features marked with an asterisk indicate they were included in principal component analysis.

CCS	CCS: CCS computed with Trajectory Method in Collidoscope ²¹⁴ for structures with charges placed on residues identified in stable charge configurations
	Percent Compaction: Percent difference in CCS between simulated and condensed-phase structure
	Percent Difference: Percent difference in CCS between simulated structure and experiment
Surface	Number of Surface Residues: Number of residues with $\geq 30\%$ solvent accessibility, identified with Swiss-PdbViewer
	*Percent Change in Number of Surface Residues: Percent difference in number of surface residues between simulated and condensed-phase structure
Interior	Interior CCS: Calculated CCS of “interior” region (defined as set of residues not identified as surface in condensed-phase structure for each protein), with a default 1+ charge at center of mass in either buffer gas as appropriate
	Percent Change in Interior CCS: Percent difference in interior CCS (for same set of residues identified as “interior” in the condensed-phase structure for each protein)
Hydrogen Bonding	Number of Hydrogen Bonds: Identified in PyMOL as pairs of donors and acceptors within distance (3.5 Å) and geometry (30°) cut-offs used in ref. 772
	Percent of HBmax: Percent of hydrogen bonds out of maximum number possible (HBmax computed based on sequence of each protein using previously-reported method) ⁷⁷²
	*Percent Change in Number of Hydrogen Bonds: Percent difference between simulated and condensed-phase structure
Surface H-Bonding	Number of Surface Hydrogen Bonds: Identified in PyMOL same as hydrogen bonds above, but for set of residues identified as “surface” in condensed-phase structure
	Number of Hydrogen Bonds per Surface Residue: Total number of surface residue hydrogen bonds divided by total number of surface residues
	*Percent Change in Number of Surface Hydrogen Bonds: Percent difference between simulated and condensed-phase structure (for same set of residues identified as surface in condensed-phase structure)
Polar Contacts	Number of Polar Contacts Involving Charged Side Chains: Number of polar contacts involving side chains (determined with PyMOL built-in feature) of residues identified in stable charge configuration
	*Percent Change in Number of Polar Contacts: Percent difference in total number of polar contacts involving charged residue side chains between simulated and condensed-phase structure
	Number of Polar Contacts per Charged Residue: Total number of polar contacts involving charged residue side chains divided by charge state
Salt Bridges	Number of Salt Bridges: Identified in PyMOL as pairs of oxygen atoms (in ASP or GLU side chains, or C-termini carboxyl) and nitrogen atoms (in LYS, ARG, or HIS side chains, or N-termini backbone amine) within 3.0 Å cut-off
	Percent of SBmax: Percent of salt bridges out of maximum number possible (SBmax computed based on sequence of each protein using previously-reported method) ⁷⁷²
	*Percent Change in Number of Salt Bridges: Percent difference between simulated and condensed-phase structure
RMSD	Root Mean Square Deviation: RMSD between simulated and condensed-phase structure determined with PyMOL align feature (sequence alignment, followed by structural superposition and refinement to reject outliers)
Secondary Structure	Secondary Structure Content: Number of residues identified as having helix or strand secondary structure (based on backbone geometry and hydrogen bonding in PyMOL) expressed as a percentage of the total number of residues
	*Percent Change in Secondary Structure Content: Percent difference in either helix or strand secondary structure content between simulated and condensed-phase structure

Table S7. Volumes and packing densities of simulated charge conformers computed with ProteinVolume. Packing density is computed as the ratio of van der Waals volume to the total volume. Values shown in bold in packing density column are the average \pm standard deviation for all charge conformers for each protein, with the deviation expressed as a percentage below this in parentheses.

Charge State	Conformer ID	Total Vol. (Å ³)	Void Vol. (Å ³)	van der Waals Vol. (Å ³)	Packing Density
β-lactoglobulin (3BLG, 18 kDa monomer)					0.717 ± 0.006 (0.9%)
7	A	20157.723	5568.819	14588.904	0.724
8	A	20505.290	5905.530	14599.760	0.712
9	A	20399.153	5793.299	14605.854	0.716
concanavalin A (3CNA, 103 kDa tetramer)					0.684 ± 0.002 (0.3%)
19	A	118756.674	37621.067	81135.608	0.683
	B	118405.736	37284.143	81121.593	0.685
	E	118883.441	37734.362	81149.080	0.683
20	A	118007.502	36896.553	81110.949	0.687
	C	118547.171	37458.083	81089.088	0.684
21	A	118579.926	37461.939	81117.987	0.684
	B	119194.306	38068.370	81125.936	0.681
	D	118782.945	37689.140	81093.806	0.683
	E	119053.263	37921.174	81132.089	0.681
22	A	118319.573	37152.883	81166.691	0.686
	B	118875.798	37730.424	81145.374	0.683
23	A	118783.881	37664.270	81119.612	0.683
	B	118319.921	37154.780	81165.142	0.686
	E	118367.591	37229.376	81138.215	0.685
glutamate dehydrogenase (3JCZ, 336 kDa hexamer)					0.674 ± 0.002 (0.3%)
37	A	393813.001	128352.248	265460.753	0.674
	C	393724.631	128239.097	265485.534	0.674
38	A	394766.280	129190.108	265576.171	0.673
	B	393407.564	127986.133	265421.432	0.675
	E	394899.005	129429.870	265469.135	0.672
39	A	394187.722	128771.087	265416.635	0.673
40	A	393068.957	127531.011	265537.946	0.676
	D	393793.709	128357.197	265436.512	0.674
41	A	392838.847	127463.435	265375.412	0.676
42	A	392666.834	127154.924	265511.910	0.676
	E	394816.032	129221.817	265594.215	0.673
43	A	396076.237	130657.683	265418.553	0.670
	C	394650.062	129082.073	265567.988	0.673
	D	393857.100	128355.103	265501.996	0.674
	E	392890.168	127352.144	265538.024	0.676

Table S8. Slope and Pearson correlation coefficient values for linear regression of experimental drift tube CCS against charge state.^{201,203} Only proteins for which there were experimental drift tube CCS measurements reported for at least three native charge states are shown.

Protein	Mass (kDa)	Buffer Gas	Charge Range	CCS Range (nm ²)	Slope	R ²
melittin	2.8	He	3-5	0.32	0.160	0.905
ubiquitin	8.6	He	4-6	0.28	0.140	0.985
β -lactoglobulin monomer	18	He	7-9	1.2	0.600	0.923
insulin hexamer	36	He	9-11	0.1	0.000	0.000
β -lactoglobulin dimer	37	He	11-13	1.1	0.550	0.997
		N ₂	11-13	2.0	1.000	0.987
transthyretin	56	He	14-16	0.3	-0.150	0.964
		N ₂	14-16	0.4	0.200	0.923
avidin	64	He	15-18	0.0	0.000	---
		N ₂	15-17	0.1	0.050	0.750
bovine serum albumin	66	He	14-17	0.6	-0.190	0.793
		N ₂	14-17	0.2	-0.020	0.067
concanavalin A	103	He	20-23	1.0	-0.370	0.892
		N ₂	19-22	0.4	-0.020	0.020
serum amyloid P pentamer	125	He	22-26	2.0	-0.510	0.988
		N ₂	22-26	3.5	-0.990	0.949
alcohol dehydrogenase	143	He	23-26	2.2	-0.770	0.891
		N ₂	23-26	0.8	0.230	0.761
pyruvate kinase	237	He	30-35	3	-0.543	0.755
		N ₂	31-35	1	-0.300	0.750
serum amyloid P decamer	250	He	31-35	3	0.600	0.692
		N ₂	31-34	1	0.000	0.000
glutamate dehydrogenase	336	He	38-43	0	0.000	---
		N ₂	37-41	1	0.200	0.500

Table S9. Principal component analysis of 7 structural features of simulated charge conformers of β -lactoglobulin, concanavalin A, and glutamate dehydrogenase (averaged for each native charge state). Principal components are listed in descending order of variation explained and with eigenvector coefficients for each of the 7 structural features.

PC	Variance Explained	% Change in # HBs	% Δ in # Surface HBs	% Δ in # Surface Residues	% Δ in # Polar Contacts with Charged Side Chains	% Δ in # SBs	% Δ in α -Helical Content	% Δ in β -Strand Content
1	66.02%	0.4422	0.4328	0.1672	-0.3671	-0.4077	0.3653	0.3934
2	25.03%	-0.2243	-0.2625	0.6919	-0.4220	-0.2967	-0.3425	-0.1365
3	6.51%	-0.0364	0.1023	0.1114	-0.2864	0.2360	0.5959	-0.6950
4	1.49%	-0.1422	-0.1866	0.3402	-0.1178	0.6654	0.2750	0.5449
5	0.64%	0.0287	-0.0840	-0.5339	-0.7652	0.2012	-0.2814	0.0429
6	0.28%	0.4918	0.4473	0.2827	0.0571	0.4543	-0.4799	-0.1953
7	0.03%	0.6999	-0.7001	0.0143	0.0491	-0.0176	0.0951	-0.0822

Table S10. Principal component analysis of 7 structural features of aggregate data set consisting of one structure of 17 native-like IM-MS calibrant proteins (using central/most-abundant charge state) simulated with each of 5 different force fields.²¹⁵ Principal components are listed in descending order of variation explained and with eigenvector coefficients for each of the 7 structural features.

PC	Variance Explained	% Change in # HBs	% Δ in # Surface HBs	% Δ in # Surface Residues	% Δ in # Polar Contacts with Charged Side Chains	% Δ in # SBs	% Δ in α -Helical Content	% Δ in β -Strand Content
1	34.4%	-0.5419	-0.5346	0.4095	0.0072	-0.1638	-0.4509	-0.1502
2	22.5%	-0.1641	-0.2538	-0.3413	0.6191	0.5531	0.0989	-0.3052
3	14.7%	0.2118	-0.1478	0.0770	0.2746	0.2478	-0.3651	0.8107
4	9.5%	0.1726	0.1334	0.4305	-0.3968	0.7278	-0.1699	-0.2262
5	8.4%	0.3971	0.3401	0.3508	0.5501	-0.2514	-0.3481	-0.3413
6	7.6%	-0.0156	-0.1415	0.6284	0.2435	0.0039	0.7084	0.1539
7	2.9%	-0.6684	0.6888	0.0811	0.1479	0.1139	-0.0416	0.1888

Table S11. Separate principal component analyses of 7 structural features of set of 17 native-like IM-MS calibrant protein simulated structures for each force field individually.²¹⁵ Eigenvector coefficients and variation explained are listed for each force field for the first and second principal components only.

First Principal Component Eigenvectors								
FF	Var. Expl.	% Change in # HBs	% Δ in # Surface HBs	% Δ in # Surface Residues	% Δ in # Polar Contacts	% Δ in # SBs	% Δ in α-Helical Content	% Δ in β-Strand Content
GROMOS 96 43a2	34.8%	-0.3995	-0.4782	0.4548	-0.2338	-0.3000	-0.5094	0.0279
GROMOS 96 54b7	32.2%	-0.5446	-0.5098	0.4382	-0.2211	-0.2126	-0.3942	-0.0450
AMBER 94	35.7%	0.5114	0.5129	-0.3172	-0.0047	0.2644	0.4342	0.3412
CHARMM 27	37.6%	-0.5246	-0.4888	0.3895	-0.0956	-0.2209	-0.4510	-0.2699
OPLS-AA/L	38.6%	-0.4755	-0.4743	0.4630	0.0138	-0.1618	-0.5252	-0.1798
Second Principal Component Eigenvectors								
FF	Var. Expl.	% Change in # HBs	% Δ in # Surface HBs	% Δ in # Surface Residues	% Δ in # Polar Contacts	% Δ in # SBs	% Δ in α-Helical Content	% Δ in β-Strand Content
GROMOS 96 43a2	26.4%	-0.3644	-0.3799	-0.2047	0.4935	0.4088	-0.0362	-0.5187
GROMOS 96 54b7	20.9%	-0.3415	-0.3646	-0.3394	0.5034	0.5556	0.0147	-0.2702
AMBER 94	25.5%	-0.2379	-0.2454	-0.4740	0.6142	0.5185	0.0025	-0.1117
CHARMM 27	26.4%	-0.0944	-0.2971	-0.2694	0.6077	0.4869	0.1074	-0.4607
OPLS-AA/L	25.2%	-0.1654	-0.3617	-0.3709	0.4765	0.5467	0.1309	-0.4014

Table S12. Dot products of first and second principal components for each pair of force fields. Dot products are duplicated on either side of the diagonal for easier comparison. Blank cells correspond to pairing of each force field with itself.

Dot Products of First Principal Component Eigenvectors					
	GROMOS96 43a2	GROMOS96 54b7	AMBER94	CHARMM27	OPLS- AA/L
GROMOS96 43a2		0.9756	-0.8836	0.9313	0.9352
GROMOS96 54b7	0.9756		-0.9206	0.9636	0.9501
AMBER94	-0.8836	-0.9206		-0.9884	-0.9655
CHARMM27	0.9313	0.9636	-0.9884		0.9815
OPLS-AA/L	0.9352	0.9501	-0.9655	0.9815	
Dot Products of Second Principal Component Eigenvectors					
	GROMOS96 43a2	GROMOS96 54b7	AMBER94	CHARMM27	OPLS- AA/L
GROMOS96 43a2		0.9475	0.8498	0.9365	0.9357
GROMOS96 54b7	0.9475		0.9590	0.9345	0.9683
AMBER94	0.8498	0.9590		0.9005	0.9252
CHARMM27	0.9365	0.9345	0.9005		0.9778
OPLS-AA/L	0.9357	0.9683	0.9252	0.9778	

REFERENCES CITED

- (1) *Analytical Characterization of Biotherapeutics*; Lill, J. R.; Sandoval, W., Eds.; John Wiley & Sons, Inc.: Hoboken, NJ, 2017.
- (2) Cerofolini, L.; Fragai, M.; Ravera, E.; Diebolder, C. A.; Renault, L.; Calderone, V. Integrative Approaches in Structural Biology: A More Complete Picture from the Combination of Individual Techniques. *Biomolecules* **2019**, *9*, 370.
- (3) Pukala, T.; Robinson, C. V. Introduction: Mass Spectrometry Applications in Structural Biology. *Chem. Rev.* **2022**, *122*, 7267-7268.
- (4) Curry, S. Structural Biology: A Century-Long Journey into an Unseen World. *Interdiscip. Sci. Rev.* **2015**, *40*, 308-328.
- (5) Dobson, C. M. Biophysical Techniques in Structural Biology. *Annu. Rev. Biochem.* **2019**, *88*, 25-33.
- (6) Eschweiler, J. D.; Kerr, R.; Rabuck-Gibbons, J.; Ruotolo, B. T. Sizing up Protein-Ligand Complexes: The Rise of Structural Mass Spectrometry Approaches in the Pharmaceutical Sciences. *Annu. Rev. Anal. Chem.* **2017**, *10*, 25-44.
- (7) Yin, H.; Flynn, A. D. Drugging Membrane Protein Interactions. *Annu. Rev. Biomed. Eng.* **2016**, *18*, 51-76.
- (8) Overington, J. P.; Al-Lazikani, B.; Hopkins, A. L. How Many Drug Targets Are There? *Nat. Rev. Drug Discov.* **2006**, *5*, 993-996.
- (9) Parker, M. W. Protein Structure from X-Ray Diffraction. *J. Biol. Phys.* **2003**, *29*, 341-362.
- (10) Spiess, H. W. 50th Anniversary Perspective: The Importance of NMR Spectroscopy to Macromolecular Science. *Macromolecules* **2017**, *50*, 1761-1777.
- (11) Markwick, P. R. L.; Malliavin, T.; Nilges, M. Structural Biology by NMR: Structure, Dynamics, and Interactions. *PLoS Comput. Biol.* **2008**, *4*, e1000168.
- (12) Fernandez-Leiro, R.; Scheres, S. H. W. Unravelling Biological Macromolecules with Cryo-Electron Microscopy. *Nature* **2016**, *537*, 339-346.
- (13) Ognjenović, J.; Grishammer, R.; Subramaniam, S. Frontiers in Cryo Electron Microscopy of Complex Macromolecular Assemblies. *Annu. Rev. Biomed. Eng.* **2019**, *21*, 395-415.
- (14) Stollar, E. J.; Smith, D. P. Uncovering Protein Structure. *Essays Biochem.* **2020**, *64*, 649-680.

- (15) Burley, S. K. Impact of Structural Biologists and the Protein Data Bank on Small-Molecule Drug Discovery and Development. *J. Biol. Chem.* **2021**, *296*, 100559.
- (16) Campbell, I. D. The March of Structural Biology. *Nat. Rev. Mol. Cell Biol.* **2002**, *3*, 377-381.
- (17) Yu, H. Extending the Size Limit of Protein Nuclear Magnetic Resonance. *Proc. Natl. Acad. Sci. U. S. A.* **1999**, *96*, 332-334.
- (18) Alewijnse, B.; Ashton, A. W.; Chambers, M. G.; Chen, S.; Cheng, A.; Ebrahim, M.; Eng, E. T.; Hagen, W. J. H.; Koster, A. J.; López, C. S.; Lukoyanova, N.; Ortega, J.; Renault, L.; Reyntjens, S.; Rice, W. J.; Scapin, G.; Schrijver, R.; Siebert, A.; Stagg, S. M.; Grum-Tokars, V.; Wright, E. R.; Wu, S.; Yu, Z.; Zhou, Z. H.; Carragher, B.; Potter, C. S. Best Practices for Managing Large CryoEM Facilities. *J. Struct. Biol.* **2017**, *199*, 225-236.
- (19) Dias, D. M.; Ciulli, A. NMR Approaches in Structure-Based Lead Discovery: Recent Developments and New Frontiers for Targeting Multi-Protein Complexes. *Prog. Biophys. Mol. Biol.* **2014**, *116*, 101-112.
- (20) Danev, R.; Yanagisawa, H.; Kikkawa, M. Cryo-Electron Microscopy Methodology: Current Aspects and Future Directions. *Trends Biochem. Sci.* **2019**, *44*, 837-848.
- (21) Renaud, J.-P.; Chari, A.; Ciferri, C.; Liu, W.-T.; Rémigy, H.-W.; Stark, H.; Wiesmann, C. Cryo-EM in Drug Discovery: Achievements, Limitations and Prospects. *Nat. Rev. Drug Discov.* **2018**, *17*, 471-492.
- (22) Bai, X.-C.; McMullan, G.; Scheres, S. H. W. How Cryo-EM Is Revolutionizing Structural Biology. *Trends Biochem. Sci.* **2015**, *40*, 49-57.
- (23) Davis, A. M.; Teague, S. J.; Kleywegt, G. J. Application and Limitations of X-Ray Crystallographic Data in Structure-Based Ligand and Drug Design. *Angew. Chem. Int. Ed.* **2003**, *42*, 2718-2736.
- (24) Gaber, A.; Pavšič, M. Modeling and Structure Determination of Homo-Oligomeric Proteins: An Overview of Challenges and Current Approaches. *Int. J. Mol. Sci.* **2021**, *22*, 9081.
- (25) Qin, J.; Gronenborn, A. M. Weak Protein Complexes: Challenging to Study but Essential for Life. *FEBS J.* **2014**, *281*, 1948-1949.
- (26) Rózycki, B.; Boura, E. Large, Dynamic, Multi-Protein Complexes: A Challenge for Structural Biology. *J. Condens. Matter Phys.* **2014**, *26*, 463103.
- (27) Ziegler, S. J.; Mallinson, S. J. B.; St. John, P. C.; Bomble, Y. J. Advances in Integrative Structural Biology: Towards Understanding Protein Complexes in Their Cellular Context. *Comput. Struct. Biotechnol. J.* **2021**, *19*, 214-225.

- (28) Lacapère, J.-J.; Pebay-Peyroula, E.; Neumann, J.-M.; Etchebest, C. Determining Membrane Protein Structures: Still a Challenge! *Trends Biochem. Sci.* **2007**, *32*, 259-270.
- (29) Bill, R. M.; Henderson, P. J. F.; Iwata, S.; Kunji, E. R. S.; Michel, H.; Neutze, R.; Newstead, S.; Poolman, B.; Tate, C. G.; Vogel, H. Overcoming Barriers to Membrane Protein Structure Determination. *Nat. Biotechnol.* **2011**, *29*, 335-340.
- (30) Raman, P.; Cherezov, V.; Caffrey, M. The Membrane Protein Data Bank. *Cell. Mol. Life Sci.* **2005**, *63*, 36.
- (31) Carpenter, E. P.; Beis, K.; Cameron, A. D.; Iwata, S. Overcoming the Challenges of Membrane Protein Crystallography. *Curr. Opin. Struct. Biol.* **2008**, *18*, 581-586.
- (32) Sanders, C. R.; Sönnichsen, F. Solution NMR of Membrane Proteins: Practice and Challenges. *Magn. Reson. Chem.* **2006**, *44*, S24-S40.
- (33) Cross, T. A.; Sharma, M.; Yi, M.; Zhou, H.-X. Influence of Solubilizing Environments on Membrane Protein Structures. *Trends Biochem. Sci.* **2011**, *36*, 117-125.
- (34) Warschawski, D. E.; Arnold, A. A.; Beaugrand, M.; Gravel, A.; Chartrand, É.; Marcotte, I. Choosing Membrane Mimetics for Nmr Structural Studies of Transmembrane Proteins. *Biochimica et Biophysica Acta (BBA) - Biomembranes* **2011**, *1808*, 1957-1974.
- (35) Kermani, A. A. A Guide to Membrane Protein X-Ray Crystallography. *FEBS J.* **2021**, *288*, 5788-5804.
- (36) Moraes, I.; Evans, G.; Sanchez-Weatherby, J.; Newstead, S.; Stewart, P. D. S. Membrane Protein Structure Determination — the Next Generation. *Biochim. Biophys. Acta Biomembr.* **2014**, *1838*, 78-87.
- (37) Privé, G. G. Detergents for the Stabilization and Crystallization of Membrane Proteins. *Methods* **2007**, *41*, 388-397.
- (38) Tate, C. G. Practical Considerations of Membrane Protein Instability During Purification and Crystallisation. In *Heterologous Expression of Membrane Proteins: Methods and Protocols*, Mus-Veteau, I., Ed.; Humana Press, 2010; pp 187-203.
- (39) Bolla, J. R.; Agasid, M. T.; Mehmood, S.; Robinson, C. V. Membrane Protein–Lipid Interactions Probed Using Mass Spectrometry. *Annu. Rev. Biochem.* **2019**, *88*, 85-111.

- (40) Lössl, P.; van de Waterbeemd, M.; Heck, A. J. The Diverse and Expanding Role of Mass Spectrometry in Structural and Molecular Biology. *EMBO J.* **2016**, *35*, 2634-2657.
- (41) Tamara, S.; den Boer, M. A.; Heck, A. J. R. High-Resolution Native Mass Spectrometry. *Chem. Rev.* **2022**, *122*, 7269-7326.
- (42) Karch, K. R.; Snyder, D. T.; Harvey, S. R.; Wysocki, V. H. Native Mass Spectrometry: Recent Progress and Remaining Challenges. *Annu. Rev. Biophys.* **2022**, *51*, 157-179.
- (43) Ruotolo, B. T.; Marty, M. T. Native Mass Spectrometry for Structural Biology: A Perspective. *Int. J. Mass Spectrom.* **2021**, *468*, 116655.
- (44) Keener, J. E.; Zhang, G.; Marty, M. T. Native Mass Spectrometry of Membrane Proteins. *Anal. Chem.* **2021**, *93*, 583-597.
- (45) Deslignière, E.; Ehkirch, A.; Duivelshof, B. L.; Toftevall, H.; Sjögren, J.; Guillarme, D.; D'Atri, V.; Beck, A.; Hernandez-Alba, O.; Cianféroni, S. State-of-the-Art Native Mass Spectrometry and Ion Mobility Methods to Monitor Homogeneous Site-Specific Antibody-Drug Conjugates Synthesis. *Pharmaceuticals* **2021**, *14*, 498.
- (46) Chen, S.; Wu, D.; Robinson, C. V.; Struwe, W. B. Native Mass Spectrometry Meets Glycomics: Resolving Structural Detail and Occupancy of Glycans on Intact Glycoproteins. *Anal. Chem.* **2021**, *93*, 10435-10443.
- (47) Barth, M.; Schmidt, C. Native Mass Spectrometry—a Valuable Tool in Structural Biology. *J. Mass Spectrom.* **2020**, *55*, e4578.
- (48) Tong, W.; Wang, G. How Can Native Mass Spectrometry Contribute to Characterization of Biomacromolecular Higher-Order Structure and Interactions? *Methods* **2018**, *144*, 3-13.
- (49) Hammerschmid, D.; van Dyck, J. F.; Sobott, F.; Calabrese, A. N. Interrogating Membrane Protein Structure and Lipid Interactions by Native Mass Spectrometry. In *Biophysics of Membrane Proteins: Methods and Protocols*; Postis, V. L. G.; Goldman, A., Eds.; Springer: New York, 2020; pp 233-261.
- (50) Boeri Erba, E.; Signor, L.; Petosa, C. Exploring the Structure and Dynamics of Macromolecular Complexes by Native Mass Spectrometry. *J. Proteom.* **2020**, *222*, 103799.
- (51) Mehmood, S.; Allison, T. M.; Robinson, C. V. Mass Spectrometry of Protein Complexes: From Origins to Applications. *Annu. Rev. Phys. Chem.* **2015**, *66*, 453-474.

- (52) Bolla, J. R.; Fiorentino, F.; Robinson, C. V. Mass Spectrometry Informs the Structure and Dynamics of Membrane Proteins Involved in Lipid and Drug Transport. *Curr. Opin. Struct. Biol.* **2021**, *70*, 53-60.
- (53) Agasid, M. T.; Robinson, C. V. Probing Membrane Protein–Lipid Interactions. *Curr. Opin. Struct. Biol.* **2021**, *69*, 78-85.
- (54) Rogawski, R.; Sharon, M. Characterizing Endogenous Protein Complexes with Biological Mass Spectrometry. *Chem. Rev.* **2022**, *122*, 7386-7414.
- (55) Laganowsky, A.; Reading, E.; Allison, T. M.; Ulmschneider, M. B.; Degiacomi, M. T.; Baldwin, A. J.; Robinson, C. V. Membrane Proteins Bind Lipids Selectively to Modulate Their Structure and Function. *Nature* **2014**, *510*, 172-175.
- (56) van Dyck, J. F.; Konijnenberg, A.; Sobott, F. Native Mass Spectrometry for the Characterization of Structure and Interactions of Membrane Proteins. In *Membrane Protein Structure and Function Characterization: Methods and Protocols*, Lacapere, J.-J., Ed.; Humana New York, 2017; pp 205-232.
- (57) Norris, C. E.; Keener, J. E.; Perera, S. M. D. C.; Weerasinghe, N.; Fried, S. D. E.; Resager, W. C.; Rohrbough, J. G.; Brown, M. F.; Marty, M. T. Native Mass Spectrometry Reveals the Simultaneous Binding of Lipids and Zinc to Rhodopsin. *Int. J. Mass Spectrom.* **2021**, *460*, 116477.
- (58) Blackwell, A. E.; Dodds, E. D.; Bandarian, V.; Wysocki, V. H. Revealing the Quaternary Structure of a Heterogeneous Noncovalent Protein Complex through Surface-Induced Dissociation. *Anal. Chem.* **2011**, *83*, 2862-2865.
- (59) Bobst, C. E.; Sperry, J.; Friese, O. V.; Kaltashov, I. A. Simultaneous Evaluation of a Vaccine Component Microheterogeneity and Conformational Integrity Using Native Mass Spectrometry and Limited Charge Reduction. *J. Am. Soc. Mass Spectrom.* **2021**, *32*, 1631-1637.
- (60) Cleary, S. P.; Prell, J. S. Distinct Classes of Multi-Subunit Heterogeneity: Analysis Using Fourier Transform Methods and Native Mass Spectrometry. *Analyst* **2020**, *145*, 4688-4697.
- (61) Morgner, N.; Robinson, C. V. Massign: An Assignment Strategy for Maximizing Information from the Mass Spectra of Heterogeneous Protein Assemblies. *Anal. Chem.* **2012**, *84*, 2939-2948.
- (62) van de Waterbeemd, M.; Fort, K. L.; Boll, D.; Reinhardt-Szyba, M.; Routh, A.; Makarov, A.; Heck, A. J. R. High-Fidelity Mass Analysis Unveils Heterogeneity in Intact Ribosomal Particles. *Nat. Methods* **2017**, *14*, 283-286.

- (63) Aquilina, J. A.; Benesch, J. L. P.; Bateman, O. A.; Slingsby, C.; Robinson, C. V. Polydispersity of a Mammalian Chaperone: Mass Spectrometry Reveals the Population of Oligomers in α B-Crystallin. *Proc. Natl. Acad. Sci. U. S. A.* **2003**, *100*, 10611-10616.
- (64) Reading, E.; Walton, T. A.; Liko, I.; Marty, M. T.; Laganowsky, A.; Rees, D. C.; Robinson, C. V. The Effect of Detergent, Temperature, and Lipid on the Oligomeric State of MscL Constructs: Insights from Mass Spectrometry. *Chem. Biol.* **2015**, *22*, 593-603.
- (65) Townsend, J. A.; Sanders, H. M.; Rolland, A. D.; Park, C. K.; Horton, N. C.; Prell, J. S.; Wang, J.; Marty, M. T. Influenza AM2 Channel Oligomerization Is Sensitive to Its Chemical Environment. *Anal. Chem.* **2021**, *93*, 16273-16281.
- (66) van Breukelen, B.; Barendregt, A.; Heck, A. J. R.; van den Heuvel, R. H. H. Resolving Stoichiometries and Oligomeric States of Glutamate Synthase Protein Complexes with Curve Fitting and Simulation of Electrospray Mass Spectra. *Rapid Commun. Mass Spectrom.* **2006**, *20*, 2490-2496.
- (67) van den Heuvel, R. H. H.; Heck, A. J. R. Native Protein Mass Spectrometry: From Intact Oligomers to Functional Machineries. *Curr. Opin. Chem. Biol.* **2004**, *8*, 519-526.
- (68) Young, L. M.; Cao, P.; Raleigh, D. P.; Ashcroft, A. E.; Radford, S. E. Ion Mobility Spectrometry–Mass Spectrometry Defines the Oligomeric Intermediates in Amylin Amyloid Formation and the Mode of Action of Inhibitors. *J. Am. Chem. Soc.* **2014**, *136*, 660-670.
- (69) Bernstein, S. L.; Dupuis, N. F.; Lazo, N. D.; Wytttenbach, T.; Condrón, M. M.; Bitan, G.; Teplow, D. B.; Shea, J. E.; Ruotolo, B. T.; Robinson, C. V.; Bowers, M. T. Amyloid-Beta Protein Oligomerization and the Importance of Tetramers and Dodecamers in the Aetiology of Alzheimer's Disease. *Nat. Chem.* **2009**, *1*, 326-331.
- (70) Barrera, N. P.; Isaacson, S. C.; Zhou, M.; Bavro, V. N.; Welch, A.; Schaedler, T. A.; Seeger, M. A.; Miguel, R. N.; Korkhov, V. M.; van Veen, H. W.; Venter, H.; Walmsley, A. R.; Tate, C. G.; Robinson, C. V. Mass Spectrometry of Membrane Transporters Reveals Subunit Stoichiometry and Interactions. *Nat. Methods* **2009**, *6*, 585-587.
- (71) Cleary, S. P.; Thompson, A. M.; Prell, J. S. Fourier Analysis Method for Analyzing Highly Congested Mass Spectra of Ion Populations with Repeated Subunits. *Anal. Chem.* **2016**, *88*, 6205-6213.
- (72) Sobott, F.; Benesch, J. L. P.; Vierling, E.; Robinson, C. V. Subunit Exchange of Multimeric Protein Complexes: Real-Time Monitoring of Subunit Exchange between Small Heat Shock Proteins by Using Electrospray Mass Spectrometry. *J. Biol. Chem.* **2002**, *277*, 38921-38929.

- (73) Taverner, T.; Hernández, H.; Sharon, M.; Ruotolo, B. T.; Matak-Vinković, D.; Devos, D.; Russell, R. B.; Robinson, C. V. Subunit Architecture of Intact Protein Complexes from Mass Spectrometry and Homology Modeling. *Acc. Chem. Res.* **2008**, *41*, 617-627.
- (74) Zhou, M.; Sandercock, A. M.; Fraser, C. S.; Ridlova, G.; Stephens, E.; Schenauer, M. R.; Yokoi-Fong, T.; Barsky, D.; Leary, J. A.; Hershey, J. W.; Doudna, J. A.; Robinson, C. V. Mass Spectrometry Reveals Modularity and a Complete Subunit Interaction Map of the Eukaryotic Translation Factor eIF3. *Proc. Natl. Acad. Sci. U. S. A.* **2008**, *105*, 18139-18144.
- (75) Wilson, J. W.; Rolland, A. D.; Klausen, G. M.; Prell, J. S. Ion Mobility-Mass Spectrometry Reveals That A-Hemolysin from *Staphylococcus aureus* Simultaneously Forms Hexameric and Heptameric Complexes in Detergent Micelle Solutions. *Anal. Chem.* **2019**, *91*, 10204-10211.
- (76) Chen, Z.; Kellie, J. F.; Hottenstein, C. S.; Szapacs, M. E. Native High-Resolution Mass Spectrometry Analysis of Noncovalent Protein Complexes up to 450 kDa. *Bioanalysis* **2020**, *12*, 1353-1362.
- (77) Sever, A. I. M.; Yin, V.; Konermann, L. Interrogating the Quaternary Structure of Noncanonical Hemoglobin Complexes by Electrospray Mass Spectrometry and Collision-Induced Dissociation. *J. Am. Soc. Mass Spectrom.* **2021**, *32*, 270-280.
- (78) Wittig, S.; Songailiene, I.; Schmidt, C. Formation and Stoichiometry of CRISPR-Cascade Complexes with Varying Spacer Lengths Revealed by Native Mass Spectrometry. *J. Am. Soc. Mass Spectrom.* **2020**, *31*, 538-546.
- (79) Liu, F. C.; Cropley, T. C.; Ridgeway, M. E.; Park, M. A.; Bleiholder, C. Structural Analysis of the Glycoprotein Complex Avidin by Tandem-Trapped Ion Mobility Spectrometry–Mass Spectrometry (Tandem-TIMS/MS). *Anal. Chem.* **2020**, *92*, 4459-4467.
- (80) Jia, M.; Sen, S.; Wachnowsky, C.; Fidai, I.; Cowan, J. A.; Wysocki, V. H. Characterization of [2Fe–2S]-Cluster-Bridged Protein Complexes and Reaction Intermediates by Use of Native Mass Spectrometric Methods. *Angew. Chem. Int. Ed.* **2020**, *59*, 6724-6728.
- (81) Walker, L. R.; Marzluff, E. M.; Townsend, J. A.; Resager, W. C.; Marty, M. T. Native Mass Spectrometry of Antimicrobial Peptides in Lipid Nanodiscs Elucidates Complex Assembly. *Anal. Chem.* **2019**, *91*, 9284-9291.
- (82) Li, H.; Nguyen, H. H.; Ogorzalek Loo, R. R.; Campuzano, I. D. G.; Loo, J. A. An Integrated Native Mass Spectrometry and Top-Down Proteomics Method That Connects Sequence to Structure and Function of Macromolecular Complexes. *Nat. Chem.* **2018**, *10*, 139-148.

- (83) Chorev, D. S.; Baker, L. A.; Wu, D.; Beilsten-Edmands, V.; Rouse, S. L.; Zeev-Ben-Mordehai, T.; Jiko, C.; Samsudin, F.; Gerle, C.; Khalid, S.; Stewart, A. G.; Matthews, S. J.; Grünewald, K.; Robinson, C. V. Protein Assemblies Ejected Directly from Native Membranes Yield Complexes for Mass Spectrometry. *Science* **2018**, *362*, 829-834.
- (84) Busch, F.; VanAernum, Z. L.; Ju, Y.; Yan, J.; Gilbert, J. D.; Quintyn, R. S.; Bern, M.; Wysocki, V. H. Localization of Protein Complex Bound Ligands by Surface-Induced Dissociation High-Resolution Mass Spectrometry. *Anal. Chem.* **2018**, *90*, 12796-12801.
- (85) Zhang, H.; Harrington, L. B.; Lu, Y.; Prado, M.; Saer, R.; Rempel, D.; Blankenship, R. E.; Gross, M. L. Native Mass Spectrometry Characterizes the Photosynthetic Reaction Center Complex from the Purple Bacterium *Rhodospirillum rubrum*. *J. Am. Soc. Mass Spectrom.* **2017**, *28*, 87-95.
- (86) Song, Y.; Nelp, M. T.; Bandarian, V.; Wysocki, V. H. Refining the Structural Model of a Heterohexameric Protein Complex: Surface Induced Dissociation and Ion Mobility Provide Key Connectivity and Topology Information. *ACS Cent. Sci.* **2015**, *1*, 477-487.
- (87) Ben-Nissan, G.; Belov, M. E.; Morgenstern, D.; Levin, Y.; Dym, O.; Arkind, G.; Lipson, C.; Makarov, A. A.; Sharon, M. Triple-Stage Mass Spectrometry Unravels the Heterogeneity of an Endogenous Protein Complex. *Anal. Chem.* **2017**, *89*, 4708-4715.
- (88) Zhou, M.; Dagan, S.; Wysocki, V. H. Protein Subunits Released by Surface Collisions of Noncovalent Complexes: Nativelike Compact Structures Revealed by Ion Mobility Mass Spectrometry. *Angew. Chem. Int. Ed.* **2012**, *51*, 4336-4339.
- (89) Pukala, T. L.; Ruotolo, B. T.; Zhou, M.; Politis, A.; Stefanescu, R.; Leary, J. A.; Robinson, C. V. Subunit Architecture of Multiprotein Assemblies Determined Using Restraints from Gas-Phase Measurements. *Structure* **2009**, *17*, 1235-1243.
- (90) Agasid, M. T.; Sørensen, L.; Urner, L. H.; Yan, J.; Robinson, C. V. The Effects of Sodium Ions on Ligand Binding and Conformational States of G Protein-Coupled Receptors—Insights from Mass Spectrometry. *J. Am. Chem. Soc.* **2021**, *143*, 4085-4089.
- (91) Gault, J.; Liko, I.; Landreh, M.; Shutin, D.; Bolla, J. R.; Jefferies, D.; Agasid, M.; Yen, H.-Y.; Ladds, M. J. G. W.; Lane, D. P.; Khalid, S.; Mullen, C.; Remes, P. M.; Huguet, R.; McAlister, G.; Goodwin, M.; Viner, R.; Syka, J. E. P.; Robinson, C. V. Combining Native and ‘Omics’ Mass Spectrometry to Identify Endogenous Ligands Bound to Membrane Proteins. *Nat. Methods* **2020**, *17*, 505-508.

- (92) Guan, S.; Trnka, M. J.; Bushnell, D. A.; Robinson, P. J. J.; Gestwicki, J. E.; Burlingame, A. L. Deconvolution Method for Specific and Nonspecific Binding of Ligand to Multiprotein Complex by Native Mass Spectrometry. *Anal. Chem.* **2015**, *87*, 8541-8546.
- (93) Gault, J.; Donlan, J. A. C.; Liko, I.; Hopper, J. T. S.; Gupta, K.; Housden, N. G.; Struwe, W. B.; Marty, M. T.; Mize, T.; Bechara, C.; Zhu, Y.; Wu, B.; Kleanthous, C.; Belov, M.; Damoc, E.; Makarov, A.; Robinson, C. V. High-Resolution Mass Spectrometry of Small Molecules Bound to Membrane Proteins. *Nat. Methods* **2016**, *13*, 333-336.
- (94) Zhou, M.; Morgner, N.; Barrera, N. P.; Politis, A.; Isaacson, S. C.; Matak-Vinkovic, D.; Murata, T.; Bernal, R. A.; Stock, D.; Robinson, C. V. Mass Spectrometry of Intact V-Type ATPases Reveals Bound Lipids and the Effects of Nucleotide Binding. *Science* **2011**, *334*, 380-385.
- (95) Čaval, T.; Tian, W.; Yang, Z.; Clausen, H.; Heck, A. J. R. Direct Quality Control of Glycoengineered Erythropoietin Variants. *Nat. Commun.* **2018**, *9*, 3342.
- (96) Roberts, D. S.; Mann, M.; Melby, J. A.; Larson, E. J.; Zhu, Y.; Brasier, A. R.; Jin, S.; Ge, Y. Structural O-Glycoform Heterogeneity of the SARS-CoV-2 Spike Protein Receptor-Binding Domain Revealed by Top-Down Mass Spectrometry. *J. Am. Chem. Soc.* **2021**, *143*, 12014-12024.
- (97) Tian, Y.; Han, L.; Buckner, A. C.; Ruotolo, B. T. Collision Induced Unfolding of Intact Antibodies: Rapid Characterization of Disulfide Bonding Patterns, Glycosylation, and Structures. *Anal. Chem.* **2015**, *87*, 11509-11515.
- (98) Tian, Y.; Ruotolo, B. T. Collision Induced Unfolding Detects Subtle Differences in Intact Antibody Glycoforms and Associated Fragments. *Int. J. Mass Spectrom.* **2018**, *425*, 1-9.
- (99) Reardon, P. N.; Jara, K. A.; Rolland, A. D.; Smith, D. A.; Hoang, H. T. M.; Prell, J. S.; Barbar, E. J. The Dynein Light Chain 8 (LC8) Binds Predominantly "in-Register" to a Multivalent Intrinsically Disordered Partner. *J. Biol. Chem.* **2020**, *295*, 4912-4922.
- (100) Miller, L. M.; Barnes, L. F.; Raab, S. A.; Draper, B. E.; El-Baba, T. J.; Lutomski, C. A.; Robinson, C. V.; Clemmer, D. E.; Jarrold, M. F. Heterogeneity of Glycan Processing on Trimeric SARS-CoV-2 Spike Protein Revealed by Charge Detection Mass Spectrometry. *J. Am. Chem. Soc.* **2021**, *143*, 3959-3966.
- (101) Loo, J. A. Studying Noncovalent Protein Complexes by Electrospray Ionization Mass Spectrometry. *Mass Spectrom. Rev.* **1997**, *16*, 1-23.
- (102) Loo, J. A. Electrospray Ionization Mass Spectrometry: A Technology for Studying Noncovalent Macromolecular Complexes. *Int. J. Mass Spectrom.* **2000**, *200*, 175-186.

- (103) Olinares, P. D. B.; Kang, J. Y.; Llewellyn, E.; Chiu, C.; Chen, J.; Malone, B.; Saecker, R. M.; Campbell, E. A.; Darst, S. A.; Chait, B. T. Native Mass Spectrometry-Based Screening for Optimal Sample Preparation in Single-Particle Cryo-EM. *Structure* **2021**, *29*, 186-195.e186.
- (104) Kebarle, P.; Verkerk, U. H. Electrospray: From Ions in Solution to Ions in the Gas Phase, What We Know Now. *Mass Spectrom. Rev.* **2009**, *28*, 898-917.
- (105) Fenn, J. B.; Mann, M.; Meng, C. K.; Wong, S. F.; Whitehouse, C. M. Electrospray Ionization-Principles and Practice. *Mass Spectrom. Rev.* **1990**, *9*, 37-70.
- (106) Takano, K.; Arai, S.; Sakamoto, S.; Ushijima, H.; Ikegami, T.; Saikusa, K.; Konuma, T.; Hamachi, I.; Akashi, S. Screening of Protein-Ligand Interactions under Crude Conditions by Native Mass Spectrometry. *Anal. Bioanal. Chem.* **2020**, *412*, 4037-4043.
- (107) Macias, L. A.; Santos, I. C.; Brodbelt, J. S. Ion Activation Methods for Peptides and Proteins. *Anal. Chem.* **2020**, *92*, 227-251.
- (108) Wilson, J. W.; Donor, M. T.; Shepherd, S. O.; Prell, J. S. Increasing Collisional Activation of Protein Complexes Using Smaller Aperture Source Sampling Cones on a Synapt Q-IM-TOF Instrument with a Stepwave Source. *J. Am. Soc. Mass Spectrom.* **2020**, *31*, 1751-1754.
- (109) Donnelly, D. P.; Rawlins, C. M.; DeHart, C. J.; Fornelli, L.; Schachner, L. F.; Lin, Z.; Lippens, J. L.; Aluri, K. C.; Sarin, R.; Chen, B.; Lantz, C.; Jung, W.; Johnson, K. R.; Koller, A.; Wolff, J. J.; Campuzano, I. D. G.; Auclair, J. R.; Ivanov, A. R.; Whitelegge, J. P.; Paša-Tolić, L.; Chamot-Rooke, J.; Danis, P. O.; Smith, L. M.; Tsybin, Y. O.; Loo, J. A.; Ge, Y.; Kelleher, N. L.; Agar, J. N. Best Practices and Benchmarks for Intact Protein Analysis for Top-Down Mass Spectrometry. *Nat. Methods* **2019**, *16*, 587-594.
- (110) Schachner, L. F.; Tran, D. P.; Lee, A. S.; McGee, J. P.; Jooss, K.; Durbin, K. R.; Seckler, H. S.; Adams, L.; Cline, E. N.; Melani, R. D.; Ives, A. N.; Soye, B. D.; Kelleher, N. L.; Patrie, S. M. Reassembling Protein Complexes after Controlled Disassembly by Top-Down Mass Spectrometry in Native Mode. *Int. J. Mass Spectrom.* **2021**, *465*, 116591.
- (111) Brodbelt, J. S. Photodissociation Mass Spectrometry: New Tools for Characterization of Biological Molecules. *Chem. Soc. Rev.* **2014**, *43*, 2757-2783.
- (112) Holden, D. D.; McGee, W. M.; Brodbelt, J. S. Integration of Ultraviolet Photodissociation with Proton Transfer Reactions and Ion Parking for Analysis of Intact Proteins. *Anal. Chem.* **2016**, *88*, 1008-1016.

- (113) Benesch, J. L. P.; Aquilina, J. A.; Ruotolo, B. T.; Sobott, F.; Robinson, C. V. Tandem Mass Spectrometry Reveals the Quaternary Organization of Macromolecular Assemblies. *Chem. Biol.* **2006**, *13*, 597-605.
- (114) Dixit, S. M.; Polasky, D. A.; Ruotolo, B. T. Collision Induced Unfolding of Isolated Proteins in the Gas Phase: Past, Present, and Future. *Curr. Opin. Chem. Biol.* **2018**, *42*, 93-100.
- (115) Wang, H.; Eschweiler, J.; Cui, W.; Zhang, H.; Frieden, C.; Ruotolo, B. T.; Gross, M. L. Native Mass Spectrometry, Ion Mobility, Electron-Capture Dissociation, and Modeling Provide Structural Information for Gas-Phase Apolipoprotein E Oligomers. *J. Am. Soc. Mass Spectrom.* **2019**, *30*, 876-885.
- (116) Zhong, Y.; Han, L.; Ruotolo, B. T. Collisional and Coulombic Unfolding of Gas-Phase Proteins: High Correlation to Their Domain Structures in Solution. *Angew. Chem. Int. Ed.* **2014**, *53*, 9209-9212.
- (117) Snyder, D. T.; Harvey, S. R.; Wysocki, V. H. Surface-Induced Dissociation Mass Spectrometry as a Structural Biology Tool. *Chem. Rev.* **2022**, *122*, 7442-7487.
- (118) Seffernick, J. T.; Canfield, S. M.; Harvey, S. R.; Wysocki, V. H.; Lindert, S. Prediction of Protein Complex Structure Using Surface-Induced Dissociation and Cryo-Electron Microscopy. *Anal. Chem.* **2021**, *93*, 7596-7605.
- (119) Harvey, S. R.; Liu, Y.; Liu, W.; Wysocki, V. H.; Laganowsky, A. Surface Induced Dissociation as a Tool to Study Membrane Protein Complexes. *Chem. Commun.* **2017**, *53*, 3106-3109.
- (120) Jones, C. M.; Beardsley, R. L.; Galhena, A. S.; Dagan, S.; Cheng, G.; Wysocki, V. H. Symmetrical Gas-Phase Dissociation of Noncovalent Protein Complexes Via Surface Collisions. *J. Am. Chem. Soc.* **2006**, *128*, 15044-15045.
- (121) Foreman, D. J.; McLuckey, S. A. Recent Developments in Gas-Phase Ion/Ion Reactions for Analytical Mass Spectrometry. *Anal. Chem.* **2020**, *92*, 252-266.
- (122) Kaltashov, I. A.; Bobst, C. E.; Pawlowski, J.; Wang, G. Mass Spectrometry-Based Methods in Characterization of the Higher Order Structure of Protein Therapeutics. *J. Pharm. Biomed. Anal.* **2020**, *184*, 113169.
- (123) Botamanenko, D. Y.; Jarrold, M. F. Ion-Ion Interactions in Charge Detection Mass Spectrometry. *J. Am. Soc. Mass Spectrom.* **2019**, *30*, 2741-2749.
- (124) Jarrold, M. F. Applications of Charge Detection Mass Spectrometry in Molecular Biology and Biotechnology. *Chem. Rev.* **2022**, *122*, 7415-7441.
- (125) Keifer, D. Z.; Pierson, E. E.; Jarrold, M. F. Charge Detection Mass Spectrometry: Weighing Heavier Things. *Analyst* **2017**, *142*, 1654-1671.

- (126) Eldrid, C.; Thalassinou, K. Developments in Tandem Ion Mobility Mass Spectrometry. *Biochem. Soc. Trans* **2020**, *48*, 2457-2466.
- (127) Liu, F. C.; Ridgeway, M. E.; Park, M. A.; Bleiholder, C. Tandem Trapped Ion Mobility Spectrometry. *Analyst* **2018**, *143*, 2249-2258.
- (128) Shepherd, D. A.; Marty, M. T.; Giles, K.; Baldwin, A. J.; Benesch, J. L. P. Combining Tandem Mass Spectrometry with Ion Mobility Separation to Determine the Architecture of Polydisperse Proteins. *Int. J. Mass Spectrom.* **2015**, *377*, 663-671.
- (129) Zubarev, R. A. Electron-Capture Dissociation Tandem Mass Spectrometry. *Curr. Opin. Biotechnol.* **2004**, *15*, 12-16.
- (130) Jhingree, J. R.; Beveridge, R.; Dickinson, E. R.; Williams, J. P.; Brown, J. M.; Bellina, B.; Barran, P. E. Electron Transfer with No Dissociation Ion Mobility–Mass Spectrometry (ETnoD IM-MS). The Effect of Charge Reduction on Protein Conformation. *Int. J. Mass Spectrom.* **2017**, *413*, 43-51.
- (131) Zubarev, R. A.; Horn, D. M.; Fridriksson, E. K.; Kelleher, N. L.; Kruger, N. A.; Lewis, M. A.; Carpenter, B. K.; McLafferty, F. W. Electron Capture Dissociation for Structural Characterization of Multiply Charged Protein Cations. *Anal. Chem.* **2000**, *72*, 563-573.
- (132) Kafader, J. O.; Durbin, K. R.; Melani, R. D.; Des Soye, B. J.; Schachner, L. F.; Senko, M. W.; Compton, P. D.; Kelleher, N. L. Individual Ion Mass Spectrometry Enhances the Sensitivity and Sequence Coverage of Top-Down Mass Spectrometry. *J. Proteome Res.* **2020**, *19*, 1346-1350.
- (133) Loo, J. A.; Edmonds, C. G.; Smith, R. D. Tandem Mass Spectrometry of Very Large Molecules: Serum Albumin Sequence Information from Multiply Charged Ions Formed by Electrospray Ionization. *Anal. Chem.* **1991**, *63*, 2488-2499.
- (134) Syka, J. E. P.; Coon, J. J.; Schroeder, M. J.; Shabanowitz, J.; Hunt, D. F. Peptide and Protein Sequence Analysis by Electron Transfer Dissociation Mass Spectrometry. *Proc. Natl. Acad. Sci. U. S. A.* **2004**, *101*, 9528-9533.
- (135) Dodds, J. N.; Baker, E. S. Ion Mobility Spectrometry: Fundamental Concepts, Instrumentation, Applications, and the Road Ahead. *J. Am. Soc. Mass Spectrom.* **2019**, *30*, 2185-2195.
- (136) *Advances in Ion Mobility-Mass Spectrometry: Fundamentals, Instrumentation and Applications*; Donald, W. A.; Prell, J. S., Eds.; Comprehensive Analytical Chemistry; Elsevier: Amsterdam, 2019; Vol. 83.
- (137) Gabelica, V. Ion Mobility–Mass Spectrometry: An Overview. In *Ion Mobility-Mass Spectrometry: Fundamentals and Applications*; Ashcroft, A. E.; Sobott, F., Eds.; The Royal Society of Chemistry, 2022; pp 1-25.

- (138) Gabelica, V.; Marklund, E. Fundamentals of Ion Mobility Spectrometry. *Curr. Opin. Chem. Biol.* **2018**, *42*, 51-59.
- (139) Konijnenberg, A.; Butterer, A.; Sobott, F. Native Ion Mobility-Mass Spectrometry and Related Methods in Structural Biology. *Biochim. Biophys. Acta Proteins Proteom.* **2013**, *1834*, 1239-1256.
- (140) Morris, C. B.; Poland, J. C.; May, J. C.; McLean, J. A. Fundamentals of Ion Mobility-Mass Spectrometry for the Analysis of Biomolecules. In *Ion Mobility-Mass Spectrometry: Methods and Protocols*; Paglia, G.; Astarita, G., Eds.; Springer US, 2020; pp 1-31.
- (141) Vallejo, D. D.; Rojas Ramírez, C.; Parson, K. F.; Han, Y.; Gadkari, V. V.; Ruotolo, B. T. Mass Spectrometry Methods for Measuring Protein Stability. *Chem. Rev.* **2022**, *122*, 7690-7719.
- (142) Benesch, J. L. P. Collisional Activation of Protein Complexes: Picking up the Pieces. *J. Am. Soc. Mass Spectrom.* **2009**, *20*, 341-348.
- (143) Westphall, M. S.; Lee, K. W.; Salome, A. Z.; Lodge, J. M.; Grant, T.; Coon, J. J. Three-Dimensional Structure Determination of Protein Complexes Using Matrix-Landing Mass Spectrometry. *Nat. Commun.* **2022**, *13*, 2276.
- (144) Novikova, I. V.; Zhou, M.; Du, C.; Parra, M.; Kim, D. N.; VanAernum, Z. L.; Shaw, J. B.; Hellmann, H.; Wysocki, V. H.; Evans, J. E. Tunable Heteroassembly of a Plant Pseudoenzyme–Enzyme Complex. *ACS Chem. Biol.* **2021**, *16*, 2315-2325.
- (145) Shaw, J. B.; Liu, W.; Vasil'ev, Y. V.; Bracken, C. C.; Malhan, N.; Guthals, A.; Beckman, J. S.; Voinov, V. G. Direct Determination of Antibody Chain Pairing by Top-Down and Middle-Down Mass Spectrometry Using Electron Capture Dissociation and Ultraviolet Photodissociation. *Anal. Chem.* **2020**, *92*, 766-773.
- (146) Tian, Y.; Lippens, J. L.; Netirojjanakul, C.; Campuzano, I. D. G.; Ruotolo, B. T. Quantitative Collision-Induced Unfolding Differentiates Model Antibody–Drug Conjugates. *Protein Sci.* **2019**, *28*, 598-608.
- (147) Xie, Y.; Zhang, J.; Yin, S.; Loo, J. A. Top-Down ESI-ECD-FT-ICR Mass Spectrometry Localizes Noncovalent Protein-Ligand Binding Sites. *J. Am. Chem. Soc.* **2006**, *128*, 14432-14433.
- (148) Rosati, S.; van den Bremer, E. T. J.; Schuurman, J.; Parren, P. W. H. I.; Kamerling, J. P.; Heck, A. J. R. In-Depth Qualitative and Quantitative Analysis of Composite Glycosylation Profiles and Other Micro-Heterogeneity on Intact Monoclonal Antibodies by High-Resolution Native Mass Spectrometry Using a Modified Orbitrap. *mAbs* **2013**, *5*, 917-924.

- (149) Sze, S. K.; Ge, Y.; Oh, H.; McLafferty, F. W. Top-Down Mass Spectrometry of a 29-kDa Protein for Characterization of Any Posttranslational Modification to within One Residue. *Proc. Natl. Acad. Sci. U. S. A.* **2002**, *99*, 1774-1779.
- (150) Čaval, T.; Buettner, A.; Habegger, M.; Reusch, D.; Heck, A. J. R. Discrepancies between High-Resolution Native and Glycopeptide-Centric Mass Spectrometric Approaches: A Case Study into the Glycosylation of Erythropoietin Variants. *J. Am. Soc. Mass Spectrom.* **2021**, *32*, 2099-2104.
- (151) Morrison, L. J.; Brodbelt, J. S. 193 nm Ultraviolet Photodissociation Mass Spectrometry of Tetrameric Protein Complexes Provides Insight into Quaternary and Secondary Protein Topology. *J. Am. Chem. Soc.* **2016**, *138*, 10849-10859.
- (152) Poltash, M. L.; McCabe, J. W.; Shirzadeh, M.; Laganowsky, A.; Clowers, B. H.; Russell, D. H. Fourier Transform-Ion Mobility-Orbitrap Mass Spectrometer: A Next-Generation Instrument for Native Mass Spectrometry. *Anal. Chem.* **2018**, *90*, 10472-10478.
- (153) van den Heuvel, R. H. H.; van Duijn, E.; Mazon, H.; Synowsky, S. A.; Lorenzen, K.; Versluis, C.; Brouns, S. J. J.; Langridge, D.; van der Oost, J.; Hoyes, J.; Heck, A. J. R. Improving the Performance of a Quadrupole Time-of-Flight Instrument for Macromolecular Mass Spectrometry. *Anal. Chem.* **2006**, *78*, 7473-7483.
- (154) Hu, Q.; Noll, R. J.; Li, H.; Makarov, A.; Hardman, M.; Cooks, R. G. The Orbitrap: A New Mass Spectrometer. *J. Mass Spectrom.* **2005**, *40*, 430-443.
- (155) Poltash, M. L.; McCabe, J. W.; Shirzadeh, M.; Laganowsky, A.; Russell, D. H. Native IM-Orbitrap MS: Resolving What Was Hidden. *Trends Anal. Chem.* **2020**, *124*, 115533.
- (156) Wörner, T. P.; Snijder, J.; Bennett, A.; Agbandje-McKenna, M.; Makarov, A. A.; Heck, A. J. R. Resolving Heterogeneous Macromolecular Assemblies by Orbitrap-Based Single-Particle Charge Detection Mass Spectrometry. *Nat. Methods* **2020**, *17*, 395-398.
- (157) Rolland, A. D.; Prell, J. S. Approaches to Heterogeneity in Native Mass Spectrometry. *Chem. Rev.* **2021**, *122*, 7909-7951.
- (158) Chorev, D. S.; Tang, H.; Rouse, S. L.; Bolla, J. R.; von Kügelgen, A.; Baker, L. A.; Wu, D.; Gault, J.; Grünewald, K.; Bharat, T. A. M.; Matthews, S. J.; Robinson, C. V. The Use of Sonicated Lipid Vesicles for Mass Spectrometry of Membrane Protein Complexes. *Nat. Protoc.* **2020**, *15*, 1690-1706.
- (159) Rogawski, R.; Rogel, A.; Bloch, I.; Gal, M.; Horovitz, A.; London, N.; Sharon, M. Intracellular Protein–Drug Interactions Probed by Direct Mass Spectrometry of Cell Lysates. *Angew. Chem. Int. Ed.* **2021**, *60*, 19637-19642.

- (160) Vimer, S.; Ben-Nissan, G.; Marty, M.; Fleishman, S. J.; Sharon, M. Direct-MS Analysis of Antibody-Antigen Complexes. *Proteomics* **2021**, *21*, 2000300.
- (161) Vimer, S.; Ben-Nissan, G.; Sharon, M. Direct Characterization of Overproduced Proteins by Native Mass Spectrometry. *Nat. Protoc.* **2020**, *15*, 236-265.
- (162) Bolla, J. R.; Corey, R. A.; Sahin, C.; Gault, J.; Hummer, A.; Hopper, J. T. S.; Lane, D. P.; Drew, D.; Allison, T. M.; Stansfeld, P. J.; Robinson, C. V.; Landreh, M. A Mass-Spectrometry-Based Approach to Distinguish Annular and Specific Lipid Binding to Membrane Proteins. *Angew. Chem. Int. Edit.* **2020**, *59*, 3523-3528.
- (163) Landreh, M.; Marty, M. T.; Gault, J.; Robinson, C. V. A Sliding Selectivity Scale for Lipid Binding to Membrane Proteins. *Curr. Opin. Struct. Biol.* **2016**, *39*, 54-60.
- (164) Bechara, C.; Noell, A.; Morgner, N.; Degiacomi, M. T.; Tampe, R.; Robinson, C. V. A Subset of Annular Lipids Is Linked to the Flippase Activity of an ABC Transporter. *Nat. Chem.* **2015**, *7*, 255-262.
- (165) Marty, M. T.; Hoi, K. K.; Gault, J.; Robinson, C. V. Probing the Lipid Annular Belt by Gas-Phase Dissociation of Membrane Proteins in Nanodiscs. *Angew. Chem. Int. Edit.* **2016**, *55*, 550-554.
- (166) Vallejo, D. D.; Kang, J.; Coghlan, J.; Ramírez, C. R.; Polasky, D. A.; Kurulugama, R. T.; Fjeldsted, J. C.; Schwendeman, A. A.; Ruotolo, B. T. Collision-Induced Unfolding Reveals Stability Differences in Infliximab Therapeutics under Native and Heat Stress Conditions. *Anal. Chem.* **2021**, *93*, 16166-16174.
- (167) Kostelic, M. M.; Marty, M. T. Deconvolving Native and Intact Protein Mass Spectra with UniDec. *ChemRxiv* **2020**, DOI: 10.26434/chemrxiv.13417118.v13417111.
- (168) Kostelic, M. M.; Ryan, A. M.; Reid, D. J.; Noun, J. M.; Marty, M. T. Expanding the Types of Lipids Amenable to Native Mass Spectrometry of Lipoprotein Complexes. *J. Am. Soc. Mass Spectrom.* **2019**, *30*, 1416-1425.
- (169) Kostelic, M. M.; Zak, C. K.; Jayasekera, H.; Marty, M. T. Assembly of Model Membrane Nanodiscs for Native Mass Spectrometry. *Anal. Chem.* **2021**, *93*, 5972-5979.
- (170) Marty, M. T. Nanodiscs and Mass Spectrometry: Making Membranes Fly. *Int. J. Mass Spectrom.* **2020**, *458*, 116436.

- (171) Marty, M. T.; Baldwin, A. J.; Marklund, E. G.; Hochberg, G. K. A.; Benesch, J. L. P.; Robinson, C. V. Bayesian Deconvolution of Mass and Ion Mobility Spectra: From Binary Interactions to Polydisperse Ensembles. *Anal. Chem.* **2015**, *87*, 4370-4376.
- (172) Marty, M. T.; Zhang, H.; Cui, W. D.; Gross, M. L.; Sligar, S. G. Interpretation and Deconvolution of Nanodisc Native Mass Spectra. *J. Am. Soc. Mass Spectrom.* **2014**, *25*, 269-277.
- (173) Cong, X.; Liu, Y.; Liu, W.; Liang, X.; Russell, D. H.; Laganowsky, A. Determining Membrane Protein-Lipid Binding Thermodynamics Using Native Mass Spectrometry. *J. Am. Chem. Soc.* **2016**, *138*, 4346-4349.
- (174) Patrick, J. W.; Boone, C. D.; Liu, W.; Conover, G. M.; Liu, Y.; Cong, X.; Laganowsky, A. Allostery Revealed within Lipid Binding Events to Membrane Proteins. *Proc. Natl. Acad. Sci. U. S. A.* **2018**, *115*, 2976-2981.
- (175) Cong, X.; Liu, Y.; Liu, W.; Liang, X.; Laganowsky, A. Allosteric Modulation of Protein-Protein Interactions by Individual Lipid Binding Events. *Nat. Commun.* **2017**, *8*, 2203.
- (176) Pierson, E. E.; Keifer, D. Z.; Asokan, A.; Jarrold, M. F. Resolving Adeno-Associated Viral Particle Diversity with Charge Detection Mass Spectrometry. *Anal. Chem.* **2016**, *88*, 6718-6725.
- (177) O'Connor, D. M.; Lutomski, C.; Jarrold, M. F.; Boulis, N. M.; Donsante, A. Lot-to-Lot Variation in Adeno-Associated Virus Serotype 9 (AAV9) Preparations. *Hum. Gene Ther. Methods* **2019**, *30*, 214-225.
- (178) van de Waterbeemd, M.; Snijder, J.; Tsvetkova, I. B.; Dragnea, B. G.; Cornelissen, J. J.; Heck, A. J. R. Examining the Heterogeneous Genome Content of Multipartite Viruses BMV and CCMV by Native Mass Spectrometry. *J. Am. Soc. Mass Spectrom.* **2016**, *27*, 1000-1009.
- (179) Yang, Y.; Niu, C.; Bobst, C. E.; Kaltashov, I. A. Charge Manipulation Using Solution and Gas-Phase Chemistry to Facilitate Analysis of Highly Heterogeneous Protein Complexes in Native Mass Spectrometry. *Anal. Chem.* **2021**, *93*, 3337-3342.
- (180) Felitsyn, N.; Peschke, M.; Kebarle, P. Origin and Number of Charges Observed on Multiply-Protonated Native Proteins Produced by ESI. *Int. J. Mass Spectrom.* **2002**, *219*, 39-62.
- (181) Peschke, M.; Verkerk, U. H.; Kebarle, P. Features of the ESI Mechanism That Affect the Observation of Multiply Charged Noncovalent Protein Complexes and the Determination of the Association Constant by the Titration Method. *J. Am. Soc. Mass Spectrom.* **2004**, *15*, 1424-1434.

- (182) Mann, M.; Meng, C. K.; Fenn, J. B. Interpreting Mass-Spectra of Multiply Charged Ions. *Anal. Chem.* **1989**, *61*, 1702-1708.
- (183) Cleary, S. P.; Li, H.; Bagal, D.; Loo, J. A.; Campuzano, I. D. G.; Prell, J. S. Extracting Charge and Mass Information from Highly Congested Mass Spectra Using Fourier-Domain Harmonics. *J. Am. Soc. Mass Spectrom.* **2018**, *29*, 2067-2080.
- (184) Wohlschlagel, T.; Scheffler, K.; Forstenlehner, I. C.; Skala, W.; Senn, S.; Damoc, E.; Holzmann, J.; Huber, C. G. Native Mass Spectrometry Combined with Enzymatic Dissection Unravels Glycoform Heterogeneity of Biopharmaceuticals. *Nat. Commun.* **2018**, *9*, 1713.
- (185) Struwe, W. B.; Robinson, C. V. Relating Glycoprotein Structural Heterogeneity to Function – Insights from Native Mass Spectrometry. *Curr. Opin. Struct. Biol.* **2019**, *58*, 241-248.
- (186) Gupta, K.; Donlan, J. A. C.; Hopper, J. T. S.; Uzdavinys, P.; Landreh, M.; Struwe, W. B.; Drew, D.; Baldwin, A. J.; Stansfeld, P. J.; Robinson, C. V. The Role of Interfacial Lipids in Stabilizing Membrane Protein Oligomers. *Nature* **2017**, *541*, 421-424.
- (187) Wu, D.; Struwe, W. B.; Harvey, D. J.; Ferguson, M. A. J.; Robinson, C. V. N-Glycan Microheterogeneity Regulates Interactions of Plasma Proteins. *Proc. Natl. Acad. Sci. U. S. A.* **2018**, *115*, 8763-8768.
- (188) Brücher, D.; Franc, V.; Smith, S. N.; Heck, A. J. R.; Plückthun, A. Malignant Tissues Produce Divergent Antibody Glycosylation of Relevance for Cancer Gene Therapy Effectiveness. *mAbs* **2020**, *12*, 1792084.
- (189) Giles, K.; Ujma, J.; Wildgoose, J.; Pringle, S.; Richardson, K.; Langridge, D.; Green, M. A Cyclic Ion Mobility-Mass Spectrometry System. *Anal. Chem.* **2019**, *91*, 8564-8573.
- (190) Giles, K.; Williams, J. P.; Campuzano, I. Enhancements in Travelling Wave Ion Mobility Resolution. *Rapid Commun. Mass Spectrom.* **2011**, *25*, 1559-1566.
- (191) Thalassinos, K.; Slade, S. E.; Jennings, K. R.; Scrivens, J. H.; Giles, K.; Wildgoose, J.; Hoyes, J.; Bateman, R. H.; Bowers, M. T. Ion Mobility Mass Spectrometry of Proteins in a Modified Commercial Mass Spectrometer. *Int. J. Mass Spectrom.* **2004**, *236*, 55-63.
- (192) Giles, K.; Pringle, S. D.; Worthington, K. R.; Little, D.; Wildgoose, J. L.; Bateman, R. H. Applications of a Travelling Wave-Based Radio-Frequency-Only Stacked Ring Ion Guide. *Rapid Commun. Mass Spectrom.* **2004**, *18*, 2401-2414.

- (193) Pringle, S. D.; Giles, K.; Wildgoose, J. L.; Williams, J. P.; Slade, S. E.; Thalassinou, K.; Bateman, R. H.; Bowers, M. T.; Scrivens, J. H. An Investigation of the Mobility Separation of Some Peptide and Protein Ions Using a New Hybrid Quadrupole/Travelling Wave IMS/oa-ToF Instrument. *Int. J. Mass Spectrom.* **2007**, *261*, 1-12.
- (194) Allen, S. J.; Eaton, R. M.; Bush, M. F. Analysis of Native-Like Ions Using Structures for Lossless Ion Manipulations. *Anal. Chem.* **2016**, *88*, 9118-9126.
- (195) Deng, L.; Ibrahim, Y. M.; Baker, E. S.; Aly, N. A.; Hamid, A. M.; Zhang, X.; Zheng, X.; Garimella, S. V. B.; Webb, I. K.; Prost, S. A.; Sandoval, J. A.; Norheim, R. V.; Anderson, G. A.; Tolmachev, A. V.; Smith, R. D. Ion Mobility Separations of Isomers Based Upon Long Path Length Structures for Lossless Ion Manipulations Combined with Mass Spectrometry. *ChemistrySelect* **2016**, *1*, 2396-2399.
- (196) Webb, I. K.; Garimella, S. V. B.; Tolmachev, A. V.; Chen, T.-C.; Zhang, X.; Norheim, R. V.; Prost, S. A.; LaMarche, B.; Anderson, G. A.; Ibrahim, Y. M.; Smith, R. D. Experimental Evaluation and Optimization of Structures for Lossless Ion Manipulations for Ion Mobility Spectrometry with Time-of-Flight Mass Spectrometry. *Anal. Chem.* **2014**, *86*, 9169-9176.
- (197) Fernandez-Lima, F. A.; Kaplan, D. A.; Park, M. A. Note: Integration of Trapped Ion Mobility Spectrometry with Mass Spectrometry. *Rev. Sci. Instrum.* **2011**, *82*, 126106-126106.
- (198) Ridgeway, M. E.; Bleiholder, C.; Mann, M.; Park, M. A. Trends in Trapped Ion Mobility – Mass Spectrometry Instrumentation. *Trends Anal. Chem.* **2019**, *116*, 324-331.
- (199) Ibrahim, Y. M.; Garimella, S. V. B.; Prost, S. A.; Wojcik, R.; Norheim, R. V.; Baker, E. S.; Rusyn, I.; Smith, R. D. Development of an Ion Mobility Spectrometry-Orbitrap Mass Spectrometer Platform. *Anal. Chem.* **2016**, *88*, 12152-12160.
- (200) Larriba-Andaluz, C.; Prell, J. S. Fundamentals of Ion Mobility in the Free Molecular Regime. Interlacing the Past, Present and Future of Ion Mobility Calculations. *Int. Rev. Phys. Chem.* **2020**, *39*, 569-623.
- (201) Bush, M. F.; Hall, Z.; Giles, K.; Hoyes, J.; Robinson, C. V.; Ruotolo, B. T. Collision Cross Sections of Proteins and Their Complexes: A Calibration Framework and Database for Gas-Phase Structural Biology. *Anal. Chem.* **2010**, *82*, 9557-9565.
- (202) Richardson, K.; Langridge, D.; Dixit, S. M.; Ruotolo, B. T. An Improved Calibration Approach for Traveling Wave Ion Mobility Spectrometry: Robust, High-Precision Collision Cross Sections. *Anal. Chem.* **2021**, *93*, 3542-3550.

- (203) Salbo, R.; Bush, M. F.; Naver, H.; Campuzano, I.; Robinson, C. V.; Pettersson, I.; Jørgensen, T. J. D.; Haselmann, K. F. Traveling-Wave Ion Mobility Mass Spectrometry of Protein Complexes: Accurate Calibrated Collision Cross-Sections of Human Insulin Oligomers. *Rapid Commun. Mass Spectrom.* **2012**, *26*, 1181-1193.
- (204) Stiving, A. Q.; Jones, B. J.; Ujma, J.; Giles, K.; Wysocki, V. H. Collision Cross Sections of Charge-Reduced Proteins and Protein Complexes: A Database for Collision Cross Section Calibration. *Anal. Chem.* **2020**, *92*, 4475-4483.
- (205) Donor, M. T.; Ewing, S. A.; Zenaidee, M. A.; Donald, W. A.; Prell, J. S. Extended Protein Ions Are Formed by the Chain Ejection Model in Chemical Supercharging Electrospray Ionization. *Anal. Chem.* **2017**, *89*, 5107-5114.
- (206) Going, C. C.; Williams, E. R. Supercharging with *m*-Nitrobenzyl Alcohol and Propylene Carbonate: Forming Highly Charged Ions with Extended, Near-Linear Conformations. *Anal. Chem.* **2015**, *87*, 3973-3980.
- (207) Marklund, E. G.; Degiacomi, M. T.; Robinson, C. V.; Baldwin, A. J.; Benesch, J. L. P. Collision Cross Sections for Structural Proteomics. *Structure* **2015**, *23*, 791-799.
- (208) Natalello, A.; Santambrogio, C.; Grandori, R. Are Charge-State Distributions a Reliable Tool Describing Molecular Ensembles of Intrinsically Disordered Proteins by Native MS? *J. Am. Soc. Mass Spectrom.* **2017**, *28*, 21-28.
- (209) Ruotolo, B. T.; Benesch, J. L. P.; Sandercock, A. M.; Hyung, S.-J.; Robinson, C. V. Ion Mobility-Mass Spectrometry Analysis of Large Protein Complexes. *Nat. Protoc.* **2008**, *3*, 1139-1152.
- (210) Santambrogio, C.; Natalello, A.; Brocca, S.; Ponzini, E.; Grandori, R. Conformational Characterization and Classification of Intrinsically Disordered Proteins by Native Mass Spectrometry and Charge-State Distribution Analysis. *Proteomics* **2019**, *19*, 1800060.
- (211) Zhang, J. D.; Donor, M. T.; Rolland, A. D.; Leeming, M. G.; Wang, H.; Trevitt, A. J.; Kabir, K. M. M.; Prell, J. S.; Donald, W. A. Protonation Isomers of Highly Charged Protein Ions Can Be Separated in FAIMS-MS. *Int. J. Mass Spectrom.* **2020**, *457*, 116425.
- (212) Allison, T. M.; Barran, P.; Cianférani, S.; Degiacomi, M. T.; Gabelica, V.; Grandori, R.; Marklund, E. G.; Menneteau, T.; Migas, L. G.; Politis, A.; Sharon, M.; Sobott, F.; Thalassinou, K.; Benesch, J. L. P. Computational Strategies and Challenges for Using Native Ion Mobility Mass Spectrometry in Biophysics and Structural Biology. *Anal. Chem.* **2020**, *92*, 10872-10880.

- (213) Bleiholder, C.; Wyttenbach, T.; Bowers, M. T. A Novel Projection Approximation Algorithm for the Fast and Accurate Computation of Molecular Collision Cross Sections (I). *Method. Int. J. Mass Spectrom.* **2011**, *308*, 1-10.
- (214) Ewing, S. A.; Donor, M. T.; Wilson, J. W.; Prell, J. S. Collidoscope: An Improved Tool for Computing Collisional Cross-Sections with the Trajectory Method. *J. Am. Soc. Mass Spectrom.* **2017**, *28*, 587-596.
- (215) Rolland, A. D.; Prell, J. S. Computational Insights into Compaction of Gas-Phase Protein and Protein Complex Ions in Native Ion Mobility-Mass Spectrometry. *Trends Anal. Chem.* **2019**, *116*, 282-291.
- (216) Bleiholder, C.; Liu, F. C. Structure Relaxation Approximation (SRA) for Elucidation of Protein Structures from Ion Mobility Measurements. *J. Phys. Chem. B* **2019**, *123*, 2756-2769.
- (217) Larriba, C.; Hogan, C. J. Free Molecular Collision Cross Section Calculation Methods for Nanoparticles and Complex Ions with Energy Accommodation. *J. Comput. Phys.* **2013**, *251*, 344-363.
- (218) Larriba-Andaluz, C.; Hogan, C. J. Collision Cross Section Calculations for Polyatomic Ions Considering Rotating Diatomic/Linear Gas Molecules. *J. Chem. Phys.* **2014**, *141*, 9.
- (219) Shvartsburg, A. A.; Jarrold, M. F. An Exact Hard-Spheres Scattering Model for the Mobilities of Polyatomic Ions. *Chem. Phys. Lett.* **1996**, *261*, 86-91.
- (220) Mesleh, M. F.; Hunter, J. M.; Shvartsburg, A. A.; Schatz, G. C.; Jarrold, M. F. Structural Information from Ion Mobility Measurements: Effects of the Long-Range Potential. *J. Phys. Chem. A* **1997**, *101*, 968-968.
- (221) Hall, Z.; Politis, A.; Bush, M. F.; Smith, L. J.; Robinson, C. V. Charge-State Dependent Compaction and Dissociation of Protein Complexes: Insights from Ion Mobility and Molecular Dynamics. *J. Am. Chem. Soc.* **2012**, *134*, 3429-3438.
- (222) Michaelevski, I.; Eisenstein, M.; Sharon, M. Gas-Phase Compaction and Unfolding of Protein Structures. *Anal. Chem.* **2010**, *82*, 9484-9491.
- (223) Rolland, A. D.; Biberic, L. S.; Prell, J. S. Investigation of Charge-State-Dependent Compaction of Protein Ions with Native Ion Mobility-Mass Spectrometry and Theory. *J. Am. Soc. Mass Spectrom.* **2022**, *33*, 369-381.
- (224) Jurneczko, E.; Barran, P. E. How Useful Is Ion Mobility Mass Spectrometry for Structural Biology? The Relationship between Protein Crystal Structures and Their Collision Cross Sections in the Gas Phase. *Analyst* **2011**, *136*, 20-28.

- (225) Scarff, C. A.; Thalassinou, K.; Hilton, G. R.; Scrivens, J. H. Travelling Wave Ion Mobility Mass Spectrometry Studies of Protein Structure: Biological Significance and Comparison with X-Ray Crystallography and Nuclear Magnetic Resonance Spectroscopy Measurements. *Rapid Commun. Mass Spectrom.* **2008**, *22*, 3297-3304.
- (226) Leney, A. C.; Heck, A. J. R. Native Mass Spectrometry: What Is in the Name? *J. Am. Soc. Mass Spectrom.* **2017**, *28*, 5-13.
- (227) Wilm, M.; Mann, M. Analytical Properties of the Nanoelectrospray Ion Source. *Anal. Chem.* **1996**, *68*, 1-8.
- (228) Susa, A. C.; Xia, Z.; Williams, E. R. Small Emitter Tips for Native Mass Spectrometry of Proteins and Protein Complexes from Nonvolatile Buffers That Mimic the Intracellular Environment. *Anal. Chem.* **2017**, *89*, 3116-3122.
- (229) Susa, A. C.; Xia, Z.; Williams, E. R. Native Mass Spectrometry from Common Buffers with Salts That Mimic the Extracellular Environment. *Angew. Chem. Int. Ed.* **2017**, *56*, 7912-7915.
- (230) Iavarone, A. T.; Udekwu, O. A.; Williams, E. R. Buffer Loading for Counteracting Metal Salt-Induced Signal Suppression in Electrospray Ionization. *Anal. Chem.* **2004**, *76*, 3944-3950.
- (231) Metwally, H.; McAllister, R. G.; Konermann, L. Exploring the Mechanism of Salt-Induced Signal Suppression in Protein Electrospray Mass Spectrometry Using Experiments and Molecular Dynamics Simulations. *Anal. Chem.* **2015**, *87*, 2434-2442.
- (232) Chen, F.; Gülbakan, B.; Weidmann, S.; Fagerer, S. R.; Ibáñez, A. J.; Zenobi, R. Applying Mass Spectrometry to Study Non-Covalent Biomolecule Complexes. *Mass Spectrom. Rev.* **2016**, *35*, 48-70.
- (233) Tanaka, K.; Waki, H.; Ido, Y.; Akita, S.; Yoshida, Y.; Yoshida, T.; Matsuo, T. Protein and Polymer Analyses up to m/z 100 000 by Laser Ionization Time-of-Flight Mass Spectrometry. *Rapid Commun. Mass Spectrom.* **1988**, *2*, 151-153.
- (234) Trimpin, S. "Magic" Ionization Mass Spectrometry. *J. Am. Soc. Mass Spectrom.* **2016**, *27*, 4-21.
- (235) Fenn, J.; Mann, M.; Meng, C.; Wong, S.; Whitehouse, C. Electrospray Ionization for Mass Spectrometry of Large Biomolecules. *Science* **1989**, *246*, 64-71.
- (236) Chowdhury, S. K.; Katta, V.; Chait, B. T. An Electrospray-Ionization Mass Spectrometer with New Features. *Rapid Commun. Mass Spectrom.* **1990**, *4*, 81-87.

- (237) Katta, V.; Chait, B. T. Observation of the Heme-Globin Complex in Native Myoglobin by Electrospray-Ionization Mass Spectrometry. *J. Am. Chem. Soc.* **1991**, *113*, 8534-8535.
- (238) Ganem, B.; Li, Y. T.; Henion, J. D. Detection of Noncovalent Receptor-Ligand Complexes by Mass Spectrometry. *J. Am. Chem. Soc.* **1991**, *113*, 6294-6296.
- (239) Light-Wahl, K. J.; Loo, J. A.; Edmonds, C. G.; Smith, R. D.; Witkowska, H. E.; Shackleton, C. H. L.; Wu, C.-S. C. Collisionally Activated Dissociation and Tandem Mass Spectrometry of Intact Hemoglobin B-Chain Variant Proteins with Electrospray Ionization. *Biol. Mass Spectrom.* **1993**, *22*, 112-120.
- (240) Miranker, A.; Robinson, C.; Radford, S.; Aplin, R.; Dobson, C. Detection of Transient Protein Folding Populations by Mass Spectrometry. *Science* **1993**, *262*, 896-900.
- (241) Light-Wahl, K. J.; Schwartz, B. L.; Smith, R. D. Observation of the Noncovalent Quaternary Associations of Proteins by Electrospray Ionization Mass Spectrometry. *J. Am. Chem. Soc.* **1994**, *116*, 5271-5278.
- (242) Mann, M.; Wilm, M. Electrospray Mass Spectrometry for Protein Characterization. *Trends Biochem. Sci.* **1995**, *20*, 219-224.
- (243) Fitzgerald, M. C.; Chernushevich, I.; Standing, K. G.; Whitman, C. P.; Kent, S. B. Probing the Oligomeric Structure of an Enzyme by Electrospray Ionization Time-of-Flight Mass Spectrometry. *Proc. Natl. Acad. Sci. U. S. A.* **1996**, *93*, 6851-6856.
- (244) Mirza, U. A.; Chait, B. T. Do Proteins Denature During Droplet Evolution in Electrospray Ionization? *Int. J. Mass Spectrom. Ion Processes* **1997**, *162*, 173-181.
- (245) Benjamin, D. R.; Robinson, C. V.; Hendrick, J. P.; Hartl, F. U.; Dobson, C. M. Mass Spectrometry of Ribosomes and Ribosomal Subunits. *Proc. Natl. Acad. Sci. U. S. A.* **1998**, *95*, 7391-7395.
- (246) Rostom, A. A.; Robinson, C. V. Detection of the Intact GroEL Chaperonin Assembly by Mass Spectrometry. *J. Am. Chem. Soc.* **1999**, *121*, 4718-4719.
- (247) van Berkel, W. J.; van den Heuvel, R. H.; Versluis, C.; Heck, A. J. Detection of Intact Megadalton Protein Assemblies of Vanillyl-Alcohol Oxidase by Mass Spectrometry. *Protein Sci.* **2000**, *9*, 435-439.
- (248) Rostom, A. A.; Fucini, P.; Benjamin, D. R.; Juenemann, R.; Nierhaus, K. H.; Hartl, F. U.; Dobson, C. M.; Robinson, C. V. Detection and Selective Dissociation of Intact Ribosomes in a Mass Spectrometer. *Proc. Natl. Acad. Sci. U. S. A.* **2000**, *97*, 5185-5190.

- (249) Tito, M. A.; Tars, K.; Valegard, K.; Hajdu, J.; Robinson, C. V. Electrospray Time-of-Flight Mass Spectrometry of the Intact MS2 Virus Capsid. *J. Am. Chem. Soc.* **2000**, *122*, 3550-3551.
- (250) Tito, M. A.; Miller, J.; Walker, N.; Griffin, K. F.; Williamson, E. D.; Despeyroux-Hill, D.; Titball, R. W.; Robinson, C. V. Probing Molecular Interactions in Intact Antibody: Antigen Complexes, an Electrospray Time-of-Flight Mass Spectrometry Approach. *Biophys. J.* **2001**, *81*, 3503-3509.
- (251) Hernández, H.; Robinson, C. V. Dynamic Protein Complexes: Insights from Mass Spectrometry. *J. Biol. Chem.* **2001**, *276*, 46685-46688.
- (252) Sobott, F.; Robinson, C. V. Characterising Electrosprayed Biomolecules Using Tandem-MS—the Noncovalent GroEL Chaperonin Assembly. *Int. J. Mass Spectrom.* **2004**, *236*, 25-32.
- (253) Ilag, L. L.; Ubarretxena-Belandia, I.; Tate, C. G.; Robinson, C. V. Drug Binding Revealed by Tandem Mass Spectrometry of a Protein–Micelle Complex. *J. Am. Chem. Soc.* **2004**, *126*, 14362-14363.
- (254) Hernández, H.; Robinson, C. V. Determining the Stoichiometry and Interactions of Macromolecular Assemblies from Mass Spectrometry. *Nat. Protoc.* **2007**, *2*, 715.
- (255) Heck, A. J. R.; van den Heuvel, R. H. H. Investigation of Intact Protein Complexes by Mass Spectrometry. *Mass Spectrom. Rev.* **2004**, *23*, 368-389.
- (256) Marcoux, J.; Robinson, Carol V. Twenty Years of Gas Phase Structural Biology. *Structure* **2013**, *21*, 1541-1550.
- (257) Hilton, G. R.; Benesch, J. L. P. Two Decades of Studying Non-Covalent Biomolecular Assemblies by Means of Electrospray Ionization Mass Spectrometry. *J. R. Soc. Interface* **2012**, *9*, 801-816.
- (258) Boeri Erba, E.; Petosa, C. The Emerging Role of Native Mass Spectrometry in Characterizing the Structure and Dynamics of Macromolecular Complexes. *Protein Sci.* **2015**, *24*, 1176-1192.
- (259) Winger, B. E.; Light-Wahl, K. J.; Ogorzalek Loo, R. R.; Udseth, H. R.; Smith, R. D. Observation and Implications of High Mass-to-Charge Ratio Ions from Electrospray Ionization Mass Spectrometry. *J. Am. Soc. Mass Spectrom.* **1993**, *4*, 536-545.
- (260) Collings, B. A.; Douglas, D. J. An Extended Mass Range Quadrupole for Electrospray Mass Spectrometry. *Int. J. Mass Spectrom. Ion Processes* **1997**, *162*, 121-127.

- (261) Olsen, J. V.; Macek, B.; Lange, O.; Makarov, A.; Horning, S.; Mann, M. Higher-Energy C-Trap Dissociation for Peptide Modification Analysis. *Nat. Methods* **2007**, *4*, 709-712.
- (262) Rose, R. J.; Damoc, E.; Denisov, E.; Makarov, A.; Heck, A. J. R. High-Sensitivity Orbitrap Mass Analysis of Intact Macromolecular Assemblies. *Nat. Methods* **2012**, *9*, 1084-1086.
- (263) Tang, X.-J.; Fred Brewer, C.; Saha, S.; Chernushevich, I.; Ens, W.; Standing, K. G.; Chait, B. T. Investigation of Protein-Protein Noncovalent Interactions in Soybean Agglutinin by Electrospray Ionization Time-of-Flight Mass Spectrometry. *Rapid Commun. Mass Spectrom.* **1994**, *8*, 750-754.
- (264) Verentchikov, A. N.; Ens, W.; Standing, K. G. Reflecting Time-of-Flight Mass Spectrometer with an Electrospray Ion Source and Orthogonal Extraction. *Anal. Chem.* **1994**, *66*, 126-133.
- (265) Morris, H. R.; Paxton, T.; Dell, A.; Langhorne, J.; Berg, M.; Bordoli, R. S.; Hoyes, J.; Bateman, R. H. High Sensitivity Collisionally-Activated Decomposition Tandem Mass Spectrometry on a Novel Quadrupole/Orthogonal-Acceleration Time-of-Flight Mass Spectrometer. *Rapid Commun. Mass Spectrom.* **1996**, *10*, 889-896.
- (266) Makarov, A. Electrostatic Axially Harmonic Orbital Trapping: A High-Performance Technique of Mass Analysis. *Anal. Chem.* **2000**, *72*, 1156-1162.
- (267) Hardman, M.; Makarov, A. A. Interfacing the Orbitrap Mass Analyzer to an Electrospray Ion Source. *Anal. Chem.* **2003**, *75*, 1699-1705.
- (268) Fuerstenau, S. D.; Benner, W. H.; Thomas, J. J.; Brugidou, C.; Bothner, B.; Siuzdak, G. Mass Spectrometry of an Intact Virus. *Angew. Chem. Int. Ed.* **2001**, *40*, 541-544.
- (269) Siuzdak, G.; Bothner, B.; Yeager, M.; Brugidou, C.; Fauquet, C. M.; Hoey, K.; Change, C.-M. Mass Spectrometry and Viral Analysis. *Chem. Biol.* **1996**, *3*, 45-48.
- (270) Barrera, N. P.; Di Bartolo, N.; Booth, P. J.; Robinson, C. V. Micelles Protect Membrane Complexes from Solution to Vacuum. *Science* **2008**, *321*, 243-246.
- (271) Laganowsky, A.; Reading, E.; Hopper, J. T. S.; Robinson, C. V. Mass Spectrometry of Intact Membrane Protein Complexes. *Nat. Protoc.* **2013**, *8*, 639-651.
- (272) Marty, M. T.; Zhang, H.; Cui, W. D.; Blankenship, R. E.; Gross, M. L.; Sligar, S. G. Native Mass Spectrometry Characterization of Intact Nanodisc Lipoprotein Complexes. *Anal. Chem.* **2012**, *84*, 8957-8960.

- (273) Hopper, J. T. S.; Yu, Y. T. C.; Li, D. F.; Raymond, A.; Bostock, M.; Liko, I.; Mikhailov, V.; Laganowsky, A.; Benesch, J. L. P.; Caffrey, M.; Nietlispach, D.; Robinson, C. V. Detergent-Free Mass Spectrometry of Membrane Protein Complexes. *Nat. Methods* **2013**, *10*, 1206-1208.
- (274) Leney, A. C.; Fan, X.; Kitova, E. N.; Klassen, J. S. Nanodiscs and Electrospray Ionization Mass Spectrometry: A Tool for Screening Glycolipids against Proteins. *Anal. Chem.* **2014**, *86*, 5271-5277.
- (275) Leney, A. C.; McMorran, L. M.; Radford, S. E.; Ashcroft, A. E. Amphipathic Polymers Enable the Study of Functional Membrane Proteins in the Gas Phase. *Anal. Chem.* **2012**, *84*, 9841-9847.
- (276) Watkinson, T. G.; Calabrese, A. N.; Giusti, F.; Zoonens, M.; Radford, S. E.; Ashcroft, A. E. Systematic Analysis of the Use of Amphipathic Polymers for Studies of Outer Membrane Proteins Using Mass Spectrometry. *Int. J. Mass Spectrom.* **2015**, *391*, 54-61.
- (277) Olivova, P.; Chen, W.; Chakraborty, A. B.; Gebler, J. C. Determination of N-Glycosylation Sites and Site Heterogeneity in a Monoclonal Antibody by Electrospray Quadrupole Ion-Mobility Time-of-Flight Mass Spectrometry. *Rapid Commun. Mass Spectrom.* **2008**, *22*, 29-40.
- (278) Liko, I.; Allison, T. M.; Hopper, J. T. S.; Robinson, C. V. Mass Spectrometry Guided Structural Biology. *Curr. Opin. Struct. Biol.* **2016**, *40*, 136-144.
- (279) van Duijn, E. Current Limitations in Native Mass Spectrometry Based Structural Biology. *J. Am. Soc. Mass Spectrom.* **2010**, *21*, 971-978.
- (280) Benesch, J. L. P.; Ruotolo, B. T. Mass Spectrometry: Come of Age for Structural and Dynamical Biology. *Curr. Opin. Struct. Biol.* **2011**, *21*, 641-649.
- (281) Wang, W.; Kitova, E. N.; Klassen, J. S. Nonspecific Protein–Carbohydrate Complexes Produced by Nanoelectrospray Ionization. Factors Influencing Their Formation and Stability. *Anal. Chem.* **2005**, *77*, 3060-3071.
- (282) Miller, Z. M.; Zhang, J. D.; Donald, W. A.; Prell, J. S. Gas-Phase Protonation Thermodynamics of Biological Lipids: Experiment, Theory, and Implications. *Anal. Chem.* **2020**, *92*, 10365-10374.
- (283) Keener, J. E.; Zambrano, D. E.; Zhang, G.; Zak, C. K.; Reid, D. J.; Deodhar, B. S.; Pemberton, J. E.; Prell, J. S.; Marty, M. T. Chemical Additives Enable Native Mass Spectrometry Measurement of Membrane Protein Oligomeric State within Intact Nanodiscs. *J. Am. Chem. Soc.* **2019**, *141*, 1054-1061.
- (284) Benesch, J. L. P.; Robinson, C. V. Mass Spectrometry of Macromolecular Assemblies: Preservation and Dissociation. *Curr. Opin. Struct. Biol.* **2006**, *16*, 245-251.

- (285) McLuckey, S. A.; Goeringer, D. E. Slow Heating Methods in Tandem Mass Spectrometry. *J. Mass Spectrom.* **1997**, *32*, 461-474.
- (286) Zhou, M.; Lantz, C.; Brown, K. A.; Ge, Y.; Paša-Tolić, L.; Loo, J. A.; Lermyte, F. Higher-Order Structural Characterisation of Native Proteins and Complexes by Top-Down Mass Spectrometry. *Chem. Sci.* **2020**, *11*, 12918-12936.
- (287) Li, H. L.; Wolff, J. J.; Van Orden, S. L.; Loo, J. A. Native Top-Down Electrospray Ionization-Mass Spectrometry of 158 kDa Protein Complex by High-Resolution Fourier Transform Ion Cyclotron Resonance Mass Spectrometry. *Anal. Chem.* **2014**, *86*, 317-320.
- (288) Zhou, M.; Liu, W.; Shaw, J. B. Charge Movement and Structural Changes in the Gas-Phase Unfolding of Multimeric Protein Complexes Captured by Native Top-Down Mass Spectrometry. *Anal. Chem.* **2020**, *92*, 1788-1795.
- (289) Zubarev, R. A.; Kelleher, N. L.; McLafferty, F. W. Electron Capture Dissociation of Multiply Charged Protein Cations. A Nonergodic Process. *J. Am. Chem. Soc.* **1998**, *120*, 3265-3266.
- (290) Coon, J. J.; Shabanowitz, J.; Hunt, D. F.; Syka, J. E. P. Electron Transfer Dissociation of Peptide Anions. *J. Am. Soc. Mass Spectrom.* **2005**, *16*, 880-882.
- (291) Holden, D. D.; Brodbelt, J. S. Ultraviolet Photodissociation of Native Proteins Following Proton Transfer Reactions in the Gas Phase. *Anal. Chem.* **2016**, *88*, 12354-12362.
- (292) O'Brien, J. P.; Li, W.; Zhang, Y.; Brodbelt, J. S. Characterization of Native Protein Complexes Using Ultraviolet Photodissociation Mass Spectrometry. *J. Am. Chem. Soc.* **2014**, *136*, 12920-12928.
- (293) Reilly, J. P. Ultraviolet Photofragmentation of Biomolecular Ions. *Mass Spectrom. Rev.* **2009**, *28*, 425-447.
- (294) Marzluff, E. M.; Campbell, S.; Rodgers, M. T.; Beauchamp, J. L. Collisional Activation of Large Molecules Is an Efficient Process. *J. Am. Chem. Soc.* **1994**, *116*, 6947-6948.
- (295) Borysik, A. J.; Robinson, C. V. Formation and Dissociation Processes of Gas-Phase Detergent Micelles. *Langmuir* **2012**, *28*, 7160-7167.
- (296) Brodbelt, J. S.; Wilson, J. J. Infrared Multiphoton Dissociation in Quadrupole Ion Traps. *Mass Spectrom. Rev.* **2009**, *28*, 390-424.
- (297) Cotham, V. C.; Shaw, J. B.; Brodbelt, J. S. High-Throughput Bioconjugation for Enhanced 193 nm Photodissociation Via Droplet Phase Initiated Ion/Ion Chemistry Using a Front-End Dual Spray Reactor. *Anal. Chem.* **2015**, *87*, 9396-9402.

- (298) Lermyte, F.; Williams, J. P.; Brown, J. M.; Martin, E. M.; Sobott, F. Extensive Charge Reduction and Dissociation of Intact Protein Complexes Following Electron Transfer on a Quadrupole-Ion Mobility-Time-of-Flight MS. *J. Am. Soc. Mass Spectrom.* **2015**, *26*, 1068-1076.
- (299) Nesatyy, V. J.; Laskin, J. Dissociation of Noncovalent Protein Complexes by Triple Quadrupole Tandem Mass Spectrometry: Comparison of Monte Carlo Simulation and Experiment. *Int. J. Mass Spectrom.* **2002**, *221*, 245-262.
- (300) Popa, V.; Trecroce, D. A.; McAllister, R. G.; Konermann, L. Collision-Induced Dissociation of Electrosprayed Protein Complexes: An All-Atom Molecular Dynamics Model with Mobile Protons. *J. Phys. Chem. B* **2016**, *120*, 5114-5124.
- (301) Rabuck-Gibbons, J. N.; Keating, J. E.; Ruotolo, B. T. Collision Induced Unfolding and Dissociation Differentiates ATP-Competitive from Allosteric Protein Tyrosine Kinase Inhibitors. *Int. J. Mass Spectrom.* **2018**, *427*, 151-156.
- (302) Schwartz, B. L.; Bruce, J. E.; Anderson, G. A.; Hofstadler, S. A.; Rockwood, A. L.; Smith, R. D.; Chilkoti, A.; Stayton, P. S. Dissociation of Tetrameric Ions of Noncovalent Streptavidin Complexes Formed by Electrospray Ionization. *J. Am. Soc. Mass Spectrom.* **1995**, *6*, 459-465.
- (303) Shaw, J. B.; Li, W.; Holden, D. D.; Zhang, Y.; Griep-Raming, J.; Fellers, R. T.; Early, B. P.; Thomas, P. M.; Kelleher, N. L.; Brodbelt, J. S. Complete Protein Characterization Using Top-Down Mass Spectrometry and Ultraviolet Photodissociation. *J. Am. Chem. Soc.* **2013**, *135*, 12646-12651.
- (304) Allison, T. M.; Barran, P.; Benesch, J. L. P.; Cianferani, S.; Degiacomi, M. T.; Gabelica, V.; Grandori, R.; Marklund, E. G.; Menneteau, T.; Migas, L. G.; Politis, A.; Sharon, M.; Sobott, F.; Thalassinou, K. Software Requirements for the Analysis and Interpretation of Native Ion Mobility Mass Spectrometry Data. *Anal. Chem.* **2020**, *92*, 10881-10890.
- (305) Peng, W.-P.; Chou, S.-W.; Patil, A. A. Measuring Masses of Large Biomolecules and Bioparticles Using Mass Spectrometric Techniques. *Analyst* **2014**, *139*, 3507-3523.
- (306) Sharon, M. How Far Can We Go with Structural Mass Spectrometry of Protein Complexes? *J. Am. Soc. Mass Spectrom.* **2010**, *21*, 487-500.
- (307) Tassi, M.; De Vos, J.; Chatterjee, S.; Sobott, F.; Bones, J.; Eeltink, S. Advances in Native High-Performance Liquid Chromatography and Intact Mass Spectrometry for the Characterization of Biopharmaceutical Products. *J. Sep. Sci.* **2018**, *41*, 125-144.
- (308) Bults, P.; Spanov, B.; Olaleye, O.; van de Merbel, N. C.; Bischoff, R. Intact Protein Bioanalysis by Liquid Chromatography – High-Resolution Mass Spectrometry. *J. Chromatogr. B* **2019**, *1110-1111*, 155-167.

- (309) Gahoual, R.; Heidenreich, A.-K.; Somsen, G. W.; Bulau, P.; Reusch, D.; Wuhrer, M.; Haberger, M. Detailed Characterization of Monoclonal Antibody Receptor Interaction Using Affinity Liquid Chromatography Hyphenated to Native Mass Spectrometry. *Anal. Chem.* **2017**, *89*, 5404-5412.
- (310) Ehkirch, A.; Hernandez-Alba, O.; Colas, O.; Beck, A.; Guillarme, D.; Cianféroni, S. Hyphenation of Size Exclusion Chromatography to Native Ion Mobility Mass Spectrometry for the Analytical Characterization of Therapeutic Antibodies and Related Products. *J. Chromatogr. B* **2018**, *1086*, 176-183.
- (311) Haberger, M.; Heidenreich, A.-K.; Hook, M.; Fichtl, J.; Lang, R.; Cymer, F.; Adibzadeh, M.; Kuhne, F.; Wegele, H.; Reusch, D.; Bonnington, L.; Bulau, P. Multiattribute Monitoring of Antibody Charge Variants by Cation-Exchange Chromatography Coupled to Native Mass Spectrometry. *J. Am. Soc. Mass Spectrom.* **2021**, *32*, 2062-2071.
- (312) Haberger, M.; Leiss, M.; Heidenreich, A.-K.; Pester, O.; Hafenmair, G.; Hook, M.; Bonnington, L.; Wegele, H.; Haindl, M.; Reusch, D.; Bulau, P. Rapid Characterization of Biotherapeutic Proteins by Size-Exclusion Chromatography Coupled to Native Mass Spectrometry. *mAbs* **2016**, *8*, 331-339.
- (313) Yan, Y.; Xing, T.; Wang, S.; Daly, T. J.; Li, N. Online Coupling of Analytical Hydrophobic Interaction Chromatography with Native Mass Spectrometry for the Characterization of Monoclonal Antibodies and Related Products. *J. Pharm. Biomed. Anal.* **2020**, *186*, 113313.
- (314) Yan, Y.; Liu, A. P.; Wang, S.; Daly, T. J.; Li, N. Ultrasensitive Characterization of Charge Heterogeneity of Therapeutic Monoclonal Antibodies Using Strong Cation Exchange Chromatography Coupled to Native Mass Spectrometry. *Anal. Chem.* **2018**, *90*, 13013-13020.
- (315) Yan, Y.; Xing, T.; Wang, S.; Daly, T. J.; Li, N. Coupling Mixed-Mode Size Exclusion Chromatography with Native Mass Spectrometry for Sensitive Detection and Quantitation of Homodimer Impurities in Bispecific IgG. *Anal. Chem.* **2019**, *91*, 11417-11424.
- (316) Ma, F.; Raoufi, F.; Bailly, M. A.; Fayadat-Dilman, L.; Tomazela, D. Hyphenation of Strong Cation Exchange Chromatography to Native Mass Spectrometry for High Throughput Online Characterization of Charge Heterogeneity of Therapeutic Monoclonal Antibodies. *mAbs* **2020**, *12*, 1763762.
- (317) Füssl, F.; Trappe, A.; Cook, K.; Scheffler, K.; Fitzgerald, O.; Bones, J. Comprehensive Characterisation of the Heterogeneity of Adalimumab Via Charge Variant Analysis Hyphenated On-Line to Native High Resolution Orbitrap Mass Spectrometry. *mAbs* **2019**, *11*, 116-128.

- (318) Füssl, F.; Cook, K.; Scheffler, K.; Farrell, A.; Mittermayr, S.; Bones, J. Charge Variant Analysis of Monoclonal Antibodies Using Direct Coupled pH Gradient Cation Exchange Chromatography to High-Resolution Native Mass Spectrometry. *Anal. Chem.* **2018**, *90*, 4669-4676.
- (319) Jooß, K.; McGee, J. P.; Melani, R. D.; Kelleher, N. L. Standard Procedures for Native CZE-MS of Proteins and Protein Complexes up to 800 kDa. *Electrophoresis* **2021**, *42*, 1050-1059.
- (320) Dykstra, A. B.; Flick, T. G.; Lee, B.; Blue, L. E.; Angell, N. Chip-Based Capillary Zone Electrophoresis Mass Spectrometry for Rapid Resolution and Quantitation of Critical Quality Attributes in Protein Biotherapeutics. *J. Am. Soc. Mass Spectrom.* **2021**, *32*, 1952-1963.
- (321) Shen, X.; Liang, Z.; Xu, T.; Yang, Z.; Wang, Q.; Chen, D.; Pham, L.; Du, W.; Sun, L. Investigating Native Capillary Zone Electrophoresis-Mass Spectrometry on a High-End Quadrupole-Time-of-Flight Mass Spectrometer for the Characterization of Monoclonal Antibodies. *Int. J. Mass Spectrom.* **2021**, *462*, 116541.
- (322) Jooß, K.; Schachner, L. F.; Watson, R.; Gillespie, Z. B.; Howard, S. A.; Cheek, M. A.; Meiners, M. J.; Sobh, A.; Licht, J. D.; Keogh, M.-C.; Kelleher, N. L. Separation and Characterization of Endogenous Nucleosomes by Native Capillary Zone Electrophoresis–Top-Down Mass Spectrometry. *Anal. Chem.* **2021**, *93*, 5151-5160.
- (323) Le-Minh, V.; Tran, N. T.; Makky, A.; Rosilio, V.; Taverna, M.; Smadja, C. Capillary Zone Electrophoresis-Native Mass Spectrometry for the Quality Control of Intact Therapeutic Monoclonal Antibodies. *J. Chromatogr. A* **2019**, *1601*, 375-384.
- (324) Gstöttner, C.; Nicolardi, S.; Habegger, M.; Reusch, D.; Wuhrer, M.; Domínguez-Vega, E. Intact and Subunit-Specific Analysis of Bispecific Antibodies by Sheathless CE-MS. *Anal. Chim. Acta* **2020**, *1134*, 18-27.
- (325) Han, M.; Rock, B. M.; Pearson, J. T.; Rock, D. A. Intact Mass Analysis of Monoclonal Antibodies by Capillary Electrophoresis—Mass Spectrometry. *J. Chromatogr. B* **2016**, *1011*, 24-32.
- (326) Yang, Y.; Du, Y.; Kaltashov, I. A. The Utility of Native MS for Understanding the Mechanism of Action of Repurposed Therapeutics in COVID-19: Heparin as a Disruptor of the SARS-CoV-2 Interaction with Its Host Cell Receptor. *Anal. Chem.* **2020**, *92*, 10930-10934.

- (327) Sacco, M. D.; Ma, C.; Lagarias, P.; Gao, A.; Townsend, J. A.; Meng, X.; Dube, P.; Zhang, X.; Hu, Y.; Kitamura, N.; Hurst, B.; Tarbet, B.; Marty, M. T.; Kolocouris, A.; Xiang, Y.; Chen, Y.; Wang, J. Structure and Inhibition of the SARS-CoV-2 Main Protease Reveal Strategy for Developing Dual Inhibitors against M^{pro} and Cathepsin L. *Sci. Adv.* **2020**, *6*, eabe0751.
- (328) Mehaffey, M. R.; Lee, J.; Jung, J.; Lanzillotti, M. B.; Escobar, E. E.; Morgenstern, K. R.; Georgiou, G.; Brodbelt, J. S. Mapping a Conformational Epitope of Hemagglutinin a Using Native Mass Spectrometry and Ultraviolet Photodissociation. *Anal. Chem.* **2020**, *92*, 11869-11878.
- (329) Zhu, W.; Li, M.; Zhang, J. Integrating Intact Mass Analysis and Middle-Down Mass Spectrometry Approaches to Effectively Characterize Trastuzumab and Adalimumab Structural Heterogeneity. *J. Proteome Res.* **2021**, *20*, 270-278.
- (330) Liu, M.; Van Voorhis, W. C.; Quinn, R. J. Development of a Target Identification Approach Using Native Mass Spectrometry. *Sci. Rep.* **2021**, *11*, 2387.
- (331) Campuzano, I. D. G.; Sandoval, W. Denaturing and Native Mass Spectrometric Analytics for Biotherapeutic Drug Discovery Research: Historical, Current, and Future Personal Perspectives. *J. Am. Soc. Mass Spectrom.* **2021**, *32*, 1861-1885.
- (332) Kellie, J. F.; Tran, J. C.; Jian, W.; Jones, B.; Mehl, J. T.; Ge, Y.; Henion, J.; Bateman, K. P. Intact Protein Mass Spectrometry for Therapeutic Protein Quantitation, Pharmacokinetics, and Biotransformation in Preclinical and Clinical Studies: An Industry Perspective. *J. Am. Soc. Mass Spectrom.* **2021**, *32*, 1886-1900.
- (333) Terral, G.; Beck, A.; Cianfèrani, S. Insights from Native Mass Spectrometry and Ion Mobility-Mass Spectrometry for Antibody and Antibody-Based Product Characterization. *J. Chromatogr. B* **2016**, *1032*, 79-90.
- (334) Kazarian, A. A.; Barnhart, W.; Campuzano, I. D. G.; Cabrera, J.; Fitch, T.; Long, J.; Sham, K.; Wu, B.; Murray, J. K. Purification of Guanine-Quadruplex Using Monolithic Stationary Phase under Ion-Exchange Conditions. *J. Chromatogr. A* **2020**, *1634*, 461633.
- (335) Skeene, K.; Khatri, K.; Soloviev, Z.; Laphorn, C. Current Status and Future Prospects for Ion-Mobility Mass Spectrometry in the Biopharmaceutical Industry. *Biochim. Biophys. Acta Proteins Proteom.* **2021**, 140697.
- (336) Zhang, Z.; Hug, C.; Tao, Y.; Bitsch, F.; Yang, Y. Solving Complex Biologics Truncation Problems by Top-Down Mass Spectrometry. *J. Am. Soc. Mass Spectrom.* **2021**, *32*, 1928-1935.

- (337) Campuzano, I. D. G.; Robinson, J. H.; Hui, J. O.; Shi, S. D. H.; Netirojjanakul, C.; Nshanian, M.; Egea, P. F.; Lippens, J. L.; Bagal, D.; Loo, J. A.; Bern, M. Native and Denaturing Ms Protein Deconvolution for Biopharma: Monoclonal Antibodies and Antibody–Drug Conjugates to Polydisperse Membrane Proteins and Beyond. *Anal. Chem.* **2019**, *91*, 9472-9480.
- (338) Patrick, J. W.; Laganowsky, A. Probing Heterogeneous Lipid Interactions with Membrane Proteins Using Mass Spectrometry. In *Lipid-Protein Interactions: Methods and Protocols*; Kleinschmidt, J. H., Ed.; Springer New York, 2019; pp 175-190.
- (339) Skilling, J. Data Analysis: The Maximum Entropy Method. *Nature* **1984**, *309*, 748-749.
- (340) Shannon, C. E. A Mathematical Theory of Communication. *Bell Sys. Tech. J.* **1948**, *27*, 379-423.
- (341) Shore, J.; Johnson, R. Axiomatic Derivation of the Principle of Maximum Entropy and the Principle of Minimum Cross-Entropy. *IEEE Trans. Inf. Theory* **1980**, *26*, 26-37.
- (342) Tikochinsky, Y.; Tishby, N. Z.; Levine, R. D. Consistent Inference of Probabilities for Reproducible Experiments. *Phys. Rev. Lett.* **1984**, *52*, 1357-1360.
- (343) Ferrige, A. G.; Seddon, M. J.; Green, B. N.; Jarvis, S. A.; Skilling, J.; Staunton, J. Disentangling Electrospray Spectra with Maximum Entropy. *Rapid Commun. Mass Spectrom.* **1992**, *6*, 707-711.
- (344) Ferrige, A. G.; Seddon, M. J.; Jarvis, S.; Skilling, J.; Aplin, R. Maximum Entropy Deconvolution in Electrospray Mass Spectrometry. *Rapid Commun. Mass Spectrom.* **1991**, *5*, 374-377.
- (345) Ferrige, A. G.; Seddon, M. J.; Jarvis, S.; Skilling, J.; Welch, J. The Application of MaxEnt to Electrospray Mass Spectrometry. In *Maximum Entropy and Bayesian Methods: Seattle, 1991*; Smith, C. R.; Erickson, G. J.; Neudorfer, P. O., Eds.; Springer Netherlands, 1992; pp 327-335.
- (346) Beck, A.; Wagner-Rousset, E.; Bussat, M.-C.; Lokteff, M.; Klinguer-Hamour, C.; Haeuw, J.-F.; Goetsch, L.; Wurch, T.; Van Dorsselaer, A.; Corvaia, N. Trends in Glycosylation, Glycoanalysis and Glycoengineering of Therapeutic Antibodies and Fc-Fusion Proteins. *Curr. Pharm. Biotechnol.* **2008**, *9*, 482-501.
- (347) Yu, Y.; Liu, H.; Yu, Z.; Witkowska, H. E.; Cheng, Y. Stoichiometry of Nucleotide Binding to Proteasome AAA+ ATPase Hexamer Established by Native Mass Spectrometry. *Mol. Cell. Proteom.* **2020**, *19*, 1997-2015.

- (348) Thompson, N. J.; Rosati, S.; Rose, R. J.; Heck, A. J. R. The Impact of Mass Spectrometry on the Study of Intact Antibodies: From Post-Translational Modifications to Structural Analysis. *Chem. Commun.* **2013**, *49*, 538-548.
- (349) Sanglier, S.; Leize, E.; van Dorsselaer, A.; Zal, F. Comparative ESI-MS Study of ~2.2 MDa Native Hemocyanins from Deep-Sea and Shore Crabs: From Protein Oligomeric State to Biotope. *J. Am. Soc. Mass Spectrom.* **2003**, *14*, 419-429.
- (350) Sanglier, S.; Ramström, H.; Haiech, J.; Leize, E.; van Dorsselaer, A. Electrospray Ionization Mass Spectrometry Analysis Revealed a ~310 kDa Noncovalent Hexamer of HPr Kinase/Phosphatase from *Bacillus subtilis*. *Int. J. Mass Spectrom.* **2002**, *219*, 681-696.
- (351) Zal, F.; Green, B. N.; Lallier, F. H.; Toulmond, A. Investigation by Electrospray Ionization Mass Spectrometry of the Extracellular Hemoglobin from the Polychaete Annelid *Alvinella pompejana*: An Unusual Hexagonal Bilayer Hemoglobin. *Biochemistry* **1997**, *36*, 11777-11786.
- (352) Robinson, C. V.; Chung, E. W.; Kragelund, B. B.; Knudsen, J.; Aplin, R. T.; Poulsen, F. M.; Dobson, C. M. Probing the Nature of Noncovalent Interactions by Mass Spectrometry. A Study of Protein–CoA Ligand Binding and Assembly. *J. Am. Chem. Soc.* **1996**, *118*, 8646-8653.
- (353) Lengqvist, J.; Svensson, R.; Evergren, E.; Morgenstern, R.; Griffiths, W. J. Observation of an Intact Noncovalent Homotrimer of Detergent-Solubilized Rat Microsomal Glutathione Transferase-1 by Electrospray Mass Spectrometry. *J. Biol. Chem.* **2004**, *279*, 13311-13316.
- (354) Ashcroft, A. E.; Brinker, A.; Coyle, J. E.; Weber, F.; Kaiser, M.; Moroder, L.; Parsons, M. R.; Jager, J.; Hartl, U. F.; Hayer-Hartl, M.; Radford, S. E. Structural Plasticity and Noncovalent Substrate Binding in the GroEL Apical Domain: A Study Using Electrospray Ionization Mass Spectrometry and Fluorescence Binding Studies. *J. Biol. Chem.* **2002**, *277*, 33115-33126.
- (355) Pinkse, M. W. H.; Heck, A. J. R.; Rumpel, K.; Pullen, F. Probing Noncovalent Protein–Ligand Interactions of the cGMP-Dependent Protein Kinase Using Electrospray Ionization Time of Flight Mass Spectrometry. *J. Am. Soc. Mass Spectrom.* **2004**, *15*, 1392-1399.
- (356) Bolgar, M. S.; Gaskell, S. J. Determination of the Sites of 4-Hydroxy-2-Nonenal Adduction to Protein by Electrospray Tandem Mass Spectrometry. *Anal. Chem.* **1996**, *68*, 2325-2330.
- (357) Bennett, K. L.; Smith, S. V.; Lambrecht, R. M.; Truscott, R. J. W.; Sheil, M. M. Rapid Characterization of Chemically-Modified Proteins by Electrospray Mass Spectrometry. *Bioconjugate Chem.* **1996**, *7*, 16-22.

- (358) De, B. K.; Woolfitt, A. R.; Barr, J. R.; Daneshvar, M. I.; Sampson, J. S.; Ades, E. W.; Carlone, G. M. Analysis of Recombinant Acylated Pneumococcal Surface Adhesin a of *Streptococcus pneumoniae* by Mass Spectrometry. *Arch. Biochem. Biophys.* **2003**, *419*, 147-157.
- (359) White, H. D.; Ashcroft, A. E. Real-Time Measurement of Myosin–Nucleotide Noncovalent Complexes by Electrospray Ionization Mass Spectrometry. *Biophys. J.* **2007**, *93*, 914-919.
- (360) Tahallah, N.; van den Heuvel, R. H. H.; van den Berg, W. A. M.; Maier, C. S.; van Berkel, W. J. H.; Heck, A. J. R. Cofactor-Dependent Assembly of the Flavoenzyme Vanillyl-Alcohol Oxidase. *J. Biol. Chem.* **2002**, *277*, 36425-36432.
- (361) Lamkemeyer, T.; Zeis, B.; Decker, H.; Jaenicke, E.; Waschbüsch, D.; Gebauer, W.; Markl, J.; Meissner, U.; Rousselot, M.; Zal, F.; Nicholson, G. J.; Paul, R. J. Molecular Mass of Macromolecules and Subunits and the Quaternary Structure of Hemoglobin from the Microcrustacean *Daphnia magna*. *FEBS J.* **2006**, *273*, 3393-3410.
- (362) Brockwell, D.; Yu, L.; Cooper, S.; Mcclelland, S.; Cooper, A.; Attwood, D.; Gaskell, S. J.; Barber, J. Physicochemical Consequences of the Perdeuteration of Glutathione S-Transferase from *S. Japonicum*. *Protein Sci.* **2001**, *10*, 572-580.
- (363) Green, B. N.; Sannes-Lowery, K. A.; Loo, J. A.; Satterlee, J. D.; Kuchumov, A. R.; Walz, D. A.; Vinogradov, S. N. Electrospray Ionization Mass Spectrometric Study of the Multiple Intracellular Monomeric and Polymeric Hemoglobins of *Glycera dibranchiata*. *J. Protein Chem.* **1998**, *17*, 85-97.
- (364) Said, N.; Gahoual, R.; Kuhn, L.; Beck, A.; François, Y.-N.; Leize-Wagner, E. Structural Characterization of Antibody Drug Conjugate by a Combination of Intact, Middle-up and Bottom-up Techniques Using Sheathless Capillary Electrophoresis – Tandem Mass Spectrometry as NanoESI Infusion Platform and Separation Method. *Anal. Chim. Acta* **2016**, *918*, 50-59.
- (365) Campuzano, I. D. G.; Li, H.; Bagal, D.; Lippens, J. L.; Svitel, J.; Kurzeja, R. J. M.; Xu, H.; Schnier, P. D.; Loo, J. A. Native MS Analysis of Bacteriorhodopsin and an Empty Nanodisc by Orthogonal Acceleration Time-of-Flight, Orbitrap and Ion Cyclotron Resonance. *Anal. Chem.* **2016**, *88*, 12427-12436.
- (366) Zhang, Z.; Guan, S.; Marshall, A. G. Enhancement of the Effective Resolution of Mass Spectra of High-Mass Biomolecules by Maximum Entropy-Based Deconvolution to Eliminate the Isotopic Natural Abundance Distribution. *J. Am. Soc. Mass Spectrom.* **1997**, *8*, 659-670.
- (367) Bruker Daltonik GmbH. *Dataanalysis 5.0*. **2017**; (accessed August 19, 2021).

- (368) Cottrell, J. C.; Green, B. N. *MaxEnt: An Essential Maximum Entropy Based Tool for Interpreting Multiply-Charged Electrospray Data*. **1998**; <https://www.waters.com/webassets/cms/library/docs/an212.pdf> (accessed August 19, 2021).
- (369) SCIEX. *Bio Tool Kit: A Complete Set of Tools for Biomolecule Characterization*. **2017**; <https://www.sciex.com/content/dam/SCIEX/pdf/tech-notes/all/BioToolKit-peakview.pdf> (accessed August 19, 2021).
- (370) Agilent Technologies. *Agilent Masshunter Bioconfirm Software*, version B.04.00; Agilent Technologies: Santa Clara, CA, 2012.
- (371) Hagen, J. J.; Monnig, C. A. Method for Estimating Molecular Mass from Electrospray Spectra. *Anal. Chem.* **1994**, *66*, 1877-1883.
- (372) Hopkins, C. E.; O'Connor, P. B.; Allen, K. N.; Costello, C. E.; Tolan, D. R. Chemical-Modification Rescue Assessed by Mass Spectrometry Demonstrates That Gamma-Thia-Lysine Yields the Same Activity as Lysine in Aldolase. *Protein Sci.* **2002**, *11*, 1591-1599.
- (373) Bunk, D. M.; Welch, M. J. Electrospray Ionization Mass Spectrometry for the Quantitation of Albumin in Human Serum. *J. Am. Soc. Mass Spectrom.* **1997**, *8*, 1247-1254.
- (374) Upmacis, R. K.; Hajjar, D. P.; Chait, B. T.; Mirza, U. A. Direct Observation of Nitrosylated Heme in Myoglobin and Hemoglobin by Electrospray Ionization Mass Spectrometry. *J. Am. Chem. Soc.* **1997**, *119*, 10424-10429.
- (375) Read, S. M.; Currie, G.; Bacic, A. Analysis of the Structural Heterogeneity of Laminarin by Electrospray-Ionisation-Mass Spectrometry. *Carbohydr. Res.* **1996**, *281*, 187-201.
- (376) Lei, Q. P.; Cui, X.; Kurtz, D. M.; Amster, I. J.; Chernushevich, I. V.; Standing, K. G. Electrospray Mass Spectrometry Studies of Non-Heme Iron-Containing Proteins. *Anal. Chem.* **1998**, *70*, 1838-1846.
- (377) Donald, L. J.; Chernushevich, I. V.; Zhou, J.; Verentchikov, A.; Poppe-Schriemer, N.; Hosfield, D. J.; Westmore, J. B.; Ens, W.; Duckworth, H. W.; Standing, K. G. Preparation and Properties of Pure, Full-Length Ic1R Protein of *Escherichia coli*. Use of Time-of-Flight Mass Spectrometry to Investigate the Problems Encountered. *Protein Sci.* **1996**, *5*, 1613-1624.
- (378) Labowsky, M.; Whitehouse, C.; Fenn, J. B. Three-Dimensional Deconvolution of Multiply Charged Spectra. *Rapid Commun. Mass Spectrom.* **1993**, *7*, 71-84.
- (379) Snijder, J.; Rose, R. J.; Veessler, D.; Johnson, J. E.; Heck, A. J. R. Studying 18 MDa Virus Assemblies with Native Mass Spectrometry. *Angew. Chem. Int. Ed.* **2013**, *52*, 4020-4023.

- (380) Reinhold, B. B.; Reinhold, V. N. Electrospray Ionization Mass Spectrometry: Deconvolution by an Entropy-Based Algorithm. *J. Am. Soc. Mass Spectrom.* **1992**, *3*, 207-215.
- (381) Zhang, Z. Q.; Marshall, A. G. A Universal Algorithm for Fast and Automated Charge State Deconvolution of Electrospray Mass-to-Charge Ratio Spectra. *J. Am. Soc. Mass Spectrom.* **1998**, *9*, 225-233.
- (382) Ro, S. Y.; Schachner, L. F.; Koo, C. W.; Purohit, R.; Remis, J. P.; Kenney, G. E.; Liauw, B. W.; Thomas, P. M.; Patrie, S. M.; Kelleher, N. L.; Rosenzweig, A. C. Native Top-Down Mass Spectrometry Provides Insights into the Copper Centers of Membrane-Bound Methane Monooxygenase. *Nat. Commun.* **2019**, *10*, 2675.
- (383) Johnson, P.; Philo, M.; Watson, A.; Mills, E. N. C. Rapid Fingerprinting of Milk Thermal Processing History by Intact Protein Mass Spectrometry with Nondenaturing Chromatography. *J. Agric. Food Chem.* **2011**, *59*, 12420-12427.
- (384) Honarvar, E.; Venter, A. R. Ammonium Bicarbonate Addition Improves the Detection of Proteins by Desorption Electrospray Ionization Mass Spectrometry. *J. Am. Soc. Mass Spectrom.* **2017**, *28*, 1109-1117.
- (385) Meng, F.; Cargile, B. J.; Patrie, S. M.; Johnson, J. R.; McLoughlin, S. M.; Kelleher, N. L. Processing Complex Mixtures of Intact Proteins for Direct Analysis by Mass Spectrometry. *Anal. Chem.* **2002**, *74*, 2923-2929.
- (386) Ariza, A.; Garzon, D.; Abánades, D. R.; de los Ríos, V.; Vistoli, G.; Torres, M. J.; Carini, M.; Aldini, G.; Pérez-Sala, D. Protein Haptenation by Amoxicillin: High Resolution Mass Spectrometry Analysis and Identification of Target Proteins in Serum. *J. Proteom.* **2012**, *77*, 504-520.
- (387) Gallagher, E. S.; Hudgens, J. W. Mapping Protein–Ligand Interactions with Proteolytic Fragmentation, Hydrogen/Deuterium Exchange-Mass Spectrometry. In *Methods Enzymol.*, Vol. 566; Kelman, Z., Ed.; Academic Press, 2016; pp 357-404.
- (388) Zhao, T.; King, F. L. Direct Determination of the Primary Binding Site of Cisplatin on Cytochrome *c* by Mass Spectrometry. *J. Am. Soc. Mass Spectrom.* **2009**, *20*, 1141-1147.
- (389) Zhao, T.; King, F. L. Mass-Spectrometric Characterization of Cisplatin Binding Sites on Native and Denatured Ubiquitin. *J. Biol. Inorg. Chem.* **2011**, *16*, 633-639.
- (390) Zheng, H.; Ojha, P. C.; McClean, S.; Black, N. D.; Hughes, J. G.; Shaw, C. Heuristic Charge Assignment for Deconvolution of Electrospray Ionization Mass Spectra. *Rapid Commun. Mass Spectrom.* **2003**, *17*, 429-436.

- (391) Thompson, N. J.; Merdanovic, M.; Ehrmann, M.; van Duijn, E.; Heck, A. J. R. Substrate Occupancy at the Onset of Oligomeric Transitions of DegP. *Structure* **2014**, *22*, 281-290.
- (392) Poliakov, A.; van Duijn, E.; Lander, G.; Fu, C.-Y.; Johnson, J. E.; Prevelige, P. E.; Heck, A. J. R. Macromolecular Mass Spectrometry and Electron Microscopy as Complementary Tools for Investigation of the Heterogeneity of Bacteriophage Portal Assemblies. *J. Struct. Biol.* **2007**, *157*, 371-383.
- (393) Snijder, J.; van de Waterbeemd, M.; Damoc, E.; Denisov, E.; Grinfeld, D.; Bennett, A.; Agbandje-McKenna, M.; Makarov, A.; Heck, A. J. R. Defining the Stoichiometry and Cargo Load of Viral and Bacterial Nanoparticles by Orbitrap Mass Spectrometry. *J. Am. Chem. Soc.* **2014**, *136*, 7295-7299.
- (394) Weiss, V. U.; Bereszczak, J. Z.; Havlik, M.; Kallinger, P.; Gössler, I.; Kumar, M.; Blaas, D.; Marchetti-Deschmann, M.; Heck, A. J. R.; Szymanski, W. W.; Allmaier, G. Analysis of a Common Cold Virus and Its Subviral Particles by Gas-Phase Electrophoretic Mobility Molecular Analysis and Native Mass Spectrometry. *Anal. Chem.* **2015**, *87*, 8709-8717.
- (395) Stengel, F.; Baldwin, A. J.; Bush, M. F.; Hilton, G. R.; Lioe, H.; Basha, E.; Jaya, N.; Vierling, E.; Benesch, J. L. P. Dissecting Heterogeneous Molecular Chaperone Complexes Using a Mass Spectrum Deconvolution Approach. *Chem. Biol.* **2012**, *19*, 599-607.
- (396) Lu, J.; Trnka, M. J.; Roh, S.-H.; Robinson, P. J. J.; Shiau, C.; Fujimori, D. G.; Chiu, W.; Burlingame, A. L.; Guan, S. Improved Peak Detection and Deconvolution of Native Electrospray Mass Spectra from Large Protein Complexes. *J. Am. Soc. Mass Spectrom.* **2015**, *26*, 2141-2151.
- (397) Marcoux, J.; Wang, S. C.; Politis, A.; Reading, E.; Ma, J.; Biggin, P. C.; Zhou, M.; Tao, H.; Zhang, Q.; Chang, G.; Morgner, N.; Robinson, C. V. Mass Spectrometry Reveals Synergistic Effects of Nucleotides, Lipids, and Drugs Binding to a Multidrug Resistance Efflux Pump. *Proc. Natl. Acad. Sci. U. S. A.* **2013**, *110*, 9704-9709.
- (398) Morgner, N.; Schmidt, C.; Beilstein-Edmands, V.; Ebong, I.-O.; Patel, N. A.; Clerico, E. M.; Kirschke, E.; Daturpalli, S.; Jackson, S. E.; Agard, D.; Robinson, C. V. Hsp70 Forms Antiparallel Dimers Stabilized by Post-Translational Modifications to Position Clients for Transfer to Hsp90. *Cell Rep.* **2015**, *11*, 759-769.
- (399) Schmidt, C.; Zhou, M.; Marriott, H.; Morgner, N.; Politis, A.; Robinson, C. V. Comparative Cross-Linking and Mass Spectrometry of an Intact F-Type ATPase Suggest a Role for Phosphorylation. *Nat. Commun.* **2013**, *4*, 1985.

- (400) Schiffrin, B.; Calabrese, A. N.; Devine, P. W. A.; Harris, S. A.; Ashcroft, A. E.; Brockwell, D. J.; Radford, S. E. Skp Is a Multivalent Chaperone of Outer-Membrane Proteins. *Nat. Struct. Mol. Biol.* **2016**, *23*, 786-793.
- (401) Henrich, E.; Peetz, O.; Hein, C.; Laguerre, A.; Hoffmann, B.; Hoffmann, J.; Dötsch, V.; Bernhard, F.; Morgner, N. Analyzing Native Membrane Protein Assembly in Nanodiscs by Combined Non-Covalent Mass Spectrometry and Synthetic Biology. *eLife* **2017**, *6*, e20954.
- (402) Krichel, B.; Falke, S.; Hilgenfeld, R.; Redecke, L.; Uetrecht, C. Processing of the SARS-CoV pp1a/ab nsp7–10 Region. *Biochem. J.* **2020**, *477*, 1009-1019.
- (403) Sauer, P. V.; Timm, J.; Liu, D.; Sitbon, D.; Boeri-Erba, E.; Velours, C.; Mücke, N.; Langowski, J.; Ochsenbein, F.; Almouzni, G.; Panne, D. Insights into the Molecular Architecture and Histone H3-H4 Deposition Mechanism of Yeast Chromatin Assembly Factor 1. *eLife* **2017**, *6*, e23474.
- (404) Dunne, M.; Leicht, S.; Krichel, B.; Mertens, H. D. T.; Thompson, A.; Krijgsveld, J.; Svergun, D. I.; Gómez-Torres, N.; Garde, S.; Uetrecht, C.; Narbad, A.; Mayer, M. J.; Meijers, R. Crystal Structure of the CTP1L Endolysin Reveals How Its Activity Is Regulated by a Secondary Translation Product. *J. Biol. Chem.* **2016**, *291*, 4882-4893.
- (405) Ebong, I.-O.; Beilsten-Edmands, V.; Patel, N. A.; Morgner, N.; Robinson, C. V. The Interchange of Immunophilins Leads to Parallel Pathways and Different Intermediates in the Assembly of Hsp90 Glucocorticoid Receptor Complexes. *Cell Discov.* **2016**, *2*, 16002.
- (406) Macek, P.; Kerfah, R.; Erba, E. B.; Crublet, E.; Moriscot, C.; Schoehn, G.; Amero, C.; Boisbouvier, J. Unraveling Self-Assembly Pathways of the 468-kDa Proteolytic Machine TET2. *Sci. Adv.* **2017**, *3*, e1601601.
- (407) Nitsche, J.; Josts, I.; Heidemann, J.; Mertens, H. D.; Maric, S.; Moulin, M.; Haertlein, M.; Busch, S.; Forsyth, V. T.; Svergun, D. I.; Uetrecht, C.; Tidow, H. Structural Basis for Activation of Plasma-Membrane Ca²⁺-ATPase by Calmodulin. *Commun. Biol.* **2018**, *1*, 206.
- (408) Wallen, J. R.; Zhang, H.; Weis, C.; Cui, W.; Foster, B. M.; Ho, C. M. W.; Hammel, M.; Tainer, J. A.; Gross, M. L.; Ellenberger, T. Hybrid Methods Reveal Multiple Flexibly Linked DNA Polymerases within the Bacteriophage T7 Replisome. *Structure* **2017**, *25*, 157-166.
- (409) Bernal, I.; Börnicke, J.; Heidemann, J.; Svergun, D.; Horstmann, J. A.; Erhardt, M.; Tuukkanen, A.; Uetrecht, C.; Kolbe, M. Molecular Organization of Soluble Type III Secretion System Sorting Platform Complexes. *J. Mol. Biol.* **2019**, *431*, 3787-3803.

- (410) Wittig, S.; Haupt, C.; Hoffmann, W.; Kostmann, S.; Pagel, K.; Schmidt, C. Oligomerisation of Synaptobrevin-2 Studied by Native Mass Spectrometry and Chemical Cross-Linking. *J. Am. Soc. Mass Spectrom.* **2019**, *30*, 149-160.
- (411) Prajapati, S.; Haselbach, D.; Wittig, S.; Patel, M. S.; Chari, A.; Schmidt, C.; Stark, H.; Tittmann, K. Structural and Functional Analyses of the Human PDH Complex Suggest a “Division-of-Labor” Mechanism by Local E1 and E3 Clusters. *Structure* **2019**, *27*, 1124-1136.
- (412) Lu, Y.; Goodson, C.; Blankenship, R. E.; Gross, M. L. Primary and Higher Order Structure of the Reaction Center from the Purple Phototrophic Bacterium *Blastochloris viridis*: A Test for Native Mass Spectrometry. *J. Proteome Res.* **2018**, *17*, 1615-1623.
- (413) Li, S.; Yen, L.; Pastor, W. A.; Johnston, J. B.; Du, J.; Shew, C. J.; Liu, W.; Ho, J.; Stender, B.; Clark, A. T.; Burlingame, A. L.; Daxinger, L.; Patel, D. J.; Jacobsen, S. E. Mouse MORC3 Is a GHKL ATPase That Localizes to H3K4me3 Marked Chromatin. *Proc. Natl. Acad. Sci. U. S. A.* **2016**, *113*, E5108-E5116.
- (414) Larson, A. G.; Elnatan, D.; Keenen, M. M.; Trnka, M. J.; Johnston, J. B.; Burlingame, A. L.; Agard, D. A.; Redding, S.; Narlikar, G. J. Liquid Droplet Formation by HP1 α Suggests a Role for Phase Separation in Heterochromatin. *Nature* **2017**, *547*, 236-240.
- (415) Mishra, S.; Chandler, S. A.; Williams, D.; Claxton, D. P.; Koteiche, H. A.; Stewart, P. L.; Benesch, J. L. P.; McHaourab, H. S. Engineering of a Polydisperse Small Heat-Shock Protein Reveals Conserved Motifs of Oligomer Plasticity. *Structure* **2018**, *26*, 1116-1126.
- (416) Hebling, C. M.; Morgan, C. R.; Stafford, D. W.; Jorgenson, J. W.; Rand, K. D.; Engen, J. R. Conformational Analysis of Membrane Proteins in Phospholipid Bilayer Nanodiscs by Hydrogen Exchange Mass Spectrometry. *Anal. Chem.* **2010**, *82*, 5415-5419.
- (417) Marty, M. T.; Wilcox, K. C.; Klein, W. L.; Sligar, S. G. Nanodisc-Solubilized Membrane Protein Library Reflects the Membrane Proteome. *Anal. Bioanal. Chem.* **2013**, *405*, 4009-4016.
- (418) Walker, L. R.; Marty, M. T. Revealing the Specificity of a Range of Antimicrobial Peptides in Lipid Nanodiscs by Native Mass Spectrometry. *Biochemistry* **2020**, *59*, 2135-2142.
- (419) Reid, D. J.; Keener, J. E.; Wheeler, A. P.; Zambrano, D. E.; Diesing, J. M.; Reinhardt-Szyba, M.; Makarov, A.; Marty, M. T. Engineering Nanodisc Scaffold Proteins for Native Mass Spectrometry. *Anal. Chem.* **2017**, *89*, 11189-11192.

- (420) Reading, E.; Liko, I.; Allison, T. M.; Benesch, J. L. P.; Laganowsky, A.; Robinson, C. V. The Role of the Detergent Micelle in Preserving the Structure of Membrane Proteins in the Gas Phase. *Angew. Chem. Int. Ed.* **2015**, *54*, 4577-4581.
- (421) Tjondro, H. C.; Ugonotti, J.; Kawahara, R.; Chatterjee, S.; Loke, I.; Chen, S.; Soltermann, F.; Hinneburg, H.; Parker, B. L.; Venkatakrisnan, V.; Dieckmann, R.; Grant, O. C.; Bylund, J.; Rodger, A.; Woods, R. J.; Karlsson-Bengtsson, A.; Struwe, W. B.; Thaysen-Andersen, M. Hyper-Truncated Asn355- and Asn391-Glycans Modulate the Activity of Neutrophil Granule Myeloperoxidase. *J. Biol. Chem.* **2021**, *296*, 100144.
- (422) Ahdash, Z.; Lau, A. M.; Byrne, R. T.; Lammens, K.; Stuetzer, A.; Urlaub, H.; Booth, P. J.; Reading, E.; Hopfner, K.-P.; Politis, A. Mechanistic Insight into the Assembly of the HerA–NurA Helicase–Nuclease DNA End Resection Complex. *Nucleic Acids Res.* **2017**, *45*, 12025-12038.
- (423) Campuzano, I. D. G.; Nshanian, M.; Spahr, C.; Lantz, C.; Netirojjanakul, C.; Li, H.; Wongkongkathep, P.; Wolff, J. J.; Loo, J. A. High Mass Analysis with a Fourier Transform Ion Cyclotron Resonance Mass Spectrometer: From Inorganic Salt Clusters to Antibody Conjugates and Beyond. *J. Am. Soc. Mass Spectrom.* **2020**, *31*, 1155-1162.
- (424) Chen, J.; Chiu, C.; Gopalkrishnan, S.; Chen, A. Y.; Olinares, P. D. B.; Saecker, R. M.; Winkelman, J. T.; Maloney, M. F.; Chait, B. T.; Ross, W.; Gourse, R. L.; Campbell, E. A.; Darst, S. A. Stepwise Promoter Melting by Bacterial RNA Polymerase. *Mol. Cell* **2020**, *78*, 275-288.
- (425) VanAernum, Z. L.; Busch, F.; Jones, B. J.; Jia, M.; Chen, Z.; Boyken, S. E.; Sahasrabudde, A.; Baker, D.; Wysocki, V. H. Rapid Online Buffer Exchange for Screening of Proteins, Protein Complexes and Cell Lysates by Native Mass Spectrometry. *Nat. Protoc.* **2020**, *15*, 1132-1157.
- (426) Townsend, J. A.; Keener, J. E.; Miller, Z. M.; Prell, J. S.; Marty, M. T. Imidazole Derivatives Improve Charge Reduction and Stabilization for Native Mass Spectrometry. *Anal. Chem.* **2019**, *91*, 14765-14772.
- (427) Kieuvongngam, V.; Olinares, P. D. B.; Palillo, A.; Oldham, M. L.; Chait, B. T.; Chen, J. Structural Basis of Substrate Recognition by a Polypeptide Processing and Secretion Transporter. *eLife* **2020**, *9*, e51492.
- (428) Mickolajczyk, K. J.; Olinares, P. D. B.; Niu, Y.; Chen, N.; Warrington, S. E.; Sasaki, Y.; Walz, T.; Chait, B. T.; Kapoor, T. M. Long-Range Intramolecular Allostery and Regulation in the Dynein-Like AAA Protein Mdn1. *Proc. Natl. Acad. Sci. U. S. A.* **2020**, *117*, 18459-18469.

- (429) Moghadamchargari, Z.; Huddleston, J.; Shirzadeh, M.; Zheng, X.; Clemmer, D. E.; M. Raushel, F.; Russell, D. H.; Laganowsky, A. Intrinsic GTPase Activity of K-RAS Monitored by Native Mass Spectrometry. *Biochemistry* **2019**, *58*, 3396-3405.
- (430) Lin, C.-W.; McCabe, J. W.; Russell, D. H.; Barondeau, D. P. Molecular Mechanism of ISC Iron–Sulfur Cluster Biogenesis Revealed by High-Resolution Native Mass Spectrometry. *J. Am. Chem. Soc.* **2020**, *142*, 6018-6029.
- (431) Wu, D.; Li, J.; Struwe, W. B.; Robinson, C. V. Probing N-Glycoprotein Microheterogeneity by Lectin Affinity Purification-Mass Spectrometry Analysis. *Chem. Sci.* **2019**, *10*, 5146-5155.
- (432) Matthews, S. J.; Pacholarz, K. J.; France, A. P.; Jowitt, T. A.; Hay, S.; Barran, P. E.; Munro, A. W. MhuD from *Mycobacterium tuberculosis*: Probing a Dual Role in Heme Storage and Degradation. *ACS Infect. Dis.* **2019**, *5*, 1855-1866.
- (433) Cruz, A. R.; den Boer, M. A.; Strasser, J.; Zwarthoff, S. A.; Beurskens, F. J.; de Haas, C. J. C.; Aerts, P. C.; Wang, G.; de Jong, R. N.; Bagnoli, F.; van Strijp, J. A. G.; van Kessel, K. P. M.; Schuurman, J.; Preiner, J.; Heck, A. J. R.; Rooijackers, S. H. M. Staphylococcal Protein A Inhibits Complement Activation by Interfering with IgG Hexamer Formation. *Proc. Natl. Acad. Sci. U. S. A.* **2021**, *118*, e2016772118.
- (434) Ma, C.; Sacco, M. D.; Hurst, B.; Townsend, J. A.; Hu, Y.; Szeto, T.; Zhang, X.; Tarbet, B.; Marty, M. T.; Chen, Y.; Wang, J. Boceprevir, GC-376, and Calpain Inhibitors II, XII Inhibit SARS-CoV-2 Viral Replication by Targeting the Viral Main Protease. *Cell Res.* **2020**, *30*, 678-692.
- (435) Delfosse, V.; Huet, T.; Harrus, D.; Granell, M.; Bourguet, M.; Gardia-Parège, C.; Chiavarina, B.; Grimaldi, M.; Le Mével, S.; Blanc, P.; Huang, D.; Gruszczuk, J.; Demeneix, B.; Cianféroni, S.; Fini, J.-B.; Balaguer, P.; Bourguet, W. Mechanistic Insights into the Synergistic Activation of the RXR–PXR Heterodimer by Endocrine Disruptor Mixtures. *Proc. Natl. Acad. Sci. U. S. A.* **2021**, *118*, e2020551118.
- (436) Marty, M. T. A Universal Score for Deconvolution of Intact Protein and Native Electrospray Mass Spectra. *Anal. Chem.* **2020**, *92*, 4395-4401.
- (437) Peris-Díaz, M. D.; Guran, R.; Zitka, O.; Adam, V.; Krężel, A. Mass Spectrometry-Based Structural Analysis of Cysteine-Rich Metal-Binding Sites in Proteins with Metaodysseus R Software. *J. Proteome Res.* **2021**, *20*, 776-785.
- (438) Reid, D. J.; Diesing, J. M.; Miller, M. A.; Perry, S. M.; Wales, J. A.; Montfort, W. R.; Marty, M. T. MetaUniDec: High-Throughput Deconvolution of Native Mass Spectra. *J. Am. Soc. Mass Spectrom.* **2018**, *30*, 118-127.

- (439) Marty, M. T. Eliminating Artifacts in Electrospray Deconvolution with a SoftMax Function. *J. Am. Soc. Mass Spectrom.* **2019**, *30*, 2174-2177.
- (440) Bern, M.; Kil, Y. J.; Becker, C. Byonic: Advanced Peptide and Protein Identification Software. *Curr. Protoc. Bioinformatics* **2012**, *40*, 13.20.11-13.20.14.
- (441) Bern, M.; Caval, T.; Kil, Y. J.; Tang, W.; Becker, C.; Carlson, E.; Kletter, D.; Sen, K. I.; Galy, N.; Hagemans, D.; Franc, V.; Heck, A. J. R. Parsimonious Charge Deconvolution for Native Mass Spectrometry. *J. Proteome Res.* **2018**, *17*, 1216-1226.
- (442) Campuzano, I. D. G.; Netirojjanakul, C.; Nshanian, M.; Lippens, J. L.; Kilgour, D. P. A.; Van Orden, S.; Loo, J. A. Native-MS Analysis of Monoclonal Antibody Conjugates by Fourier Transform Ion Cyclotron Resonance Mass Spectrometry. *Anal. Chem.* **2018**, *90*, 745-751.
- (443) Leblanc, Y.; Faid, V.; Lauber, M. A.; Wang, Q.; Bihoreau, N.; Chevreux, G. A Generic Method for Intact and Subunit Level Characterization of mAb Charge Variants by Native Mass Spectrometry. *J. Chromatogr. B* **2019**, *1133*, 121814.
- (444) Lin, Y.-H.; Zhu, J.; Meijer, S.; Franc, V.; Heck, A. J. R. Glycoproteogenomics: A Frequent Gene Polymorphism Affects the Glycosylation Pattern of the Human Serum Fetuin/ α -2-HS-Glycoprotein. *Mol. Cell. Proteom.* **2019**, *18*, 1479-1490.
- (445) Neviani, V.; van Deventer, S.; Wörner, T. P.; Xenaki, K. T.; van de Waterbeemd, M.; Rodenburg, R. N. P.; Wortel, I. M. N.; Kuiper, J. K.; Huisman, S.; Granneman, J.; van Bergen en Henegouwen, P. M. P.; Heck, A. J. R.; van Spriell, A. B.; Gros, P. Site-Specific Functionality and Tryptophan Mimicry of Lipidation in Tetraspanin CD9. *FEBS J.* **2020**, *287*, 5323-5344.
- (446) Tseng, Y.-H.; Uetrecht, C.; Yang, S.-C.; Barendregt, A.; Heck, A. J. R.; Peng, W.-P. Game-Theory-Based Search Engine to Automate the Mass Assignment in Complex Native Electrospray Mass Spectra. *Anal. Chem.* **2013**, *85*, 11275-11283.
- (447) Tseng, Y.-H.; Uetrecht, C.; Heck, A. J. R.; Peng, W.-P. Interpreting the Charge State Assignment in Electrospray Mass Spectra of Bioparticles. *Anal. Chem.* **2011**, *83*, 1960-1968.
- (448) Prebyl, B. S.; Cook, K. D. Use of Fourier Transform for Deconvolution of the Unresolved Envelope Observed in Electrospray Ionization Mass Spectrometry of Strongly Ionic Synthetic Polymers. *Anal. Chem.* **2004**, *76*, 127-136.
- (449) Gábor, D. Theory of Communication. *J. Inst. Electr. Eng.* **1946**, *93*, 429-460.
- (450) Cleary, S. P.; Prell, J. S. Liberating Native Mass Spectrometry from Dependence on Volatile Salt Buffers by Use of Gábor Transform. *ChemPhysChem* **2019**, *20*, 519-523.

- (451) Yang, S. H.; Chen, B.; Wang, J.; Zhang, K. Characterization of High Molecular Weight Multi-Arm Functionalized PEG–Maleimide for Protein Conjugation by Charge-Reduction Mass Spectrometry Coupled to Two-Dimensional Liquid Chromatography. *Anal. Chem.* **2020**, *92*, 8584-8590.
- (452) Bagal, D.; Zhang, H.; Schnier, P. D. Gas-Phase Proton-Transfer Chemistry Coupled with TOF Mass Spectrometry and Ion Mobility-MS for the Facile Analysis of Poly(Ethylene Glycols) and Pegylated Polypeptide Conjugates. *Anal. Chem.* **2008**, *80*, 2408-2418.
- (453) Hoi, K. K.; Robinson, C. V.; Marty, M. T. Unraveling the Composition and Behavior of Heterogeneous Lipid Nanodiscs by Mass Spectrometry. *Anal. Chem.* **2016**, *88*, 6199-6204.
- (454) Donor, M. T.; Wilson, J. W.; Shepherd, S. O.; Prell, J. S. Lipid Head Group Adduction to Soluble Proteins Follows Gas-Phase Basicity Predictions: Dissociation Barriers and Charge Abstraction. *Int. J. Mass Spectrom.* **2021**, *469*, 116670.
- (455) Kitov, P. I.; Han, L.; Kitova, E. N.; Klassen, J. S. Sliding Window Adduct Removal Method (SWARM) for Enhanced Electrospray Ionization Mass Spectrometry Binding Data. *J. Am. Soc. Mass Spectrom.* **2019**, *30*, 1446-1454.
- (456) Kitov, P. I.; Kitova, E. N.; Han, L.; Li, Z.; Jung, J.; Rodrigues, E.; Hunter, C. D.; Cairo, C. W.; Macauley, M. S.; Klassen, J. S. A Quantitative, High-Throughput Method Identifies Protein–Glycan Interactions Via Mass Spectrometry. *Commun. Biol.* **2019**, *2*, 268.
- (457) Báez Bolivar, E. G.; Bui, D. T.; Kitova, E. N.; Han, L.; Zheng, R. B.; Lubber, E. J.; Sayed, S. Y.; Mahal, L. K.; Klassen, J. S. Submicron Emitters Enable Reliable Quantification of Weak Protein–Glycan Interactions by ESI-MS. *Anal. Chem.* **2021**, *93*, 4231-4239.
- (458) Kendrick, E. A Mass Scale Based on $\text{CH}_2 = 14.0000$ for High Resolution Mass Spectrometry of Organic Compounds. *Anal. Chem.* **1963**, *35*, 2146-2154.
- (459) Fouquet, T. N. J. The Kendrick Analysis for Polymer Mass Spectrometry. *J. Mass Spectrom.* **2019**, *54*, 933-947.
- (460) Hughey, C. A.; Hendrickson, C. L.; Rodgers, R. P.; Marshall, A. G.; Qian, K. Kendrick Mass Defect Spectrum: A Compact Visual Analysis for Ultrahigh-Resolution Broadband Mass Spectra. *Anal. Chem.* **2001**, *73*, 4676-4681.
- (461) Lee, H.; An, H. J.; Lerno Jr, L. A.; German, J. B.; Lebrilla, C. B. Rapid Profiling of Bovine and Human Milk Gangliosides by Matrix-Assisted Laser Desorption/Ionization Fourier Transform Ion Cyclotron Resonance Mass Spectrometry. *Int. J. Mass Spectrom.* **2011**, *305*, 138-150.

- (462) Nakamura, S.; Fouquet, T.; Sato, H. Molecular Characterization of High Molecular Weight Polyesters by Matrix-Assisted Laser Desorption/Ionization High-Resolution Time-of-Flight Mass Spectrometry Combined with On-Plate Alkaline Degradation and Mass Defect Analysis. *J. Am. Soc. Mass Spectrom.* **2019**, *30*, 355-367.
- (463) Shi, Y.; Bajrami, B.; Yao, X. Passive and Active Fragment Ion Mass Defect Labeling: Distinct Proteomics Potential of Iodine-Based Reagents. *Anal. Chem.* **2009**, *81*, 6438-6448.
- (464) Harvey, S. R.; VanAernum, Z. L.; Kostelic, M. M.; Marty, M. T.; Wysocki, V. H. Probing the Structure of Nanodiscs Using Surface-Induced Dissociation Mass Spectrometry. *Chem. Commun.* **2020**, *56*, 15651-15654.
- (465) Eschweiler, J. D.; Frank, A. T.; Ruotolo, B. T. Coming to Grips with Ambiguity: Ion Mobility-Mass Spectrometry for Protein Quaternary Structure Assignment. *J. Am. Soc. Mass Spectrom.* **2017**, *28*, 1991-2000.
- (466) Ben-Nissan, G.; Sharon, M. The Application of Ion-Mobility Mass Spectrometry for Structure/Function Investigation of Protein Complexes. *Curr. Opin. Chem. Biol.* **2018**, *42*, 25-33.
- (467) Bleiholder, C. Structure Elucidation from Ion Mobility-Mass Spectrometry Data: Are Detailed Structures Amenable? *Proceedings of Advancing Mass Spectrometry for Biophysics and Structural Biology Meeting*; Advancing Mass Spectrometry: Ann Arbor, MI, 2017.
- (468) Canzani, D.; Laszlo, K. J.; Bush, M. F. Ion Mobility of Proteins in Nitrogen Gas: Effects of Charge State, Charge Distribution, and Structure. *J. Phys. Chem. A* **2018**, *122*, 5625-5634.
- (469) Wyttenbach, T.; Bowers, M. T. Structural Stability from Solution to the Gas Phase: Native Solution Structure of Ubiquitin Survives Analysis in a Solvent-Free Ion Mobility–Mass Spectrometry Environment. *J. Phys. Chem. B* **2011**, *115*, 12266-12275.
- (470) Bleiholder, C.; Dupuis, N. F.; Wyttenbach, T.; Bowers, M. T. Ion Mobility–Mass Spectrometry Reveals a Conformational Conversion from Random Assembly to β -Sheet in Amyloid Fibril Formation. *Nat. Chem.* **2011**, *3*, 172-177.
- (471) Ewing, M. A.; Glover, M. S.; Clemmer, D. E. Hybrid Ion Mobility and Mass Spectrometry as a Separation Tool. *J. Chromatogr. A* **2016**, *1439*, 3-25.
- (472) Hall, Z.; Politis, A.; Robinson, C. V. Structural Modeling of Heteromeric Protein Complexes from Disassembly Pathways and Ion Mobility-Mass Spectrometry. *Structure* **2012**, *20*, 1596-1609.

- (473) Lanucara, F.; Holman, S. W.; Gray, C. J.; Eyers, C. E. The Power of Ion Mobility-Mass Spectrometry for Structural Characterization and the Study of Conformational Dynamics. *Nat. Chem.* **2014**, *6*, 281-294.
- (474) Maurer, M. M.; Donohoe, G. C.; Valentine, S. J. Advances in Ion Mobility-Mass Spectrometry Instrumentation and Techniques for Characterizing Structural Heterogeneity. *Analyst* **2015**, *140*, 6782-6798.
- (475) May, J. C.; McLean, J. A. Ion Mobility-Mass Spectrometry: Time-Dispersive Instrumentation. *Anal. Chem.* **2015**, *87*, 1422-1436.
- (476) Saikusa, K.; Fuchigami, S.; Takahashi, K.; Asano, Y.; Nagadoi, A.; Tachiwana, H.; Kurumizaka, H.; Ikeguchi, M.; Nishimura, Y.; Akashi, S. Gas-Phase Structure of the Histone Multimers Characterized by Ion Mobility Mass Spectrometry and Molecular Dynamics Simulation. *Anal. Chem.* **2013**, *85*, 4165-4171.
- (477) Wytttenbach, T.; Pierson, N. A.; Clemmer, D. E.; Bowers, M. T. Ion Mobility Analysis of Molecular Dynamics. *Annu. Rev. Phys. Chem.* **2014**, *65*, 175-196.
- (478) Zhou, M.; Politis, A.; Davies, R. B.; Liko, I.; Wu, K.-J.; Stewart, A. G.; Stock, D.; Robinson, C. V. Ion Mobility–Mass Spectrometry of a Rotary ATPase Reveals ATP-Induced Reduction in Conformational Flexibility. *Nat. Chem.* **2014**, *6*, 208-215.
- (479) Ma, X.; Zhou, M.; Wysocki, V. H. Surface Induced Dissociation Yields Quaternary Substructure of Refractory Noncovalent Phosphorylase B and Glutamate Dehydrogenase Complexes. *J. Am. Soc. Mass Spectrom.* **2014**, *25*, 368-379.
- (480) Ma, X.; Loo, J. A.; Wysocki, V. H. Surface Induced Dissociation Yields Substructure of *Methanosarcina thermophila* 20S Proteasome Complexes. *Int. J. Mass Spectrom.* **2015**, *377*, 201-204.
- (481) Quintyn, R. S.; Zhou, M.; Yan, J.; Wysocki, V. H. Surface-Induced Dissociation Mass Spectra as a Tool for Distinguishing Different Structural Forms of Gas-Phase Multimeric Protein Complexes. *Anal. Chem.* **2015**, *87*, 11879-11886.
- (482) Seffernick, J. T.; Harvey, S. R.; Wysocki, V. H.; Lindert, S. Predicting Protein Complex Structure from Surface-Induced Dissociation Mass Spectrometry Data. *ACS Cent. Sci.* **2019**, *5*, 1330-1341.
- (483) Wysocki, V. H.; Joyce, K. E.; Jones, C. M.; Beardsley, R. L. Surface-Induced Dissociation of Small Molecules, Peptides, and Non-Covalent Protein Complexes. *J. Am. Soc. Mass Spectrom.* **2008**, *19*, 190-208.
- (484) Zhou, M.; Jones, C. M.; Wysocki, V. H. Dissecting the Large Noncovalent Protein Complex Groel with Surface-Induced Dissociation and Ion Mobility–Mass Spectrometry. *Anal. Chem.* **2013**, *85*, 8262-8267.

- (485) Zhou, M.; Wysocki, V. H. Surface Induced Dissociation: Dissecting Noncovalent Protein Complexes in the Gas Phase. *Acc. Chem. Res.* **2014**, *47*, 1010-1018.
- (486) Seffernick, J. T.; Lindert, S. Hybrid Methods for Combined Experimental and Computational Determination of Protein Structure. *J. Chem. Phys.* **2020**, *153*, 240901.
- (487) Gault, J.; Robinson, C. V. Cracking Complexes to Build Models of Protein Assemblies. *ACS Cent. Sci.* **2019**, *5*, 1310-1311.
- (488) Liu, X. R.; Zhang, M. M.; Gross, M. L. Mass Spectrometry-Based Protein Footprinting for Higher-Order Structure Analysis: Fundamentals and Applications. *Chem. Rev.* **2020**, *120*, 4355-4454.
- (489) Russel, D.; Lasker, K.; Webb, B.; Velázquez-Muriel, J.; Tjioe, E.; Schneidman-Duhovny, D.; Peterson, B.; Sali, A. Putting the Pieces Together: Integrative Modeling Platform Software for Structure Determination of Macromolecular Assemblies. *PLoS Biol.* **2012**, *10*, e1001244.
- (490) Politis, A.; Park, A. Y.; Hyung, S.-J.; Barsky, D.; Ruotolo, B. T.; Robinson, C. V. Integrating Ion Mobility Mass Spectrometry with Molecular Modelling to Determine the Architecture of Multiprotein Complexes. *PLoS One* **2010**, *5*, e12080.
- (491) Baldwin, Andrew J.; Lioe, H.; Hilton, Gillian R.; Baker, Lindsay A.; Rubinstein, John L.; Kay, Lewis E.; Benesch, Justin L. P. The Polydispersity of α B-Crystallin Is Rationalized by an Interconverting Polyhedral Architecture. *Structure* **2011**, *19*, 1855-1863.
- (492) Hilton, G. R.; Hochberg, G. K. A.; Laganowsky, A.; McGinnigle, S. I.; Baldwin, A. J.; Benesch, J. L. P. C-Terminal Interactions Mediate the Quaternary Dynamics of α B-Crystallin. *Philos. Trans. R. Soc. B* **2013**, *368*, 20110405.
- (493) Sinz, A.; Arlt, C.; Chorev, D.; Sharon, M. Chemical Cross-Linking and Native Mass Spectrometry: A Fruitful Combination for Structural Biology. *Protein Sci.* **2015**, *24*, 1193-1209.
- (494) Yu, C.; Huang, L. Cross-Linking Mass Spectrometry: An Emerging Technology for Interactomics and Structural Biology. *Anal. Chem.* **2018**, *90*, 144-165.
- (495) Schreiber, A.; Stengel, F.; Zhang, Z.; Enchev, R. I.; Kong, E. H.; Morris, E. P.; Robinson, C. V.; da Fonseca, P. C. A.; Barford, D. Structural Basis for the Subunit Assembly of the Anaphase-Promoting Complex. *Nature* **2011**, *470*, 227-232.
- (496) Sharon, M.; Mao, H.; Boeri Erba, E.; Stephens, E.; Zheng, N.; Robinson, C. V. Symmetrical Modularity of the COP9 Signalosome Complex Suggests Its Multifunctionality. *Structure* **2009**, *17*, 31-40.

- (497) Chorev, D. S.; Moscovitz, O.; Geiger, B.; Sharon, M. Regulation of Focal Adhesion Formation by a Vinculin-Arp2/3 Hybrid Complex. *Nat. Commun.* **2014**, *5*, 3758.
- (498) Casañal, A.; Kumar, A.; Hill, C. H.; Easter, A. D.; Emsley, P.; Degliesposti, G.; Gordiyenko, Y.; Santhanam, B.; Wolf, J.; Wiederhold, K.; Dornan, G. L.; Skehel, M.; Robinson, C. V.; Passmore, L. A. Architecture of Eukaryotic mRNA 3'-End Processing Machinery. *Science* **2017**, *358*, 1056-1059.
- (499) Hernández, H.; Makarova, O. V.; Makarov, E. M.; Morgner, N.; Muto, Y.; Krummel, D. P.; Robinson, C. V. Isoforms of U1-70K Control Subunit Dynamics in the Human Spliceosomal U1 snRNP. *PLoS One* **2009**, *4*, e7202.
- (500) Politis, A.; Schmidt, C.; Tjioe, E.; Sandercock, A. M.; Lasker, K.; Gordiyenko, Y.; Russel, D.; Sali, A.; Robinson, C. V. Topological Models of Heteromeric Protein Assemblies from Mass Spectrometry: Application to the Yeast eIF3:eIF5 Complex. *Chem. Biol.* **2015**, *22*, 117-128.
- (501) Shakeel, S.; Rajendra, E.; Alcón, P.; O'Reilly, F.; Chorev, D. S.; Maslen, S.; Degliesposti, G.; Russo, C. J.; He, S.; Hill, C. H.; Skehel, J. M.; Scheres, S. H. W.; Patel, K. J.; Rappsilber, J.; Robinson, C. V.; Passmore, L. A. Structure of the *Fanconi anaemia* Monoubiquitin Ligase Complex. *Nature* **2019**, *575*, 234-237.
- (502) Lane, L. A.; Nadeau, O. W.; Carlson, G. M.; Robinson, C. V. Mass Spectrometry Reveals Differences in Stability and Subunit Interactions between Activated and Nonactivated Conformers of the $(\alpha\beta\gamma\delta)_4$ Phosphorylase Kinase Complex. *Mol. Cell. Proteom.* **2012**, *11*, 1768-1776.
- (503) Kleiner, D.; Shmulevich, F.; Zarivach, R.; Shahar, A.; Sharon, M.; Ben-Nissan, G.; Bershtein, S. The Interdimeric Interface Controls Function and Stability of *Ureaplasma urealiticum* Methionine S-Adenosyltransferase. *J. Mol. Biol.* **2019**, *431*, 4796-4816.
- (504) Lössl, P.; Snijder, J.; Heck, A. J. R. Boundaries of Mass Resolution in Native Mass Spectrometry. *J. Am. Soc. Mass Spectrom.* **2014**, *25*, 906-917.
- (505) Chen, X.; Westphall, M. S.; Smith, L. M. Mass Spectrometric Analysis of DNA Mixtures: Instrumental Effects Responsible for Decreased Sensitivity with Increasing Mass. *Anal. Chem.* **2003**, *75*, 5944-5952.
- (506) Bruce, J. E.; Cheng, X.; Bakhtiar, R.; Wu, Q.; Hofstadler, S. A.; Anderson, G. A.; Smith, R. D. Trapping, Detection, and Mass Measurement of Individual Ions in a Fourier Transform Ion Cyclotron Resonance Mass Spectrometer. *J. Am. Chem. Soc.* **1994**, *116*, 7839-7847.
- (507) Benner, W. H. A Gated Electrostatic Ion Trap to Repetitiously Measure the Charge and m/z of Large Electrospray Ions. *Anal. Chem.* **1997**, *69*, 4162-4168.

- (508) Fuerstenau, S. D.; Benner, W. H. Molecular Weight Determination of Megadalton DNA Electrospray Ions Using Charge Detection Time-of-Flight Mass Spectrometry. *Rapid Commun. Mass Spectrom.* **1995**, *9*, 1528-1538.
- (509) Draper, B. E.; Jarrold, M. F. Real-Time Analysis and Signal Optimization for Charge Detection Mass Spectrometry. *J. Am. Soc. Mass Spectrom.* **2019**, *30*, 898-904.
- (510) Elliott, A. G.; Harper, C. C.; Lin, H.-W.; Susa, A. C.; Xia, Z.; Williams, E. R. Simultaneous Measurements of Mass and Collisional Cross-Section of Single Ions with Charge Detection Mass Spectrometry. *Anal. Chem.* **2017**, *89*, 7701-7708.
- (511) Harper, C. C.; Elliott, A. G.; Oltrogge, L. M.; Savage, D. F.; Williams, E. R. Multiplexed Charge Detection Mass Spectrometry for High-Throughput Single Ion Analysis of Large Molecules. *Anal. Chem.* **2019**, *91*, 7458-7465.
- (512) Harper, C. C.; Williams, E. R. Enhanced Multiplexing in Fourier Transform Charge Detection Mass Spectrometry by Decoupling Ion Frequency from Mass to Charge Ratio. *J. Am. Soc. Mass Spectrom.* **2019**, *30*, 2637-2645.
- (513) Keifer, D. Z.; Shinholt, D. L.; Jarrold, M. F. Charge Detection Mass Spectrometry with Almost Perfect Charge Accuracy. *Anal. Chem.* **2015**, *87*, 10330-10337.
- (514) Todd, A. R.; Jarrold, M. F. Dramatic Improvement in Sensitivity with Pulsed Mode Charge Detection Mass Spectrometry. *Anal. Chem.* **2019**, *91*, 14002-14008.
- (515) Keifer, D. Z.; Jarrold, M. F. Single-Molecule Mass Spectrometry. *Mass Spectrom. Rev.* **2017**, *36*, 715-733.
- (516) Doussineau, T.; Mathevon, C.; Altamura, L.; Vendrely, C.; Dugourd, P.; Forge, V.; Antoine, R. Mass Determination of Entire Amyloid Fibrils by Using Mass Spectrometry. *Angew. Chem. Int. Ed.* **2016**, *55*, 2340-2344.
- (517) Contino, N. C.; Pierson, E. E.; Keifer, D. Z.; Jarrold, M. F. Charge Detection Mass Spectrometry with Resolved Charge States. *J. Am. Soc. Mass Spectrom.* **2013**, *24*, 101-108.
- (518) Keifer, D. Z.; Motwani, T.; Teschke, C. M.; Jarrold, M. F. Acquiring Structural Information on Virus Particles with Charge Detection Mass Spectrometry. *J. Am. Soc. Mass Spectrom.* **2016**, *27*, 1028-1036.
- (519) Keifer, D. Z.; Pierson, E. E.; Hogan, J. A.; Bedwell, G. J.; Prevelige, P. E.; Jarrold, M. F. Charge Detection Mass Spectrometry of Bacteriophage P22 Procapsid Distributions above 20 MDa. *Rapid Commun. Mass Spectrom.* **2014**, *28*, 483-488.

- (520) Pierson, E. E.; Keifer, D. Z.; Contino, N. C.; Jarrold, M. F. Probing Higher Order Multimers of Pyruvate Kinase with Charge Detection Mass Spectrometry. *Int. J. Mass Spectrom.* **2013**, *337*, 50-56.
- (521) Schultz, J. C.; Hack, C. A.; Benner, W. H. Mass Determination of Megadalton-DNA Electrospray Ions Using Charge Detection Mass Spectrometry. *J. Am. Soc. Mass Spectrom.* **1998**, *9*, 305-313.
- (522) Philip, M. A.; Gelbard, F.; Arnold, S. An Absolute Method for Aerosol Particle Mass and Charge Measurement. *J. Colloid Interface Sci.* **1983**, *91*, 507-515.
- (523) Hars, G.; Tass, Z. Application of Quadrupole Ion Trap for the Accurate Mass Determination of Submicron Size Charged Particles. *J. Appl. Phys.* **1995**, *77*, 4245-4250.
- (524) Halim, M. A.; Bertorelle, F.; Doussineau, T.; Antoine, R. Direct Determination of Molecular Weight Distribution of Calf-Thymus DNAs and Study of Their Fragmentation under Ultrasonic and Low-Energy Infrared Irradiations. A Charge Detection Mass Spectrometry Investigation. *Rapid Commun. Mass Spectrom.* **2019**, *33*, 35-39.
- (525) Contino, N. C.; Jarrold, M. F. Charge Detection Mass Spectrometry for Single Ions with a Limit of Detection of 30 Charges. *Int. J. Mass Spectrom.* **2013**, *345-347*, 153-159.
- (526) Dunbar, C. A.; Rayaprolu, V.; Wang, J. C. Y.; Brown, C. J.; Leishman, E.; Jones-Burrage, S.; Trinidad, J. C.; Bradshaw, H. B.; Clemmer, D. E.; Mukhopadhyay, S.; Jarrold, M. F. Dissecting the Components of Sindbis Virus from Arthropod and Vertebrate Hosts: Implications for Infectivity Differences. *ACS Infect. Dis.* **2019**, *5*, 892-902.
- (527) Mabbett, S. R.; Zilch, L. W.; Maze, J. T.; Smith, J. W.; Jarrold, M. F. Pulsed Acceleration Charge Detection Mass Spectrometry: Application to Weighing Electrosprayed Droplets. *Anal. Chem.* **2007**, *79*, 8431-8439.
- (528) Elliott, A. G.; Merenbloom, S. I.; Chakrabarty, S.; Williams, E. R. Single Particle Analyzer of Mass: A Charge Detection Mass Spectrometer with a Multi-Detector Electrostatic Ion Trap. *Int. J. Mass Spectrom.* **2017**, *414*, 45-55.
- (529) Elliott, A. G.; Harper, C. C.; Lin, H.-W.; Williams, E. R. Mass, Mobility and MSⁿ Measurements of Single Ions Using Charge Detection Mass Spectrometry. *Analyst* **2017**, *142*, 2760-2769.
- (530) Harper, C. C.; Elliott, A. G.; Lin, H.-W.; Williams, E. R. Determining Energies and Cross Sections of Individual Ions Using Higher-Order Harmonics in Fourier Transform Charge Detection Mass Spectrometry (FT-CDMS). *J. Am. Soc. Mass Spectrom.* **2018**, *29*, 1861-1869.

- (531) Kafader, J. O.; Melani, R. D.; Durbin, K. R.; Ikwuagwu, B.; Early, B. P.; Fellers, R. T.; Beu, S. C.; Zabrouskov, V.; Makarov, A. A.; Maze, J. T.; Shinholt, D. L.; Yip, P. F.; Tullman-Ercek, D.; Senko, M. W.; Compton, P. D.; Kelleher, N. L. Multiplexed Mass Spectrometry of Individual Ions Improves Measurement of Proteoforms and Their Complexes. *Nat. Methods* **2020**, *17*, 391-394.
- (532) McGee, J. P.; Melani, R. D.; Yip, P. F.; Senko, M. W.; Compton, P. D.; Kafader, J. O.; Kelleher, N. L. Isotopic Resolution of Protein Complexes up to 466 kDa Using Individual Ion Mass Spectrometry. *Anal. Chem.* **2021**, *93*, 2723-2727.
- (533) Kafader, J. O.; Melani, R. D.; Senko, M. W.; Makarov, A. A.; Kelleher, N. L.; Compton, P. D. Measurement of Individual Ions Sharply Increases the Resolution of Orbitrap Mass Spectra of Proteins. *Anal. Chem.* **2019**, *91*, 2776-2783.
- (534) Bernstein, S. L.; Liu, D.; Wyttenbach, T.; Bowers, M. T.; Lee, J. C.; Gray, H. B.; Winkler, J. R. α -Synuclein: Stable Compact and Extended Monomeric Structures and pH Dependence of Dimer Formation. *J. Am. Soc. Mass Spectrom.* **2004**, *15*, 1435-1443.
- (535) Ridgeway, M. E.; Silveira, J. A.; Meier, J. E.; Park, M. A. Microheterogeneity within Conformational States of Ubiquitin Revealed by High Resolution Trapped Ion Mobility Spectrometry. *Analyst* **2015**, *140*, 6964-6972.
- (536) Utrecht, C.; Barbu, I. M.; Shoemaker, G. K.; van Duijn, E.; Heck, A. J. R. Interrogating Viral Capsid Assembly with Ion Mobility–Mass Spectrometry. *Nat. Chem.* **2011**, *3*, 126-132.
- (537) Snijder, J.; Utrecht, C.; Rose, R. J.; Sanchez-Eugenía, R.; Marti, G. A.; Agirre, J.; Guérin, D. M. A.; Wuite, G. J. L.; Heck, A. J. R.; Roos, W. H. Probing the Biophysical Interplay between a Viral Genome and Its Capsid. *Nat. Chem.* **2013**, *5*, 502-509.
- (538) El-Baba, T. J.; Lutomski, C. A.; Wang, B.; Trimpin, S. Characterizing Synthetic Polymers and Additives Using New Ionization Methods for Mass Spectrometry. *Rapid Commun. Mass Spectrom.* **2014**, *28*, 1175-1184.
- (539) Loo, J. A.; Berhane, B.; Kaddis, C. S.; Wooding, K. M.; Xie, Y.; Kaufman, S. L.; Chernushevich, I. V. Electrospray Ionization Mass Spectrometry and Ion Mobility Analysis of the 20S Proteasome Complex. *J. Am. Soc. Mass Spectrom.* **2005**, *16*, 998-1008.
- (540) Marcoux, J.; Champion, T.; Colas, O.; Wagner-Rousset, E.; Corvaia, N.; Van Dorsselaer, A.; Beck, A.; Cianfèrani, S. Native Mass Spectrometry and Ion Mobility Characterization of Trastuzumab Emtansine, a Lysine-Linked Antibody Drug Conjugate. *Protein Sci.* **2015**, *24*, 1210-1223.

- (541) Österlund, N.; Moons, R.; Ilag, L. L.; Sobott, F.; Gräslund, A. Native Ion Mobility-Mass Spectrometry Reveals the Formation of β -Barrel Shaped Amyloid- β Hexamers in a Membrane-Mimicking Environment. *J. Am. Chem. Soc.* **2019**, *141*, 10440-10450.
- (542) Kłoniecki, M.; Jabłonowska, A.; Poznański, J.; Langridge, J.; Hughes, C.; Campuzano, I.; Giles, K.; Dadlez, M. Ion Mobility Separation Coupled with MS Detects Two Structural States of Alzheimer's Disease A β 1–40 Peptide Oligomers. *J. Mol. Biol.* **2011**, *407*, 110-124.
- (543) Woods, L. A.; Radford, S. E.; Ashcroft, A. E. Advances in Ion Mobility Spectrometry–Mass Spectrometry Reveal Key Insights into Amyloid Assembly. *Biochim. Biophys. Acta Proteins Proteom.* **2013**, *1834*, 1257-1268.
- (544) Young, L. M.; Saunders, J. C.; Mahood, R. A.; Revill, C. H.; Foster, R. J.; Tu, L.-H.; Raleigh, D. P.; Radford, S. E.; Ashcroft, A. E. Screening and Classifying Small-Molecule Inhibitors of Amyloid Formation Using Ion Mobility Spectrometry–Mass Spectrometry. *Nat. Chem.* **2015**, *7*, 73-81.
- (545) Shvartsburg, A. A.; Smith, R. D. Fundamentals of Traveling Wave Ion Mobility Spectrometry. *Anal. Chem.* **2008**, *80*, 9689-9699.
- (546) Dodds, J. N.; May, J. C.; McLean, J. A. Correlating Resolving Power, Resolution, and Collision Cross Section: Unifying Cross-Platform Assessment of Separation Efficiency in Ion Mobility Spectrometry. *Anal. Chem.* **2017**, *89*, 12176-12184.
- (547) Richardson, K.; Langridge, D.; Giles, K. Fundamentals of Travelling Wave Ion Mobility Revisited: I. Smoothly Moving Waves. *Int. J. Mass Spectrom.* **2018**, *428*, 71-80.
- (548) Michelmann, K.; Silveira, J. A.; Ridgeway, M. E.; Park, M. A. Fundamentals of Trapped Ion Mobility Spectrometry. *J. Am. Soc. Mass Spectrom.* **2015**, *26*, 14-24.
- (549) Wu, C.; Siems, W. F.; Klasmeier, J.; Hill, H. H. Separation of Isomeric Peptides Using Electrospray Ionization/High-Resolution Ion Mobility Spectrometry. *Anal. Chem.* **2000**, *72*, 391-395.
- (550) Clowers, B. H.; Hill, H. H. Mass Analysis of Mobility-Selected Ion Populations Using Dual Gate, Ion Mobility, Quadrupole Ion Trap Mass Spectrometry. *Anal. Chem.* **2005**, *77*, 5877-5885.
- (551) Bohrer, B. C.; Merenbloom, S. I.; Koeniger, S. L.; Hilderbrand, A. E.; Clemmer, D. E. Biomolecule Analysis by Ion Mobility Spectrometry. *Annu. Rev. Anal. Chem.* **2008**, *1*, 293-327.
- (552) Sanda, M.; Morrison, L.; Goldman, R. N- and O-Glycosylation of the SARS-CoV-2 Spike Protein. *Anal. Chem.* **2021**, *93*, 2003-2009.

- (553) Sisley, E. K.; Ujma, J.; Palmer, M.; Giles, K.; Fernandez-Lima, F. A.; Cooper, H. J. LESA Cyclic Ion Mobility Mass Spectrometry of Intact Proteins from Thin Tissue Sections. *Anal. Chem.* **2020**, *92*, 6321-6326.
- (554) Eldrid, C.; Ujma, J.; Kalfas, S.; Tomczyk, N.; Giles, K.; Morris, M.; Thalassinos, K. Gas Phase Stability of Protein Ions in a Cyclic Ion Mobility Spectrometry Traveling Wave Device. *Anal. Chem.* **2019**, *91*, 7554-7561.
- (555) Hofmann, J.; Hahm, H. S.; Seeberger, P. H.; Pagel, K. Identification of Carbohydrate Anomers Using Ion Mobility–Mass Spectrometry. *Nature* **2015**, *526*, 241-244.
- (556) Pagel, K.; Harvey, D. J. Ion Mobility–Mass Spectrometry of Complex Carbohydrates: Collision Cross Sections of Sodiated N-Linked Glycans. *Anal. Chem.* **2013**, *85*, 5138-5145.
- (557) Kyle, J. E.; Zhang, X.; Weitz, K. K.; Monroe, M. E.; Ibrahim, Y. M.; Moore, R. J.; Cha, J.; Sun, X.; Lovelace, E. S.; Wagoner, J.; Polyak, S. J.; Metz, T. O.; Dey, S. K.; Smith, R. D.; Burnum-Johnson, K. E.; Baker, E. S. Uncovering Biologically Significant Lipid Isomers with Liquid Chromatography, Ion Mobility Spectrometry and Mass Spectrometry. *Analyst* **2016**, *141*, 1649-1659.
- (558) Helmer, P. O.; Nordhorn, I. D.; Korf, A.; Behrens, A.; Buchholz, R.; Zubeil, F.; Karst, U.; Hayen, H. Complementing Matrix-Assisted Laser Desorption Ionization-Mass Spectrometry Imaging with Chromatography Data for Improved Assignment of Isobaric and Isomeric Phospholipids Utilizing Trapped Ion Mobility-Mass Spectrometry. *Anal. Chem.* **2021**, *93*, 2135-2143.
- (559) Dodds, J. N.; May, J. C.; McLean, J. A. Investigation of the Complete Suite of the Leucine and Isoleucine Isomers: Toward Prediction of Ion Mobility Separation Capabilities. *Anal. Chem.* **2017**, *89*, 952-959.
- (560) Kliman, M.; May, J. C.; McLean, J. A. Lipid Analysis and Lipidomics by Structurally Selective Ion Mobility-Mass Spectrometry. *Biochim. Biophys. Acta Mol. Cell Biol. Lipids* **2011**, *1811*, 935-945.
- (561) Groessl, M.; Graf, S.; Knochenmuss, R. High Resolution Ion Mobility-Mass Spectrometry for Separation and Identification of Isomeric Lipids. *Analyst* **2015**, *140*, 6904-6911.
- (562) Jeanne Dit Fouque, K.; Ramirez, C. E.; Lewis, R. L.; Koelmel, J. P.; Garrett, T. J.; Yost, R. A.; Fernandez-Lima, F. Effective Liquid Chromatography–Trapped Ion Mobility Spectrometry–Mass Spectrometry Separation of Isomeric Lipid Species. *Anal. Chem.* **2019**, *91*, 5021-5027.

- (563) Pu, Y.; Ridgeway, M. E.; Glaskin, R. S.; Park, M. A.; Costello, C. E.; Lin, C. Separation and Identification of Isomeric Glycans by Selected Accumulation-Trapped Ion Mobility Spectrometry-Electron Activated Dissociation Tandem Mass Spectrometry. *Anal. Chem.* **2016**, *88*, 3440-3443.
- (564) Fernandez-Lima, F.; Kaplan, D. A.; Suetering, J.; Park, M. A. Gas-Phase Separation Using a Trapped Ion Mobility Spectrometer. *Int. J. Ion Mobil. Spectrom.* **2011**, *14*, 93-98.
- (565) Liu, F. C.; Kirk, S. R.; Bleiholder, C. On the Structural Denaturation of Biological Analytes in Trapped Ion Mobility Spectrometry – Mass Spectrometry. *Analyst* **2016**, *141*, 3722-3730.
- (566) Silveira, J. A.; Ridgeway, M. E.; Park, M. A. High Resolution Trapped Ion Mobility Spectrometry of Peptides. *Anal. Chem.* **2014**, *86*, 5624-5627.
- (567) Jeanne Dit Fouque, K.; Fernandez-Lima, F. Recent Advances in Biological Separations Using Trapped Ion Mobility Spectrometry – Mass Spectrometry. *Trends Anal. Chem.* **2019**, *116*, 308-315.
- (568) Ridgeway, M. E.; Lubeck, M.; Jordens, J.; Mann, M.; Park, M. A. Trapped Ion Mobility Spectrometry: A Short Review. *Int. J. Mass Spectrom.* **2018**, *425*, 22-35.
- (569) Borotto, N. B.; Graham, K. A. Fragmentation and Mobility Separation of Peptide and Protein Ions in a Trapped-Ion Mobility Device. *Anal. Chem.* **2021**, *93*, 9959-9964.
- (570) Adams, K. J.; Montero, D.; Aga, D.; Fernandez-Lima, F. Isomer Separation of Polybrominated Diphenyl Ether Metabolites Using NanoESI-TIMS-MS. *Int. J. Ion Mobil. Spectrom.* **2016**, *19*, 69-76.
- (571) Poltash, M. L.; McCabe, J. W.; Patrick, J. W.; Laganowsky, A.; Russell, D. H. Development and Evaluation of a Reverse-Entry Ion Source Orbitrap Mass Spectrometer. *J. Am. Soc. Mass Spectrom.* **2019**, *30*, 192-198.
- (572) Knorr, F. J.; Eatherton, R. L.; Siems, W. F.; Hill, H. H. Fourier Transform Ion Mobility Spectrometry. *Anal. Chem.* **1985**, *57*, 402-406.
- (573) Morrison, K. A.; Siems, W. F.; Clowers, B. H. Augmenting Ion Trap Mass Spectrometers Using a Frequency Modulated Drift Tube Ion Mobility Spectrometer. *Anal. Chem.* **2016**, *88*, 3121-3129.
- (574) Clowers, B. H.; Siems, W. F.; Yu, Z.; Davis, A. L. A Two-Phase Approach to Fourier Transform Ion Mobility Time-of-Flight Mass Spectrometry. *Analyst* **2015**, *140*, 6862-6870.

- (575) Davis, A. L.; Reinecke, T.; Morrison, K. A.; Clowers, B. H. Optimized Reconstruction Techniques for Multiplexed Dual-Gate Ion Mobility Mass Spectrometry Experiments. *Anal. Chem.* **2019**, *91*, 1432-1440.
- (576) Lyu, J.; Liu, Y.; McCabe, J. W.; Schrecke, S.; Fang, L.; Russell, D. H.; Laganowsky, A. Discovery of Potent Charge-Reducing Molecules for Native Ion Mobility Mass Spectrometry Studies. *Anal. Chem.* **2020**, *92*, 11242-11249.
- (577) Poltash, M. L.; Shirzadeh, M.; McCabe, J. W.; Moghadamchargari, Z.; Laganowsky, A.; Russell, D. H. New Insights into the Metal-Induced Oxidative Degradation Pathways of Transthyretin. *Chem. Commun.* **2019**, *55*, 4091-4094.
- (578) Davis, A. L.; Liu, W.; Siems, W. F.; Clowers, B. H. Correlation Ion Mobility Spectrometry. *Analyst* **2017**, *142*, 292-301.
- (579) Deng, L.; Webb, I. K.; Garimella, S. V. B.; Hamid, A. M.; Zheng, X.; Norheim, R. V.; Prost, S. A.; Anderson, G. A.; Sandoval, J. A.; Baker, E. S.; Ibrahim, Y. M.; Smith, R. D. Serpentine Ultralong Path with Extended Routing (SUPER) High Resolution Traveling Wave Ion Mobility-MS Using Structures for Lossless Ion Manipulations. *Anal. Chem.* **2017**, *89*, 4628-4634.
- (580) Hollerbach, A. L.; Conant, C. R.; Nagy, G.; Monroe, M. E.; Gupta, K.; Donor, M.; Giberson, C. M.; Garimella, S. V. B.; Smith, R. D.; Ibrahim, Y. M. Dynamic Time-Warping Correction for Shifts in Ultrahigh Resolving Power Ion Mobility Spectrometry and Structures for Lossless Ion Manipulations. *J. Am. Soc. Mass Spectrom.* **2021**, *32*, 996-1007.
- (581) Herron, W. J.; Goeringer, D. E.; McLuckey, S. A. Product Ion Charge State Determination Via Ion/Ion Proton Transfer Reactions. *Anal. Chem.* **1996**, *68*, 257-262.
- (582) McLuckey, S. A.; Goeringer, D. E. Ion/Molecule Reactions for Improved Effective Mass Resolution in Electrospray Mass Spectrometry. *Anal. Chem.* **1995**, *67*, 2493-2497.
- (583) Stephenson, J. L.; McLuckey, S. A. Charge Manipulation for Improved Mass Determination of High-Mass Species and Mixture Components by Electrospray Mass Spectrometry. *J. Mass Spectrom.* **1998**, *33*, 664-672.
- (584) Catalina, M. I.; van den Heuvel, R. H. H.; van Duijn, E.; Heck, A. J. R. Decharging of Globular Proteins and Protein Complexes in Electrospray. *Chem. Eur. J.* **2005**, *11*, 960-968.
- (585) Iavarone, A. T.; Jurchen, J. C.; Williams, E. R. Supercharged Protein and Peptide Ions Formed by Electrospray Ionization. *Anal. Chem.* **2001**, *73*, 1455-1460.

- (586) Cheng, X.; Gale, D. C.; Udseth, H. R.; Smith, R. D. Charge State Reduction of Oligonucleotide Negative Ions from Electrospray Ionization. *Anal. Chem.* **1995**, *67*, 586-593.
- (587) Ebeling, D. D.; Westphall, M. S.; Scalf, M.; Smith, L. M. Corona Discharge in Charge Reduction Electrospray Mass Spectrometry. *Anal. Chem.* **2000**, *72*, 5158-5161.
- (588) Frey, B. L.; Lin, Y.; Westphall, M. S.; Smith, L. M. Controlling Gas-Phase Reactions for Efficient Charge Reduction Electrospray Mass Spectrometry of Intact Proteins. *J. Am. Soc. Mass Spectrom.* **2005**, *16*, 1876-1887.
- (589) Scalf, M.; Westphall, M. S.; Krause, J.; Kaufman, S. L.; Smith, L. M. Controlling Charge States of Large Ions. *Science* **1999**, *283*, 194-197.
- (590) Scalf, M.; Westphall, M. S.; Smith, L. M. Charge Reduction Electrospray Mass Spectrometry. *Anal. Chem.* **2000**, *72*, 52-60.
- (591) Campuzano, I. D. G.; Schnier, P. D. Coupling Electrospray Corona Discharge, Charge Reduction and Ion Mobility Mass Spectrometry: From Peptides to Large Macromolecular Protein Complexes. *Int. J. Ion Mobil. Spectrom.* **2013**, *16*, 51-60.
- (592) Schnier, P. D.; Gross, D. S.; Williams, E. R. On the Maximum Charge State and Proton Transfer Reactivity of Peptide and Protein Ions Formed by Electrospray Ionization. *J. Am. Soc. Mass Spectrom.* **1995**, *6*, 1086-1097.
- (593) Sun, J.; Kitova, E. N.; Klassen, J. S. Method for Stabilizing Protein-Ligand Complexes in Nanoelectrospray Ionization Mass Spectrometry. *Anal. Chem.* **2007**, *79*, 416-425.
- (594) Lomeli, S. H.; Peng, I. X.; Yin, S.; Ogorzalek Loo, R. R.; Loo, J. A. New Reagents for Increasing ESI Multiple Charging of Proteins and Protein Complexes. *J. Am. Soc. Mass Spectrom.* **2010**, *21*, 127-131.
- (595) Lomeli, S. H.; Yin, S.; Ogorzalek Loo, R. R.; Loo, J. A. Increasing Charge While Preserving Noncovalent Protein Complexes for ESI-MS. *J. Am. Soc. Mass Spectrom.* **2009**, *20*, 593-596.
- (596) Smith, L. M. Is Charge Reduction in ESI Really Necessary? *J. Am. Soc. Mass Spectrom.* **2008**, *19*, 629-631.
- (597) Pan, P.; McLuckey, S. A. The Effect of Small Cations on the Positive Electrospray Responses of Proteins at Low pH. *Anal. Chem.* **2003**, *75*, 5468-5474.
- (598) Sterling, H. J.; Kintzer, A. F.; Feld, G. K.; Cassou, C. A.; Krantz, B. A.; Williams, E. R. Supercharging Protein Complexes from Aqueous Solution Disrupts Their Native Conformations. *J. Am. Soc. Mass Spectrom.* **2012**, *23*, 191-200.

- (599) Polfer, N. C. Supercharging Proteins: How Many Charges Can a Protein Carry? *Angew. Chem. Int. Ed.* **2017**, *56*, 8335-8337.
- (600) Abaye, D. A.; Agbo, I. A.; Nielsen, B. V. Current Perspectives on Supercharging Reagents in Electrospray Ionization Mass Spectrometry. *RSC Adv.* **2021**, *11*, 20355-20369.
- (601) Cassou, C. A.; Williams, E. R. Desalting Protein Ions in Native Mass Spectrometry Using Supercharging Reagents. *Analyst* **2014**, *139*, 4810-4819.
- (602) Iavarone, A. T.; Williams, E. R. Mechanism of Charging and Supercharging Molecules in Electrospray Ionization. *J. Am. Chem. Soc.* **2003**, *125*, 2319-2327.
- (603) Sterling, H. J.; Cassou, C. A.; Susa, A. C.; Williams, E. R. Electrothermal Supercharging of Proteins in Native Electrospray Ionization. *Anal. Chem.* **2012**, *84*, 3795-3801.
- (604) Sterling, H. J.; Cassou, C. A.; Trnka, M. J.; Burlingame, A. L.; Krantz, B. A.; Williams, E. R. The Role of Conformational Flexibility on Protein Supercharging in Native Electrospray Ionization. *Phys. Chem. Chem. Phys.* **2011**, *13*, 18288-18296.
- (605) Sterling, H. J.; Daly, M. P.; Feld, G. K.; Thoren, K. L.; Kintzer, A. F.; Krantz, B. A.; Williams, E. R. Effects of Supercharging Reagents on Noncovalent Complex Structure in Electrospray Ionization from Aqueous Solutions. *J. Am. Soc. Mass Spectrom.* **2010**, *21*, 1762-1774.
- (606) Sterling, H. J.; Prell, J. S.; Cassou, C. A.; Williams, E. R. Protein Conformation and Supercharging with DMSO from Aqueous Solution. *J. Am. Soc. Mass Spectrom.* **2011**, *22*, 1178-1186.
- (607) Sterling, H. J.; Williams, E. R. Origin of Supercharging in Electrospray Ionization of Noncovalent Complexes from Aqueous Solution. *J. Am. Soc. Mass Spectrom.* **2009**, *20*, 1933-1943.
- (608) Zenaidee, M. A.; Donald, W. A. Extremely Supercharged Proteins in Mass Spectrometry: Profiling the pH of Electrospray Generated Droplets, Narrowing Charge State Distributions, and Increasing Ion Fragmentation. *Analyst* **2015**, *140*, 1894-1905.
- (609) Teo, C. A.; Donald, W. A. Solution Additives for Supercharging Proteins Beyond the Theoretical Maximum Proton-Transfer Limit in Electrospray Ionization Mass Spectrometry. *Anal. Chem.* **2014**, *86*, 4455-4462.
- (610) Zenaidee, M. A.; Leeming, M. G.; Zhang, F.; Funston, T. T.; Donald, W. A. Highly Charged Protein Ions: The Strongest Organic Acids to Date. *Angew. Chem. Int. Ed.* **2017**, *56*, 8522-8526.

- (611) Going, C. C.; Xia, Z.; Williams, E. R. New Supercharging Reagents Produce Highly Charged Protein Ions in Native Mass Spectrometry. *Analyst* **2015**, *140*, 7184-7194.
- (612) Sterling, H. J.; Williams, E. R. Real-Time Hydrogen/Deuterium Exchange Kinetics Via Supercharged Electrospray Ionization Tandem Mass Spectrometry. *Anal. Chem.* **2010**, *82*, 9050-9057.
- (613) Yin, S.; Loo, J. A. Top-Down Mass Spectrometry of Supercharged Native Protein–Ligand Complexes. *Int. J. Mass Spectrom.* **2011**, *300*, 118-122.
- (614) Zhang, J.; Ogorzalek Loo, R. R.; Loo, J. A. Increasing Fragmentation of Disulfide-Bonded Proteins for Top-Down Mass Spectrometry by Supercharging. *Int. J. Mass Spectrom.* **2015**, *377*, 546-556.
- (615) Dyachenko, A.; Gruber, R.; Shimon, L.; Horovitz, A.; Sharon, M. Allosteric Mechanisms Can Be Distinguished Using Structural Mass Spectrometry. *Proc. Natl. Acad. Sci. U. S. A.* **2013**, *110*, 7235-7239.
- (616) Lemaire, D.; Marie, G.; Serani, L.; Laprevote, O. Stabilization of Gas-Phase Noncovalent Macromolecular Complexes in Electrospray Mass Spectrometry Using Aqueous Triethylammonium Bicarbonate Buffer. *Anal. Chem.* **2001**, *73*, 1699-1706.
- (617) Verkerk, U. H.; Peschke, M.; Kebarle, P. Effect of Buffer Cations and of H₃O⁺ on the Charge States of Native Proteins. Significance to Determinations of Stability Constants of Protein Complexes. *J. Mass Spectrom.* **2003**, *38*, 618-631.
- (618) Pacholarz, K. J.; Barran, P. E. Use of a Charge Reducing Agent to Enable Intact Mass Analysis of Cysteine-Linked Antibody-Drug-Conjugates by Native Mass Spectrometry. *EuPA Open Proteom.* **2016**, *11*, 23-27.
- (619) Patrick, J. W.; Laganowsky, A. Generation of Charge-Reduced Ions of Membrane Protein Complexes for Native Ion Mobility Mass Spectrometry Studies. *J. Am. Soc. Mass Spectrom.* **2019**, *30*, 886-892.
- (620) Zhou, M.; Dagan, S.; Wysocki, V. H. Impact of Charge State on Gas-Phase Behaviors of Noncovalent Protein Complexes in Collision Induced Dissociation and Surface Induced Dissociation. *Analyst* **2013**, *138*, 1353-1362.
- (621) Harvey, S. R.; VanAernum, Z. L.; Wysocki, V. H. Surface-Induced Dissociation of Anionic Vs Cationic Native-Like Protein Complexes. *J. Am. Chem. Soc.* **2021**, *143*, 7698-7706.
- (622) Laszlo, K. J.; Bush, M. F. Analysis of Native-Like Proteins and Protein Complexes Using Cation to Anion Proton Transfer Reactions (CAPTR). *J. Am. Soc. Mass Spectrom.* **2015**, *26*, 2152-2161.

- (623) Laszlo, K. J.; Munger, E. B.; Bush, M. F. Folding of Protein Ions in the Gas Phase after Cation-to-Anion Proton-Transfer Reactions. *J. Am. Chem. Soc.* **2016**, *138*, 9581-9588.
- (624) Lermyte, F.; Łački, M. K.; Valkenburg, D.; Gambin, A.; Sobott, F. Conformational Space and Stability of ETD Charge Reduction Products of Ubiquitin. *J. Am. Soc. Mass Spectrom.* **2017**, *28*, 69-76.
- (625) Abzalimov, R. R.; Kaltashov, I. A. Electrospray Ionization Mass Spectrometry of Highly Heterogeneous Protein Systems: Protein Ion Charge State Assignment Via Incomplete Charge Reduction. *Anal. Chem.* **2010**, *82*, 7523-7526.
- (626) Pitts-McCoy, A. M.; Harrilal, C. P.; McLuckey, S. A. Gas-Phase Ion/Ion Chemistry as a Probe for the Presence of Carboxylate Groups in Polypeptide Cations. *J. Am. Soc. Mass Spectrom.* **2019**, *30*, 329-338.
- (627) Abdillahi, A. M.; Lee, K. W.; McLuckey, S. A. Mass Analysis of Macromolecular Analytes Via Multiply-Charged Ion Attachment. *Anal. Chem.* **2020**, *92*, 16301-16306.
- (628) Huguet, R.; Mullen, C.; Srzentić, K.; Greer, J. B.; Fellers, R. T.; Zabrouskov, V.; Syka, J. E. P.; Kelleher, N. L.; Fornelli, L. Proton Transfer Charge Reduction Enables High-Throughput Top-Down Analysis of Large Proteoforms. *Anal. Chem.* **2019**, *91*, 15732-15739.
- (629) Zhang, G.; Keener, J. E.; Marty, M. T. Measuring Remodeling of the Lipid Environment Surrounding Membrane Proteins with Lipid Exchange and Native Mass Spectrometry. *Anal. Chem.* **2020**, *92*, 5666-5669.
- (630) Weidner, S. M.; Trimpin, S. Mass Spectrometry of Synthetic Polymers. *Anal. Chem.* **2008**, *80*, 4349-4361.
- (631) Prebyl, B. S.; Johnson, J. D.; Cook, K. D. Calibration for Determining Monomer Ratios in Copolymers by Electrospray Ionization Mass Spectrometry. *Int. J. Mass Spectrom.* **2004**, *238*, 207-214.
- (632) Prebyl, B. S.; Johnson, J. D.; Tuinman, A. A.; Zhou, S. L.; Cook, K. D. Qualitative Assessment of Monomer Ratios in Putative Ionic Terpolymer Samples by Electrospray Ionization Mass Spectrometry with Collision-Induced Dissociation. *J. Am. Soc. Mass Spectrom.* **2002**, *13*, 921-927.
- (633) Denisov, I. G.; Grinkova, Y. V.; Lazarides, A. A.; Sligar, S. G. Directed Self-Assembly of Monodisperse Phospholipid Bilayer Nanodiscs with Controlled Size. *J. Am. Chem. Soc.* **2004**, *126*, 3477-3487.
- (634) Denisov, I. G.; Sligar, S. G. Nanodiscs in Membrane Biochemistry and Biophysics. *Chem. Rev.* **2017**, *117*, 4669-4713.

- (635) Lai, G.; Forti, K. M.; Renthall, R. Kinetics of Lipid Mixing between Bicelles and Nanolipoprotein Particles. *Biophys. Chem.* **2015**, *197*, 47-52.
- (636) Nakano, M.; Fukuda, M.; Kudo, T.; Miyazaki, M.; Wada, Y.; Matsuzaki, N.; Endo, H.; Handa, T. Static and Dynamic Properties of Phospholipid Bilayer Nanodiscs. *J. Am. Chem. Soc.* **2009**, *131*, 8308-8312.
- (637) Prell, J. S. Modelling Collisional Cross Sections. In *Advances in Ion Mobility-Mass Spectrometry: Fundamentals, Instrumentation, and Applications*, Comprehensive Analytical Chemistry: Vol. 83; Donald, W. A.; Prell, J. S., Eds.; Elsevier, 2019; pp 1-22.
- (638) Zheng, X.; Aly, N. A.; Zhou, Y.; Dupuis, K. T.; Bilbao, A.; Paurus, Vanessa L.; Orton, D. J.; Wilson, R.; Payne, S. H.; Smith, R. D.; Baker, E. S. A Structural Examination and Collision Cross Section Database for over 500 Metabolites and Xenobiotics Using Drift Tube Ion Mobility Spectrometry. *Chem. Sci.* **2017**, *8*, 7724-7736.
- (639) Zhou, Z.; Luo, M.; Chen, X.; Yin, Y.; Xiong, X.; Wang, R.; Zhu, Z.-J. Ion Mobility Collision Cross-Section Atlas for Known and Unknown Metabolite Annotation in Untargeted Metabolomics. *Nat. Commun.* **2020**, *11*, 4334.
- (640) Ross, D. H.; Cho, J. H.; Xu, L. Breaking Down Structural Diversity for Comprehensive Prediction of Ion-Neutral Collision Cross Sections. *Anal. Chem.* **2020**, *92*, 4548-4557.
- (641) May, J. C.; Morris, C. B.; McLean, J. A. Ion Mobility Collision Cross Section Compendium. *Anal. Chem.* **2017**, *89*, 1032-1044.
- (642) Picache, J. A.; Rose, B. S.; Balinski, A.; Leaptrot, Katrina L.; Sherrod, S. D.; May, J. C.; McLean, J. A. Collision Cross Section Compendium to Annotate and Predict Multi-Omic Compound Identities. *Chem. Sci.* **2019**, *10*, 983-993.
- (643) Hines, K. M.; Ross, D. H.; Davidson, K. L.; Bush, M. F.; Xu, L. Large-Scale Structural Characterization of Drug and Drug-Like Compounds by High-Throughput Ion Mobility-Mass Spectrometry. *Anal. Chem.* **2017**, *89*, 9023-9030.
- (644) Hines, K. M.; Herron, J.; Xu, L. Assessment of Altered Lipid Homeostasis by HILIC-Ion Mobility-Mass Spectrometry-Based Lipidomics. *J. Lipid Res.* **2017**, *58*, 809-819.
- (645) Tolić, L. P.; Anderson, G. A.; Smith, R. D.; Brothers, H. M.; Spindler, R.; Tomalia, D. A. Electrospray Ionization Fourier Transform Ion Cyclotron Resonance Mass Spectrometric Characterization of High Molecular Mass Starburst™ Dendrimers. *Int. J. Mass Spectrom. Ion Processes* **1997**, *165*, 405-418.

- (646) de la Mora, J. F. Electrospray Ionization of Large Multiply Charged Species Proceeds Via Dole's Charged Residue Mechanism. *Anal. Chim. Acta* **2000**, *406*, 93-104.
- (647) Nesatyy, V. J.; Suter, M. J. F. On the Conformation-Dependent Neutralization Theory and Charging of Individual Proteins and Their Non-Covalent Complexes in the Gas Phase. *J. Mass Spectrom.* **2004**, *39*, 93-97.
- (648) Kaltashov, I. A.; Mohimen, A. Estimates of Protein Surface Areas in Solution by Electrospray Ionization Mass Spectrometry. *Anal. Chem.* **2005**, *77*, 5370-5379.
- (649) Testa, L.; Brocca, S.; Grandori, R. Charge-Surface Correlation in Electrospray Ionization of Folded and Unfolded Proteins. *Anal. Chem.* **2011**, *83*, 6459-6463.
- (650) Testa, L.; Brocca, S.; Santambrogio, C.; D'Urzo, A.; Habchi, J.; Longhi, S.; Uversky, V. N.; Grandori, R. Extracting Structural Information from Charge-State Distributions of Intrinsically Disordered Proteins by Non-Denaturing Electrospray-Ionization Mass Spectrometry. *Intrinsically Disord. Proteins* **2013**, *1*, e25068.
- (651) Dole, M.; Mack, L. L.; Hines, R. L.; Mobley, R. C.; Ferguson, L. D.; Alice, M. B. Molecular Beams of Macroions. *J. Chem. Phys.* **1968**, *49*, 2240-2249.
- (652) Ilag, L. L.; Videler, H.; McKay, A. R.; Sobott, F.; Fucini, P.; Nierhaus, K. H.; Robinson, C. V. Heptameric (L12)₆/L10 Rather Than Canonical Pentameric Complexes Are Found by Tandem MS of Intact Ribosomes from Thermophilic Bacteria. *Proc. Natl. Acad. Sci. U. S. A.* **2005**, *102*, 8192-8197.
- (653) Xia, Z.; DeGrandchamp, J. B.; Williams, E. R. Native Mass Spectrometry Beyond Ammonium Acetate: Effects of Nonvolatile Salts on Protein Stability and Structure. *Analyst* **2019**, *144*, 2565-2573.
- (654) Susa, A. C.; Lippens, J. L.; Xia, Z.; Loo, J. A.; Campuzano, I. D. G.; Williams, E. R. Submicrometer Emitter ESI Tips for Native Mass Spectrometry of Membrane Proteins in Ionic and Nonionic Detergents. *J. Am. Soc. Mass Spectrom.* **2018**, *29*, 203-206.
- (655) Panczyk, E. M.; Gilbert, J. D.; Jagdale, G. S.; Stiving, A. Q.; Baker, L. A.; Wysocki, V. H. Ion Mobility and Surface Collisions: Submicrometer Capillaries Can Produce Native-Like Protein Complexes. *Anal. Chem.* **2020**, *92*, 2460-2467.
- (656) Nguyen, G. T. H.; Tran, T. N.; Podgorski, M. N.; Bell, S. G.; Supuran, C. T.; Donald, W. A. Nanoscale Ion Emitters in Native Mass Spectrometry for Measuring Ligand-Protein Binding Affinities. *ACS Cent. Sci.* **2019**, *5*, 308-318.
- (657) McKay, A. R.; Ruotolo, B. T.; Ilag, L. L.; Robinson, C. V. Mass Measurements of Increased Accuracy Resolve Heterogeneous Populations of Intact Ribosomes. *J. Am. Chem. Soc.* **2006**, *128*, 11433-11442.

- (658) Cunniff, J. B.; Vouros, P. Mass and Charge State Assignment for Proteins and Peptide Mixtures Via Noncovalent Adduction in Electrospray Mass Spectrometry. *J. Am. Soc. Mass Spectrom.* **1995**, *6*, 1175-1182.
- (659) Liepold, L.; Oltrogge, L. M.; Suci, P. A.; Young, M. J.; Douglas, T. Correct Charge State Assignment of Native Electrospray Spectra of Protein Complexes. *J. Am. Soc. Mass Spectrom.* **2009**, *20*, 435-442.
- (660) Maleknia, S. D.; Downard, K. M. Charge Ratio Analysis Method: Approach for the Deconvolution of Electrospray Mass Spectra. *Anal. Chem.* **2005**, *77*, 111-119.
- (661) Almudaris, A.; Ashton, D. S.; Beddell, C. R.; Cooper, D. J.; Craig, S. J.; Oliver, R. W. A. The Assignment of Charge States in Complex Electrospray Mass Spectra. *Eur. J. Mass Spectrom.* **1996**, *2*, 57-67.
- (662) Tabb, D. L.; Shah, M. B.; Strader, M. B.; Connelly, H. M.; Hettich, R. L.; Hurst, G. B. Determination of Peptide and Protein Ion Charge States by Fourier Transformation of Isotope-Resolved Mass Spectra. *J. Am. Soc. Mass Spectrom.* **2006**, *17*, 903-915.
- (663) Winkler, R. Esiprot: A Universal Tool for Charge State Determination and Molecular Weight Calculation of Proteins from Electrospray Ionization Mass Spectrometry Data. *Rapid Commun. Mass Spectrom.* **2010**, *24*, 285-294.
- (664) Smith, R.; Mathis, A. D.; Ventura, D.; Prince, J. T. Proteomics, Lipidomics, Metabolomics: A Mass Spectrometry Tutorial from a Computer Scientist's Point of View. *BMC Bioinform.* **2014**, *15*, S9.
- (665) Chouinard, C. D.; Nagy, G.; Smith, R. D.; Baker, E. S. Ion Mobility-Mass Spectrometry in Metabolomic, Lipidomic, and Proteomic Analyses. In *Advances in Ion Mobility-Mass Spectrometry: Fundamentals, Instrumentation, and Applications*, Comprehensive Analytical Chemistry: Vol. 83; Donald, W. A.; Prell, J. S., Eds.; Elsevier, 2019; pp 123-159.
- (666) Konermann, L. Addressing a Common Misconception: Ammonium Acetate as Neutral pH "Buffer" for Native Electrospray Mass Spectrometry. *J. Am. Soc. Mass Spectrom.* **2017**, *28*, 1827-1835.
- (667) Urner, L. H.; Liko, I.; Yen, H.-Y.; Hoi, K.-K.; Bolla, J. R.; Gault, J.; Almeida, F. G.; Schweder, M.-P.; Shutin, D.; Ehrmann, S.; Haag, R.; Robinson, C. V.; Pagel, K. Modular Detergents Tailor the Purification and Structural Analysis of Membrane Proteins Including G-Protein Coupled Receptors. *Nat. Commun.* **2020**, *11*, 564.
- (668) Kundlacz, T.; Bender, J.; Schmidt, C. Effects of Non-Ionic and Zwitterionic Detergents on Soluble Proteins During Native Mass Spectrometry Experiments. *Int. J. Mass Spectrom.* **2021**, *468*, 116652.

- (669) Han, L.; Xue, X.; Roy, R.; Kitova, E. N.; Zheng, R. B.; St-Pierre, Y.; Lowary, T. L.; Klassen, J. S. Neoglycolipids as Glycosphingolipid Surrogates for Protein Binding Studies Using Nanodiscs and Native Mass Spectrometry. *Anal. Chem.* **2020**, *92*, 14189-14196.
- (670) Hoi, K. K.; Bada Juarez, J. F.; Judge, P. J.; Yen, H.-Y.; Wu, D.; Vinals, J.; Taylor, G. F.; Watts, A.; Robinson, C. V. Detergent-Free Lipodisc Nanoparticles Facilitate High-Resolution Mass Spectrometry of Folded Integral Membrane Proteins. *Nano Letters* **2021**, *21*, 2824-2831.
- (671) Landreh, M.; Costeira-Paulo, J.; Gault, J.; Marklund, E. G.; Robinson, C. V. Effects of Detergent Micelles on Lipid Binding to Proteins in Electrospray Ionization Mass Spectrometry. *Anal. Chem.* **2017**, *89*, 7425-7430.
- (672) Benesch, J. L. P.; Ruotolo, B. T.; Simmons, D. A.; Barrera, N. P.; Morgner, N.; Wang, L.; Saibil, H. R.; Robinson, C. V. Separating and Visualising Protein Assemblies by Means of Preparative Mass Spectrometry and Microscopy. *J. Struct. Biol.* **2010**, *172*, 161-168.
- (673) Jore, M. M.; Lundgren, M.; van Duijn, E.; Bultema, J. B.; Westra, E. R.; Waghmare, S. P.; Wiedenheft, B.; Pul, Ü.; Wurm, R.; Wagner, R.; Beijer, M. R.; Barendregt, A.; Zhou, K.; Snijders, A. P. L.; Dickman, M. J.; Doudna, J. A.; Boekema, E. J.; Heck, A. J. R.; van der Oost, J.; Brouns, S. J. J. Structural Basis for CRISPER RNA-Guided DNA Recognition by Cascade. *Nat. Struct. Mol. Biol.* **2011**, *18*, 529-536.
- (674) Su, C.-C.; Lyu, M.; Morgan, C. E.; Bolla, J. R.; Robinson, C. V.; Yu, E. W. A 'Build and Retrieve' Methodology to Simultaneously Solve Cryo-EM Structures of Membrane Proteins. *Nat. Methods* **2021**, *18*, 69-75.
- (675) Wu, D.; Robinson, C. V. Connecting 'Multi-Omics' Approaches to Endogenous Protein Complexes. *Trends Chem.* **2021**, *3*, 445-455.
- (676) Yin, Z.; Huang, J.; Miao, H.; Hu, O.; Li, H. High-Pressure Electrospray Ionization Yields Supercharged Protein Complexes from Native Solutions While Preserving Noncovalent Interactions. *Anal. Chem.* **2020**, *92*, 12312-12321.
- (677) Saikusa, K.; Kato, D.; Nagadoi, A.; Kurumizaka, H.; Akashi, S. Native Mass Spectrometry of Protein and DNA Complexes Prepared in Nonvolatile Buffers. *J. Am. Soc. Mass Spectrom.* **2020**, *31*, 711-718.
- (678) Sakamoto, W.; Azegami, N.; Konuma, T.; Akashi, S. Single-Cell Native Mass Spectrometry of Human Erythrocytes. *Anal. Chem.* **2021**, *93*, 6583-6588.
- (679) Gan, J.; Ben-Nissan, G.; Arkind, G.; Tarnavsky, M.; Trudeau, D.; Noda Garcia, L.; Tawfik, D. S.; Sharon, M. Native Mass Spectrometry of Recombinant Proteins from Crude Cell Lysates. *Anal. Chem.* **2017**, *89*, 4398-4404.

- (680) Ben-Nissan, G.; Vimer, S.; Warszawski, S.; Katz, A.; Yona, M.; Unger, T.; Peleg, Y.; Morgenstern, D.; Cohen-Dvashi, H.; Diskin, R.; Fleishman, S. J.; Sharon, M. Rapid Characterization of Secreted Recombinant Proteins by Native Mass Spectrometry. *Commun. Biol.* **2018**, *1*, 213.
- (681) Tadeo, X.; López-Méndez, B.; Castaño, D.; Trigueros, T.; Millet, O. Protein Stabilization and the Hofmeister Effect: The Role of Hydrophobic Solvation. *Biophys. J.* **2009**, *97*, 2595-2603.
- (682) Kunz, W.; Henle, J.; Ninham, B. W. ‘Zur Lehre Von Der Wirkung Der Salze’ (About the Science of the Effect of Salts): Franz Hofmeister's Historical Papers. *Curr. Opin. Colloid Interface Sci.* **2004**, *9*, 19-37.
- (683) National Resource for Native MS-Guided Structural Biology. <https://nativems.osu.edu/> (accessed August 19, 2021).
- (684) Quetschlich, D.; Esser, T. K.; Newport, T. D.; Fiorentino, F.; Shutin, D.; Chen, S.; Davis, R.; Lovera, S.; Liko, I.; Stansfeld, P. J.; Robinson, C. V. NaViA: A Program for the Visual Analysis of Complex Mass Spectra. *Bioinformatics* **2021**, *37*, 4876-4878.
- (685) Wu, Z.; Roberts, D. S.; Melby, J. A.; Wenger, K.; Wetzel, M.; Gu, Y.; Ramanathan, S. G.; Bayne, E. F.; Liu, X.; Sun, R.; Ong, I. M.; McIlwain, S. J.; Ge, Y. Mash Explorer: A Universal Software Environment for Top-Down Proteomics. *J. Proteome Res.* **2020**, *19*, 3867-3876.
- (686) Mortensen, D. N.; Williams, E. R. Theta-Glass Capillaries in Electrospray Ionization: Rapid Mixing and Short Droplet Lifetimes. *Anal. Chem.* **2014**, *86*, 9315-9321.
- (687) Fisher, C. M.; Kharlamova, A.; McLuckey, S. A. Affecting Protein Charge State Distributions in Nano-Electrospray Ionization Via In-Spray Solution Mixing Using Theta Capillaries. *Anal. Chem.* **2014**, *86*, 4581-4588.
- (688) Wang, H.; Yong, G.; Brown, S. L.; Lee, H. E.; Zenaidee, M. A.; Supuran, C. T.; Donald, W. A. Supercharging Protein Ions in Native Mass Spectrometry Using Theta Capillary Nanoelectrospray Ionization Mass Spectrometry and Cyclic Alkylcarbonates. *Anal. Chim. Acta* **2018**, *1003*, 1-9.
- (689) Laskin, J.; Futrell, J. On the Efficiency of Energy Transfer in Collisional Activation of Small Peptides. *J. Chem. Phys.* **2002**, *116*, 4302-4310.
- (690) Ruotolo, B. T.; Hyung, S.-J.; Robinson, P. M.; Giles, K.; Bateman, R. H.; Robinson, C. V. Ion Mobility–Mass Spectrometry Reveals Long-Lived, Unfolded Intermediates in the Dissociation of Protein Complexes. *Angew. Chem. Int. Ed.* **2007**, *46*, 8001-8004.

- (691) Hyung, S.-J.; Robinson, C. V.; Ruotolo, B. T. Gas-Phase Unfolding and Disassembly Reveals Stability Differences in Ligand-Bound Multiprotein Complexes. *Chem. Biol.* **2009**, *16*, 382-390.
- (692) Hopper, J. T. S.; Oldham, N. J. Collision Induced Unfolding of Protein Ions in the Gas Phase Studied by Ion Mobility-Mass Spectrometry: The Effect of Ligand Binding on Conformational Stability. *J. Am. Soc. Mass Spectrom.* **2009**, *20*, 1851-1858.
- (693) Donor, M. T.; Mroz, A. M.; Prell, J. S. Experimental and Theoretical Investigation of Overall Energy Deposition in Surface-Induced Unfolding of Protein Ions. *Chem. Sci.* **2019**, *10*, 4097-4106.
- (694) Donor, M. T.; Shepherd, S. O.; Prell, J. S. Rapid Determination of Activation Energies for Gas-Phase Protein Unfolding and Dissociation in a Q-IM-TOF Mass Spectrometer. *J. Am. Soc. Mass Spectrom.* **2020**, *31*, 602-610.
- (695) Cheung See Kit, M.; Shepherd, S. O.; Prell, J. S.; Webb, I. K. Experimental Determination of Activation Energies for Covalent Bond Formation Via Ion/Ion Reactions and Competing Processes. *J. Am. Soc. Mass Spectrom.* **2021**, *32*, 2313-2321.
- (696) Laszlo, K. J.; Bush, M. F. Effects of Charge State, Charge Distribution, and Structure on the Ion Mobility of Protein Ions in Helium Gas: Results from Trajectory Method Calculations. *J. Phys. Chem. A* **2017**, *121*, 7768-7777.
- (697) Konermann, L.; Rodriguez, A. D.; Liu, J. On the Formation of Highly Charged Gaseous Ions from Unfolded Proteins by Electrospray Ionization. *Anal. Chem.* **2012**, *84*, 6798-6804.
- (698) Landreh, M.; Liko, I.; Uzdavinys, P.; Coincon, M.; Hopper, J. T. S.; Drew, D.; Robinson, C. V. Controlling Release, Unfolding and Dissociation of Membrane Protein Complexes in the Gas Phase through Collisional Cooling. *Chem. Commun.* **2015**, *51*, 15582-15584.
- (699) Silveira, J. A.; Fort, K. L.; Kim, D.; Servage, K. A.; Pierson, N. A.; Clemmer, D. E.; Russell, D. H. From Solution to the Gas Phase: Stepwise Dehydration and Kinetic Trapping of Substance P Reveals the Origin of Peptide Conformations. *J. Am. Chem. Soc.* **2013**, *135*, 19147-19153.
- (700) Benesch, J. L. P.; Ruotolo, B. T.; Simmons, D. A.; Robinson, C. V. Protein Complexes in the Gas Phase: Technology for Structural Genomics and Proteomics. *Chem. Rev.* **2007**, *107*, 3544-3567.
- (701) Wheeler, L. C.; Donor, M. T.; Prell, J. S.; Harms, M. J. Multiple Evolutionary Origins of Ubiquitous Cu²⁺ and Zn²⁺ Binding in the S100 Protein Family. *PLoS One* **2016**, *11*, e0164740.

- (702) Wolynes, P. G. Biomolecular Folding in Vacuo!!!(?). *Proc. Natl. Acad. Sci. U. S. A.* **1995**, *92*, 2426-2427.
- (703) Schnier, P. D.; Gross, D. S.; Williams, E. R. Electrostatic Forces and Dielectric Polarizability of Multiply Protonated Gas-Phase Cytochrome *c* Ions Probed by Ion/Molecule Chemistry. *J. Am. Chem. Soc.* **1995**, *117*, 6747-6757.
- (704) Breuker, K.; McLafferty, F. W. Stepwise Evolution of Protein Native Structure with Electrospray into the Gas Phase, 10^{-12} to 10^2 s. *Proc. Natl. Acad. Sci. U. S. A.* **2008**, *105*, 18145-18152.
- (705) Steinberg, M. Z.; Elber, R.; McLafferty, F. W.; Gerber, R. B.; Breuker, K. Early Structural Evolution of Native Cytochrome *c* after Solvent Removal. *ChemBioChem* **2008**, *9*, 2417-2423.
- (706) Bakhtiari, M.; Konermann, L. Protein Ions Generated by Native Electrospray Ionization: Comparison of Gas Phase, Solution, and Crystal Structures. *J. Phys. Chem. B* **2019**, *123*, 1784-1796.
- (707) Polfer, N. C. Infrared Multiple Photon Dissociation Spectroscopy of Trapped Ions. *Chem. Soc. Rev.* **2011**, *40*, 2211-2221.
- (708) Steill, J. D.; Oomens, J. Gas-Phase Deprotonation of *p*-Hydroxybenzoic Acid Investigated by IR Spectroscopy: Solution-Phase Structure Is Retained Upon ESI. *J. Am. Chem. Soc.* **2009**, *131*, 13570-13571.
- (709) Stuchfield, D.; Barran, P. Unique Insights to Intrinsically Disordered Proteins Provided by Ion Mobility Mass Spectrometry. *Curr. Opin. Chem. Biol.* **2018**, *42*, 177-185.
- (710) Warnke, S.; Von Helden, G.; Pagel, K. Protein Structure in the Gas Phase: The Influence of Side-Chain Microsolvation. *J. Am. Chem. Soc.* **2013**, *135*, 1177-1180.
- (711) Kaltashov, I. A.; Fenselau, C. Stability of Secondary Structural Elements in a Solvent-Free Environment: The α Helix. *Proteins* **1997**, *27*, 165-170.
- (712) Hudgins, R. R.; Mao, Y.; Ratner, M. A.; Jarrold, M. F. Conformations of Gly_nH^+ and Ala_nH^+ Peptides in the Gas Phase. *Biophys. J.* **1999**, *76*, 1591-1597.
- (713) Li, J.; Lyu, W.; Rossetti, G.; Konijnenberg, A.; Natalello, A.; Ippoliti, E.; Orozco, M.; Sobott, F.; Grandori, R.; Carloni, P. Proton Dynamics in Protein Mass Spectrometry. *J. Phys. Chem. Lett.* **2017**, *8*, 1105-1112.
- (714) Florance, H. V.; Stopford, A. P.; Kalapothakis, J. M.; McCullough, B. J.; Bretherick, A.; Barran, P. E. Evidence for α -Helices in the Gas Phase: A Case Study Using Melittin from Honey Bee Venom. *Analyst* **2011**, *136*, 3446-3452.

- (715) Kulesza, A.; Marklund, E. G.; MacAleese, L.; Chirot, F.; Dugourd, P. Bringing Molecular Dynamics and Ion-Mobility Spectrometry Closer Together: Shape Correlations, Structure-Based Predictors, and Dissociation. *J. Phys. Chem. B* **2018**, *122*, 8317-8329.
- (716) Pagel, K.; Natan, E.; Hall, Z.; Fersht, A. R.; Robinson, C. V. Intrinsically Disordered p53 and Its Complexes Populate Compact Conformations in the Gas Phase. *Angew. Chem. Int. Ed.* **2013**, *52*, 361-365.
- (717) Chen, S.-H.; Russell, D. H. How Closely Related Are Conformations of Protein Ions Sampled by IM-MS to Native Solution Structures? *J. Am. Soc. Mass Spectrom.* **2015**, *26*, 1433-1443.
- (718) Krone, M. G.; Baumketner, A.; Bernstein, S. L.; Wyttenbach, T.; Lazo, N. D.; Teplow, D. B.; Bowers, M. T.; Shea, J.-E. Effects of Familial Alzheimer's Disease Mutations on the Folding Nucleation of the Amyloid B-Protein. *J. Mol. Biol.* **2008**, *381*, 221-228.
- (719) Segev, E.; Wyttenbach, T.; Bowers, M. T.; Gerber, R. B. Conformational Evolution of Ubiquitin Ions in Electrospray Mass Spectrometry: Molecular Dynamics Simulations at Gradually Increasing Temperatures. *Phys. Chem. Chem. Phys.* **2008**, *10*, 3077-3082.
- (720) Cole, H. L.; Kalapothakis, J. M. D.; Bennett, G.; Barran, P. E.; MacPhee, C. E. Characterizing Early Aggregates Formed by an Amyloidogenic Peptide by Mass Spectrometry. *Angew. Chem. Int. Ed.* **2010**, *49*, 9448-9451.
- (721) Marchese, R.; Grandori, R.; Carloni, P.; Raugei, S. A Computational Model for Protein Ionization by Electrospray Based on Gas-Phase Basicity. *J. Am. Soc. Mass Spectrom.* **2012**, *23*, 1903-1910.
- (722) Konermann, L. Molecular Dynamics Simulations on Gas-Phase Proteins with Mobile Protons: Inclusion of All-Atom Charge Solvation. *J. Phys. Chem. B* **2017**, *121*, 8102-8112.
- (723) Ly, T.; Julian, R. R. Elucidating the Tertiary Structure of Protein Ions *In Vacuo* with Site Specific Photoinitiated Radical Reactions. *J. Am. Chem. Soc.* **2010**, *132*, 8602-8609.
- (724) Meyer, T.; de la Cruz, X.; Orozco, M. An Atomistic View to the Gas Phase Proteome. *Structure* **2009**, *17*, 88-95.
- (725) Patriksson, A.; Adams, C. M.; Kjeldsen, F.; Zubarev, R. A.; van der Spoel, D. A Direct Comparison of Protein Structure in the Gas and Solution Phase: The Trp-Cage. *J. Phys. Chem. B* **2007**, *111*, 13147-13150.
- (726) Jarrold, M. F. Unfolding, Refolding, and Hydration of Proteins in the Gas Phase. *Acc. Chem. Res.* **1999**, *32*, 360-367.

- (727) Devine, P. W. A.; Fisher, H. C.; Calabrese, A. N.; Whelan, F.; Higazi, D. R.; Potts, J. R.; Lowe, D. C.; Radford, S. E.; Ashcroft, A. E. Investigating the Structural Compaction of Biomolecules Upon Transition to the Gas-Phase Using ESI-TWIMS-MS. *J. Am. Soc. Mass Spectrom.* **2017**, *28*, 1855-1862.
- (728) Baumketner, A.; Bernstein, S. L.; Wyttenbach, T.; Bitan, G.; Teplow, D. B.; Bowers, M. T.; Shea, J.-E. Amyloid B-Protein Monomer Structure: A Computational and Experimental Study. *Protein Sci.* **2006**, *15*, 420-428.
- (729) McAllister, R. G.; Metwally, H.; Sun, Y.; Konermann, L. Release of Native-Like Gaseous Proteins from Electrospray Droplets Via the Charged Residue Mechanism: Insights from Molecular Dynamics Simulations. *J. Am. Chem. Soc.* **2015**, *137*, 12667-12676.
- (730) Duez, Q.; Metwally, H.; Konermann, L. Electrospray Ionization of Polypropylene Glycol: Rayleigh-Charged Droplets, Competing Pathways, and Charge State-Dependent Conformations. *Anal. Chem.* **2018**, *90*, 9912-9920.
- (731) Borysik, A. J.; Kovacs, D.; Guharoy, M.; Tompa, P. Ensemble Methods Enable a New Definition for the Solution to Gas-Phase Transfer of Intrinsically Disordered Proteins. *J. Am. Chem. Soc.* **2015**, *137*, 13807-13817.
- (732) Steinberg, M. Z.; Breuker, K.; Elber, R.; Gerber, R. B. The Dynamics of Water Evaporation from Partially Solvated Cytochrome *c* in the Gas Phase. *Phys. Chem. Chem. Phys.* **2007**, *9*, 4690-4697.
- (733) Fegan, S. K.; Thachuk, M. Suitability of the MARTINI Force Field for Use with Gas-Phase Protein Complexes. *J. Chem. Theory Comput.* **2012**, *8*, 1304-1313.
- (734) Valentine, S. J.; Clemmer, D. E. Temperature-Dependent H/D Exchange of Compact and Elongated Cytochrome *c* Ions in the Gas Phase. *J. Am. Soc. Mass Spectrom.* **2002**, *13*, 506-517.
- (735) Konermann, L.; Metwally, H.; McAllister, R. G.; Popa, V. How to Run Molecular Dynamics Simulations on Electrospray Droplets and Gas Phase Proteins: Basic Guidelines and Selected Applications. *Methods* **2018**, *144*, 104-112.
- (736) Guvench, O.; MacKerell, A. D. Comparison of Protein Force Fields for Molecular Dynamics Simulations. In *Molecular Modeling of Proteins*, Methods in Molecular Biology: Vol. 443; Kukol, A., Ed.; Humana Press, 2008; pp 63-88.
- (737) Smith, M. D.; Rao, J. S.; Segelken, E.; Cruz, L. Force-Field Induced Bias in the Structure of A β ₂₁₋₃₀: A Comparison of OPLS, AMBER, CHARMM, and GROMOS Force Fields. *J. Chem. Inf. Model.* **2015**, *55*, 2587-2595.
- (738) Williams, E. R. Proton Transfer Reactivity of Large Multiply Charged Ions. *J. Mass Spectrom.* **1996**, *31*, 831-842.

- (739) Bazzo, R.; Tappin, M. J.; Pastore, A.; Harvey, T. S.; Carver, J. A.; Campbell, I. D. The Structure of Melittin. *Eur. J. Biochem.* **1988**, *173*, 139-146.
- (740) Friemann, R.; Larsson, D. S. D.; Wang, Y.; van der Spoel, D. Molecular Dynamics Simulations of a Membrane Protein–Micelle Complex *In Vacuo*. *J. Am. Chem. Soc.* **2009**, *131*, 16606-16607.
- (741) Pliotas, C.; Dahl, A. C. E.; Rasmussen, T.; Mahendran, K. R.; Smith, T. K.; Marius, P.; Gault, J.; Banda, T.; Rasmussen, A.; Miller, S.; Robinson, C. V.; Bayley, H.; Sansom, M. S. P.; Booth, I. R.; Naismith, J. H. The Role of Lipids in Mechanosensation. *Nat. Struct. Mol. Biol.* **2015**, *22*, 991-998.
- (742) Nagornova, N. S.; Guglielmi, M.; Doemer, M.; Tavernelli, I.; Rothlisberger, U.; Rizzo, T. R.; Boyarkin, O. V. Cold-Ion Spectroscopy Reveals the Intrinsic Structure of a Decapeptide. *Angew. Chem. Int. Ed.* **2011**, *50*, 5383-5386.
- (743) Roy, T. K.; Nagornova, N. S.; Boyarkin, O. V.; Gerber, R. B. A Decapeptide Hydrated by Two Waters: Conformers Determined by Theory and Validated by Cold Ion Spectroscopy. *J. Phys. Chem. A* **2017**, *121*, 9401-9408.
- (744) Bleiholder, C. A Local Collision Probability Approximation for Predicting Momentum Transfer Cross Sections. *Analyst* **2015**, *140*, 6804-6813.
- (745) Wyttenbach, T.; von Helden, G.; Batka, J. J.; Carlat, D.; Bowers, M. T. Effect of the Long-Range Potential on Ion Mobility Measurements. *J. Am. Soc. Mass Spectrom.* **1997**, *8*, 275-282.
- (746) Paizs, B. A Divide-and-Conquer Approach to Compute Collision Cross Sections in the Projection Approximation Method. *Int. J. Mass Spectrom.* **2015**, *378*, 360-363.
- (747) Shvartsburg, A. A.; Mashkevich, S. V.; Siu, K. W. M. Incorporation of Thermal Rotation of Drifting Ions into Mobility Calculations: Drastic Effect for Heavier Buffer Gases. *J. Phys. Chem. A* **2000**, *104*, 9448-9453.
- (748) Larriba-Andaluz, C.; Fernandez-Garcia, J.; Ewing, M. A.; Hogan, C. J.; Clemmer, D. E. Gas Molecule Scattering & Ion Mobility Measurements for Organic Macro-Ions in He Versus N₂ Environments. *Phys. Chem. Chem. Phys.* **2015**, *17*, 15019-15029.
- (749) Zanutto, L.; Heerdt, G.; Souza, P. C. T.; Araujo, G.; Skaf, M. S. High Performance Collision Cross Section Calculation—HPCCS. *J. Comput. Chem.* **2018**, *39*, 1675-1681.
- (750) Ieritano, C.; Crouse, J.; Campbell, J. L.; Hopkins, W. S. A Parallelized Molecular Collision Cross Section Package with Optimized Accuracy and Efficiency. *Analyst* **2019**, *144*, 1660-1670.

- (751) Cino, E. A.; Choy, W.-Y.; Karttunen, M. Comparison of Secondary Structure Formation Using 10 Different Force Fields in Microsecond Molecular Dynamics Simulations. *J. Chem. Theory Comput.* **2012**, *8*, 2725-2740.
- (752) Vijay-Kumar, S.; Bugg, C. E.; Cook, W. J. Structure of Ubiquitin Refined at 1.8 Å Resolution. *J. Mol. Biol.* **1987**, *194*, 531-544.
- (753) Weber, P. L.; Brown, S. C.; Mueller, L. Sequential Proton NMR Assignments and Secondary Structure Identification of Human Ubiquitin. *Biochemistry* **1987**, *26*, 7282-7290.
- (754) Ibarra-Molero, B.; Makhatadze, G. I.; Sanchez-Ruiz, J. M. Cold Denaturation of Ubiquitin. *Biochim. Biophys. Acta-Protein Struct. Molec. Enzym.* **1999**, *1429*, 384-390.
- (755) Koeniger, S. L.; Clemmer, D. E. Resolution and Structural Transitions of Elongated States of Ubiquitin. *J. Am. Soc. Mass Spectrom.* **2007**, *18*, 322-331.
- (756) Bartman, C. E.; Metwally, H.; Konermann, L. Effects of Multidentate Metal Interactions on the Structure of Collisionally Activated Proteins: Insights from Ion Mobility Spectrometry and Molecular Dynamics Simulations. *Anal. Chem.* **2016**, *88*, 6905-6913.
- (757) Wagner, N. D.; Kim, D.; Russell, D. H. Increasing Ubiquitin Ion Resistance to Unfolding in the Gas Phase Using Chloride Adduction: Preserving More “Native-Like” Conformations Despite Collisional Activation. *Anal. Chem.* **2016**, *88*, 5934-5940.
- (758) Vogel, H. Comparison of the Conformation and Orientation of Alamethicin and Melittin in Lipid Membranes. *Biochemistry* **1987**, *26*, 4562-4572.
- (759) Seo, J.; Hoffmann, W.; Warnke, S.; Bowers, M. T.; Pagel, K.; von Helden, G. Retention of Native Protein Structures in the Absence of Solvent: A Coupled Ion Mobility and Spectroscopic Study. *Angew. Chem. Int. Ed.* **2016**, *55*, 14173-14176.
- (760) Ruotolo, B. T.; Giles, K.; Campuzano, I.; Sandercock, A. M.; Bateman, R. H.; Robinson, C. V. Evidence for Macromolecular Protein Rings in the Absence of Bulk Water. *Science* **2005**, *310*, 1658-1661.
- (761) Liu, Y.; Cong, X.; Liu, W.; Laganowsky, A. Characterization of Membrane Protein–Lipid Interactions by Mass Spectrometry Ion Mobility Mass Spectrometry. *J. Am. Soc. Mass Spectrom.* **2017**, *28*, 579-586.
- (762) Ahadi, E.; Konermann, L. Modeling the Behavior of Coarse-Grained Polymer Chains in Charged Water Droplets: Implications for the Mechanism of Electrospray Ionization. *J. Phys. Chem. B* **2012**, *116*, 104-112.

- (763) Consta, S.; In Oh, M.; Kwan, V.; Malevanets, A. Strengths and Weaknesses of Molecular Simulations of Electrosprayed Droplets. *J. Am. Soc. Mass Spectrom.* **2018**, *29*, 2287-2296.
- (764) Oh, M. I.; Malevanets, A.; Paliy, M.; Frenkel, D.; Consta, S. When Droplets Become Stars: Charged Dielectric Droplets Beyond the Rayleigh Limit. *Soft Matter* **2017**, *13*, 8781-8795.
- (765) Consta, S.; Oh, M. I.; Sharawy, M.; Malevanets, A. Macroion–Solvent Interactions in Charged Droplets. *J. Phys. Chem. A* **2018**, *122*, 5239-5250.
- (766) Cornell, W. D.; Cieplak, P.; Bayly, C. I.; Gould, I. R.; Merz, K. M.; Ferguson, D. M.; Spellmeyer, D. C.; Fox, T.; Caldwell, J. W.; Kollman, P. A. A Second Generation Force Field for the Simulation of Proteins, Nucleic Acids, and Organic Molecules. *J. Am. Chem. Soc.* **1995**, *117*, 5179-5197.
- (767) Kaminski, G. A.; Friesner, R. A.; Tirado-Rives, J.; Jorgensen, W. L. Evaluation and Reparametrization of the OPLS-AA Force Field for Proteins Via Comparison with Accurate Quantum Chemical Calculations on Peptides. *J. Phys. Chem. B* **2001**, *105*, 6474-6487.
- (768) MacKerell, A. D.; Bashford, D.; Bellott, M.; Dunbrack, R. L.; Evanseck, J. D.; Field, M. J.; Fischer, S.; Gao, J.; Guo, H.; Ha, S.; Joseph-McCarthy, D.; Kuchnir, L.; Kuczera, K.; Lau, F. T. K.; Mattos, C.; Michnick, S.; Ngo, T.; Nguyen, D. T.; Prodhom, B.; Reiher, W. E.; Roux, B.; Schlenkrich, M.; Smith, J. C.; Stote, R.; Straub, J.; Watanabe, M.; Wiórkiewicz-Kuczera, J.; Yin, D.; Karplus, M. All-Atom Empirical Potential for Molecular Modeling and Dynamics Studies of Proteins. *J. Phys. Chem. B* **1998**, *102*, 3586-3616.
- (769) MacKerell, A. D.; Feig, M.; Brooks III, C. L. Extending the Treatment of Backbone Energetics in Protein Force Fields: Limitations of Gas-Phase Quantum Mechanics in Reproducing Protein Conformational Distributions in Molecular Dynamics Simulations. *J. Comput. Chem.* **2004**, *25*, 1400-1415.
- (770) Schuler, L. D.; Van Gunsteren, W. F. On the Choice of Dihedral Angle Potential Energy Functions for *n*-Alkanes. *Mol. Simulat.* **2000**, *25*, 301-319.
- (771) Schmid, N.; Eichenberger, A. P.; Choutko, A.; Riniker, S.; Winger, M.; Mark, A. E.; van Gunsteren, W. F. Definition and Testing of the GROMOS Force-Field Versions 54a7 and 54b7. *Eur. Biophys. J.* **2011**, *40*, 843-856.
- (772) van der Spoel, D.; Marklund, E. G.; Larsson, D. S. D.; Caleman, C. Proteins, Lipids, and Water in the Gas Phase. *Macromol. Biosci.* **2011**, *11*, 50-59.
- (773) Allison, T. M.; Landreh, M.; Benesch, J. L. P.; Robinson, C. V. Low Charge and Reduced Mobility of Membrane Protein Complexes Has Implications for Calibration of Collision Cross Section Measurements. *Anal. Chem.* **2016**, *88*, 5879-5884.

- (774) Hall, Z.; Robinson, C. V. Do Charge State Signatures Guarantee Protein Conformations? *J. Am. Soc. Mass Spectrom.* **2012**, *23*, 1161-1168.
- (775) Grandori, R. Origin of the Conformation Dependence of Protein Charge-State Distributions in Electrospray Ionization Mass Spectrometry. *J. Mass Spectrom.* **2003**, *38*, 11-15.
- (776) Shelimov, K. B.; Clemmer, D. E.; Hudgins, R. R.; Jarrold, M. F. Protein Structure *in Vacuo*: Gas-Phase Conformations of BPTI and Cytochrome *c*. *J. Am. Chem. Soc.* **1997**, *119*, 2240-2248.
- (777) Raab, S. A.; El-Baba, T. J.; Laganowsky, A.; Russell, D. H.; Valentine, S. J.; Clemmer, D. E. Protons Are Fast and Smart; Proteins Are Slow and Dumb: On the Relationship of Electrospray Ionization Charge States and Conformations. *J. Am. Soc. Mass Spectrom.* **2021**, *32*, 1553-1561.
- (778) Hong, S.; Bush, M. F. Collision-Induced Unfolding Is Sensitive to the Polarity of Proteins and Protein Complexes. *J. Am. Soc. Mass Spectrom.* **2019**, *30*, 2430-2437.
- (779) Allen, S. J.; Schwartz, A. M.; Bush, M. F. Effects of Polarity on the Structures and Charge States of Native-Like Proteins and Protein Complexes in the Gas Phase. *Anal. Chem.* **2013**, *85*, 12055-12061.
- (780) Edwards, A. N.; Tran, H. M.; Gallagher, E. S. Propagating Error through Traveling-Wave Ion Mobility Calibration. *J. Am. Soc. Mass Spectrom.* **2021**, *32*, 2621-2630.
- (781) Li, A.; Fenselau, C.; Kaltashov, I. A. Stability of Secondary Structural Elements in a Solvent-Free Environment. II: The Beta-Pleated Sheets. *Proteins* **1998**, *Suppl* 2, 22-27.
- (782) Metwally, H.; McAllister, R. G.; Popa, V.; Konermann, L. Mechanism of Protein Supercharging by Sulfolane and *m*-Nitrobenzyl Alcohol: Molecular Dynamics Simulations of the Electrospray Process. *Anal. Chem.* **2016**, *88*, 5345-5354.
- (783) Prell, J. S.; Chang, T. M.; O'Brien, J. T.; Williams, E. R. Hydration Isomers of Protonated Phenylalanine and Derivatives: Relative Stabilities from Infrared Photodissociation. *J. Am. Chem. Soc.* **2010**, *132*, 7811-7819.
- (784) Chang, T. M.; Prell, J. S.; Warrick, E. R.; Williams, E. R. Where's the Charge? Protonation Sites in Gaseous Ions Change with Hydration. *J. Am. Chem. Soc.* **2012**, *134*, 15805-15813.
- (785) Bush, M. F.; Prell, J. S.; Saykally, R. J.; Williams, E. R. One Water Molecule Stabilizes the Cationized Arginine Zwitterion. *J. Am. Chem. Soc.* **2007**, *129*, 13544-13553.

- (786) Servage, K. A.; Silveira, J. A.; Fort, K. L.; Russell, D. H. Cryogenic Ion Mobility-Mass Spectrometry: Tracking Ion Structure from Solution to the Gas Phase. *Acc. Chem. Res.* **2016**, *49*, 1421-1428.
- (787) Lee, J. H.; Pollert, K.; Konermann, L. Testing the Robustness of Solution Force Fields for MD Simulations on Gaseous Protein Ions. *J. Phys. Chem. B* **2019**, *123*, 6705-6715.
- (788) Larriba, C.; Hogan, C. J. Ion Mobilities in Diatomic Gases: Measurement Versus Prediction with Non-Specular Scattering Models. *J. Phys. Chem. A* **2013**, *117*, 3887-3901.
- (789) Chen, C. R.; Makhatadze, G. I. Protein volume: Calculating Molecular van der Waals and Void Volumes in Proteins. *BMC Bioinform.* **2015**, *16*, 101.
- (790) Laszlo, K. J.; Buckner, J. H.; Munger, E. B.; Bush, M. F. Native-Like and Denatured Cytochrome *c* Ions Yield Cation-to-Anion Proton Transfer Reaction Products with Similar Collision Cross-Sections. *J. Am. Soc. Mass Spectrom.* **2017**, *28*, 1382-1391.
- (791) Lee, J. W.; Davidson, K. L.; Bush, M. F.; Kim, H. I. Collision Cross Sections and Ion Structures: Development of a General Calculation Method Via High-Quality Ion Mobility Measurements and Theoretical Modeling. *Analyst* **2017**, *142*, 4289-4298.
- (792) Chalk, R.; Borkowska, O.; Azeez, K. A.; Oerum, S.; Born, P.; Gileadi, O.; Burgess-Brown, N. Electrospray Surface Charge Describes Protein Molecular Motion. *bioRxiv* **2019**, DOI: 10.1101/571091.
- (793) Turzo, S. M. B. A.; Seffernick, J. T.; Rolland, A. D.; Donor, M. T.; Heinze, S.; Prell, J. S.; Wysocki, V.; Lindert, S. Protein Shape Sampled by Ion Mobility Mass Spectrometry Consistently Improves Protein Structure Prediction. *bioRxiv* **2021**, DOI: 10.1101/2021.1105.1127.445812.
- (794) Biehn, S. E.; Lindert, S. Protein Structure Prediction with Mass Spectrometry Data. *Annu. Rev. Phys. Chem.* **2022**, *73*, 1-19.
- (795) Allen, S. J.; Giles, K.; Gilbert, T.; Bush, M. F. Ion Mobility Mass Spectrometry of Peptide, Protein, and Protein Complex Ions Using a Radio-Frequency Confining Drift Cell. *Analyst* **2016**, *141*, 884-891.
- (796) Porrini, M.; Rosu, F.; Rabin, C.; Darré, L.; Gómez, H.; Orozco, M.; Gabelica, V. Compaction of Duplex Nucleic Acids Upon Native Electrospray Mass Spectrometry. *ACS Cent. Sci.* **2017**, *3*, 454-461.
- (797) Demireva, M.; O'Brien, J. T.; Williams, E. R. Water-Induced Folding of 1,7-Diammoniumheptane. *J. Am. Chem. Soc.* **2012**, *134*, 11216-11224.

- (798) Frick, M.; Schmidt, C. Mass Spectrometry—a Versatile Tool for Characterising the Lipid Environment of Membrane Protein Assemblies. *Chem. Phys. Lipids* **2019**, *221*, 145-157.
- (799) Marty, M. T.; Hoi, K. K.; Robinson, C. V. Interfacing Membrane Mimetics with Mass Spectrometry. *Acc. Chem. Res.* **2016**, *49*, 2459-2467.
- (800) Gupta, K.; Li, J.; Liko, I.; Gault, J.; Bechara, C.; Wu, D.; Hopper, J. T. S.; Giles, K.; Benesch, J. L. P.; Robinson, C. V. Identifying Key Membrane Protein Lipid Interactions Using Mass Spectrometry. *Nat. Protoc.* **2018**, *13*, 1106-1120.
- (801) Cosentino, K.; Ros, U.; García-Sáez, A. J. Assembling the Puzzle: Oligomerization of α -Pore Forming Proteins in Membranes. *Biochim. Biophys. Acta Biomembr.* **2016**, *1858*, 457-466.
- (802) Del Castillo, F. J.; Leal, S. C.; Moreno, F.; Castillo, I. D. The *Escherichia coli* K-12 sheA Gene Encodes a 34-kDa Secreted Haemolysin. *Mol. Microbiol.* **1997**, *25*, 107-115.
- (803) Ludwig, A.; Rhein, C. v.; Bauer, S.; Hüttinger, C.; Goebel, W. Molecular Analysis of Cytolysin A (ClyA) in Pathogenic *Escherichia coli* Strains. *J. Bacteriol.* **2004**, *186*, 5311-5320.
- (804) Oscarsson, J.; Westermark, M.; Löfdahl, S.; Olsen, B.; Palmgren, H.; Mizunoe, Y.; Wai, S. N.; Uhlin, B. E. Characterization of a Pore-Forming Cytotoxin Expressed by *Salmonella enterica* Serovars Typhi and Paratyphi A. *Infect. Immun.* **2002**, *70*, 5759-5769.
- (805) Murase, K. Cytolysin A (ClyA): A Bacterial Virulence Factor with Potential Applications in Nanopore Technology, Vaccine Development, and Tumor Therapy. *Toxins* **2022**, *14*, 78.
- (806) Lu, B.; Stokes, C.; Fahie, M.; Chen, M.; Golovchenko, J. A.; Hau, L. V. Protein Motion and Configurations in a Form-Fitting Nanopore: Avidin in ClyA. *Biophys. J.* **2018**, *115*, 801-808.
- (807) Scott, A. J.; Niitsu, A.; Kratochvil, H. T.; Lang, E. J. M.; Sengel, J. T.; Dawson, W. M.; Mahendran, K. R.; Mravic, M.; Thomson, A. R.; Brady, R. L.; Liu, L.; Mulholland, A. J.; Bayley, H.; DeGrado, W. F.; Wallace, M. I.; Woolfson, D. N. Constructing Ion Channels from Water-Soluble α -Helical Barrels. *Nat. Chem.* **2021**, *13*, 643-650.
- (808) Stewart, M. P.; Langer, R.; Jensen, K. F. Intracellular Delivery by Membrane Disruption: Mechanisms, Strategies, and Concepts. *Chem. Rev.* **2018**, *118*, 7409-7531.
- (809) Ayub, M.; Bayley, H. Engineered Transmembrane Pores. *Curr. Opin. Chem. Biol.* **2016**, *34*, 117-126.

- (810) Galenkamp, N. S.; Van Meervelt, V.; Mutter, N. L.; van der Heide, N. J.; Wloka, C.; Maglia, G. Preparation of Cytolysin A (ClyA) Nanopores. In *Nanopore Technology: Methods and Protocols*; Fahie, M. A. V., Ed.; Springer US, 2021; pp 11-18.
- (811) Li, X.; Lee, K. H.; Shorkey, S.; Chen, J.; Chen, M. Different Anomeric Sugar Bound States of Maltose Binding Protein Resolved by a Cytolysin A Nanopore Tweezer. *ACS Nano* **2020**, *14*, 1727-1737.
- (812) Dingfelder, F.; Macocco, I.; Benke, S.; Nettels, D.; Faccioli, P.; Schuler, B. Slow Escape from a Helical Misfolded State of the Pore-Forming Toxin Cytolysin A. *JACS Au* **2021**, *1*, 1217-1230.
- (813) Nomidis, S. K.; Hooyberghs, J.; Maglia, G.; Carlon, E. DNA Capture into the ClyA Nanopore: Diffusion-Limited Versus Reaction-Limited Processes. *J. Condens. Matter Phys.* **2018**, *30*, 304001.
- (814) Long, Q.; Zheng, P.; Zheng, X.; Li, W.; Hua, L.; Yang, Z.; Huang, W.; Ma, Y. Engineered Bacterial Membrane Vesicles Are Promising Carriers for Vaccine Design and Tumor Immunotherapy. *Adv. Drug Deliv. Rev.* **2022**, *186*, 114321.
- (815) Wu, Y.; Gooding, J. J. The Application of Single Molecule Nanopore Sensing for Quantitative Analysis. *Chem. Soc. Rev.* **2022**, *51*, 3862-3885.
- (816) Sathyanarayana, P.; Visweswariah, S. S.; Ayappa, K. G. Mechanistic Insights into Pore Formation by an α -Pore Forming Toxin: Protein and Lipid Bilayer Interactions of Cytolysin A. *Acc. Chem. Res.* **2021**, *54*, 120-131.
- (817) Sathyanarayana, P.; Maurya, S.; Behera, A.; Ravichandran, M.; Visweswariah, S. S.; Ayappa, K. G.; Roy, R. Cholesterol Promotes Cytolysin A Activity by Stabilizing the Intermediates During Pore Formation. *Proc. Natl. Acad. Sci. U. S. A.* **2018**, *115*, E7323-E7330.
- (818) Desikan, R.; Maiti, P. K.; Ayappa, K. G. Assessing the Structure and Stability of Transmembrane Oligomeric Intermediates of an α -Helical Toxin. *Langmuir* **2017**, *33*, 11496-11510.
- (819) Giri Rao, V. V. H.; Desikan, R.; Ayappa, K. G.; Gosavi, S. Capturing the Membrane-Triggered Conformational Transition of an α -Helical Pore-Forming Toxin. *J. Phys. Chem. B* **2016**, *120*, 12064-12078.
- (820) Vaidyanathan, M. S.; Sathyanarayana, P.; Maiti, P. K.; Visweswariah, S. S.; Ayappa, K. G. Lysis Dynamics and Membrane Oligomerization Pathways for Cytolysin A (ClyA) Pore-Forming Toxin. *RSC Adv.* **2014**, *4*, 4930-4942.
- (821) Benke, S.; Roderer, D.; Wunderlich, B.; Nettels, D.; Glockshuber, R.; Schuler, B. The Assembly Dynamics of the Cytolytic Pore Toxin ClyA. *Nat. Commun.* **2015**, *6*, 6198.

- (822) Agrawal, A.; Apoorva, K.; Ayappa, K. G. Transmembrane Oligomeric Intermediates of Pore Forming Toxin Cytolysin A Determine Leakage Kinetics. *RSC Adv.* **2017**, *7*, 51750-51762.
- (823) Sathyanarayana, P.; Desikan, R.; Ayappa, K. G.; Visweswariah, S. S. The Solvent-Exposed C-Terminus of the Cytolysin A Pore-Forming Toxin Directs Pore Formation and Channel Function in Membranes. *Biochemistry* **2016**, *55*, 5952-5961.
- (824) Roderer, D.; Benke, S.; Müller, M.; Fäh-Rechsteiner, H.; Ban, N.; Schuler, B.; Glockshuber, R. Characterization of Variants of the Pore-Forming Toxin ClyA from *Escherichia coli* Controlled by a Redox Switch. *Biochemistry* **2014**, *53*, 6357-6369.
- (825) Fahie, M.; Romano, F. B.; Chisholm, C.; Heuck, A. P.; Zbinden, M.; Chen, M. A Non-Classical Assembly Pathway of *Escherichia coli* Pore-Forming Toxin Cytolysin A. *J. Biol. Chem.* **2013**, *288*, 31042-31051.
- (826) Fahie, M. A.; Liang, L.; Avelino, A. R.; Pham, B.; Limpikirati, P.; Vachet, R. W.; Chen, M. Disruption of the Open Conductance in the B-Tongue Mutants of Cytolysin A. *Sci. Rep.* **2018**, *8*, 3796.
- (827) Roderer, D.; Benke, S.; Schuler, B.; Glockshuber, R. Soluble Oligomers of the Pore-Forming Toxin Cytolysin A from *Escherichia coli* Are Off-Pathway Products of Pore Assembly. *J. Biol. Chem.* **2016**, *291*, 5652-5663.
- (828) Roderer, D.; Glockshuber, R. Assembly Mechanism of the α -Pore-Forming Toxin Cytolysin A from *Escherichia coli*. *Philos. Trans. R. Soc. B* **2017**, *372*, 20160211.
- (829) Peraro, M. D.; van der Goot, F. G. Pore-Forming Toxins: Ancient, but Never Really out of Fashion. *Nat. Rev. Microbiol.* **2016**, *14*, 77-92.
- (830) Lata, K.; Singh, M.; Chatterjee, S.; Chattopadhyay, K. Membrane Dynamics and Remodelling in Response to the Action of the Membrane-Damaging Pore-Forming Toxins. *J. Membr. Biol.* **2022**, DOI: 10.1007/s00232-022-00227-z.
- (831) Los, F. C. O.; Randis, T. M.; Aroian, R. V.; Ratner, A. J. Role of Pore-Forming Toxins in Bacterial Infectious Diseases. *Microbiol. Mol. Biol. Rev.* **2013**, *77*, 173-207.
- (832) Verma, P.; Gandhi, S.; Lata, K.; Chattopadhyay, K. Pore-Forming Toxins in Infection and Immunity. *Biochem. Soc. Trans* **2021**, *49*, 455-465.
- (833) Wallace, A. J.; Stillman, T. J.; Atkins, A.; Jamieson, S. J.; Bullough, P. A.; Green, J.; Artymiuk, P. J. *E. coli* Hemolysin E (HlyE, ClyA, SheA): X-Ray Crystal Structure of the Toxin and Observation of Membrane Pores by Electron Microscopy. *Cell* **2000**, *100*, 265-276.

- (834) Eifler, N.; Vetsch, M.; Gregorini, M.; Ringler, P.; Chami, M.; Philippsen, A.; Fritz, A.; Müller, S. A.; Glockshuber, R.; Engel, A.; Grauschopf, U. Cytotoxin ClyA from *Escherichia coli* Assembles to a 13-Meric Pore Independent of Its Redox-State. *EMBO J.* **2006**, *25*, 2652-2661.
- (835) Soskine, M.; Biesemans, A.; De Maeyer, M.; Maglia, G. Tuning the Size and Properties of ClyA Nanopores Assisted by Directed Evolution. *J. Am. Chem. Soc.* **2013**, *135*, 13456-13463.
- (836) Peng, W.; de Souza Santos, M.; Li, Y.; Tomchick, D. R.; Orth, K. High-Resolution Cryo-EM Structures of the *E. coli* Hemolysin ClyA Oligomers. *PLoS One* **2019**, *14*, e0213423.
- (837) Mueller, M.; Grauschopf, U.; Maier, T.; Glockshuber, R.; Ban, N. The Structure of a Cytolytic α -Helical Toxin Pore Reveals Its Assembly Mechanism. *Nature* **2009**, *459*, 726-730.
- (838) Tzokov, S. B.; Wyborn, N. R.; Stillman, T. J.; Jamieson, S.; Czudnochowski, N.; Artymiuk, P. J.; Green, J.; Bullough, P. A. Structure of the Hemolysin E (HlyE, ClyA, and SheA) Channel in Its Membrane-Bound Form. *J. Biol. Chem.* **2006**, *281*, 23042-23049.
- (839) Borysik, A. J.; Hewitt, D. J.; Robinson, C. V. Detergent Release Prolongs the Lifetime of Native-Like Membrane Protein Conformations in the Gas-Phase. *J. Am. Chem. Soc.* **2013**, *135*, 6078-6083.
- (840) Jurchen, J. C.; Williams, E. R. Origin of Asymmetric Charge Partitioning in the Dissociation of Gas-Phase Protein Homodimers. *J. Am. Chem. Soc.* **2003**, *125*, 2817-2826.
- (841) Sciuto, S. V.; Liu, J.; Konermann, L. An Electrostatic Charge Partitioning Model for the Dissociation of Protein Complexes in the Gas Phase. *J. Am. Soc. Mass Spectrom.* **2011**, *22*, 1679.
- (842) Beardsley, R. L.; Jones, C. M.; Galhena, A. S.; Wysocki, V. H. Noncovalent Protein Tetramers and Pentamers with “*n*” Charges Yield Monomers with *n*/4 and *n*/5 Charges. *Anal. Chem.* **2009**, *81*, 1347-1356.
- (843) Harvey, S. R.; Seffernick, J. T.; Quintyn, R. S.; Song, Y.; Ju, Y.; Yan, J.; Sahasrabudde, A. N.; Norris, A.; Zhou, M.; Behrman, E. J.; Lindert, S.; Wysocki, V. H. Relative Interfacial Cleavage Energetics of Protein Complexes Revealed by Surface Collisions. *Proc. Natl. Acad. Sci. U. S. A.* **2019**, *116*, 8143-8148.
- (844) Quintyn, R. S.; Yan, J.; Wysocki, V. H. Surface-Induced Dissociation of Homotetramers with D2 Symmetry Yields Their Assembly Pathways and Characterizes the Effect of Ligand Binding. *Chem. Biol.* **2015**, *22*, 583-592.

- (845) Stiving, A. Q.; VanAernum, Z. L.; Busch, F.; Harvey, S. R.; Sarni, S. H.; Wysocki, V. H. Surface-Induced Dissociation: An Effective Method for Characterization of Protein Quaternary Structure. *Anal. Chem.* **2019**, *91*, 190-209.
- (846) Pratihar, S.; Kohale, S. C.; Bhakta, D. G.; Laskin, J.; Hase, W. L. Dynamics of Energy Transfer and Soft-Landing in Collisions of Protonated Dialanine with Perfluorinated Self-Assembled Monolayer Surfaces. *Phys. Chem. Chem. Phys.* **2014**, *16*, 23769-23778.
- (847) Žabka, J.; Dolejšek, Z.; Herman, Z. Energy Partitioning in Collisions of Slow Polyatomic Ions with Surfaces: Ethanol Molecular Ions on Surfaces Covered by Self-Assembled Monolayers (CF-SAM, CH-SAM, COOH-SAM). *J. Phys. Chem. A* **2002**, *106*, 10861-10869.
- (848) Laskin, J. Ion–Surface Collisions in Mass Spectrometry: Where Analytical Chemistry Meets Surface Science. *Int. J. Mass Spectrom.* **2015**, *377*, 188-200.
- (849) Laskin, J.; Futrell, J. H. Surface-Induced Dissociation of Peptide Ions: Kinetics and Dynamics. *J. Am. Soc. Mass Spectrom.* **2003**, *14*, 1340-1347.
- (850) Meroueh, O.; Hase, W. L. Energy Transfer Pathways in the Collisional Activation of Peptides. *Int. J. Mass Spectrom.* **2000**, *201*, 233-244.
- (851) Meroueh, O.; Hase, W. L. Dynamics of Energy Transfer in Peptide–Surface Collisions. *J. Am. Chem. Soc.* **2002**, *124*, 1524-1531.
- (852) Meroueh, S. O.; Wang, Y.; Hase, W. L. Direct Dynamics Simulations of Collision- and Surface-Induced Dissociation of N-Protonated Glycine. Shattering Fragmentation. *J. Phys. Chem. A* **2002**, *106*, 9983-9992.
- (853) Raz, T.; Levine, R. D. On the Shattering of Clusters by Surface Impact Heating. *J. Chem. Phys.* **1996**, *105*, 8097-8102.
- (854) Hoxha, A.; Collette, C.; De Pauw, E.; Leyh, B. Mechanism of Collisional Heating in Electrospray Mass Spectrometry: Ion Trajectory Calculations. *J. Phys. Chem. A* **2001**, *105*, 7326-7333.
- (855) Pratihar, S.; Kohale, S. C.; Vázquez, S. A.; Hase, W. L. Intermolecular Potential for Binding of Protonated Peptide Ions with Perfluorinated Hydrocarbon Surfaces. *J. Phys. Chem. B* **2014**, *118*, 5577-5588.
- (856) Galhena, A. S.; Dagan, S.; Jones, C. M.; Beardsley, R. L.; Wysocki, V. H. Surface-Induced Dissociation of Peptides and Protein Complexes in a Quadrupole/Time-of-Flight Mass Spectrometer. *Anal. Chem.* **2008**, *80*, 1425-1436.

- (857) Snyder, D. T.; Jones, B. J.; Lin, Y.-F.; Cooper-Shepherd, D. A.; Hewitt, D.; Wildgoose, J.; Brown, J. M.; Langridge, J. I.; Wysocki, V. H. Surface-Induced Dissociation of Protein Complexes on a Cyclic Ion Mobility Spectrometer. *Analyst* **2021**, *146*, 6861-6873.
- (858) Snyder, D. T.; Panczyk, E.; Stiving, A. Q.; Gilbert, J. D.; Somogyi, A.; Kaplan, D.; Wysocki, V. Design and Performance of a Second-Generation Surface-Induced Dissociation Cell for Fourier Transform Ion Cyclotron Resonance Mass Spectrometry of Native Protein Complexes. *Anal. Chem.* **2019**, *91*, 14049-14057.
- (859) VanAernum, Z. L.; Gilbert, J. D.; Belov, M. E.; Makarov, A. A.; Horning, S. R.; Wysocki, V. H. Surface-Induced Dissociation of Noncovalent Protein Complexes in an Extended Mass Range Orbitrap Mass Spectrometer. *Anal. Chem.* **2019**, *91*, 3611-3618.
- (860) Wysocki, V. H.; Ding, J.-M.; Jones, J. L.; Callahan, J. H.; King, F. L. Surface-Induced Dissociation in Tandem Quadrupole Mass Spectrometers: A Comparison of Three Designs. *J. Am. Soc. Mass Spectrom.* **1992**, *3*, 27-32.
- (861) Yan, J.; Zhou, M.; Gilbert, J. D.; Wolff, J. J.; Somogyi, Á.; Pedder, R. E.; Quintyn, R. S.; Morrison, L. J.; Easterling, M. L.; Paša-Tolić, L.; Wysocki, V. H. Surface-Induced Dissociation of Protein Complexes in a Hybrid Fourier Transform Ion Cyclotron Resonance Mass Spectrometer. *Anal. Chem.* **2017**, *89*, 895-901.
- (862) Zhou, M.; Huang, C.; Wysocki, V. H. Surface-Induced Dissociation of Ion Mobility-Separated Noncovalent Complexes in a Quadrupole/Time-of-Flight Mass Spectrometer. *Anal. Chem.* **2012**, *84*, 6016-6023.
- (863) Laskin, J.; Denisov, E. V.; Shukla, A. K.; Barlow, S. E.; Futrell, J. H. Surface-Induced Dissociation in a Fourier Transform Ion Cyclotron Resonance Mass Spectrometer: Instrument Design and Evaluation. *Anal. Chem.* **2002**, *74*, 3255-3261.
- (864) Tamara, S.; Dyachenko, A.; Fort, K. L.; Makarov, A. A.; Scheltema, R. A.; Heck, A. J. R. Symmetry of Charge Partitioning in Collisional and UV Photon-Induced Dissociation of Protein Assemblies. *J. Am. Chem. Soc.* **2016**, *138*, 10860-10868.
- (865) Aquilina, J. A. The Major Toxin from the Australian Common Brown Snake Is a Hexamer with Unusual Gas-Phase Dissociation Properties. *Proteins* **2009**, *75*, 478-485.
- (866) Boeri Erba, E.; Ruotolo, B. T.; Barsky, D.; Robinson, C. V. Ion Mobility-Mass Spectrometry Reveals the Influence of Subunit Packing and Charge on the Dissociation of Multiprotein Complexes. *Anal. Chem.* **2010**, *82*, 9702-9710.

- (867) Dodds, E. D.; Blackwell, A. E.; Jones, C. M.; Holso, K. L.; O'Brien, D. J.; Cordes, M. H. J.; Wysocki, V. H. Determinants of Gas-Phase Disassembly Behavior in Homodimeric Protein Complexes with Related yet Divergent Structures. *Anal. Chem.* **2011**, *83*, 3881-3889.
- (868) Kükrrer, B.; Barbu, I. M.; Copps, J.; Hogan, P.; Taylor, S. S.; van Duijn, E.; Heck, A. J. R. Conformational Isomers of Calcineurin Follow Distinct Dissociation Pathways. *J. Am. Soc. Mass Spectrom.* **2012**, *23*, 1534-1543.
- (869) Versluis, C.; van der Staaij, A.; Stokvis, E.; Heck, A. J. R.; de Craene, B. Metastable Ion Formation and Disparate Charge Separation in the Gas-Phase Dissection of Protein Assemblies Studied by Orthogonal Time-of-Flight Mass Spectrometry. *J. Am. Soc. Mass Spectrom.* **2001**, *12*, 329-336.
- (870) Yewdall, N. A.; Allison, Timothy M.; Pearce, F. G.; Robinson, C. V.; Gerrard, J. A. Self-Assembly of Toroidal Proteins Explored Using Native Mass Spectrometry. *Chem. Sci.* **2018**, *9*, 6099-6106.
- (871) Hall, Z.; Hernández, H.; Marsh, Joseph A.; Teichmann, Sarah A.; Robinson, Carol V. The Role of Salt Bridges, Charge Density, and Subunit Flexibility in Determining Disassembly Routes of Protein Complexes. *Structure* **2013**, *21*, 1325-1337.
- (872) Leney, A. C. Subunit pI Can Influence Protein Complex Dissociation Characteristics. *J. Am. Soc. Mass Spectrom.* **2019**, *30*, 1389-1395.
- (873) Li, G.; Huang, J.; Zheng, Z.; Cao, Q.; Tian, Y.; Huang, G.; Li, L.; Ruotolo, B. T. Bicarbonate Buffers Can Promote Crosslinking and Alternative Gas-Phase Dissociation Pathways for Multiprotein Complexes. *Int. J. Mass Spectrom.* **2021**, *469*, 116687.
- (874) Loo, R. R. O.; Loo, J. A. Salt Bridge Rearrangement (SaBRe) Explains the Dissociation Behavior of Noncovalent Complexes. *J. Am. Soc. Mass Spectrom.* **2016**, *27*, 975-990.
- (875) McAlary, L.; Harrison, J. A.; Aquilina, J. A.; Fitzgerald, S. P.; Kelso, C.; Benesch, J. L. P.; Yerbury, J. J. Trajectory Taken by Dimeric Cu/Zn Superoxide Dismutase through the Protein Unfolding and Dissociation Landscape Is Modulated by Salt Bridge Formation. *Anal. Chem.* **2020**, *92*, 1702-1711.
- (876) Pagel, K.; Hyung, S.-J.; Ruotolo, B. T.; Robinson, C. V. Alternate Dissociation Pathways Identified in Charge-Reduced Protein Complex Ions. *Anal. Chem.* **2010**, *82*, 5363-5372.
- (877) Jurchen, J. C.; Garcia, D. E.; Williams, E. R. Gas-Phase Dissociation Pathways of Multiply Charged Peptide Clusters. *J. Am. Soc. Mass Spectrom.* **2003**, *14*, 1373-1386.

- (878) Jurchen, J. C.; Garcia, D. E.; Williams, E. R. Further Studies on the Origins of Asymmetric Charge Partitioning in Protein Homodimers. *J. Am. Soc. Mass Spectrom.* **2004**, *15*, 1408-1415.
- (879) Fegan, S. K.; Thachuk, M. Controlling Dissociation Channels of Gas-Phase Protein Complexes Using Charge Manipulation. *J. Am. Soc. Mass Spectrom.* **2014**, *25*, 722-728.
- (880) Thachuk, M.; Fegan, S. K.; Raheem, N. Description and Control of Dissociation Channels in Gas-Phase Protein Complexes. *J. Chem. Phys.* **2016**, *145*, 065101.
- (881) Wanasundara, S. N.; Thachuk, M. Theoretical Investigations of the Dissociation of Charged Protein Complexes in the Gas Phase. *J. Am. Soc. Mass Spectrom.* **2007**, *18*, 2242-2253.
- (882) Wanasundara, S. N.; Thachuk, M. Free Energy Barrier Estimation for the Dissociation of Charged Protein Complexes in the Gas Phase. *J. Phys. Chem. A* **2009**, *113*, 3814-3821.
- (883) Wanasundara, S. N.; Thachuk, M. Toward an Improved Understanding of the Dissociation Mechanism of Gas Phase Protein Complexes. *J. Phys. Chem. B* **2010**, *114*, 11646-11653.
- (884) Kitova, E. N.; Sinelnikov, I.; Deng, L.; Klassen, J. S. Thermal Dissociation of Streptavidin Homotetramer in the Gas Phase: Subunit Loss Versus Backbone Fragmentation. *Int. J. Mass Spectrom.* **2013**, *345-347*, 97-103.
- (885) Sinelnikov, I.; Kitova, E. N.; Klassen, J. S. Influence of Coulombic Repulsion on the Dissociation Pathways and Energetics of Multiprotein Complexes in the Gas Phase. *J. Am. Soc. Mass Spectrom.* **2007**, *18*, 617-631.
- (886) Sinelnikov, I.; Kitova, E. N.; Klassen, J. S.; Armstrong, G. D. Effects of Single Amino Acid Substitution on the Dissociation of Multiply Charged Multiprotein Complexes in the Gas Phase. *J. Am. Soc. Mass Spectrom.* **2007**, *18*, 688-692.
- (887) Yefremova, Y.; Melder, F. T. I.; Danquah, B. D.; Opuni, K. F. M.; Koy, C.; Ehrens, A.; Frommholz, D.; Illges, H.; Koelbel, K.; Sobott, F.; Glocker, M. O. Apparent Activation Energies of Protein-Protein Complex Dissociation in the Gas-Phase Determined by Electrospray Mass Spectrometry. *Anal. Bioanal. Chem.* **2017**, *409*, 6549-6558.
- (888) Compton, P. D.; Fornelli, L.; Kelleher, N. L.; Skinner, O. S. Probing Asymmetric Charge Partitioning of Protein Oligomers During Tandem Mass Spectrometry. *Int. J. Mass Spectrom.* **2015**, *390*, 132-136.

- (889) Yen, H.-Y.; Abramsson, M. L.; Agasid, M. T.; Lama, D.; Gault, J.; Liko, I.; Kaldmäe, M.; Saluri, M.; Qureshi, A. A.; Suades, A.; Drew, D.; Degiacomi, M. T.; Marklund, E. G.; Allison, T. M.; Robinson, C. V.; Landreh, M. Electrospray Ionization of Native Membrane Proteins Proceeds Via a Charge Equilibration Step. *RSC Adv.* **2022**, *12*, 9671-9680.
- (890) Rahrt, R.; Auth, T.; Demireva, M.; Armentrout, P. B.; Koszinowski, K. Benzhydrylpyridinium Ions: A New Class of Thermometer Ions for the Characterization of Electrospray-Ionization Mass Spectrometers. *Anal. Chem.* **2019**, *91*, 11703-11711.
- (891) Sztáray, J.; Memboeuf, A.; Drahos, L.; Vékey, K. Leucine Enkephalin—a Mass Spectrometry Standard. *Mass Spectrom. Rev.* **2011**, *30*, 298-320.
- (892) Schnier, P. D.; Price, W. D.; Strittmatter, E. F.; Williams, E. R. Dissociation Energetics and Mechanisms of Leucine Enkephalin (M + H)⁺ and (2M + X)⁺ Ions (X = H, Li, Na, K, and Rb) Measured by Blackbody Infrared Radiative Dissociation. *J. Am. Soc. Mass Spectrom.* **1997**, *8*, 771-780.
- (893) Bornschein, R. E.; Ruotolo, B. T. Ion Mobility-Mass Spectrometry of Charge-Reduced Protein Complexes Reveals General Trends in the Collisional Ejection of Compact Subunits. *Analyst* **2015**, *140*, 7020-7029.
- (894) Pitteri, S. J.; Chrisman, P. A.; Badman, E. R.; McLuckey, S. A. Charge-State Dependent Dissociation of a Trypsin/Inhibitor Complex Via Ion Trap Collisional Activation. *Int. J. Mass Spectrom.* **2006**, *253*, 147-155.
- (895) Sipe, S. N.; Brodbelt, J. S. Impact of Charge State on 193 nm Ultraviolet Photodissociation of Protein Complexes. *Phys. Chem. Chem. Phys.* **2019**, *21*, 9265-9276.
- (896) Rocha, M. A.; Sprague-Piercy, M. A.; Kwok, A. O.; Roskamp, K. W.; Martin, R. W. Chemical Properties Determine Solubility and Stability in β -Crystallins of the Eye Lens. *ChemBioChem* **2021**, *22*, 1329-1346.
- (897) Truscott, R. J. W. Macromolecular Deterioration as the Ultimate Constraint on Human Lifespan. *Ageing Res. Rev.* **2011**, *10*, 397-403.
- (898) Truscott, R. J. W.; Augusteyn, R. C. Changes in Human Lens Proteins During Nuclear Cataract Formation. *Exp. Eye Res.* **1977**, *24*, 159-170.
- (899) Truscott, R. J. W.; Schey, K. L.; Friedrich, M. G. Old Proteins in Man: A Field in Its Infancy. *Trends Biochem. Sci.* **2016**, *41*, 654-664.
- (900) Friedrich, M. G. Spontaneous Breakdown of Long-Lived Proteins in Aging and Their Implications in Disease. In *Long-Lived Proteins in Human Aging and Disease*; Truscott, R., Ed.; Wiley-VCH GmbH, 2021; pp 97-125.

- (901) Truscott, R. J. W. Degradation of Long-Lived Proteins as a Cause of Autoimmune Diseases. In *Long-Lived Proteins in Human Aging and Disease*; Truscott, R., Ed.; Wiley-VCH GmbH, 2021; pp 159-173.
- (902) Vaquer-Alicea, J.; Diamond, M. I. Propagation of Protein Aggregation in Neurodegenerative Diseases. *Annu. Rev. Biochem.* **2019**, *88*, 785-810.
- (903) Friedrich, M. G.; Wang, Z.; Schey, K. L.; Truscott, R. J. W. Spontaneous Cleavage at Glu and Gln Residues in Long-Lived Proteins. *ACS Chem. Biol.* **2021**, *16*, 2244-2254.
- (904) Hains, P. G.; Truscott, R. J. W. Post-Translational Modifications in the Nuclear Region of Young, Aged, and Cataract Human Lenses. *J. Proteome Res.* **2007**, *6*, 3935-3943.
- (905) Hains, P. G.; Truscott, R. J. W. Age-Dependent Deamidation of Lifelong Proteins in the Human Lens. *Invest. Ophthalmol. Vis. Sci.* **2010**, *51*, 3107-3114.
- (906) Hooi, M. Y. S.; Raftery, M. J.; Truscott, R. J. W. Age-Dependent Deamidation of Glutamine Residues in Human γ S Crystallin: Deamidation and Unstructured Regions. *Protein Sci.* **2012**, *21*, 1074-1079.
- (907) Hooi, M. Y. S.; Raftery, M. J.; Truscott, R. J. W. Racemization of Two Proteins over Our Lifespan: Deamidation of Asparagine 76 in γ S Crystallin Is Greater in Cataract Than in Normal Lenses across the Age Range. *Invest. Ophthalmol. Vis. Sci.* **2012**, *53*, 3554-3561.
- (908) Truscott, R. J. W. Age-Related Nuclear Cataract—Oxidation Is the Key. *Exp. Eye Res.* **2005**, *80*, 709-725.
- (909) Brubaker, W. D.; Freites, J. A.; Golchert, K. J.; Shapiro, R. A.; Morikis, V.; Tobias, D. J.; Martin, R. W. Separating Instability from Aggregation Propensity in γ S-Crystallin Variants. *Biophys. J.* **2011**, *100*, 498-506.
- (910) Jiang, J.; Golchert, K. J.; Kingsley, C. N.; Brubaker, W. D.; Martin, R. W.; Mukamel, S. Exploring the Aggregation Propensity of γ S-Crystallin Protein Variants Using Two-Dimensional Spectroscopic Tools. *J. Phys. Chem. B* **2013**, *117*, 14294-14301.
- (911) Roskamp, K. W.; Montelongo, D. M.; Anorma, C. D.; Bandak, D. N.; Chua, J. A.; Malecha, K. T.; Martin, R. W. Multiple Aggregation Pathways in Human γ S-Crystallin and Its Aggregation-Prone G18V Variant. *Invest Ophthalmol Vis Sci* **2017**, *58*, 2397-2405.
- (912) Boros, S.; Wilmarth, P. A.; Kamps, B.; de Jong, W. W.; Bloemendal, H.; Lampi, K.; Boelens, W. C. Tissue Transglutaminase Catalyzes the Deamidation of Glutamines in Lens β B2- and β B3-Crystallins. *Exp. Eye Res.* **2008**, *86*, 383-393.

- (913) Harms, M. J.; Wilmarth, P. A.; Kapfer, D. M.; Steel, E. A.; David, L. L.; Bächinger, H. P.; Lampi, K. J. Laser Light-Scattering Evidence for an Altered Association of Beta B1-Crystallin Deamidated in the Connecting Peptide. *Protein Sci.* **2004**, *13*, 678-686.
- (914) Kim, Y. H.; Kapfer, D. M.; Boekhorst, J.; Lubsen, N. H.; Bächinger, H. P.; Shearer, T. R.; David, L. L.; Feix, J. B.; Lampi, K. J. Deamidation, but Not Truncation, Decreases the Urea Stability of a Lens Structural Protein, β B1-Crystallin. *Biochemistry* **2002**, *41*, 14076-14084.
- (915) Lampi, K. J.; Amyx, K. K.; Ahmann, P.; Steel, E. A. Deamidation in Human Lens β B2-Crystallin Destabilizes the Dimer. *Biochemistry* **2006**, *45*, 3146-3153.
- (916) Lampi, K. J.; Fox, C. B.; David, L. L. Changes in Solvent Accessibility of Wild-Type and Deamidated β B2-Crystallin Following Complex Formation with α A-Crystallin. *Exp. Eye Res.* **2012**, *104*, 48-58.
- (917) Lampi, K. J.; Kim, Y. H.; Bachinger, H. P.; Boswell, B. A.; Lindner, R. A.; Carver, J. A.; Shearer, T. R.; David, L. L.; Kapfer, D. M. Decreased Heat Stability and Increased Chaperone Requirement of Modified Human BetaB1-Crystallins. *Mol. Vis.* **2002**, *8*, 359-366.
- (918) Lampi, K. J.; Ma, Z.; Hanson, S. R. A.; Azuma, M.; Shih, M.; Shearer, T. R.; Smith, D. L.; Smith, J. B.; David, L. L. Age-Related Changes in Human Lens Crystallins Identified by Two-Dimensional Electrophoresis and Mass Spectrometry. *Exp. Eye Res.* **1998**, *67*, 31-43.
- (919) Lampi, K. J.; Murray, M. R.; Peterson, M. P.; Eng, B. S.; Yue, E.; Clark, A. R.; Barbar, E.; David, L. L. Differences in Solution Dynamics between Lens β -Crystallin Homodimers and Heterodimers Probed by Hydrogen–Deuterium Exchange and Deamidation. *Biochim. Biophys. Acta Gen. Subj.* **2016**, *1860*, 304-314.
- (920) Lampi, K. J.; Oxford, J. T.; Bachinger, H. P.; Shearer, T. R.; David, L. L.; Kapfer, D. M. Deamidation of Human β B1 Alters the Elongated Structure of the Dimer. *Exp. Eye Res.* **2001**, *72*, 279-288.
- (921) Takata, T.; Oxford, J. T.; Demeler, B.; Lampi, K. J. Deamidation Destabilizes and Triggers Aggregation of a Lens Protein, BetaA3-Crystallin. *Protein Sci.* **2008**, *17*, 1565-1575.
- (922) Takata, T.; Woodbury, L. G.; Lampi, K. J. Deamidation Alters Interactions of Beta-Crystallins in Hetero-Oligomers. *Mol. Vis.* **2009**, *15*, 241-249.
- (923) David, L. L. Modifications of Long-Lived Proteins That Affect Protein Solubility. In *Long-Lived Proteins in Human Aging and Disease*; Truscott, R., Ed.; Wiley-VCH GmbH, 2021; pp 127-158.

- (924) Julian, R. R. How Isomerization and Epimerization in Long-Lived Proteins Affect Lysosomal Degradation and Proteostasis. In *Long-Lived Proteins in Human Aging and Disease*; Truscott, R., Ed.; Wiley-VCH GmbH, 2021; pp 175-188.
- (925) Basak, A.; Bateman, O.; Slingsby, C.; Pande, A.; Asherie, N.; Ogun, O.; Benedek, G. B.; Pande, J. High-Resolution X-Ray Crystal Structures of Human γ D Crystallin (1.25Å) and the R58H Mutant (1.15Å) Associated with Aculeiform Cataract. *J. Mol. Biol.* **2003**, *328*, 1137-1147.
- (926) Bateman, O. A.; Slingsby, C. Structural Studies on β H-Crystallin from Bovine Eye Lens. *Exp. Eye Res.* **1992**, *55*, 127-133.
- (927) Bax, B.; Lapatto, R.; Nalini, V.; Driessen, H.; Lindley, P. F.; Mahadevan, D.; Blundell, T. L.; Slingsby, C. X-Ray Analysis of β B2-Crystallin and Evolution of Oligomeric Lens Proteins. *Nature* **1990**, *347*, 776-780.
- (928) Bloemendal, H.; de Jong, W.; Jaenicke, R.; Lubsen, N. H.; Slingsby, C.; Tardieu, A. Ageing and Vision: Structure, Stability and Function of Lens Crystallins. *Prog. Biophys. Mol. Biol.* **2004**, *86*, 407-485.
- (929) Carver, J. A. Probing the Structure and Interactions of Crystallin Proteins by NMR Spectroscopy. *Prog. Retin. Eye Res.* **1999**, *18*, 431-462.
- (930) Kroone, R. C.; Elliott, G. S.; Ferszt, A.; Slingsby, C.; Lubsen, N. H.; Schoenmakers, J. G. G. The Role of the Sequence Extensions in β -Crystallin Assembly. *Protein Eng. Des. Sel.* **1994**, *7*, 1395-1399.
- (931) Lapatto, R.; Nalini, V.; Bax, B.; Driessen, H.; Lindley, P. F.; Blundell, T. L.; Slingsby, C. High Resolution Structure of an Oligomeric Eye Lens B-Crystallin: Loops, Arches, Linkers and Interfaces in β B2 Dimer Compared to a Monomeric γ -Crystallin. *J. Mol. Biol.* **1991**, *222*, 1067-1083.
- (932) Nalini, V.; Bax, B.; Driessen, H.; Moss, D. S.; Lindley, P. F.; Slingsby, C. Close Packing of an Oligomeric Eye Lens β -Crystallin Induces Loss of Symmetry and Ordering of Sequence Extensions. *J. Mol. Biol.* **1994**, *236*, 1250-1258.
- (933) Purkiss, A. G.; Bateman, O. A.; Goodfellow, J. M.; Lubsen, N. H.; Slingsby, C. The X-Ray Crystal Structure of Human γ S-Crystallin C-Terminal Domain. *J. Biol. Chem.* **2002**, *277*, 4199-4205.
- (934) Slingsby, C.; Bateman, O. A. Quaternary Interactions in Eye Lens β -Crystallins: Basic and Acidic Subunits Of β -Crystallins Favor Heterologous Association. *Biochemistry* **1990**, *29*, 6592-6599.
- (935) van Montfort, R. L. M.; Bateman, O. A.; Lubsen, N. H.; Slingsby, C. Crystal Structure of Truncated Human β B1-Crystallin. *Protein Sci.* **2003**, *12*, 2606-2612.

- (936) Grosas, A. B.; Carver, J. A. Eye Lens Crystallins: Remarkable Long-Lived Proteins. In *Long-Lived Proteins in Human Aging and Disease*; Truscott, R., Ed.; Wiley-VCH GmbH, 2021; pp 59-96.
- (937) Congdon, N.; O'Colmain, B.; Klaver, C. C. W.; Klein, R.; Munoz, B.; Friedman, D. S.; Kempen, J.; Taylor, H. R.; Mitchell, P. Causes and Prevalence of Visual Impairment among Adults in the United States. *Arch. Ophthalmol.* **2004**, *122*, 477-485.
- (938) Wilmarth, P.; David, L.; Lampi, K. Normal Age-Related Changes: Crystallin Modifications, Lens Hardening. In *Encyclopedia of the Eye*; Elsevier, 2010; pp 161-166.
- (939) Wilmarth, P. A.; Tanner, S.; Dasari, S.; Nagalla, S. R.; Riviere, M. A.; Bafna, V.; Pevzner, P. A.; David, L. L. Age-Related Changes in Human Crystallins Determined from Comparative Analysis of Post-Translational Modifications in Young and Aged Lens: Does Deamidation Contribute to Crystallin Insolubility? *J. Proteome Res.* **2006**, *5*, 2554-2566.
- (940) Lampi, K. J.; Wilmarth, P. A.; Murray, M. R.; David, L. L. Lens β -Crystallins: The Role of Deamidation and Related Modifications in Aging and Cataract. *Prog. Biophys. Mol. Biol.* **2014**, *115*, 21-31.
- (941) Graw, J. The Crystallins: Genes, Proteins and Diseases. *Biol. Chem.* **1997**, *378*, 1331-1348.
- (942) Horwitz, J. Alpha-Crystallin Can Function as a Molecular Chaperone. *Proc. Natl. Acad. Sci. U. S. A.* **1992**, *89*, 10449-10453.
- (943) V  r  tout, F.; Tardieu, A. The Protein Concentration Gradient within Eye Lens Might Originate from Constant Osmotic Pressure Coupled to Differential Interactive Properties of Crystallins. *Eur. Biophys. J.* **1989**, *17*, 61-68.
- (944) Huizinga, A.; Bot, A. C.; de Mul, F. F.; Vrensen, G. F.; Greve, J. Local Variation in Absolute Water Content of Human and Rabbit Eye Lenses Measured by Raman Microspectroscopy. *Exp. Eye Res.* **1989**, *48*, 487-496.
- (945) Uhlhorn, S. R.; Borja, D.; Manns, F.; Parel, J.-M. Refractive Index Measurement of the Isolated Crystalline Lens Using Optical Coherence Tomography. *Vis. Res.* **2008**, *48*, 2732-2738.
- (946) Martin, R. W. NMR Studies of Eye Lens Crystallins. In *eMagRes*, Vol. 3; John Wiley & Sons, Ltd., 2014; pp 139-152.
- (947) Smith, M. A.; Bateman, O. A.; Jaenicke, R.; Slingsby, C. Mutation of Interfaces in Domain-Swapped Human β B2-Crystallin. *Protein Sci.* **2007**, *16*, 615-625.

- (948) Xi, Z.; Whitley, M. J.; Gronenborn, A. M. Human β B2-Crystallin Forms a Face-En-Face Dimer in Solution: An Integrated NMR and SAXS Study. *Structure* **2017**, *25*, 496-505.
- (949) Sagar, V.; Chaturvedi, S. K.; Schuck, P.; Wistow, G. Crystal Structure of Chicken γ S-Crystallin Reveals Lattice Contacts with Implications for Function in the Lens and the Evolution of the $\beta\gamma$ -Crystallins. *Structure* **2017**, *25*, 1068-1078.e1062.
- (950) Forsythe, H. M.; Vetter, C. J.; Jara, K. A.; Reardon, P. N.; David, L. L.; Barbar, E. J.; Lampi, K. J. Altered Protein Dynamics and Increased Aggregation of Human γ S-Crystallin Due to Cataract-Associated Deamidations. *Biochemistry* **2019**, *58*, 4112-4124.
- (951) Vetter, C. J.; Thorn, D. C.; Wheeler, S. G.; Mundorff, C. C.; Halverson, K. A.; Wales, T. E.; Shinde, U. P.; Engen, J. R.; David, L. L.; Carver, J. A.; Lampi, K. J. Cumulative Deamidations of the Major Lens Protein γ S-Crystallin Increase Its Aggregation During Unfolding and Oxidation. *Protein Sci.* **2020**, *29*, 1945-1963.
- (952) Khago, D.; Bierma, J. C.; Roskamp, K. W.; Kozlyuk, N.; Martin, R. W. Protein Refractive Index Increment Is Determined by Conformation as Well as Composition. *J. Condens. Matter Phys.* **2018**, *30*, 435101.
- (953) Slingsby, C.; Wistow, G. J.; Clark, A. R. Evolution of Crystallins for a Role in the Vertebrate Eye Lens. *Protein Sci.* **2013**, *22*, 367-380.
- (954) Kalligeraki, A. A.; Quinlan, R. A. Structural Proteins | Crystallins of the Mammalian Eye Lens. In *Encyclopedia of Biological Chemistry III (Third Edition)*, Vol. 3; Jez, J., Ed.; Elsevier, 2021; pp 639-667.
- (955) Bari, K. J. The Structural Biology of Crystallin Aggregation: Challenges and Outlook. *FEBS J.* **2021**, *288*, 5888-5902.
- (956) Bari, K. J.; Sharma, S. A Perspective on Biophysical Studies of Crystallin Aggregation and Implications for Cataract Formation. *J. Phys. Chem. B* **2020**, *124*, 11041-11054.
- (957) Baldwin, A. J.; Lioe, H.; Robinson, C. V.; Kay, L. E.; Benesch, J. L. P. α B-Crystallin Polydispersity Is a Consequence of Unbiased Quaternary Dynamics. *J. Mol. Biol.* **2011**, *413*, 297-309.
- (958) Takata, T.; Oxford, J. T.; Brandon, T. R.; Lampi, K. J. Deamidation Alters the Structure and Decreases the Stability of Human Lens β A3-Crystallin. *Biochemistry* **2007**, *46*, 8861-8871.
- (959) Bateman, O. A.; Sarra, R.; van Genesen, S. T.; Kappé, G.; Lubsen, N. H.; Slingsby, C. The Stability of Human Acidic β -Crystallin Oligomers and Hetero-Oligomers. *Exp. Eye Res.* **2003**, *77*, 409-422.

- (960) Lampi, K. J.; Ma, Z.; Shih, M.; Shearer, T. R.; Smith, J. B.; Smith, D. L.; David, L. L. Sequence Analysis of β A3, β B3, and β A4 Crystallins Completes the Identification of the Major Proteins in Young Human Lens. *J. Biol. Chem.* **1997**, *272*, 2268-2275.
- (961) Michiel, M.; Duprat, E.; Skouri-Panet, F.; Lampi, J. A.; Tardieu, A.; Lampi, K. J.; Finet, S. Aggregation of Deamidated Human β B2-Crystallin and Incomplete Rescue by α -Crystallin Chaperone. *Exp. Eye Res.* **2010**, *90*, 688-698.